Lecture Notes in Mechanical Engineering

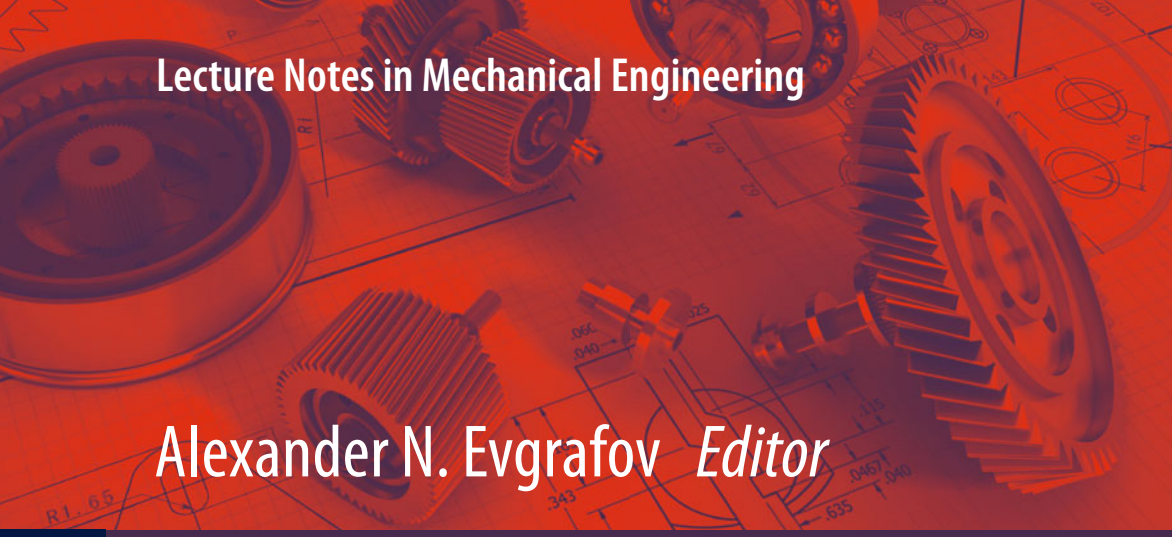

Alexander N. Evgrafov *Editor*

# Advances in Mechanical Engineering

## Selected Contributions from the Conference "Modern Engineering: Science and Education", Saint Petersburg, Russia, May 2018

Springer

# Lecture Notes in Mechanical Engineering

**Lecture Notes in Mechanical Engineering (LNME)** publishes the latest developments in Mechanical Engineering—quickly, informally and with high quality. Original research reported in proceedings and post-proceedings represents the core of LNME. Volumes published in LNME embrace all aspects, subfields and new challenges of mechanical engineering. Topics in the series include:

- Engineering Design
- Machinery and Machine Elements
- Mechanical Structures and Stress Analysis
- Engine Technology
- Aerospace Technology and Astronautics
- Nanotechnology and Microengineering
- Control, Robotics, Mechatronics
- Theoretical and Applied Mechanics
- Dynamical Systems, Control
- Fluid Mechanics
- Engineering Thermodynamics, Heat and Mass Transfer
- Precision Engineering, Instrumentation, Measurement
- Materials Engineering
- Tribology and Surface Technology

To submit a proposal or request further information, please contact the appropriate Springer Editor:

Li Shen at li.shen@springer.com (China)
Dr. Akash Chakraborty at akash.chakraborty@springernature.com (India)
Dr. Leontina Di Cecco at Leontina.dicecco@springer.com (all other Countries)
Please check the Springer Tracts in Mechanical Engineering at http://www.springer.com/series/11693 if you are interested in monographs, textbooks or edited books. To submit a proposal, please contact Leontina.dicecco@springer.com and Li.shen@springer.com.

**Indexed by SCOPUS. The books of the series are submitted for indexing to Web of Science.**

More information about this series at http://www.springer.com/series/11236

Alexander N. Evgrafov
Editor

# Advances in Mechanical Engineering

## Selected Contributions from the Conference "Modern Engineering: Science and Education", Saint Petersburg, Russia, May 2018

Springer

*Editor*
Alexander N. Evgrafov
Peter the Great St. Petersburg
Polytechnic University
Saint Petersburg, Russia

ISSN 2195-4356 ISSN 2195-4364 (electronic)
Lecture Notes in Mechanical Engineering
ISBN 978-3-030-11980-5 ISBN 978-3-030-11981-2 (eBook)
https://doi.org/10.1007/978-3-030-11981-2

Library of Congress Control Number: 2019930981



This Springer imprint is published by the registered company Springer Nature Switzerland AG
The registered company address is: Gewerbestrasse 11, 6330 Cham, Switzerland

# Preface

The "Modern Mechanical Engineering: Science and Education" (MMESE) conference was initially organized by the Mechanical Engineering Department of Peter the Great St. Petersburg Polytechnic University in June 2011, in St. Petersburg, Russia. It was envisioned as a forum to bring together scientists, university professors, graduate students, and mechanical engineers, presenting new science, technology, and engineering ideas and achievements.

The idea of holding such a forum proved to be highly relevant. Moreover, both the location and timing of the conference were quite appealing. Late June is a wonderful and romantic season in St. Petersburg—one of the most beautiful cities, located on the Neva riverbanks and surrounded by charming greenbelts. The conference attracted many participants, working in various fields of engineering: design, mechanics, materials, etc. The success of the conference inspired the organizers to turn the conference into an annual event.

More than 70 papers were presented at the seventh conference MMESE-2018. They covered topics ranging from the mechanics of machines, material engineering, structural strength, and tribological behavior to transport technologies, machinery quality, and innovations, in addition to dynamics of machines, walking mechanisms, and computational methods. All presenters contributed greatly to the success of the conference. However, for the purposes of this book, only 20 papers, authored by research groups representing various universities and institutes, were selected for inclusion.

I am particularly grateful to the authors for their contributions and all the participating experts for their valuable advice. Furthermore, I thank the staff and management of the university for their cooperation and support, and especially all members of the program committee and the organizing committee for their work in preparing and organizing the conference. Last but not least, I thank Springer for its professional assistance and particularly Mr. Pierpaolo Riva who supported this publication.

Saint Petersburg, Russia — Alexander N. Evgrafov

# Contents

# Packing Compaction Algorithm for Problems of Resource Placement Optimization


**Vladislav A. Chekanin and Alexander V. Chekanin**

**Abstract** The paper is devoted to a new heuristic packing compaction algorithm for the rectangular cutting and orthogonal packing problems. This algorithm is based on the idea of iterative local replacement of some objects placed in a container. Six selection rules for deleting placed objects and subsequent redistribution of them with the aim to obtain a packing with a better density are proposed. The effectiveness of the packing compaction algorithm has been investigated on the standard test instances of the rectangular cutting problem.

**Keywords** Packing compaction algorithm · Optimization · Orthogonal packing problem · Rectangular cutting problem · Resource placement problem

## 1 Introduction

The class of resource placement problems unites a large number of optimization problems that are classical problems of the mathematical theory of operations research. The solution of these problems is to find the most rational ways of placement resources of one type (called by objects) among resources of another type (called by containers). A detailed classification of resource placement problems was proposed by G. Wascher, H. Haubner, and H. Schumann in 2007 [1], during the preparation of which 445 scientific articles were reviewed. The wide distribution of practical applications of resource placement problems in industry and economics [2–6] makes it urgent to develop new effective algorithms and methods for solving the problems, which is confirmed by the presence of a large number of scientific publications on this topic [7–9].

V. A. Chekanin (✉) · A. V. Chekanin
Moscow State University of Technology «STANKIN», Moscow, Russia
e-mail: vladchekanin@rambler.ru

A. V. Chekanin
e-mail: avchekanin@rambler.ru



A. N. Evgrafov (ed.), *Advances in Mechanical Engineering*,
Lecture Notes in Mechanical Engineering,
https://doi.org/10.1007/978-3-030-11981-2_1

Solving all the optimization problems related to the placement or allocation of orthogonal resources presented in the form of rectangles or parallelepipeds is reduced to solving the combinatorial NP-hard problem of orthogonal packing, which is a classical discrete optimization problem [10]. To obtain the optimal solutions of these problems, it is required to use the resource-intensive optimization algorithms, while in practice it turns out to be ineffective due to the considerable time resources. Therefore, to solve NP-hard orthogonal packing problems are often used heuristic and metaheuristic optimization algorithms that provide approximate (suboptimal) solutions in an acceptable time [11–14]. To improve the quality of the suboptimal solutions is proposed an iterative packing compaction algorithm based on the idea of local replacement of some placed in a container objects.

## 2 Problem Statement

Consider the statement of the $D$-dimensional ($D = 2, 3$) orthogonal packing problem in the form of the problem of packing the orthogonal objects into one container. Here is given a set of $n$ orthogonal objects with the dimensions $\left\{w_i^1, w_i^2, \ldots, w_i^D\right\}$, $i \in \{1, \ldots, n\}$ as well as an orthogonal container with the dimensions $\left\{W^1, W^2, \ldots, W^D\right\}$. The superscript in all formulas indicates the dimension. We denote by $\left(x_i^1; x_i^2; \ldots; x_i^D\right)$ the position of an object $i$ inside the container. The goal of the problem is to find the most density placement of all the objects within the container under the conditions of the correct placement [2, 6].

The statement of the $D$-dimensional orthogonal packing problem includes specifying of a load direction of a container as the priority selection list $\{L\} = \left\{L^1; L^2; \ldots; L^D\right\}$ of its coordinate axes, where $L^d \in [1; D]$ $\forall d \in \{1, \ldots, D\}$. When placing each new object into a container, the selection of its free spaces for the object must be satisfied in the order specified by the priority list $\{L\}$ [6, 15].

The quality of a placement is estimated by the criteria of length minimization of the filled part of the container (the length is measured along the coordinate axis $l = L^D$), i.e., the minimized fitness function is calculated as $S = \max\left(x_i^l + w_i^l\right)$, $i = 1, \ldots, n$, and it defines the position of the most remote object in the container.

We will use the developed model of potential containers for describing a current state of the container in the process of placing the objects into it. This model describes all the free spaces of the container as a set of so-called potential containers which are orthogonal objects with the largest dimensions that potentially can be placed into the container [15, 16]. A potential container $k$ is described by a vector $\left\{p_k^1; p_k^2; \ldots; p_k^D\right\}$ containing its overall dimensions, as well as a vector $\left\{x_k^1; x_k^2; \ldots; x_k^D\right\}$ containing the position of its coordinate system origin relative to the coordinate system of the container.

A solution of any packing problem is represented by a so-called placement string (also known as a chromosome) which contains a sequence of objects selected for placing into a container. To get a packing, it is necessary to decode the placement string and select the most suitable free spaces of the container for each object to


**Fig. 1** Objects selected by the method AREA

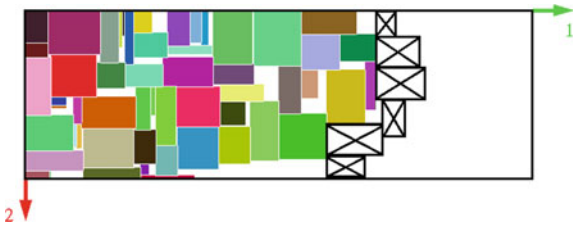


**Fig. 2** Objects selected by the method LAST

be placed into it. For this purpose is used the deterministic strategy of choice the free spaces of the container. This strategy is the sequential selection of potential containers previously sorted in accordance with the given packing loading direction [15]. Effective ordering of all potential containers is achieved with the multilevel linked data structure, described in detail in papers [17, 18].

## 3 Packing Compaction Algorithm

The proposed packing compacting algorithm is based on the use of rules which select the placed objects for deleting them with subsequent more rational filling of the freed spaces in the container with these objects. The implementation of the algorithm for deleting objects designed, especially for the model of potential containers, is described in detail in paper [19]. The object selection rules are based on the methods given below.

1. Method AREA selects from the container all objects contacting with the most remote edges of an imaginary orthogonal object with the dimensions $V^d = W^d \, \forall d \neq l$, $V^l = \max\left(x_i^l + w_i^l\right)$, $i = 1, \ldots, n$ which encloses the packing (Fig. 1);
2. Method LAST selects from the container all objects contacting with potential containers, the edges of which along the coordinate axis $l$ match to the border of the container, i.e., the potential containers for which $x_k^l + p_k^l = W^l$ (Fig. 2);
3. Method MAX selects from the container all objects contacting with a potential container that has the maximal volume (area) and is located inside the packing, i.e., the potential container for which $x_k^l + p_k^l < W^l$ (on Fig. 3 the found potential container is shown as a rectangle without color fill);

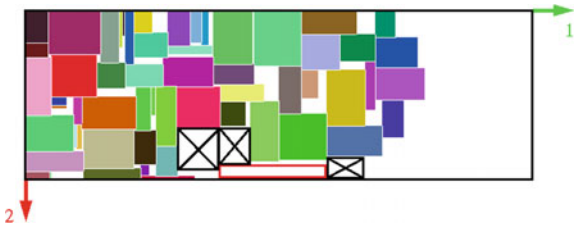


**Fig. 3** Objects selected by the method MAX

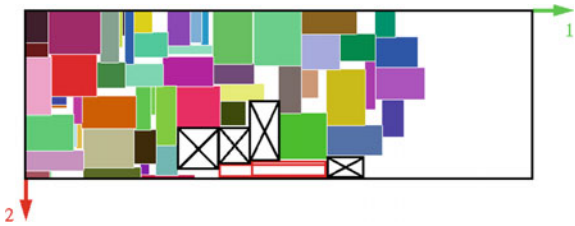


**Fig. 4** Objects selected by the method DOUBLE

4. Method DOUBLE selects from the container all objects contacting with two potential containers that have maximal volumes (areas) and located inside the packing (Fig. 4).

The methods of the first group (AREA and LAST) are intended to select objects located as far away from the origin of the container. The methods of the second group (MAX and DOUBLE) are intended to select the objects located close to the largest free spaces in the container. Based on these methods, six object selection rules for local reallocation of placed objects in a container have been implemented (see Table 1).

In order to optimize the placement of previously deleted objects, a one-pass heuristic algorithm with a population consisting of ten placement strings (chromosomes) is used, composed as follows:

- chromosome 1 contains sequence of objects in the order as they recorded in the considered packing problem;
- chromosome 2 contains sequence of objects ordered by descending of their volumes (areas);
- chromosome 3 contains sequence of objects ordered by ascending of their volumes (areas);
- chromosome 4 contains sequence of objects ordered by descending of their dimensions measured along the coordinate axis $l$;
- chromosome 5 contains sequence of objects ordered by ascending of their dimensions measured along the coordinate axis $l$;
- chromosomes 6–10 contain pseudorandom sequences of objects.

If any chromosome of this heuristic algorithm provides obtaining of a packing with the better density (i.e., with the smaller value of the fitness function), then the best found solution is saved, after which is performed an attempt to compact this

**Table 1** Object selection rules

| No. | Rule | Method 1 | Method 2 | Description |
|---|---|---|---|---|
| 1 | MAX_AREA | AREA | MAX | Cooperative application of the two methods |
| 2 | MAX_LAST | LAST | MAX | Cooperative application of the two methods |
| 3 | DOUBLE_AREA | AREA | DOUBLE | Cooperative application of the two methods |
| 4 | DOUBLE_LAST | LAST | DOUBLE | Cooperative application of the two methods |
| 5 | MAXMAX_AREA | AREA | MAX | Application of the method AREA as well as application of the method MAX to the packing obtained after deleting of all objects previously found by the method MAX |
| 6 | MAXMAX_LAST | LAST | MAX | Application of the method LAST as well as application of the method MAX to the packing obtained after deleting of all objects previously found by the method MAX |

packing again. This process is repeated iteratively while the packing compaction algorithm provides a better density of the placement or until the stop criteria will be performed which is the achievement of a predefined number of iterations of the algorithm.

Figure 5 shows the block diagram of the packing compaction algorithm.

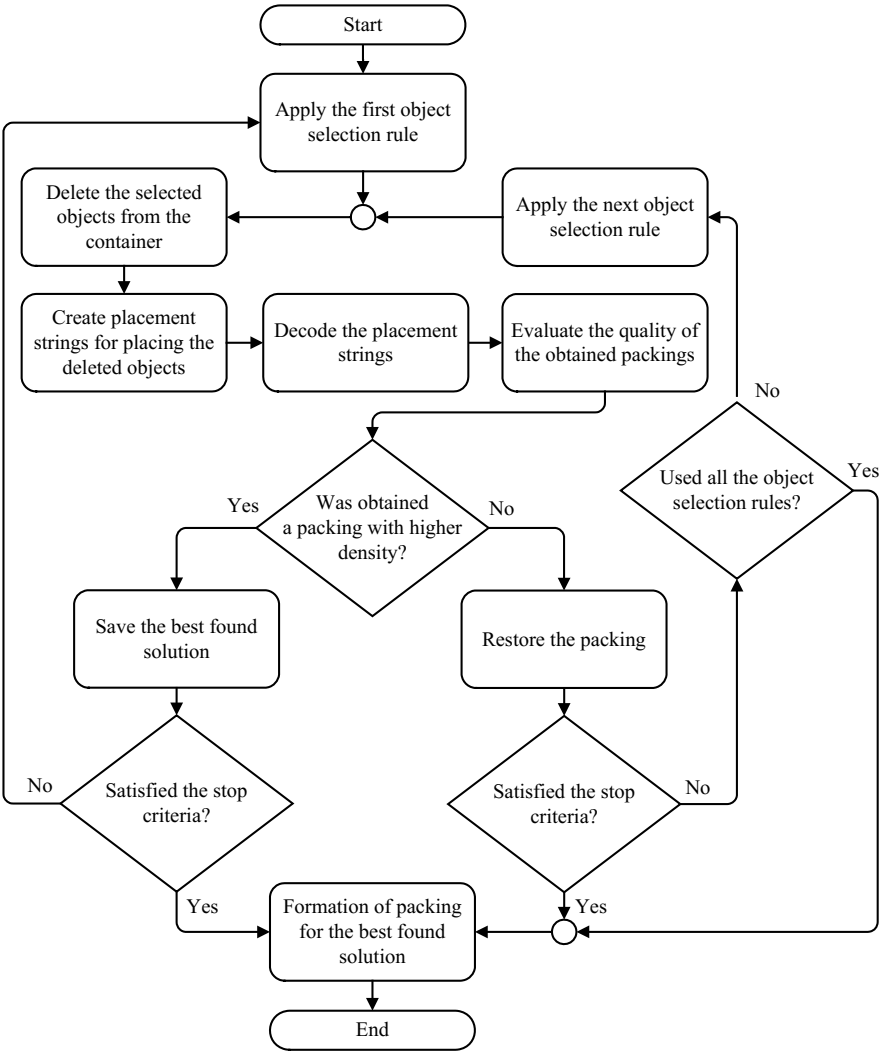


**Fig. 5** Packing compaction algorithm

## 4 Computational Experiments

The efficiency of the packing compaction algorithm has been investigated on the standard two-dimensional strip packing problems (rectangular cutting problems) which presented in the paper [20] (classes of instances C1–C6) as well as presented in the paper [21] (classes of instances C7–C10). We consider 500 problem instances (10 classes with 50 instances in each). Every class contains from 20 to 100 rectangular

**Table 2** Results of compaction obtained on random solutions

| Test class | Average value of the fitness function before compaction | Average value of the fitness function after compaction | Average time, s | The compaction quality, % |
|---|---|---|---|---|
| C1 | 203.98 | 201.76 | 1.06 | 1.53 |
| C2 | 69.34 | 65.56 | 1.29 | 6.72 |
| C3 | 577.88 | 573.20 | 1.15 | 1.55 |
| C4 | 229.82 | 218.98 | 1.75 | 6.65 |
| C5 | 1817.86 | 1804.08 | 1.19 | 1.34 |
| C6 | 608.02 | 579.32 | 1.97 | 5.68 |
| C7 | 1685.78 | 1676.24 | 1.07 | 0.78 |
| C8 | 1644.70 | 1603.48 | 1.48 | 3.53 |
| C9 | 3398.78 | 3394.94 | 1.04 | 0.26 |
| C10 | 1052.94 | 1034.88 | 1.36 | 2.17 |
| Average | 1128.91 | 1115.24 | 1.34 | 3.02 |

objects. The maximal number of iterations of the packing compaction algorithm was chosen equal to 20. The rotation of objects is not allowed.

The compaction quality is estimated by the evaluation $\mu = (S_0 - S_1) \big/ S_0 \times 100\%$, where $S_0$ is a value of the fitness function before compacting and $S_1$—a value of the fitness function after compacting.

All the computational experiments were carried out using the designed software intended for optimizing the orthogonal packing and rectangular cutting problems [22] on the personal computer (CPU—Intel Core i5-3350P 3.10 GHz; RAM—6.00 GB).

On the basis of the averaged obtained test results, the following order of usage of the object selection rules is set for the packing compaction algorithm (the rules are listed in decreasing order of the compaction quality $\mu$): MAXMAX_LAST ($\mu = 2.07\%$), DOUBLE_LAST ($\mu = 1.75\%$), MAXMAX_AREA ($\mu = 1.52\%$), MAX_LAST ($\mu = 1.44\%$), DOUBLE_AREA ($\mu = 1.23\%$), MAX_AREA ($\mu = 0.86\%$).

Table 2 contains the results of testing the packing compaction algorithm on random (non-optimized) solutions. For this purpose were used the placement schemes obtained as the result of decoding the placement strings which contain objects in order as they recorded in the considered test instances (as in the chromosome 1).

The packing compaction algorithm also was applied to the placement schemes obtained as the result of decoding the best chromosomes of the described above the one-pass heuristic algorithm. The averaged test results are given in Table 3.

The carried-out computational experiments showed that the proposed algorithm provides increasing of the density of placement schemes for all classes of the considered test problems. This algorithm ensures the least efficient of compacting when it is applied to objects the width of which is almost the same as the width of the container (test classes C7 and C9).

**Table 3** Results of compaction obtained on optimized solutions

| Test class | Average value of the fitness function before compaction | Average value of the fitness function after compaction | Average time, s | The compaction quality, % |
|---|---|---|---|---|
| C1 | 190.94 | 190.82 | 0.94 | 0.09 |
| C2 | 62.76 | 62.62 | 0.95 | 0.52 |
| C3 | 532.20 | 530.38 | 1.08 | 0.65 |
| C4 | 209.28 | 208.18 | 1.11 | 0.86 |
| C5 | 1692.66 | 1690.12 | 1.04 | 0.19 |
| C6 | 553.70 | 550.90 | 1.35 | 0.62 |
| C7 | 1620.84 | 1619.92 | 1.01 | 0.07 |
| C8 | 1535.38 | 1521.14 | 1.42 | 1.02 |
| C9 | 3354.86 | 3354.80 | 0.98 | 0.01 |
| C10 | 966.12 | 965.36 | 1.05 | 0.12 |
| Average | 1071.87 | 1069.42 | 1.09 | 0.42 |

## 5 Conclusion

The packing compaction algorithm has been proposed for the rectangular cutting and orthogonal packing problems. The work of this algorithm is based on the idea of iterative reallocation of some objects already placed in a container. The effectiveness of application of the algorithm has been investigated on the standard test problems of rectangular cutting also known as two-dimensional strip packing problems. The developed algorithm has been described invariantly relative to the dimension of the problem, and hence it is possible to apply the packing compaction algorithm for the rectangular cutting and orthogonal packing problems of arbitrary dimension.

## References

1. Wascher G, Haubner H, Schumann H (2007) An improved typology of cutting and packing problems. EJOR 183(3):1109–1130
2. Bortfeldt A, Wascher G (2013) Constraints in container loading—a state-of-the-art review. EJOR 229(1):1–20
3. Lodi A, Martello S, Monaci M (2002) Two-dimensional packing problems: a survey. EJOR 141(2):241–252
4. Goncalves JF, Resende MGC (2013) A biased random key genetic algorithm for 2D and 3D bin packing problems. Int J Prod Econ 145(2):500–510
5. Motorin DE, Popov SG, Chuvatov MV, Kurochkin MA, Kurochkin LM (2017) A study of the evaluation function for the cost of transport operations in distribution of purpose in a group of robots. In: Proceedings of 2017 20th IEEE international conference on soft computing and measurements, SCM 2017, pp 536–538. https://doi.org/10.1109/SCM.2017.7970642
6. Chekanin VA, Chekanin AV (2016) Implementation of packing methods for the orthogonal packing problems. J Theor Appl Inform Technol 88(3):421–430

7. Kierkosz I, Luczak M (2014) A hybrid evolutionary algorithm for the two-dimensional packing problem. Cent Eur J Oper Res 22(4):729–753
8. Boschetti MA (2004) New lower bounds for the finite three-dimensional bin packing problem. Discrete Appl Math 140:241–258
9. Martinez MAA, Clautiaux F, Dell'Amico M, Iori M (2013) Exact algorithms for the bin packing problem with fragile objects. Discrete Optim 10(3):210–223
10. Garey M, Johnson D (1979) Computers intractability: a guide to the theory of NP-completeness. W.H.Freeman, San Francisco, p 338
11. Leung SCH, Zhang DF, Zhou CL, Wu T (2012) A hybrid simulated annealing metaheuristic algorithm for the two-dimensional knapsack packing problem. Comput Oper Res 39(1):64–73
12. Gao YQ, Guan HB, Qi ZW, Hou Y, Liu L (2013) A multi-objective ant colony system algorithm for virtual machine placement in cloud computing. J Comput Syst Sci 79(8):1230–1242
13. Chekanin VA, Chekanin AV (2018) Design of library of metaheuristic algorithms for solving the problems of discrete optimization. In: Evgrafov A (ed) Advances in mechanical engineering. Lecture notes in mechanical engineering., Springer, Cham, pp 25–32
14. Filippova AS (2006) Modeling of evolution algorithms for rectangular packing problems based on block structure technology. In: Inf Technol (Informacionnye Tehnologii). Appendix, 32 p (in Russian)
15. Chekanin VA, Chekanin AV (2016) Algorithms for management objects in orthogonal packing problems. ARPN J Eng Appl Sci 11(13):8436–8446
16. Chekanin VA, Chekanin AV (2015) An efficient model for the orthogonal packing problem. Adv Mech Eng 22:33–38
17. Chekanin VA, Chekanin AV (2014) Multilevel linked data structure for the multidimensional orthogonal packing problem. Appl Mech Mater 598:387–391
18. Chekanin VA, Chekanin AV (2016) New effective data structure for multidimensional optimization orthogonal packing problems. In: Advances in mechanical engineering. Springer International Publishing, pp 87–92
19. Chekanin VA, Chekanin AV (2017) Deleting objects algorithm for the optimization of orthogonal packing problems. In: Advances in Mechanical Engineering. Springer International Publishing, pp 27–35
20. Berkey O, Wang P (1987) Two-dimensional finite bin-packing algorithms. J Oper Res Soc 38(5):423–429
21. Martello S, Vigo D (1998) Exact solution of the two-dimensional finite bin packing problem. Manage Sci 44:388–399
22. Chekanin VA, Chekanin AV (2015) Development of optimization software to solve practical packing and cutting problems. In: Proceedings of the 2015 International Conference on Artificial Intelligence and Industrial Engineering (AIIE 2015). Advances in Intelligent Systems Research 123:379–382. https://doi.org/10.2991/aiie-15.2015.104

# Wave Processes in the Periodically Loaded Infinite Shell


**George V. Filippenko**

**Abstract** The wave processes in the infinite and finite periodic shells (cylinder shell, beam, and rod) are explored. Look-alike systems can model different elements of buildings, hydro-technical constructions, bridges, oil rigs, different pipes, etc. The statement of the problem is considered the rigorous statement. In the infinite systems, Floquet solution is founded. The comparison of the wave processes in the rod and beam is fulfilled. The energy fluxes in them are calculated. The main effects are explored with the attraction of the analysis of vibrations, corresponding to different pass- and stopbands. The dependence of character and «heterogeneity degree» of wave process in the finite systems via the position of corresponding wave number in relation to passbands is considered. The modes of free vibrations of a periodic cell in the case of its asymmetry are analyzed with special attention to edge effects via the parameters of the problem.

**Keywords** Periodic structures · Energy flux · Pass- and stopbands

## 1 Introduction and Statement of the Problem

The cylinder shells, plates, beams, and rods (sometimes multilayered and periodically loaded) are often used in civil engineering construction. Look-alike systems can model different elements of buildings, hydro-technical constructions, bridges, oil rigs, different pipes, etc. [1–18]. An extensive bibliography of wave phenomena in different periodic systems is presented in [1]. Calculation of these complicated systems demands major computing resources. Therefore, the consideration of simpler model problems which have an analytical solution [1–10] is very actual. On these models, it is possible to analytically explore main effects and also to use them as the

G. V. Filippenko (✉)
Institute of Problems of Mechanical Engineering, V.O., Bolshoj Pr., 61,
St. Petersburg 199178, Russia
e-mail: g.filippenko@spbu.ru

St. Petersburg State University, 7-9, Universitetskaya nab., St. Petersburg 199034, Russia



A. N. Evgrafov (ed.), *Advances in Mechanical Engineering*,
Lecture Notes in Mechanical Engineering,
https://doi.org/10.1007/978-3-030-11981-2_2

test problems for computing packages. The analytical and computational analyses which used energy fluxes in such systems are intensively applied [13–18].

Consider an infinite cylindrical shell occupying in cylindrical coordinate system $(r, \varphi, z)$, the domain $\{R - h/2 < r < R + h/2, \quad 0 \leqslant \varphi < 2\pi, \quad -\infty < z < \infty\}$, where $R$ is the radius of the midsurface, $h$ is the thickness of the shell.

Let us assume that the action of environment on the shell can be modeled by distributed loads and periodically concentrated loads of two kinds which are gathered in the vector $\mathbf{q}$. The first kind of them is the inertial masses (acting in Dalamber forces), and second one is the loads proportional to the displacement vector of the shell $\mathbf{u} = (u_t, u_z, u_n)^{\mathrm{T}}$ ($T$—is a badge of transposing) as an analog of a plate on Winkler foundation. Here, $u_t, u_z, u_n$ are the components of the midsurface displacement in the circumferential, longitudinal, and radial directions, respectively.

The equations of motion according to the Kirchhoff–Love-type theory of the shells can be written in the form

$$\frac{Eh}{(1-\nu^2)R^2}\mathbf{L}^0\mathbf{u} + \mathbf{q} = \mathbf{0}, \tag{1}$$

where $\mathbf{L}^0$ is the matrix differential operator 3*3 [12]

$$\mathbf{L}^0 \equiv \begin{pmatrix} \alpha_1[\nu_-\partial_z^2 + \partial_\varphi^2] & \nu_+\partial_\varphi\partial_z & \partial_\varphi(1 + 2\alpha^2[1 - \partial_\varphi^2 - \partial_z^2]) \\ L_{21} & \partial_z^2 + \nu_-\partial_\varphi^2 & \nu\partial_z \\ L_{31} & L_{32} & \alpha^2(2\nu\partial_z^2 + 2\partial_\varphi^2 - 1 - [\partial_z^2 + \partial_\varphi^2]^2) - 1 \end{pmatrix}. \tag{2}$$

Here $\partial_z := R\frac{\partial}{\partial z}$, $L_{21} = L_{12}$, $L_{31} = -L_{13}$, $L_{32} = -L_{23}$, $\nu_\pm = (1 \pm \nu)/2$, $\alpha_1 = 1 + 4\alpha^2$, and $w = \omega R/c_{\mathrm{s}}$. The dimensionless parameter $\alpha^2 = \frac{1}{12}\left(\frac{h}{R}\right)^2$ describing the relative thickness of the cylindrical shell is introduced.

The properties of a material of the shell are characterized by $E$, $\nu$, and $\rho_{\mathrm{s}}$ which denote Young's module, Poisson coefficient, and volumetric density, respectively.

The surface density of the shell $\rho$ ($\rho = \rho_{\mathrm{s}}h$) and $c_{\mathrm{s}}$—the velocity of median surface deformation waves of the cylindrical shell $c_{\mathrm{s}} = \sqrt{E/\big((1-\nu^2)\rho\big)}$, are introduced.

The structure of vector of the loads $\mathbf{q}$ is following $\mathbf{q} = \big(\omega^2(\rho\mathbf{I} + \mathbf{R}) - \mathbf{K}\big)\mathbf{u} + \sum_{j=-\infty}^{\infty} \delta(z - z_j)\big(\omega^2\mathbf{M} - \mathbf{B}\big)\mathbf{u}$. Here, in the general case, the distributed inertial mass is described by diagonal matrix $\mathbf{R} = \mathrm{diag}\{\rho_t, \rho_z, \rho_n\}$ and distributed load is described by diagonal matrix $\mathbf{K} = \mathrm{diag}\{k_t, k_z, k_n\}$. The concentrated inertial masses and loads are placed at the equally spaced lines $z = z_j = jl$ ($j \in \mathrm{Z}$). Each concentrated inertial mass and load is described by diagonal matrixes $\mathbf{M} = \mathrm{diag}\{\mu_t, \mu_z, \mu_n\}$ and $\mathbf{B} = \mathrm{diag}\{\beta_t, \beta_z, \beta_n\}$ correspondingly, and $\mathbf{I} = \mathrm{diag}\{1, 1, 1\}$ is the unit matrix. Note that the symbol $\delta$ denotes the Dirac delta function.

The propagation of stationary waves from $z = -\infty$ to $z = +\infty$ with angular frequency $\omega$ is considered. The factor $\exp(-i\omega t)$ is omitted everywhere. The equa-

tion of motion is supplemented by boundary conditions (BCs) (often called contact conditions in this case) on the lines $z = z_j = jl,\ \ j \in \mathrm{Z}$.

It is useful to introduce the vector of generalized displacements $\mathbf{u}^4 \equiv \left(u_t, u_z, u_n, u_p\right)^{\mathrm{T}}$ (where $u_p = -\partial_z u_n$) and following matrixes: $\mathbf{K}^4 = \mathrm{diag}\{k_t, k_z, k_n,\ 0\}$, $\mathbf{R}^4 = \mathrm{diag}\{\rho_t, \rho_z, \rho_n,\ 0\}$, $\mathbf{B}^4 = \mathrm{diag}\{\beta_t, \beta_z, \beta_n,\ 0\}$, $\mathbf{V}^4 = \mathrm{diag}\{1,\ 1,\ 1,\ 1\}$ , $\mathbf{M}^4 = \mathrm{diag}\{\mu_t, \mu_z, \mu_n,\ 0\}$ and

$$\mathbf{F}^4 = \frac{E}{1-\nu^2}\frac{h}{R}\begin{pmatrix} -\nu_-\alpha_1\partial_z & -\nu_-\partial_\varphi & 0 & -4\nu_-\alpha^2\partial_\varphi \\ -\nu\partial_\varphi & -\partial_z & -\nu & 0 \\ -2\alpha^2\partial_z\partial_\varphi & 0 & 0 & -\alpha^2\left[(2-\nu)\partial_\varphi^2 - \nu + \partial_z^2\right] \\ -2\alpha^2 R\nu\partial_\varphi & 0 & \alpha^2 R\nu(\partial_\varphi^2 - 1) & -\alpha^2 R\partial_z \end{pmatrix}. \tag{3}$$

In these terms, BCs at $z = z_j = jl,\ \ j \in \mathrm{Z}$ are following.

$$\begin{cases} \mathbf{V}^4\mathbf{u}^4(z_j + 0) - \mathbf{V}^4\mathbf{u}^4(z_j - 0) = \mathbf{0} \quad \Rightarrow \quad \mathbf{u}^4(z_j + 0) = \mathbf{u}^4(z_j - 0) \\ \mathbf{F}^4\mathbf{u}^4(z_j + 0) - \mathbf{F}^4\mathbf{u}^4(z_j - 0) = \left(\omega^2\mathbf{M}^4 - \mathbf{B}^4\right)\mathbf{u}^4(z_j + 0) \end{cases}. \tag{4}$$

It expresses the continuity of generalized displacements and jump of generalized forces.

## 2 Determination of the General Representation for Vibrational Field

The Floquet solution of Eq. (1) is built by the contact method, cf. Ref. [1]. At first, the solution of this equation on the interval $z \in (0,\ l)$ is constructed. On this interval, the equation has the view

$$\mathbf{L}^1\mathbf{u} \equiv \left(\mathbf{L}^0 - \frac{\left(1-\nu^2\right)R^2}{Eh}\mathbf{K} + \frac{\omega^2 R^2}{c^2}\left(\mathbf{I} + \frac{1}{\rho}\mathbf{R}\right)\right)\mathbf{u} = \mathbf{0}\ . \tag{5}$$

The solution is searched in the form

$$\mathbf{u}(\varphi, z) = \sum_{m=0}^{\infty} \mathrm{e}^{i\lambda_m z}\begin{pmatrix} u_t^m(z)\sin(m\varphi + \varphi_m^0) \\ u_z^m(z)\cos(m\varphi + \varphi_m^0) \\ u_n^m(z)\cos(m\varphi + \varphi_m^0) \end{pmatrix}. \tag{6}$$

In this case, the equation of motions (1) and BCs (4) are split for each harmonic on $m$. For convenience, the designation for the vector of displacements $\mathbf{u}$ will be transferred for the vector of amplitudes of fixed harmonic (index $m$ will be omitted) $\mathbf{u}(z) = (u_t(z), u_z(z), u_n(z))^{\mathrm{T}} = \mathrm{e}^{i\lambda z}\left(u_t^0, u_t^0, u_t^0\right)^{\mathrm{T}} \equiv \mathrm{e}^{i\lambda z}\tilde{\mathbf{u}}^0$. As a result,

the following algebraic system is obtained: $\mathbf{L}^1_\lambda \tilde{\mathbf{u}}_0 = \mathbf{0}$; $\mathbf{L}^1_\lambda \equiv \mathbf{L}^1_\lambda(\omega, \lambda)$. Here, the linear algebraic operator $\mathbf{L}^1_\lambda$ is the result of acting of operator $\mathbf{L}$ on vector (6). The dispersion equation $\det \mathbf{L}^1_\lambda = 0$ is obtained from the condition of existence of non-trivial solution of this system. This equation has eight different complex roots $\lambda_j$, $j = 1, \ldots, 8$ in general case. So, homogeneous solution (for fixed harmonic) has the form $\mathbf{u}(z) = \sum\limits_{j=1}^{8} a_j \mathrm{e}^{i\lambda_j z}\left(u_t^j, u_t^j, u_t^j\right)^T \equiv \sum\limits_{j=1}^{8} a_j \mathrm{e}^{i\lambda_j z}\mathbf{u}^j$, where $\mathbf{u}^j$ are the appropriate eigenvectors of the matrix $\mathbf{L}^1_\lambda$ normalized to unity and $a_j$ are the arbitrary constants.

Floquet solution of our problem must satisfy the condition $\mathbf{u}(z+l) = \mathbf{u}(z)\mathrm{e}^{i\alpha}$ and $\forall z \in (-\infty, +\infty)$, where $\mathrm{e}^{i\alpha}$ is the Floquet factor between the cells of periodicity, and parameter $\alpha$ will be determined later. So the solution on an interval $z \in (0,\ 2l)$ has the structure

$$\mathbf{u}(z) = \begin{cases} \mathrm{e}^{i\alpha}\mathbf{u}^0(z-l) \equiv \mathbf{u}^1(z), & z \in (l,\ 2l) \\ \mathbf{u}^0(z), & z \in (0,\ l) \end{cases} \tag{7}$$

and BCs on line $z = l$ have the form

$$\begin{cases} \mathbf{V}^4\mathbf{u}^4(l+0) - \mathbf{V}^4\mathbf{u}^4(l-0) = \mathbf{0} \quad \Rightarrow \quad \mathbf{u}^4(l+0) = \mathbf{u}^4(l-0) \\ \mathbf{F}^4\mathbf{u}^4(l+0) - \mathbf{F}^4\mathbf{u}^4(l-0) = \left(\omega^2\mathbf{M}^4 - \mathbf{B}^4\right)\mathbf{u}^4(l+0) \end{cases}. \tag{8}$$

Note that $\mathbf{u}(z) = \mathbf{u}(z-l)\mathrm{e}^{i\alpha} \ \Rightarrow \ \mathbf{u}(z)|_{z=l+0} = \mathbf{u}(z)\mathrm{e}^{i\alpha}\big|_{z=+0}$. Hence

$$\begin{cases} \mathbf{u}^4(+0)\mathrm{e}^{i\alpha} = \mathbf{u}^4(l-0) = \mathbf{u}^4(l+0) \\ \mathrm{e}^{i\alpha}\mathbf{F}^4\mathbf{u}^4(+0) - \left(\mathbf{F}^4 + \omega^2\mathbf{M}^4\right)\mathbf{u}^4(l-0) = \mathbf{0} \end{cases}. \tag{9}$$

Note that the vector of generalized displacements $\mathbf{u}^4$ can be rewritten in the form

$$\mathbf{u}^4(z) \equiv \begin{pmatrix} u_t(z) \\ u_z(z) \\ u_n(z) \\ -\partial_z u_n(z) \end{pmatrix} = \sum_{j=1}^{8} a_j \mathrm{e}^{i\lambda_j z}\begin{pmatrix} u_t^j \\ u_z^j \\ u_n^j \\ -i\lambda_j u_n^j \end{pmatrix}$$
$$= \begin{pmatrix} \mathrm{e}^{i\lambda_1 z}u_t^1 & \ldots & \mathrm{e}^{i\lambda_8 z}u_t^8 \\ \mathrm{e}^{i\lambda_1 z}u_z^1 & \ldots & \mathrm{e}^{i\lambda_8 z}u_z^8 \\ \mathrm{e}^{i\lambda_1 z}u_n^1 & \ldots & \mathrm{e}^{i\lambda_8 z}u_n^8 \\ -i\lambda_1\mathrm{e}^{i\lambda_1 z}u_n^1 & \ldots & -i\lambda_8\mathrm{e}^{i\lambda_8 z}u_n^8 \end{pmatrix}\begin{pmatrix} a_1 \\ a_2 \\ \ldots \\ a_8 \end{pmatrix} \equiv \mathbf{U}\mathbf{a}$$

Then BCs (9) obtain the form

$$\begin{cases} \mathrm{e}^{i\alpha}\,\mathbf{U}|_{z=0}\mathbf{a} - \mathbf{U}|_{z=l}\mathbf{a} = \mathbf{0} \\ \mathrm{e}^{i\alpha}\left(\mathbf{F}^4\mathbf{U}\right)\big|_{z=0}\mathbf{a} - \left(\mathbf{F}^4 + \omega^2\mathbf{M}^4\right)\mathbf{U}\big|_{z=l}\mathbf{a} = \mathbf{0} \end{cases}. \tag{10}$$

The condition of existence of non-trivial solution of this system leads to equation on $\alpha$

$$\det\begin{pmatrix} \mathrm{e}^{i\alpha}\,\mathbf{U}|_{z=0} - \mathbf{U}|_{z=l} \\ - - - - - - - - - - - - - - - - - - - - \\ \mathrm{e}^{i\alpha}\left(\mathbf{F}^4\mathbf{U}\right)\big|_{z=0} - \left(\mathbf{F}^4 + \omega^2\mathbf{M}^4\right)\mathbf{U}\big|_{z=l} \end{pmatrix} = 0. \tag{11}$$

Hence, one can obtain Floquet parameter $\alpha$ and then obtain vector $\mathbf{a}$ as the solution of appropriate linear algebraic system (10). So the solution on interval $z \in (0,\ l)$ has the form $\mathbf{u}(z) = A\sum_{j=1}^{8} a_j \mathrm{e}^{i\lambda_j z}\mathbf{u}^j$, where vector $\mathbf{a}$ is normalized to unity and $A$ is an arbitrary constant. The common solution on the interval $z \in (-\infty,\ +\infty)$ has the view

$$\mathbf{u}(\varphi, z) = \sum_{m=0}^{\infty} A_m \mathrm{e}^{i\alpha_m[z/l]} \sum_{j=1}^{8} a_{j,m} \mathrm{e}^{i\lambda_{j,m}\{z/l\}} \begin{pmatrix} u_t^{j,m}(z)\sin(m\varphi + \varphi_m^0) \\ u_z^{j,m}(z)\cos(m\varphi + \varphi_m^0) \\ u_n^{j,m}(z)\cos(m\varphi + \varphi_m^0) \end{pmatrix} \tag{12}$$

where $[z/l]$ and $\{z/l\}$ designate integer and fractional parts of the real number $z/l$ correspondingly.

Energy flux in such a shell can be obtained as in [17, 18]. The similar problem is considered further for two simplest models of the shell: rod and beam.

## 3 Periodic Rod and Beam

The propagation of stationary waves $u(x)$ in an infinitely long homogeneous linearly elastic rod [6] and beam (Bernoulli beam) [9] with the specific structural mass density $\mu$ and concentrated non-structural masses of magnitudes $M$ attached at the equally spaced points $x_j = x - jl$ $(j = -\infty, \ldots, +\infty)$ along the coordinate axis $x$ is considered.

The equation

$$ES u''(x) + \omega^2\left(\mu + M\sum_{j=-\infty}^{+\infty}\delta(x - jl)\right)u(x) = 0; \quad x \in (-\infty, +\infty) \tag{13}$$

where $E$ is Young's modulus and $S$ is the cross-sectional area of the rod, which describe the propagation of the longitudinal waves. The equation

$$-D_c u''''(x) + \omega^2\left(\mu + M\sum_{j=-\infty}^{+\infty}\delta(x - jl)\right)u(x) = 0; \quad x \in (-\infty, +\infty) \tag{14}$$

where $D_c$ is the bending stiffness which describes the propagation of the bending waves. For convenience, we shall now non-dimensionalize the above dimensional parameters $\omega$ and $M$, independent variable $x$, and functions $u(x)$ and $\delta(x)$, by defining their dimensionless counterparts as $m = M/\mu l$, $x := x/l$, $u(x) := u(x)/l$, and $k^2 = \frac{\mu\omega^2 l^2}{ES} = \frac{\omega^2 l^2}{c_r^2}$ in the case of the rod and $k^4 = \frac{\mu\omega^2 l^2}{D_c} = \frac{\omega^2 l^2}{c_b^2}$ in the case of the beam. In terms of these dimensionless parameters, Eqs. (13) and (14) take the dimensionless forms (15) and (16) correspondingly:

$$u''(x) + k^2\left(1 + m\sum_{j=-\infty}^{+\infty}\delta(x-j)\right)u(x) = 0; \quad x \in (-\infty, +\infty) \tag{15}$$

$$-u''''(x) + k^4\left(1 + m\sum_{j=-\infty}^{+\infty}\delta(x-j)\right)u(x) = 0; \quad x \in (-\infty, +\infty) \tag{16}$$

In the case of the rod BCs at the points $x_j = x - j$, $j \in \mathrm{Z}$ have the view

$$\begin{cases} u(x_j + 0) = u(x_j - 0) \equiv u(x_j) \\ u'(x_j + 0) - u'(x_j - 0) = -k^2 m u(x_j) \end{cases} \tag{17}$$

and BCs have the view

$$\begin{cases} u^{(i)}(x_j + 0) - u^{(i)}(x_j - 0) = 0, \quad i = 0,\ 1,\ 2 \\ u'''(x_j + 0) - u'''(x_j - 0) = k^4 m u(x_j) \end{cases} \tag{18}$$

in the case of the beam. The solution of the problem in the case of the rod [6] and beam [9] is similar to that considered above in the case of the cylindrical shell.

The dimensioned energy flux (averaged on the period of oscillations) has the form $\Pi = \frac{\omega}{2} ES\,\mathrm{Im}(u'\overline{u})$in the case of the rod and it has the form $\Pi = \frac{\omega}{2} D_c \mathrm{Im}\left(\frac{\partial^3 \overline{u}}{\partial x^3} u - \frac{\partial^2 \overline{u}}{\partial x^2}\frac{\partial u}{\partial x}\right)$ in the case of the beam. Further, during calculations, both energy fluxes are normalized on the energy flux of the corresponding wave $A\mathrm{e}^{ikx}$ propagating in the homogeneous rod or beam correspondingly.

From another side, the vibrations of corresponding finite periodic rod and beam can be explored. In this case, a finite segment ($x \in [a, b]$), where $a = -n_1 - 1 + s$, $b = n_2 + s$, $n_1,\ n_2 \in \mathrm{N}$, $0 < s < 1$, consisting several ($N = n_1 + n_2$) cells of periodicity of the infinite periodic system (rod or beam), is considered. In Eqs. (15) and (16), series $\sum_{j=-\infty}^{+\infty}\delta(x - jl)$ are changed to finite sum $\sum_{j=-n_1}^{n_2}\delta(x - j)$ in this case. Following BCs are considered in the points $a$ and $b$: symmetrical (BCs in the point $a$ and in the point $b$ are of the same type, for example, both BCs are fixed) and asymmetrical (BCs of the different types, for example, fixed and free). The problem on eigennumbers $k_j$, $j \in \mathrm{N}$ and corresponding eigenmodes $u_j(x) \equiv u(x, k_j)$, $x \in (a,\ b)$ is appeared in this case.

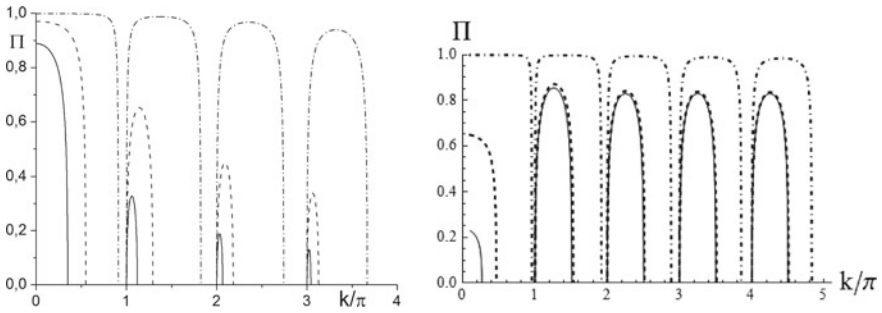


(a) $m = 0.1, 1.0, 3.0$ (b) $m = 0.1, 10.0, 100.0$

**Fig. 1** Normalized energy flux as a function of $m$ in the rod (**a**) and beam (**b**)

## 4 Numerical Examples

At first, the infinite periodic rod and beam will be considered. Fixing the values of mass $m$ and solving the received dispersion equation with respect to wavenumber $k$, an infinite set of the wave numbers serving the borders of pass- and stopbands is obtained. Overdrawing all possible $m \in (0, +\infty)$, the set of curves on the plane $(m, k)$, separating alternating passbands and stopbands, is received [6, 9]. They will be called the borders of the stopbands for convenience.

The dependence of the normalized energy flux $\Pi$ on wavenumber $k/\pi$ in the rod is presented in Fig. 1a. The dot-dashed, dashed, and full lines on this figure correspond to masses $m = 0.1,\ 1.0,\ 3.0$, respectively. The energy flux is equal to zero in intervals corresponding to stopbands, and it is non-zero outside them (i.e., in the passbands). If $m \to 0$, the limiting case of the rod without point masses is obtained. In this case, the amplitude of energy flux and width of passbands tend to unite. In the situation with increasing masses $m$ , the reduction in passband widths and amplitudes of energy flux occurs. It is related to the increase in the dynamic loading on point mass inserts with frequency growth (it is proportional to $\omega^2 m$).

The dependence of the normalized energy flux on wavenumber $k/\pi$ in the beam is presented on Fig. 1b. The dot-dashed, dashed, and full lines on Fig. 1b correspond to masses $m = 0.1,\ 10.0,\ 100.0$, respectively. The main effects are similar to the ones in the case of rod, but relative power flow attenuation in the first passband (which belongs to the interval $k/\pi \in (0,\ 1)$) in comparison with other passbands, with the increase in masses of inertial inclusions in the beam, is observed.

The corresponding finite periodic rod and beam are examined now. Calculations are fulfilled for the case of five dot inclusions of mass $m$, located in the points $x = 0, \pm 1, \pm 2$ of the rod. The influence of asymmetry of different kinds on the eigenmodes will be considered: The asymmetry of BCs on the opposite sides of the interval$(a, b)$, asymmetry caused by the fact that $s \neq 0.5$, and the combination of these two asymmetries.

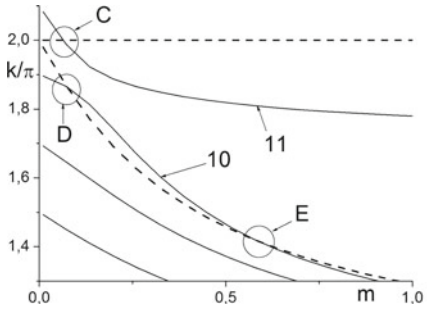


(a) Eigenfrequencies as functions of $m$

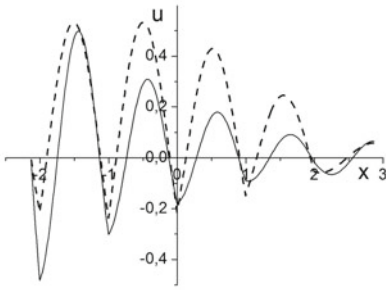


(b) Tenth mode in the stop band $m = 0.3$ (full line) and in the pass band $m = 1.0$ (dashed line)

**Fig. 2** Rod, asymmetry BCs, $s = 0.87$

For example, in Fig. 2a, the full curves depict the dimensionless eigenfrequencies $k/\pi$ as functions of mass $m$ for a finite system, and the dashed curves correspond to the boundary of stopbands of the infinite system.

In the fully symmetric case (BCs are symmetric and $s = 0.5$), all the curves representing eigenfrequencies do not overstep the bounds of the stopbands [2, 6, 9], and the borders of the stopbands coincide with the corresponding eigenfrequency curves as it was for the symmetric system with single mass. The reason is that the equation for the spectrum of the system with five masses contains the spectrum of the system with single mass.

If BCs are symmetric but $s \neq 0.5$, one of the curves from each interval $(n, n + 1)$, $n = 0, 1$ on axes $k$ is fully located in the stop band. These curves can be interpreted as the eigenfrequency curves related to the border cells (masses). It is well visible that these modes, unlike the corresponding mode for the symmetrical case, look like nonhomogeneous waves, i.e., oscillations modulated by decreasing or increasing exponent. Both the directions of decrease and increase are realized for different modes. This "decaying" mode (standing wave) can be interpreted as the combination of non-homogeneous waves from the stopband of the corresponding infinite periodic structure. This reasoning is analogous to the case of the standing wave as the combination of propagating waves in a finite homogeneous rod.

But in the case of asymmetrical BCs, not only border cells take part in the formation of these curves in the stopbands. New opportunities are realized in this situation. For example, the curve can penetrate from passband into the stopband and interact with another curve in the stopband (implying change of the mode shapes) in the points of quasi-cross-cutting. This effect is shown in the example of the tenth and eleventh modes (curves 10 and 11) for $s = 0.87$ in Fig. 2a (when $m \approx 0.13$). The evolution of these modes when the parameter $m$ is assigned the increasing values $m = 0.3,\ 1.0$ is demonstrated in Fig. 2b. Starting as homogeneous waves at $m \in (0.0,\ 0.1)$, they penetrate into the stopband and become "nonhomogeneous." At $m \approx 0.13$, these

modes intensively interact and have the intermediate view. The direction of decrease of these modes is changed to opposite after quasi-cross-cutting of the corresponding eigenfrequency curves. Furthermore, double crossing of the stopband boundary by the eigenfrequency curve is possible (circles $D$, $E$ in Fig. 1a). It comes back from the stopband into the passband at $m \approx 0.65$ and becomes "homogeneous" again. At the same time, the eleventh mode remains "nonhomogeneous," and its localization near the border increases. It is the common situation that localization of the modes from the stopband near the border increases, while the parameter $m$ increases.

Edge effects in the corresponding finite periodic beam are similar, and they are considered in [9].

## 5 Conclusions

Longitudinal waves in the periodic cylinder shell [$m = 0$ in (6)] can be modeled by the periodic rod and bending waves, and [$m = 1$ in (6)] can be modeled by periodic beam to a certain degree. So we can expect the similar effects in the shell like that considered above in the case of the rod and beam.

The discovered effects can be useful for design of periodic structures with given arrangement of eigenfrequencies (inside pass- or stopbands) and for estimating edge effects in them.

## References

1. Mead DJ (1996) Wave propagation in continuous periodic structures: research contribution from Southampton, 1964–1995. J Sound and Vibr 190(3):495–524
2. Olhoff N, Niu B, Cheng G (2012) Optimum design of band-gap beam structures. Int J Solids Struct 49:3158–3169
3. Sorokin SV, Ershova OA (2004) Plane wave propagation and frequency band gaps in periodic plates and cylindrical shells with and without heavy fluid loading. J Sound Vibr 278(3):501–526. https://doi.org/10.1016/j.jsv.2003.10.042
4. Jensen JS (2003) Phononic band gaps and vibrations in one- and two-dimensional mass-spring structures. J Sound Vibr 266(5):1053–1078
5. Du J, Olhoff N (2007) Topological design of freely vibrating continuum structures for maximum values of simple and multiple eigenfrequencies and frequency gaps. Struct Multi Optim 34(2):91–110. Editors Erratum in 34:91. https://doi.org/10.1007/s00158-007-0101-y
6. Filippenko GV (2013) The location of pass and stop bands of an infinite periodic structure versus the eigenfrequencies of its finite segment consisting of several 'periodicity cells'. In: 4th ECCOMAS thematic conference on computational methods in structural dynamics and earthquake engineering COMPDYN 2013, Kos Island, Greece, 12–14 June 2013. CD format. Paper №1690, 12 pages. https://files.eccomasproceedia.org/papers/compdyn-2013/C1690.pdf, http://www.eccomasproceedings.org/cs2013/pdf/1690.pdf
7. Hvatov A, Sorokin S (2015) Free vibrations of finite periodic structures in pass-and stop-bands of the counterpart infinite waveguides. J Sound Vibr 347:200–217. http://dx.doi.org/10.1016/j.jsv.2015.03.003

8. Zhuchkova MG (2016) Wave propagation in a floating elastic plate with a periodic support. In: Proceedings of the international conference "Days on diffraction 2016", 27 June–1 July 2016, St. Petersburg, Russia, pp 455–460
9. Filippenko GV (2015) The banding waves in the beam with periodically located point masses. Vycisl. meh. splos. sred—Comput Continuum Mech 8(2):153–163. http://dx.doi.org/10.7242/1999-6691/2015.8.2.13
10. Eliseev VV, Zinovieva TV (2018) Lagrangian mechanics of classical shells: theory and calculation of shells of revolution. In: Shell structures: theory and applications, vol 4, Proceedings of the 11th international conference, Published by Taylor & Francis Group, London, pp 73–76
11. Zinovieva TV (2017) Calculation of shells of revolution with arbitrary meridian oscillations. In: Evgrafov A (ed) Advances in mechanical engineering. Selected contributions from the conference "Modern Engineering: science and education", Saint Petersburg, Russia, June 2016, Springer International Publishing, Switzerland, Lecture notes in mechanical engineering, 2017, pp 165–176. ISSN 2195-4356. https://doi.org/10.1007/978-3-319-53363-6
12. Filippenko GV (2016) The vibrations of reservoirs and cylindrical supports of hydro technical constructions partially submerged into the liquid. Evgrafov A (ed) Advances in mechanical engineering. Selected contributions from the conference "Modern engineering: science and education", Saint Petersburg, Russia, June 2014, Springer International Publishing, Switzerland, Lecture notes in mechanical engineering, 2016, pp 115–126. ISSN 2195-4356. https://doi.org/10.1007/978-3-319-29574-4
13. Veshev VA, Kouzov DP, Mirolyubova NA (1999) Energy flows and dispersion of the normal bending waves in the X-shaped beam. Acoust Phys 45(3):331–337
14. Kouzov DP, Mirolubova NA (2012) Local energy fluxes of forced vibrations of a thin elastic band. Vycisl. meh. splos. sred—Comput Continuum Mech 5(4):397–404. http://dx.doi.org/10.7242/1999-6691/2012.5.4.47
15. Sorokin SV (2002) Analysis of vibrations and energy flows in sandwich plates bearing concentrated masses and springlike inclusions in heavy fluid loading conditions. J Sound Vibr 253:485–505. https://doi.org/10.1006/jsvi.2001.4065
16. Sorokin SV, Nielsen JB, Olhoff N (2004) Green's matrix and the boundary integral equations method for analysis of vibrations and energy flows in cylindrical shells with and without internal fluid loading. J. Sound Vibr 271(3–5):815–847
17. Filippenko GV (2017) Energy-flux analysis of the bending waves in an infinite cylindrical shell filled with acoustical fluid. In: Evgrafov A (ed) Advances in mechanical engineering. Selected contributions from the conference "Modern engineering: science and education", Saint Petersburg, Russia, June 2016, Springer International Publishing, Switzerland, Lecture notes in mechanical engineering, 2017, pp 57–64. ISSN 2195-4356. https://doi.org/10.1007/978-3-319-53363-6
18. Filippenko GV (2017) Waves with the negative group velocity in the cylindrical shell, filled with compressible liquid. In: Evgrafov A (ed) Advances in mechanical engineering. Selected contributions from the conference "Modern engineering: science and education", Saint Petersburg, Russia, June 2017, Springer International Publishing, Switzerland, Lecture notes in mechanical engineering, 2018, pp 93–104. ISSN 2195-4356. https://doi.org/10.1007/978-3-319-72929-9

# Inspection of Welded Joints of New Pressure Vessels Using the Acoustic Emission Method Capabilities


**Victor P. Gomera, Anatoly D. Smirnov, Evgeny J. Nefedyev and Anastasiya V. Grigorieva**

**Abstract** An example of weld-joint testing of a new pressure vessel made of stainless steel is considered. The main methods of testing were the method of radiography and the method of acoustic emission. Dangerous defects in the refinery column were detected before running began as a result of the joint application of these methods. This example demonstrates the effectiveness of using such the properties of acoustic emission method, as the integral nature of testing, high sensitivity and the ability to record developing (the most hazardous) defects in the application to the diagnosis of the industrial pressure vessels state. Also, the results of metallographic examination of the specimen of column shell with detected defects are presented. The question of the sequence of application of different methods of non-destructive testing for optimization of the procedure for inspection of large-sized equipment is discussed.

**Keywords** Acoustic emission · Radiographic testing · Pressure vessels · Stainless steel · Cracks in the welds · Sequence of application of testing methods

## 1 Introduction

The universal capabilities of the acoustic emission (AE) method make it possible to effectively use it both in the field of research the properties of structural materials [1–8], and in non-destructive testing (NDT) of a wide range of industrial equipment [9–11], in particular—oil refining equipment [12–22]. To a separate subclass of such

V. P. Gomera (✉) · A. D. Smirnov
KINEF Ltd, Kirishi, Leningrad Region, Russia
e-mail: Gomera-V-P@yandex.ru

E. J. Nefedyev
Krylov Scientific Center, St. Petersburg, Russia
e-mail: ne246@ya.ru

A. V. Grigorieva
St. Petersburg State University, St. Petersburg, Russia
e-mail: a.v.grigorieva@spbu.ru



A. N. Evgrafov (ed.), *Advances in Mechanical Engineering*,
Lecture Notes in Mechanical Engineering,
https://doi.org/10.1007/978-3-030-11981-2_3

equipment can be attributed to the newly manufactured pressure vessels. For these objects, there are some features of the interpretation of the results of AE testing associated with the recording of data caused by the relaxation of recent welding stresses [10, 23].

An additional factor that distinguishes new equipment into a separate group of objects of testing is the conditions noted in [24]. As a result of a long period of use of imported equipment for the modernization of the oil refining industry, the development of domestic chemical engineering has slowed down to a large extent, and the quality of its products has decreased. This causes new, more serious than previously, requirements for the entrance inspection of new equipment of domestic production for the entire period of solving the problem of replacing imported equipment. Accordingly, there is the task of improving the quality of technical diagnostics without a fundamental increase in the use of traditional local methods of NDT, since this entails a significant increase in the time and economic costs of such diagnostics. To solve this problem, it is advisable to use modern integral methods of NDT, such as the AE method. In this paper, an example of such use is demonstrated and the results obtained are analyzed.

At random radiographic testing (RT) in welds of column manufactured for use in the process treatment unit for sulfur cleaning from petroleum products (photograph in Fig. 1), some internal defects were revealed. Defects were generated as a result of irregularities in welding procedure at manufacturing facility. Column dimensions: body height is 23,800 mm, diameter is 1800 mm, wall thickness is 20 mm. Metal—austenitic stainless steel 12Cr18Ni10T. The column was being prepared to commissioning in the production cycle.

The results of random testing were the reason for conducting a complete NDT of welds of column body, including welds of eight nozzles with the diameter of 500 mm. Herewith, the application of ultrasonic (UT) testing method was impossible due to features of column metal structure. RT method was used for testing. Total length of tested weld joints was over 160 m. Test duration, including activities on organization of two-side access to testing areas necessary for RT, exceeded 3 weeks.

As the result of RT, there were revealed more than 30 weld-joint areas containing internal cracks and non-metallic inclusions. More than half of these areas (18) were located in T-shaped intersections of welds, 13 of 18 areas contained large cracks. The article presents some results of a metallographic study of a seam in one of these sites.

Revealed defects were repaired. AE method was supposed to be the final testing step in column general inspection procedure. As the large scope of RT application allowed assuming with high probability that all major defects are revealed, the main objective of AE testing was the assessment of repair quality of welds with eliminated defects. Additional objective of the AE was inspection of some welds difficult to access for RT due to the design features of column.

The results of AE testing revealed no defects that tend to develop in repaired welds. Consequently, main objective of AE method application was fulfilled. Besides, as the result of AE testing there were detected five more areas containing AE source characteristics for developing defects that were not revealed during RT. In two cases,

**Fig. 1** General view of the new column during installation

these areas were within the zones skipped during RT due to their inaccessibility for local NDT methods. After special activities on organization of access to these zones, the presence of defects in them was confirmed with the RT method, as well as for other three areas (including two nozzles) after repeated RT and thorough analysis of RT images. In the latter case, the shape and the orientation of defects made their detection unlikely with the RT method during first inspection, while AE method is capable of detecting such defects independently of their size and orientation.

This paper presents some results of analysis of AE testing data and RT images of revealed defects.

The issue on the sequence of implementation of different NDT methods for optimization of inspection procedure for large-scale equipment is also discussed.

## 2 Equipment for Column Inspection

Radiographic testing was conducted by the "Smart-225" device using a radiographic Agfa D5 film with a resolution of 0.50 mm.

The use of the other traditional test method—ultrasonic inspection—was impossible for a given metal thickness due to significant attenuation of ultrasonic signal and its reflection at the alloying elements of the austenitic steel.

To identify the cause of cracking, the shell section with a defect at the intersection of circular and longitudinal welds was cut and subjected to metallographic investigations.

The AMSY-5 system with integrated resonant transducers VS150-RIC was used for AE testing. The frequency range was set as $\Delta f = 90 \ldots 450$ kHz. Threshold was fixed as Thr = 40 dB. The number of supervisory channels was equal to 36.

Practical difficulties were faced at sensors mounting to the non-magnetic shell. This problem was solved by gluing of carbon steel small plates to the body with polyvinyl adhesive (photograph in Fig. 2a, b). This allowed use magnetic holders for sensor mounting. The plates of 110 × 70 × 2 mm curved to comply with the shell having a central hole with the diameter slightly larger than the diameter of the sensor were glued to the body at spots prepared for sensors. The clearance stipulated with the plate thickness was compensated with round rubber gaskets placed in the magnetic holder groove: two gaskets 1 mm thick (1/2 plate thickness) were used. The plates were left on the column for possible further testing.

This method of sensor mounting was stipulated with the drawbacks of alternative methods for particular application. In the case of using bandage straps, their length should be very long and their uniform adjustment would be quite challenging. In addition, a large number of prominent structural elements on the outer part of the column obstruct the straps installation (Fig. 2a). Welding of any additional parts not provided by the design was prohibited. Attaching the sensors by adhesives was

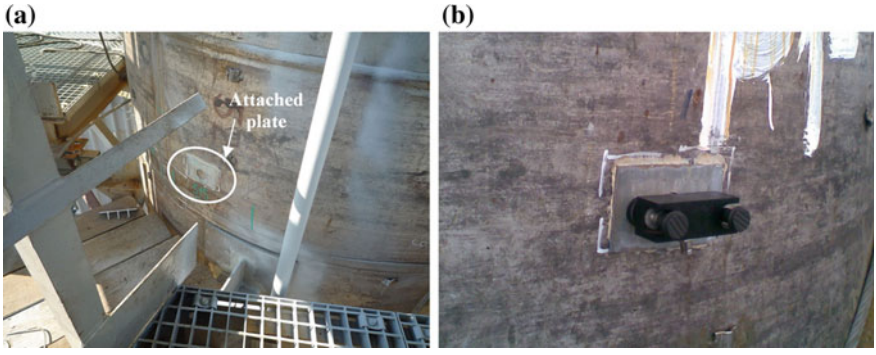


**Fig. 2** Method of sensors installation on the column non-magnetic surface: **a** magnetic metal plate with a hole for sensor is glued to the non-magnetic shell; **b** sensor is mounted on the plate using a standard magnetic holder

not considered because of the risk of damage during removal. The use of adhesive tapes or other palliative methods for sensors mounting was unreliable under the field test conditions. The test results have proven that the proposed method of sensor attachment was a good solution for sensor attaching to non-magnetic surface.

## 3 Results of Radiographic Testing

The defects of weld joints at the intersections of circular and longitudinal welds were revealed by the RT. The most significant defects were 13 cracks of 10–100 mm long. The features of these cracks: they are located in the longitudinal welds and start from the junction with circular welds; cracks were primarily open along the axis of the symmetry of the weld; branching from the main cracks was readily observed in both directions; opening of side cracks was found smaller than that of the central crack, so that some side cracks are not detected due to the sensitivity limits of the RT.

## 4 Results of Metallographic Investigation

The piece of body at the intersection of the longitudinal and circular weld was taken for the metallographic study (Fig. 3a). Figure 2b shows the crack indication 80 mm long at lower generator of metal mechanical sample of the longitudinal weld 150 mm long and up to 7 mm deep after capillary testing. The crack starts from the intersection of welds.

The specimens cutting scheme for metallographic investigations are shown in Fig. 3c. Large cracks, which represent the fragments of cracks oriented along axis of the longitudinal weld, as well as numerous microcracks were found in specimens

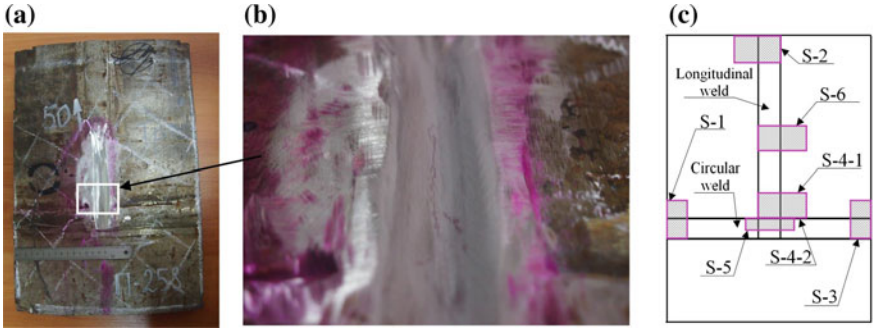


**Fig. 3** **a** Piece of shell that was cut out for the study; **b** crack indication in the longitudinal weld at capillary testing; **c** the scheme of cutting of specimens from the piece of shell for metallographic investigation of welds

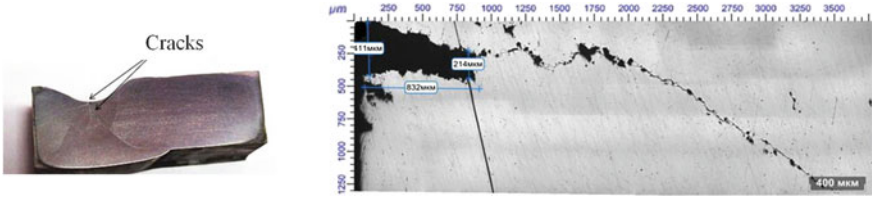


**Fig. 4** Specimen S-4-1. General view (left) and metal destruction to a depth of 832 microns and intergranular crack of 2.5 mm directed into the depth of the longitudinal weld, ×50 (right)

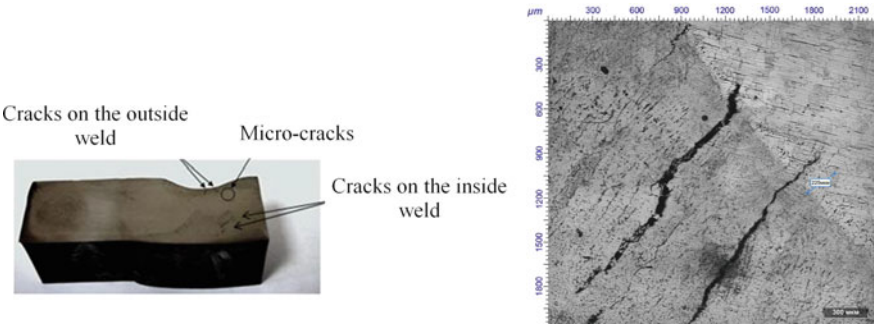


**Fig. 5** Specimen S-4-2. General view (left) and microcracks in the fusion zone, penetrating 225 microns into the base metal, ×50 (right)

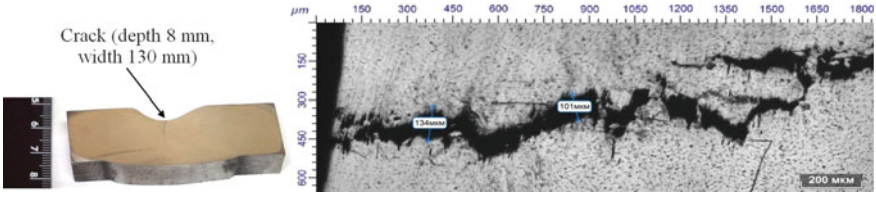


**Fig. 6** Specimen S-6. General view (left) and crack and numerous intergranular cracks formed from it, ×50 (right)

S-4 and S-6. The view of metallographic images of some specimens containing the cracks is presented in Figs. 4, 5, and 6.

The longitudinal crack refers to hot cracks. The presence of hot macrocracks is accompanied with the formation of microcracks. Formation of the cracks is related to high stress due to inappropriate choice of welding technology. No cracks were observed in the areas remote from intersections in either circular or longitudinal welds.

All the cracks found during the inspection of the column were formed as a result of infringement of the welding technology. Issues of manufacturing high-quality weld-joints are considered in [25–28].

## 5 Results of AE Testing and Additional RT

According to the analysis of the AE data, a visual inspection of the test object was carried out in order to establish the correlation of the AE activity zones with the location of the structural elements of the column and temporary structures for installation work that could contact the surface of the column.

Visual inspection allowed excluding from consideration the areas of AE activity, which are clearly not related to potential defects of the body For example, it was the area for attachment of maintenance platforms with new weld joints. For additional RT, five zones were chosen. Figure 7 shows the location of these zones on the reamer of the column shell. The scheme of the reamer is combined with the diagram of the planar location of the AE sources in this figure.

As a result of additional RT in Zones 1, 3, 4, 5, the presence of unacceptable defects was confirmed: Zone 1—24 mm crack and slag (Fig. 8a), Zone 3—15 mm crack (the position of zone 3 is shown in Fig. 9a; the photograph shows that this site is difficult to access for any local testing methods), Zone 4—large slag inclusions (up to 8 × 2 mm) and pores in the weld of nozzle $F1$, Zone 5—welding defects (photograph in Fig. 9b) and large slag inclusions (up to 10 × 1.5 mm) in the weld of the lower hatch-manhole $H6$ (photograph in Fig. 8b). In Zone 2, permissible size defects (pores and slag inclusions) in the weld were detected.

The graph of the location of AE sources in Fig. 7 is one of many elements of the analysis of AE data. Sources of AE are evaluated by the energy characteristics of the generated signals, by the trends of these characteristics, by the connection of the time of registration of signals with the stages of application of the load, and by the characteristics of location clusters and other parameters. For example, Fig. 10 shows a graph of the correlation for two energy characteristics of AE signals (Amplitude and Counts) which associated with the registration of localized events on the shell of the column to a height of approximately 14,000 cm for channels ##1–12, 16–24. Triangles are signals on channels 3 and 5. In the ellipse area in the right corner of the graph, there are signals registered on channels 3 and 5, associated with the registration of defects in Zone 4 and Zone 5. Signals from the cluster formed by the ellipse, registered on other channels, also considered as signs of registration of defects. However, the main part of these signals during the analysis was excluded from consideration by other estimated parameters.

## 6 Results and Discussion

Let us consider the results of solution of basic tasks set to AE testing:

1. No growing defects were identified in repaired welds. Therefore, a good quality of repairs of pre-detected defects has been confirmed.
2. Cracks detected in Zone 1 and Zone 3 were similar to cracks considered during metallographic study. Prior to AE testing, it was possible to estimate the proba-

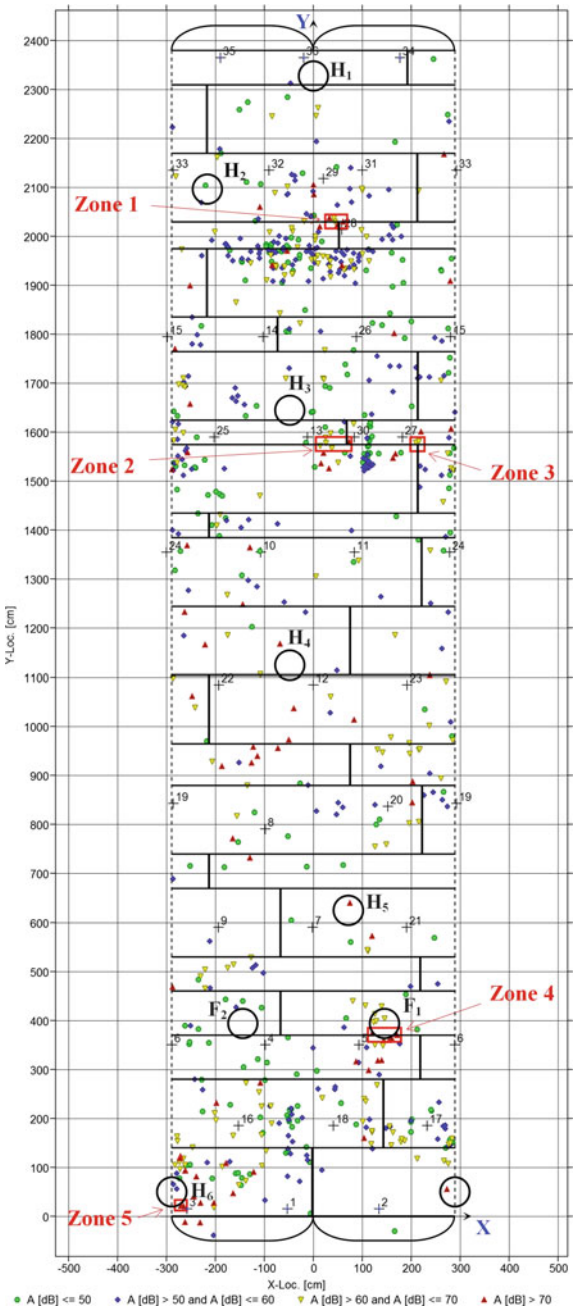


**Fig. 7** Location of AE sources on the shell and location of zones defined for additional RT

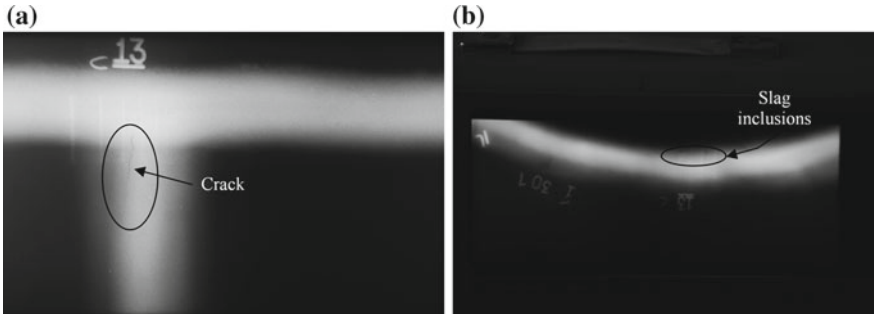


**Fig. 8** Radiographic images of the defects: **a** in a T-shaped weld, **b** in the weld between the hatch-manhole and the shell

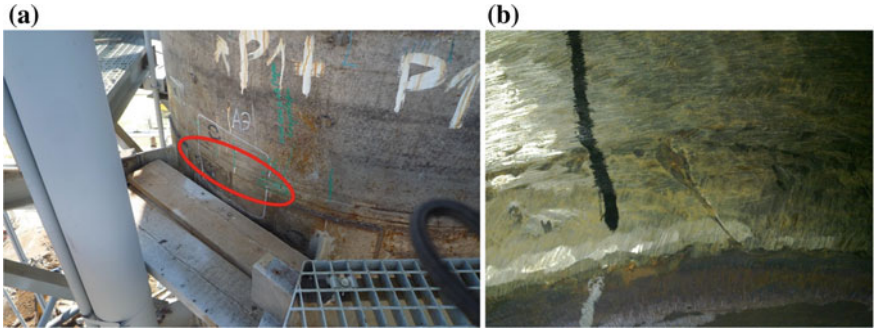


**Fig. 9** Some photographs of areas for additional testing: **a** position of Zone 3 on the column shell, **b** one of welding defect in Zone 5

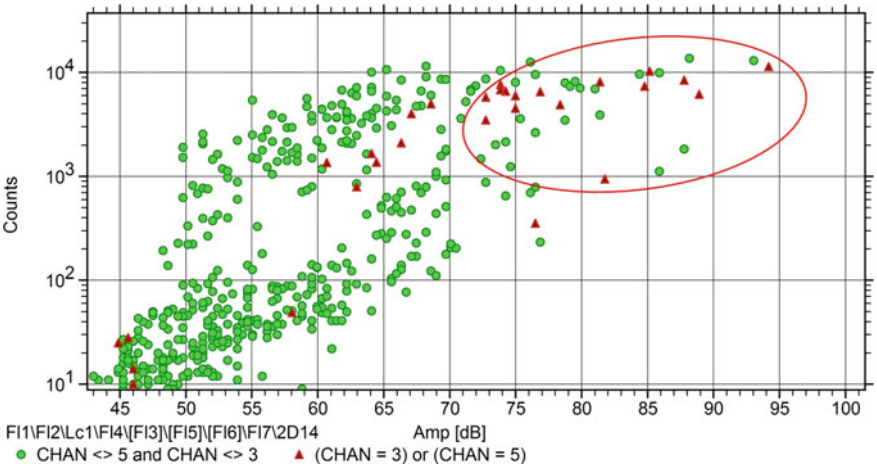


**Fig. 10** Correlation for two energy characteristics of AE signals associated with the registration of localized events on the shell of the column to a height of approximately 14,000 cm for channels ## 1–12, 16–24

bility of having not-detected cracks which then could have been detected in the T-shaped welds (provided that the cracks grow during the AE testing). The number of RT-examined T-shaped welds (40), the number of detected large cracks in these welds (13), as well as the number of welds, which was not included in the area of RT (4), were known. Consequently, the probability of finding at least one crack in the T-shaped welds, which is not controlled during RT, can be evaluated as $P = 1\text{-}(1\text{-}13/40)^4 \approx 0.79$. Actually, cracks in two of these four welds were detected.

3. Beside the cracks in T-welds, considerable defects have also been found in the welds of two nozzles: large slag inclusions. Recording of active AE sources in their location indicates the presence of growing defects associated with those inclusions. Welds of nozzles are objects difficult for control by any method. Besides, slag inclusions are not always classified as critical defects. Nevertheless, the AE activity recording in the vicinity of inclusions followed by a thorough analysis of images obtained during additional RT allowed revealing those defects which might be prone to growth. After removal of all defects, the column has been successfully operated for more than four years.

Preparation and conducting of AE testing, as well as the data analysis, took about three days. Herewith, major part of this time was spent for column preparation to hydraulic testing, which anyway is obligatory conducted after body repairs. Inspection scheme is defined depending on technical specifications of the facilities, their number, available NDT means and other factors. Formally, the optimum scheme is the scheme, in which the scope and the sequence of NDT methods minimize the inspection time while preserving its quality. This gives a substantial economic effect due to a possibility of reduction of equipment downtime. In fact, the sequence of application of testing methods is determined by the management of mechanical service of the facilities and presently prioritizes the use of traditional and standardized testing methods, such as RT or US. The AE method is usually used as additional means. This approach is enforced not only to testing of the individual facilities, but also to larger groups of new equipment, for example, during reconstruction of technological units. When the inspection with traditional methods covers near 100% of the facilities, this way requires a lot of time and expenditures.

Let us denote the inspection time first with RT, and then with AE method (first option) as $t_1$, and the time for inspection in the inverse order (second option) as $t_2$. Then:

$$t_1 = t_1^{RT} + t^{AE} = k \times V_1^{RT} + \left(t_{\min}^{AE} + t_q^{AE}\right) \tag{1}$$

$$t_2 = t^{AE} + t_2^{RT} = t^{AE} + k \times 2dV_0, \tag{2}$$

where $t_1^{RT}$, $t_2^{RT}$ is the time of testing with RT method in the first and the second option, $V_0$ is the relative volume of testing, total (sum of structural elements equal by size to standard areas of testing with local methods, e.g., sections of welds equal in length, T-shaped sections of welds or other elements), $V_1^{RT}$ is the relative volume of testing

during *RT*, $k$ is the proportionality factor (mean time of testing of one element of volume), $t_{\min}^{AE}$ is the minimum time required for conduction of AE testing that allows conducting of planar location of defects with the size not less than the specified one, $t_q^{AE}$ is additional time used to enhance sensitivity of AE testing system at the expense of increase of the number of sensors and their packing density. Coefficient d is the share of $V_0$, areas specified for testing with RT method according to the AE results for determination of defect geometrical parameters. Additional multiplier "2" in the expression (2) is defined with our experience in AE testing and is probably related to the following circumstance. AE does not reveal "sleeping" defects which do not grow during current hydraulic testing. However, there exists the possibility that these defects may further grow under action of processing factors. In order to verify if these defects exist, it is advisable to add arbitrary testing of areas found during AE with testing of other random areas in the quantity proportional to the number of areas revealed during the AE (e.g., by doubling this quantity).

With due account of known parameters of considered inspection, we may accept:

$$t^{AE} \approx 0.1 \times t_1^{RT};\ V_1^{RT} \approx 0.9 \times V_0;\ t_{\min}^{AE} >> t_q^{AE} \tag{3}$$

Then, the time benefit in the second option shall amount:

$$\Delta t = t_2 - t_1 = k \times V_0(0.9 - 2d) \tag{4}$$

According to the expression (4), maximum efficiency of AE method implementation as primary testing is achieved when the structure contains small number of defects. So, the difference between the two options in the considered example is insignificant. However, by using this example, it is possible to make useful assessment for $d$. Let us assume that AE testing was conducted in the first place, and only a half of 18 defects in T-shaped joints revealed during RT would behave as the AE sources during hydraulic testing (i.e., they would grow). Then, by adding two sections detected during AE after RT, we obtain: $18/2 + 2 = 11$. By dividing this number by 44 (total volume $V_0$ for these elements), we obtain $d = 0.25$. Thus, if according to AE testing results we obtained $d \geq 0.25$, this is a compelling reason for conduction of 100% testing of any structural elements by local testing method (in our case—by RT), as the probability of containing defects in a large number of these elements is very high.

Implementation of AE method as initial testing method for industrial equipment is not seen a large progress as yet. As a rule, it allows reduction in time and, consequently, in cost of inspection, however, there exist some issues with method adapting to the effective normative rules at evaluation of testing results. Some problems related to the complexity of interpretation of AE testing results also remain unsolved. However, our experience in AE method application shows that it can be a useful NDT instrument in different combinations of AE and traditional testing methods.

## 7 Conclusions

1. The considered example shows that the AE method is an effective tool for non-destructive testing of large-sized structures. During testing of these structures, particular advantages of AE method are: possibility of 100% testing of structural material; high sensitivity; high performance; possibility of precise locating of the defect; possibility of detecting of growing defects independently of their size, orientation and location within the material.
2. The definite problem of the AE method is that for large-sized structures, in some cases, only qualitative or indirect estimates of the geometric characteristics of the defect using the AE data are possible. It is successfully solved by combining the AE integral method of and local testing methods (RT, capillary testing, UT, etc.). In general, joint implementation of integral method and local methods allows mutual reduction of level of uncertainty characteristic for each method, which arises during inspection of large-scale structures. AE method reduces uncertainty in selecting the spots for local testing and, as a result, substantially increases the efficiency of application of local testing methods. Local methods reduce the uncertainty in determination of nature of recorded sources of AE activity.
3. Maximum efficiency of AE method application for testing of large-scale structures may probably be achieved in case of its application as initial testing method in general inspection procedure.

**Acknowledgements** The authors thank Legostaev D.A. and Makarov A.V. from SPA "Lenkor" for the materials provided for use in this work and A. Vinogradov, professor at the Norwegian University of Science and Technology, Trondheim, for useful comments on the article.

## References

1. Semashko NA et al (2002) Acoustic emission in experimental materials science. In: Semashko, Sprite VI (eds) Mechanical Engineering, 240 p
2. Nefedyev E et al (2017) Determination of the Degree of Danger of crack-like defects in 17G1C Steel by the acoustic emission method. In: Radkevich MM, Evgrafov AN (eds) Modern Engineering. Science and Education, St. Petersburg, Publishing House of Polytechnic University, pp 387–401
3. Kovalev D, Nefedyev E, Tkachev V (2012) Acoustic emission control testing of steel corrugated pipes of circular and static loading. In: Radkevich MM, Evgrafov AN (eds) Modern Engineering. Science and Education, St. Petersburg, Publishing House of Polytechnic University, pp 382–390
4. Nefedyev E (2013) The use of acoustic emission method with spectral analysis of signals to determine the parameters of a leak in the pipeline ITER. In: Radkevich MM, Evgrafov AN (ed) Modern Engineering. Science and Education, St. Petersburg, Publishing House of Polytechnic University, pp 347–355
5. Belogur V, Semashko N, Kulesh A (2016) Methodological approaches to the diagnosis of products from Titanium alloys by acoustic emission (AE). In Radkevich MM, Evgrafov AN (eds) Modern Engineering. Science and Education. Publishing House of Polytechnic University, St. Petersburg, pp 350–358

6. Gomera V, Nefedyev E, Smirnov A (2017) On the possibility of production defect-free welds under acoustic emission monitoring. In: Evgrafov A, Egorova O (eds) International Review of Mechanical Engineering (IREME), vol 11, no 5, Special issue on "Advances in Modern Mechanical Engineering Research", ISSN 1970-8734, pp 343–349
7. Nefedyev E, Gomera V, Smirnov A (2018) Determination of a pre-destructive state during hydraulic testing of steel pipes with defects by the acoustic-emission method. In: Evgrafov A (ed) Advances in Mechanical Engineering, Lecture Notes in Mechanical Engineering, Springer International Publishing AG, pp 115–127. http://doi.org/10/1007/978-3-319-72929-9
8. Belousova V, Grigorieva A (2018) Development of software package for data analysis of acoustic emission control. CEUR Workshop Proceedings of 3rd conference on Software Engineering and Information Management, SEIM 2018, vol 2135. Russian Federation, Saint Petersburg, pp 61–66, 14 April 2018
9. GOST Ru 52727-2007. Technical diagnostics. Acoustic-emission diagnostics. General requirements
10. PB 03-593-03. Rules for the organization and conduct of acoustic emission control of pressure vessels, boilers, apparatus and process pipelines
11. Proust A, Lenain JC (2000) Use of acoustic emission to detect localized corrosion. Philosophy of industrial use, illustrated with real examples. In: Proceedings of the EWGAE-2000, Senlis, France, pp 153–160, 24–26 May 2000
12. Gomera V et al (2014) Modern practice of using non-destructive testing at refineries. In Yearbook of the Petersburg Power Engineering Institute for Advanced Studies. PEIPK, St. Petersburg, pp 81–103
13. Gomera V, Rastegaev I (2015) The possibility of the early identification of delamination in the walls of pressure vessels by the ultrasonic and acoustic emission inspection. Testing Diagn 1(199):82–89
14. Gomera V, Smirnov A, Nefedyev E (2014) Increase of AE testing reliability of equipment containing internal devices. NDT World 3(65):20–24
15. Development of methods to increase efficiency AE control of heat exchangers. In: Radkevich MM, Evgrafov AN (eds) Modern Engineering. Science and Education. Publishing House of Polytechnic University, St. Petersburg, pp 408–418
16. Kabanov B, Gomera V, Sokolov V et al (2000) Acoustic emission method for pressure vessel diagnostics at a refinery. J Acoust Emission 18:111–117 (2000)
17. Kabanov B, Gomera V, Sokolov V et al (2002) AE technology as a key element of the safe operation system at refinery. J Acoust Emission 20:218–228
18. Kabanov B, Gomera V, Sokolov V et al (2006) AE testing of refinery structures. In: Advanced materials research, vol 13–14, pp 133–138
19. Gomera V, Sokolov V, Fedorov V (2008) Implementation of acoustic emission method to the conventional NDT structure in oil refinery. J Acoust Emission 26:279–289
20. Gomera V, Sokolov V, Fedorov V et al (2010) Use of AE method for detection of steel lamination in the industrial pressure vessel. J Acoust Emission 28:234–245
21. Nefedyev E, Gomera V, Smirnov A (2016) Use of the capabilities of acoustic-emission technique for diagnostics of separate heat exchanger elements. In: Evgrafov A (ed) Advances in mechanical engineering, Lecture Notes in Mechanical Engineering. Springer International Publishing Switzerland, pp 183–194. http://doi.org/10/1007/978-3-319-29579-4_19
22. Zotov K, Rastegaev I, Gomera V et al (2016) The detection of different stages of the delaminating in the pressure vessels by the ultrasonic and acoustic emission technique. In: Book of Abstracts of the 19th World Conference on NDT (WCNDT). Munich, Germany, p 209, 13–17 June 2016
23. Cole P, Gautrey S (2004) Acoustic emission experience with AE monitoring of new vessels during initial proof test. In: Proceedings of the EWGAE-2004. Berlin, Germany, pp 75–81, 15–17 September 2004
24. Dobrotvorsky AM et al (2015) Problems of quality of manufacturing of refinery equipment in connection with the task of import substitution. Chem Eng 1:16–18

25. Sokolov S (2017) The model of the elastic-plastic deformation of a structural member. Lecture Notes in Mechanical Engineering, pp 125–132
26. Sokolov S (2018) Analysis of the fatigue strength of welds in terms of local stress. Russian Engineering Research 38(3):151–156
27. Evgrafov A, Petrov G (2017) Computer simulation of mechanisms. Lecture Notes in Mechanical Engineering, pp 45–56
28. Manzhula K, Shlepetinskii A (2016) Stress and strain concentration in weld-joint flaws. Russian Eng Res 36(9):722–726

# Reduction of Contact and Bending Stresses in the Bevel Gear Teeth While Maintaining the Same Overall Dimensions


**Vladimir I. Medvedev, Dmitry S. Matveenkov and Andrey E. Volkov**

**Abstract** The proposed article contains a technique for optimizing the parameters of a gear pair with circular teeth, which can be used both in the design of a new gearbox and in the modernization of an existing gearbox. In both cases, the initial data for the design of the transmission, which is part of the gearbox, are its gear ratio, dimensions and transmitted loads. The only difference is that in the second case, as a rule, it is necessary to place a couple in the same housing, which imposes more stringent restrictions on its size. Two examples of the optimal design search by varying the angle of the spiral and by varying the number of teeth while maintaining the same gear ratio are given.

**Keywords** Spiral bevel gears · Optimization · Instantaneous contact area · Localized bearing contact · Contact pressure · Bending stress · Machine-tool settings

## 1 Mathematical Model for Research

To optimize the macro-geometry of transmission (spiral angle, face width, number of teeth, tooth height, etc.), it is necessary to be able to select the shape (micro-geometry) of the side surfaces of the transmission teeth, providing optimal contact pressure and bending stress in meshing. Constructive parameters (the macro-geometry) of transmission are assumed to be given. If this problem is solved, optimization by macro-geometric parameters can be performed simply by varying these parameters. The search for micro-geometry problem involves, in turn, solving two problems: the

V. I. Medvedev · D. S. Matveenkov · A. E. Volkov (✉)
Moscow State University of Technology "Stankin", Moscow, Russia
e-mail: volkov411@gmail.com

V. I. Medvedev
e-mail: vladimir.ivanovich.medvedev@gmail.com

D. S. Matveenkov
e-mail: 1mdiman@mail.ru



A. N. Evgrafov (ed.), *Advances in Mechanical Engineering*,
Lecture Notes in Mechanical Engineering,
https://doi.org/10.1007/978-3-030-11981-2_4

problem of constructing the side surface of the teeth (synthesis) and the problem of determining the quality of meshing (analysis). Many studies have been published on improving the methods of analysis of bevel gears [1–5], as well as improving the quality of meshing by improving the parameters of the tool and settings of gear-cutting machines, causing an improvement in the micro-geometry of the tooth [1, 6–13]. A common disadvantage of the mentioned methods of synthesis is the necessity of selection of synthesis parameters interactively. That makes high demands on the qualification of the designer. In this paper, we propose an algorithm to automate the construction of optimal micro-geometry of the tooth on the basis of simple enough to understand the initial data, which are the required distances from the bearing contact to the edges of the teeth at a given load.

Determination of the shape of the tooth is carried out using the synthesis algorithm of gear set [11–13] and algorithms for analyzing the quality of the produced gear [14–16], based on elasticity theory that takes into account:

– the real flank obtained on the gear-manufacturing machine;
– distribution of the bending moment along the length of the tooth obtained by solving the problem of contact of elastic bodies bounded by surfaces of double curvature;
– comparability of tooth sizes in each of the three directions.

The second task is to improve the design of the existing gearbox using a refined test calculation of bending stresses.

To reduce the level of bending stresses in the gear teeth, without changing the design of the transmission, it is possible either by obtaining a more uniform contact load along the length of the tooth or by reducing the load on the tooth. This can be achieved by increasing either the length of the instantaneous contact area or the total contact ratio by selecting the appropriate shape of the contacting surfaces, determined by the machine-tool settings used for processing the teeth. Herewith, contact pressures are also reduced. However, this increase will eventually lead to edge contact and excessive contact pressure. In Fig. 1a, there is a bearing contact on the gear teeth surface, and in Fig. 1b, there is a graph of the maximum contact pressure $\sigma_H$, MPa dependence on the meshing phase. The instantaneous contact area extends to the upper edge of the tooth. Even in the absence of technological and assembling errors, there is a concentration of contact pressures on this edge. The location of the maximum contact pressure is indicated in the figure by a circle. Instantaneous contact area in which the maximum pressure is located is highlighted in black. It has the shape of an ellipse cut by the transverse edge of the tooth.

Machine-tool settings, providing a given length $a_{max} = 0.6b$ of the greater semi-axis of the instantaneous contact area ($b$ is the face width) under the condition of infinity of the tooth surface, were determined by the algorithm [2]. Simulation of the meshing process, the results of which are built in Fig. 1, was made with the help of the "Expert" program [11] to solve the contact problem based on the consideration of teeth as elastic three-dimensional bodies.

This example and many others that can be cited are showing that the minimum contact pressures should be sought among the surfaces that provide some detach-

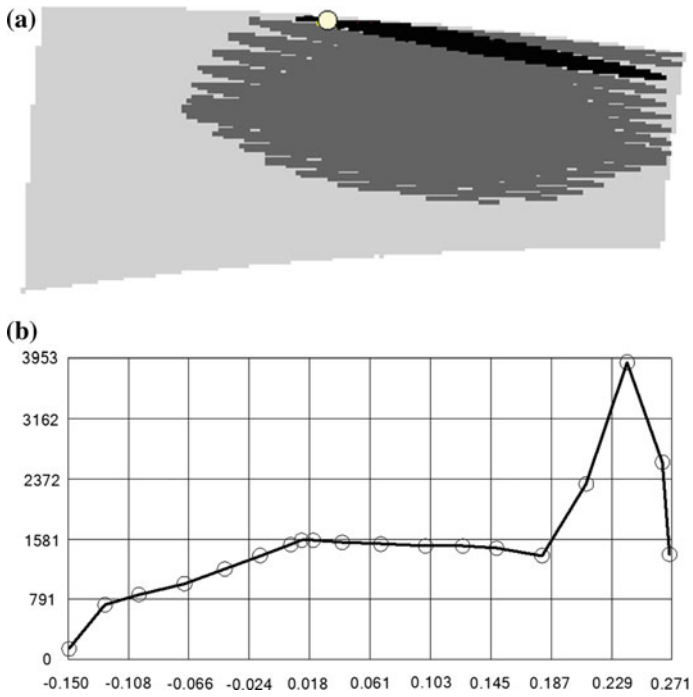


**Fig. 1** Solution of the contact problem from the standpoint of elasticity theory: **a** bearing contact and **b** graph of the maximum contact pressure dependence on the meshing phase

ment of the bearing contact from the edges of the teeth, even in the presence of technological and installation errors. This contact we will call a localized contact.

Calculations based on the algorithm of the non-Hertz solution [2] are quite time-consuming and do not allow to use it in the process of minimization. As a tool for the tooth contact analysis in the process of minimization, the analysis program based on the solution of H. Hertz is utilized [12]. A large number of numerical experiments showed that if none of the contact ellipses go beyond the surface of the tooth, the contact pressures obtained based on the Hertz solution differ from the pressures obtained using a more accurate solution by no more than 3%. For comparison, in Fig. 2 the results of the analysis of the considered meshing based on Hertz theory are presented. Since the Hertz solution assumes that the contacting surfaces are infinite in size, the instantaneous contact areas (shown in Fig. 2a, various shades of gray) go beyond the boundaries of the lateral surface of the tooth. In addition, there is no concentration of contact stresses, which depend on the phase of meshing as shown in Fig. 2b on the right. In gearing phases where there is no edge contact, the results of the two solutions are almost the same.

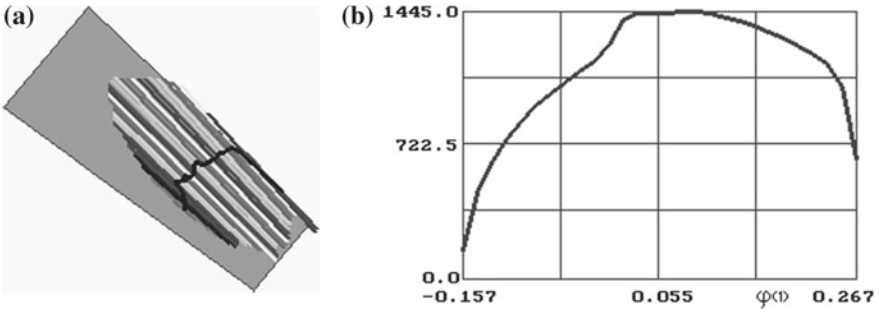


**Fig. 2** Some results of the contact problem solution based on Hertz approach: **a** bearing contact and **b** graph of the maximum contact pressure dependence on the meshing phase

## 2 Formulation of the Optimization Synthesis Problem

The optimal side surfaces of the teeth are the surfaces providing the maximum half of length $a_\xi$ of instantaneous contact area (Fig. 3) in the middle of the meshing interval, which provides localized contact. The degree of contact localization is determined by fourth value (Fig. 3):

- distances (detachment) $\Delta_{a1}$, $\Delta_{a2}$ of bearing contact from the tooth upper edge of pinion and gear;
- distances (detachments) $\Delta_e$, $\Delta_i$ of bearing contact from the outer and inner transverse edges of the tooth.

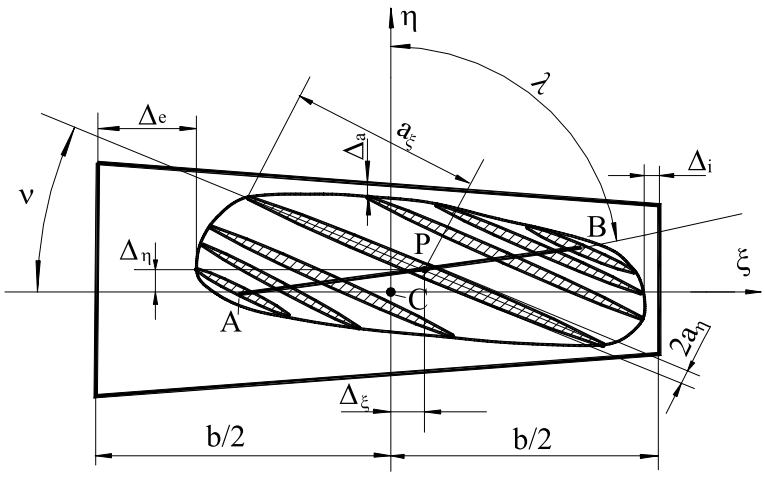


**Fig. 3** Location of the bearing contact and the instantaneous contact ellipses in case of localized contact

Distance from the edge is considered positive if all the contact ellipses lie on the tooth surface.

The required values of $\Delta_{ar}$, $\Delta_{er}$, $\Delta_{ir}$ of these separation detachments are the input data for solving the problem. The detachment $\Delta_{ar}$ is recommended to choose $\Delta_{ar} \geq m_n / 10$, where $m_n$—mean normal module. The other two detachments should be selected as follows: $\Delta_{er} \geq b / 10$; $\Delta_{ir} \approx 0.25\Delta_{er}$.

Note that the optimal machine-tool settings and the optimal shape of the side surfaces of the teeth depend on the load. At a load greater than the accepted as the maximum permissible at minimization, the edge contact is possible. At the edge contact, the obtained solution becomes not optimal due to a sharp increase in contact pressures.

The optimization problem is reduced to the construction of tooth surfaces providing the maximum half-length $a_\xi$ of the greater semi-axis of the instantaneous contact ellipse in the middle of the meshing interval of a pair of teeth. Clearly, the growth of $a_\xi$ is limited by the size of the flank. As constraints for minimization, we accept

$$|\Delta_{a1} - \Delta_{a2}| < 0.2Y \tag{1}$$

$$Y = \Delta_{a1} + \Delta_{a2} > 1.8\Delta_{ar} \tag{2}$$

$$|\Delta_i - \Delta_{ir}| < 0,3\Delta_{ir} \tag{3}$$

$$|\Delta_e - \Delta_{er}| < 0.2\Delta_{er} \tag{4}$$

$$f < 0.7w_0 \tag{5}$$

The index "1" refers to the pinion, and the index "2" refers to gear; $f$ is the transmission error; $w_0$ is the elastic approach of the teeth under load, when the center of contact ellipse is at point P. Distances $\Delta_{a1}$, $\Delta_{a2}$, $\Delta_e$, $\Delta_i$ of bearing contact from tooth edges are to be nonnegative.

Restrictions are formulated in the form of inequalities, because the valued: $\Delta_{a1}$, $\Delta_{a2}$ $\Delta_e$, $\Delta_i$ are determined with considerable error. This is because the algorithm used determines the position of the ends of the instantaneous contact area with an error of 1–2% of the face width $b$. Thus, the error of determining the distances $\Delta_{a1}$, $\Delta_{a2}$ can reach 20%, but this accuracy is sufficient for practical purposes.

The algorithm for solving the optimization synthesis problem is based on the purposeful selection of the synthesis parameter values that ensure the validity of inequalities (1)–(5). The following values are used as synthesis parameters (Fig. 3):

- offset $\Delta_\xi$, $\Delta_\eta$ of teeth meshing interval midpoint P from point C that is located in the tooth in the middle of tooth line;
- length $a_\xi$ of the large semi-axis of the instantaneous contact area at the contact of the teeth in the middle of the meshing interval (point P);
- angle $\lambda$ between the contact path AB and perpendicular to the gear tooth line (axis $\xi$);

– maximum transmission error $f$.

Because the error in determining the distances $\Delta_{a1}$, $\Delta_{a2}$, $\Delta_e$, $\Delta_i$ is large (10% or more), the use of differential methods of minimization is not possible. The minimization is performed by step method; at the same time, the value of only one synthesis parameter is changed at each step. For given values of the synthesis parameters, synthesis of transmission is carried out. After that, analysis of obtained gear set is accomplished. The analysis results are actual distances $\Delta_{a1}$, $\Delta_{a2}$, $\Delta_e$, $\Delta_i$. The actual distances are compared with the required distances. On the basis of comparison we determine the parameter of the synthesis to be changed and its new value. After that, the re-synthesis and analysis are carried out. The process is repeated until conditions (1)–(5) are met.

For the first iteration, it is necessary to set initial approximations of variable parameters.

1. Offset $\Delta_\xi$ the contact patch toward the toe in the absence of deformation of the shafts serves to compensate the displacement of the bearing contact in the heel direction under load. As the first approximation, we will take $\Delta_\xi = -(\Delta_{er} - \Delta_{ir})/2$.
2. The value of the displacement $\Delta_\eta$ is determined from the condition of equal detachment of the bearing contact from the tooth head on the pinion and on the gear. Gears, as a rule, have an addendum modification, determined by the addendum modification factor $x_n$. So, the middle point C of the pinion flank, located on the pitch cone, is shifted to bottom land, and on the surface of the gear tooth—to the top land. If you select the calculated point P on the pitch cone, the bearing contact will be displaced in these directions relative to the middle of the tooth surface profile. For the first iteration, it is possible to take $\Delta_\eta = 0.75 \cdot m_n x_n$.
3. The choice of the initial approximation of values $\lambda$ and $a_\xi$ as well of the strategy of search of optimum surfaces depends on two parameters:
   – the ratio of the face width $b$ and the average height of the active tooth profile $h_w = 2h_a^* m_n$ (here $h_a^*$ is addendum factor);
   – spiral angle $\beta$.

The orientation of the contact ellipse is determined by the angle $\nu$ (Fig. 3) between the tooth line and the greater half-axis of the ellipse. The estimation of the value of this angle, which does not change much in meshing, is given by the relation

$$\nu = \operatorname{arctg}(\sin\alpha \cdot \operatorname{tg}\beta) \tag{6}$$

The pressure angle $\alpha$ usually is close to 20°. The range of applicable spiral angles is wide. Spiral angle affects strongly on contact ellipse inclination.

If the face width b significantly (more than four times) exceeds the height $h_w$ of active surface (Fig. 4a), then it is possible to ensure the location of the moving instantaneous contact area of large length inside the tooth in all phases of meshing only if the direction of its movement (shown in the figure by the arrow) is close to the

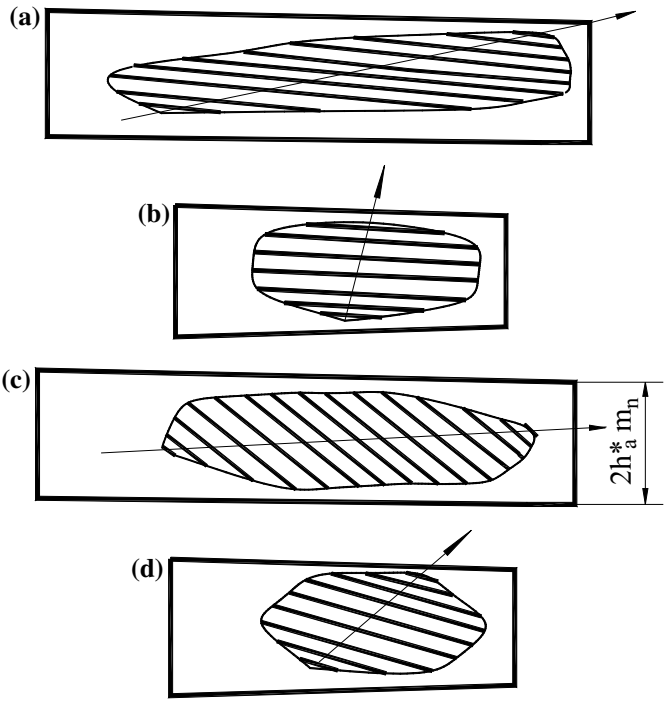


**Fig. 4** Expected bearing contacts and the directions of the contact paths: **a** large face width, small spiral angle; **b** small face width, small spiral angle; **c** large face width, large spiral angle; **d** small face width, large spiral angle

direction of the tooth line. In this case, we set $\lambda = 70°$ and relative length of contact area $c = a_\xi / b = 0.33$ as the initial approximation of the parameters.

Otherwise (small gear face width and small spiral angle, see Fig. 4b), movement of the instantaneous contact area in the transverse direction is preferable. In this case, we can increase the sum of distances $Y$ from the longitudinal edges, increasing the transmission error $f$ and thereby reducing the length of the contact path AB (Fig. 3). Only if this is not possible [leads to a violation of condition (5)], further increase of $Y$ is carried out by increasing the angle $\lambda$. It is possible to get the localized contact in case of relatively small spiral angles ($\beta \leq 20°$) at the inclination $\lambda$ of the contact path, close to 20°. This value of $\lambda$ is taken as the initial approximation.

In case of large spiral angles, the localization of the bearing contact with instantaneous contact areas of considerable length is possible only at significant angles $\lambda$ (Fig. 4d). As initial approximation can be adopted, angle $\lambda = 50°$. The relative length $c$ of the contact area decreases with the growth of spiral angle. We take $c = 0.3$ as an initial approximation.

At large spiral angles and large relative tooth lengths (Fig. 4c), the main limitation on the length of the instantaneous contact area is the possibility of placing it in

the interval between the tip of the tooth and the border of the fillet. The distance between these lines in the middle section is approximately $h_w$. Therefore, the initial approximation of $a_\xi$ is determined by the relation

$$a_\xi = \min\left(cb;\ 0.4h_w \big/ \sin\nu\right) \tag{7}$$

The coefficient of 0.4 is introduced in order to obtain positive value of $Y$ and to be able to localize the contact in the direction of the contact line, slightly different from the longitudinal direction ($\lambda < 90°$). The recommended initial approximation of spiral angle is 80°.

4. On the basis of selected values of the variable parameters $\Delta_\xi$, $\Delta_\eta$, $\lambda$ and $a_\xi$, the transmission is synthesized. Since the transmission error before the synthesis is not known and the value of $w_0$ is slightly dependent on $f$, the synthesis is performed at $f = 0$. In the process of synthesis, the elastic approach $w_0$ of the teeth at a single-pair contact at the point P is calculated; after that, the initial approximation of the value $f$ is determined as follows

$$f = \left(2w_0 + f_{pt1} + f_{pt2}\right) \big/ k. \tag{8}$$

Here, $f_{pt1}$, $f_{pt2}$ are the permissible pinion and gear circular pitch errors; $k = 8$ in case $b > 4h_w$ and $k = 6$ otherwise. The coefficient $k$ is chosen from the condition that at the most unfavorable combination of pitch errors the total contact ratio $\varepsilon < 2$.

The algorithm execution includes the following actions:

1. creation of the required sum $Y$ of distances from the bearing contact boundary to tip edges of pinion and gear due to the increase of transmission error $f$ or the angle $\lambda$ of inclination of the contact path;
2. alignment of distances from bearing contact to the tooth tips of pinion and gear by changing the parameter $\Delta_\eta$ to satisfy inequality (1);
3. increasing the length of the instantaneous contact area if the sum $X = \Delta_e + \Delta_i$ of the distances from the transverse edges significantly exceeds the required value $X_r = \Delta_{er} + \Delta_{ir}$;
4. displacement of the bearing contact along the tooth line to create the required detachment from the transverse edges of the tooth. Additional displacement $\delta\Delta_\xi$ is determined from the system of equations

$$\Delta_e - \delta\Delta_\xi = \Delta_{er},\ \Delta_i + \delta\Delta_\xi = \Delta_{ir}. \tag{9}$$

Equation (9) is the condition that after the displacement $\Delta_\xi + \delta\Delta_\xi$ the required distances from tooth heel and from tooth toe will be obtained. By solving the system (9), we have

$$\delta\Delta_\xi = (\Delta_{ir} - \Delta_{er} + \Delta_e - \Delta_i) \big/ 2. \tag{10}$$

To automate the optimization process, a computer program has been developed, the initial data of which are the design parameters of the gear pair, the design load and the parameters of the tool for processing the teeth, as well as the required distances of bearing contact from the edges of the teeth. The results are the machine-tool settings and the meshing characteristics.

## 3 The Optimization of Transmission by Variation Spiral Angle and Tooth Thickness Modification Factor

Optimization preserves the previous values of the following characteristics:

- mechanical properties of materials of gear and pinion;
- numbers $z_p$, $z_g$ of pinion and gear teeth;
- face width $b$;
- face angles and root cone angles;
- addendum modification factor $x_\mathrm{n}$ and radial clearance $c^*$;
- parameters of tools (grinding wheels or cutter heads) used in the processing of teeth, except for the diameters;
- mean cone distance $L_\mathrm{m}$.

In addition, it is assumed that the deviation of the pinion and gear outer tip diameters $d_{\mathrm{ae}1}$, $d_{\mathrm{ae}2}$ from their original values do not exceed several tenths of a millimeter, which allows to place the transmission in the former housing.

Let $\beta_0$ be the initial spiral angle and $m_{\mathrm{n}0}$ be the initial value of the transmission mean normal module; conserving the original value of mean cone distance can be achieved by changing the mean normal module. The new module is determined by the relation

$$m_\mathrm{n} = m_{\mathrm{n}0} \cos\beta \Big/ \cos\beta_0. \tag{11}$$

Note that the decrease in the angle of the spiral leads to an increase in the thickness of the tooth according to the normal and a decrease in the load on the tooth while maintaining the torque on the shaft.

To preserve the pinion and gear outer tip diameters during the optimization process, the addendum factor $h_\mathrm{a}^*$ is recounted as follows

$$h_\mathrm{a}^* = h_{\mathrm{a}0}^* m_{\mathrm{n}0} \Big/ m_\mathrm{n}, \tag{12}$$

where $h_{\mathrm{a}0}^*$ is the initial value of the factor.

As the target function for optimization, we take the durability $t$ of the transmission, which is equal to the smallest of the three values: contact durability $t_\mathrm{H}$, bending durability of the pinion $t_\mathrm{FP}$ and bending durability of the gear $t_\mathrm{FG}$. The input data for calculating the values of $t_\mathrm{H}$, $t_\mathrm{FP}$ and $t_\mathrm{FG}$ are:

– loading cyclogram, which determines the fraction $\nu_i$ of the total time of loading, falling on the $i$th mode ($i = 1,2,\ldots, k$), the torque $M_i$ on the gear shaft and the number of $N_i$ revolutions of the gear shaft per minute; $k$ is the number of loading modes;
– contact pressure $\sigma_{\mathrm{H}i}$ and bending stress $\sigma_{\mathrm{FP}i}$, $\sigma_{\mathrm{FG}i}$ in loading mode number $i$;
– permissible contact pressure $[\sigma_{\mathrm{H}}]$ at the base number $N_0\mathrm{H}$ of loading cycles, which can be estimated using the expression (Russian standard GOST 21354-87)

$$[\sigma_{\mathrm{H}}] = \sigma_{\mathrm{H\,lim}} Z_{\mathrm{R}} Z_{\mathrm{V}} \big/ S_{\mathrm{H}}; \tag{13}$$

– permissible bending stress $[\sigma_{\mathrm{F}}]$ at the base number $N_0\mathrm{F}$ of the loading cycles, defined as follows

$$[\sigma_{\mathrm{F}}] = \sigma_{\mathrm{F\,lim}} Y_{\mathrm{A}} Y_{\mathrm{R}} Y_{\mathrm{V}} \big/ S_{\mathrm{F}}. \tag{14}$$

Here, $\sigma_{\mathrm{H\,lim}}$ , $\sigma_{\mathrm{F\,lim}}$ are the limits of contact and bending endurance, respectively (for simplicity, we assume that the pinion and gear are made of the same materials), $S_{\mathrm{H}}$, $S_{\mathrm{F}}$ are the safety factors, $Z_{\mathrm{V}}$, $Y_{\mathrm{V}}$ are the dynamic coefficients, $Z_{\mathrm{R}}$, $Y_{\mathrm{R}}$ are the coefficients of roughness, and $Y_{\mathrm{A}}$ is the coefficient of reversibility of rotation.

The number of revolutions $N_{\mathrm{T}}$ of gear before failure (resource) is determined on the basis of the hypothesis of linear summation of damage as follows

$$N_{\mathrm{T}} \sum_i \frac{\nu_i}{N_i} = 1, \quad (i = 1, 2, \ldots, k) \tag{15}$$

where each of the terms in the left part of the equation determines the contribution of the $i$th loading mode to the degree of damage to the part, which at the time of failure of the part is assumed to be equal to one. The values of $N_i$ represent the number of cycles to failure during operation from the beginning of operation to failure only in the $i$th mode. The relation (15) is used to compute the transmission contact endurance $N_{\mathrm{TH}}$ and to calculate resources $N_{\mathrm{TFP}}$, $N_{\mathrm{TFG}}$ of pinion and gear on the flexural durability.

In the first case, instead of $N_i$ in the ratio (15) should be the number $N_{\mathrm{H}i}$ of cycles to failure as a result of contact fatigue, which will be considered associated with the permissible contact stress at the base number of cycles as follows

$$[\sigma_{\mathrm{H}}]^{q_{\mathrm{H}}} N_0\mathrm{H} = \sigma_{\mathrm{H}i}^{q_{\mathrm{H}}} N_{\mathrm{H}i}. \tag{16}$$

According to GOST 21354-87, $q_{\mathrm{H}} = 6$ at $\sigma_{\mathrm{H}i} \le [\sigma_{\mathrm{H}}]$ and $q_{\mathrm{H}} = 20$ otherwise.

In the second case, in the relation (15) instead of $N_i$ is substituted by the number of $N_{\mathrm{F}i}$ cycles up to failure as a result of flexural fatigue, which is determined by a relation similar to the relation (16)

$$[\sigma_{\mathrm{F}}]^{q_{\mathrm{F}}} N_0\mathrm{F} = \sigma_{\mathrm{F}i}^{q_{\mathrm{F}}} N_{\mathrm{F}i}, \tag{17}$$

where $q_F = 9$ for cemented or nitrided gears with a non-grinded fillet surface. In other cases, $q_F = 6$.

According to the relations (16) and (17), even for the approximate estimation of the transmission durability, it is necessary to calculate the contact and bending stresses with a very high degree of accuracy. For example, an error of $\sigma_H$ of 3% leads to an error of $N_{TH}$ approximately equal to 100% $(1.03^{20} - 1) = 80\%$. Therefore, even when using the most precise methods of calculation of stresses only a rough estimate of the durability of the transmission may be obtained. However, the purpose of the proposed work is not so much to determine the durability itself, as to determine the parameters of the optimal in terms of durability of the bevel gear structure. At the same time, it can be assumed with a high degree of confidence that the stress reduction will cause an increase in the life durability.

Consider a specific example. Suppose you want to optimize an orthogonal transmission that has the following parameters: Numbers of teeth are $z_p = 31$; $z_g = 73$; mean normal module is $m_n = 6.0$ mm; spiral angle is $\beta = 30°$; face width is $b = 70$ mm. The face angles are $\delta_{a1} = 24° 58'$, $\delta_{a2} = 68° 02'$; the root cone angles are $\delta_{f1} = 21° 58'$ and $\delta_{f2} = 65° 02'$, respectively. The addendum factor is $h_a^* = 1.0$; the radial clearance coefficient is $c^* = 0.25$; the addendum modification factor is $x_n = 0.34$; tooth thickness modification factor is $x_\tau = 0.06$. A backlash of 0.2 mm is formed by reducing the thickness of the pinion tooth. Tooth-to-tooth composite tolerance we will take one and the same for pinion and gear $f_{pt} = 0.02$ mm.

Both the gear and the wheel are made of chrome–nickel steel. The hardness of the cemented surfaces of the teeth HRC = 64. Young's modulus $E = 2.0 \times 10^5$ MPa, and Poisson's ratio $\mu = 0.3$. Limits of contact and flexural endurance are: $\sigma_{H\,lim} = 1470$ MPa; $\sigma_{F\,lim} = 800$ MPa at numbers of cycle $N_0H = 1.2 \times 10^8$ and $N_0F = 4.0 \times 10^6$. Allowable stress at the base number of cycles is $[\sigma_H] = 1220$ MPa; $[\sigma_F] = 600$ MPa.

The loading cyclogram includes two modes: $M_1 = 1.0 \cdot 10^4$ Nm, $\nu_1 = 0.001$; $n_1 = 3000$ rpm and $M_2 = 0.75 \cdot 10^4$ Nm, $\nu_2 = 0.999$; $n_2 = 3000$ rpm.

The required bearing contact distances from the edges at maximum load $M_1$ are $\Delta_{ar} = 0$; $\Delta_{er} = 9$ mm; $\Delta_{ir} = 3$ mm.

When finishing the surfaces of the teeth of the pinion and gear, grinding wheels of nominal diameter 500 mm with a profile angle of the inner side equal to 20° 45′ and profile angle 20° 45′ outside surface are used. Modification of the roll motion is not used during processing.

Changes in the design parameters of the wheels, the length of the instantaneous contact areas, contact pressures and bending stresses, contact and bending durability at the angles of the spiral in the range from 10° to 35° are shown in Table 1.

Figure 5 shows how the contact pressure $\sigma_{H2}$ (upper continuous curve) and bending stresses $\sigma_{FP2}$ (lower continuous curve), $\sigma_{FG2}$ (lowest dashed line) in the loading mode 2, depend on the spiral angle $\beta$.

An increase of spiral angle is the cause of decrease of the mean normal module, and hence the thickness of the tooth decreases. It leads to an increase in the level of bending stress. In addition, to transfer the same moment at a greater angle of the spiral a larger contact force is required.

**Table 1** Characteristics of the gear transmission at different angles of spiral

| $\beta$ | 10° | 15° | 20° | 22° | 25° | 30° | 35° |
|---|---|---|---|---|---|---|---|
| $m_n$ (mm) | 6.823 | 6.692 | 6.510 | 6.468 | 6.279 | 6.00 | 5.675 |
| $h_a^*$ | 0.879 | 0.897 | 0.922 | 0.934 | 0.956 | 1.00 | 1.057 |
| $L_m$ (mm) | 274.74 | 274.74 | 274.74 | 274.74 | 274.74 | 274.74 | 274.74 |
| $d_{ae1}$ (mm) | 259.65 | 259.57 | 259.46 | 259.40 | 259.31 | 259.14 | 258.93 |
| $d_{ae2}$ (mm) | 573.56 | 573.60 | 573.65 | 573.67 | 573.71 | 573.78 | 573.87 |
| $a_\xi$ (mm) | 24.50 | 24.50 | 24.50 | 24.50 | 24.50 | 22.45 | 18.69 |
| $\sigma_{H1}$ (MPa) | 1264 | 1234 | 1224 | 1201 | 1184 | 1199 | 1301 |
| $\sigma_{H2}$ (MPa) | 1119 | 1111 | 1091 | 1076 | 1066 | 1089 | 1190 |
| $\sigma_{FP1}$ (MPa) | 379 | 384 | 400 | 410 | 420 | 475 | 572 |
| $\sigma_{FG1}$ (MPa) | 398 | 411 | 420 | 431 | 441 | 486 | 577 |
| $\sigma_{FP2}$ (MPa) | 298 | 305 | 324 | 326 | 337 | 374 | 451 |
| $\sigma_{FG2}$ (MPa) | 317 | 324 | 331 | 345 | 349 | 385 | 451 |
| $t_{FP}$ (h) | 11,990 | 9740 | 5650 | 5350 | 3970 | 1550 | 290 |
| $t_{FG}$ (h) | 16,210 | 13,300 | 10,980 | 8620 | 6820 | 2820 | 680 |
| $t_H$ (h) | 3760 | 4340 | 6240 | 8230 | 9920 | 6470 | 1100 |

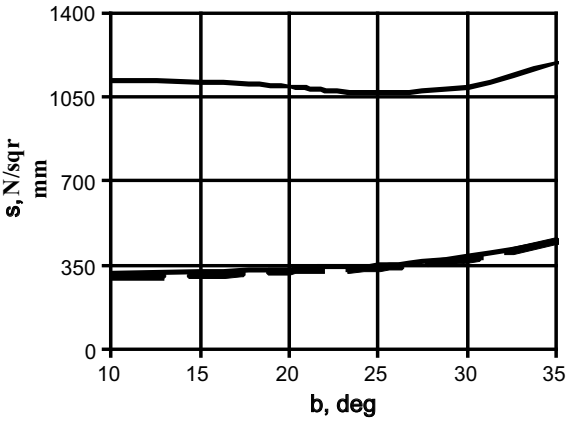


**Fig. 5** Stress dependences on the spiral angle

Despite the fact that the coefficient of the height of the tooth with the increase of the spiral angle also increases, the height of the tooth remains virtually unchanged, which makes it impossible to increase the length $a_\xi$ of the instantaneous contact area. Starting from the angle $\beta \approx 25°$, the contact area decreases, and this together with the growth factor of the normal force to the tooth surface leads to an increase in contact pressures. The mean cone distance, as well as the internal and external cone distances, remains unchanged since the normal module is recalculated by the ratio (11). Changes in the outer diameter of the pinion and gear are tenths of a millimeter that makes it possible to place the transmission in the former housing.

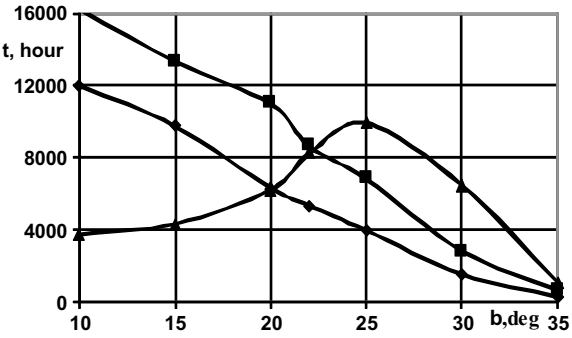


**Fig. 6** Longevity dependences on the spiral angle

In Fig. 6, the curve, marked with markers in the form of triangles, gives the dependence of the contact durability of the transmission on the angle of the spiral; the curves of the bending durability of the pinion and gear are marked with markers in the form of diamonds and squares, respectively. It can be seen that relatively small changes in contact pressures (about 10%) and bending stresses (about 40%) have a very large impact on the durability of the transmission.

Figure 6 shows that the highest longevity occurs in the interval $20° < \beta < 22°$. Assume that the optimal value $\beta = 21°$ is in the middle of this interval. When the adopted value of the tooth thickness modification factor is $x_\tau = 0.06$, the bending durability of the gear greatly exceeds the bending durability of the pinion (Fig. 6). This is because the number of loading cycles of the pinion tooth for the same period is 2.35 times greater. Varying the values of the factor $x_\tau$, we obtain that at $x_\tau = 0.12$ the bending durability of the pinion and gear takes close values: $t_{\mathrm{FP}} = 7080$ h, $t_{\mathrm{FG}} = 6990$ h. Contact durability $t_{\mathrm{H}} = 7500$ h at the same time does not change. It is not possible to obtain a more accurate coincidence of the values of all three considered durations due to errors in the determination of stresses having an order of 2–3%.

Thus, as a result of optimization it was possible to increase the estimated transmission life from 1550 h (see Table 1) up to 6690 h, i.e., more than four times.

## 4 The Optimization of Transmission by the Number of Teeth

In order that the new gear pair with the increased loading capacity could be placed in the free space of the old reducer shown in Fig. 7 (would be interchangeable with a pair of the former construction), the equity of the following inequalities is sufficient:

$$x_p \min \geq x_p^* \min;\ x_p \max \leq x_p^* \max;\ R_g \min \geq R_g^* \min;$$
$$R_g \max \leq R_g^* \max;\ x_g \max \leq x_g^* \max;\ x_g \min \geq x_g^* \min;$$

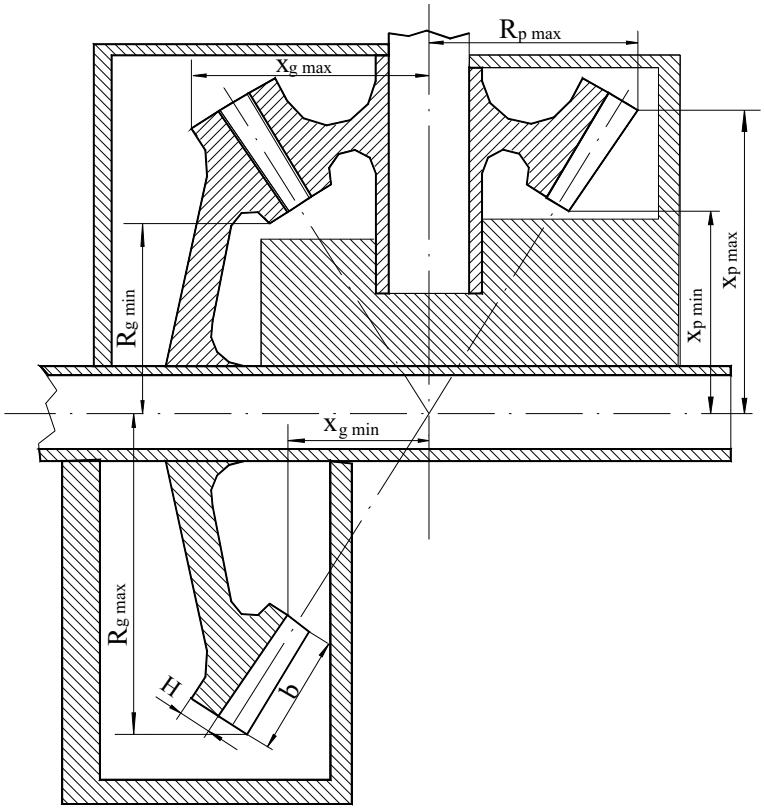


**Fig. 7** Gear housing design

$$R_p\,\min \geq R^*_p\,\min;\; R_p\,\max \leq R^*_p\,\max; \tag{18}$$

The index $p$ in the inequalities (18) determines the parameter of pinion; the index $g$ determines the parameter of gear. Dimensions $R_{\max}$, $R_{\min}$, $x_{\max}$ and $x_{\min}$ are shown in Fig. 7. The upper index "asterisk" marked values related to the original transmission design. The values contained in the inequalities (18) are expressed through the external $L_e$ and the inner $L_i$ cone distances, outer and inner $h_{ae}$, $h_{ai}$ addendums, and external and internal dedendums $h_{fe}$, $h_{fi}$ as follows

$$\begin{aligned} R_g\,\max &= L_e \sin\delta_g + h_{ae}\cos\delta_g; \quad R_g\,\min = L_i \sin\delta_g - (h_{fe}+H)\cos\delta_g; \\ R_p\,\max &= L_e \sin\delta_p + h_{ae}\cos\delta_p; \quad R_p\,\min = L_i \sin\delta_p - (h_{fe}+H)\cos\delta_p; \end{aligned} \tag{19}$$

$$\begin{aligned} x_g\,\max &= L_e \cos\delta_g + (h_{fe}+H)\sin\delta_g; \quad x_g\,\min = L_i \cos\delta_g - h_{ae}\sin\delta_g; \\ x_p\,\max &= L_e \cos\delta_p + (h_{fe}+H)\sin\delta_p; \quad x_p\,\min = L_i \cos\delta_p - h_{ae}\sin\delta_p, \end{aligned} \tag{20}$$

where (Fig. 7) $H$ is the thickness of the tooth rim; according to the recommendations of [9], this value is taken to be equal to the total external tooth height $H = h_{\mathrm{e}} = h_{\mathrm{fe}} + h_{\mathrm{ae}}$; $\delta_p$ and $\delta_g$ are angles of the pinion and gear pitch cones.

We define addendums using relations

$$h_{\mathrm{a}g} = m_{\mathrm{n}}\left(h_{\mathrm{a}}^* - x_{\mathrm{n}}\right);\ h_{\mathrm{a}p} = m_{\mathrm{n}}\left(h_{\mathrm{a}}^* + x_{\mathrm{n}}\right) \tag{21}$$

Expressions for gear and pinion dedendums are

$$h_{\mathrm{f}g} = m_{\mathrm{n}}\left(h_{\mathrm{a}}^* + c^* - x_{\mathrm{n}}\right);\ h_{\mathrm{f}p} = m_{\mathrm{n}}\left(h_{\mathrm{a}}^* + c^* + x_{\mathrm{n}}\right) \tag{22}$$

The remaining values present in the ratios (19) and (20) are defined as follows (since the ratios are the same for the pinion and the gear, the indices $p$ or $g$ are omitted):

$$\begin{aligned} &L_{\mathrm{e}} = L_{\mathrm{m}} + b/2;\ L_{\mathrm{i}} = L_{\mathrm{m}} - b/2;\ h_{\mathrm{ae}} = h_{\mathrm{a}} + b \cdot \mathrm{tg}\ \theta_{\mathrm{a}}/2; \\ &h_{fe} = h_{\mathrm{f}} + b \cdot \mathrm{tg}\ \theta_{\mathrm{f}}/2;\ h_{\mathrm{ai}} = h_{\mathrm{a}} - b \cdot \mathrm{tg}\ \theta_{\mathrm{a}}/2;\ h_{\mathrm{fi}} = h_{\mathrm{f}} - b \cdot \mathrm{tg}\ \theta_{\mathrm{f}}/2, \end{aligned} \tag{23}$$

where the addendum angle is $\theta_{\mathrm{a}} = \delta_{\mathrm{a}} - \delta$ and the dedendum angle is $\theta_{\mathrm{f}} = \delta - \delta_{\mathrm{f}}$.

The mean cone distance $L_{\mathrm{m}}$ is equal

$$L_{\mathrm{m}} = \tfrac{1}{2} m_{\mathrm{n}} \sqrt{z_p^2 + z_g^2}. \tag{24}$$

Since the bending stresses of the cantilever beam are inversely proportional to its thickness, it should be expected that the bending stresses in the tooth decrease with an increase in the normal module $m_{\mathrm{n}}$ of the gear.

The number $z_g$ of gear teeth when changing the number $z_p$ of pinion teeth is determined from the condition of obtaining the closest to the original gear ratio as follows: $z_g = u \cdot z_p$, where $u = z_g^*/z_p^*$, then rounded to the nearest entire number. To conserve the initial cone distance, the mean normal $m_{\mathrm{n}}$ modulus with decreasing number of $z_g$ teeth is determined by the relation resulting from the first of the relationship (24):

$$m_{\mathrm{n}} = m_{\mathrm{n}}^* \sqrt{\frac{z_p^{*\,2} + z_g^{*\,2}}{z_p^2 + z_g^2}}, \tag{25}$$

where $m_{\mathrm{n}}^*$ is the normal module and $z_p^*$, $z_g^*$ are the numbers of teeth of the original pair.

Next, we find the maximum value of the parameter $b$, at which all the inequalities (18) are true. Since one cannot satisfy all the conditions at the same time, you have to choose the most important one. In case of gearbox housing shown in Fig. 7, these conditions should be imposed on $x_p\ \mathrm{max}$, $x_p\ \mathrm{min}$, $R_g\ \mathrm{min}$ and $R_g\ \mathrm{min}$. The remaining conditions can be met by a small design change.

**Table 2** Characteristics of the gear transmission at different numbers of teeth

| $z_p$ | 31 | 29 | 27 | 25 | 23 | 21 |
|---|---|---|---|---|---|---|
| $z_g$ | 73 | 68 | 64 | 59 | 54 | 49 |
| $\Delta u$ (%) | 0% | −0.4 | 0.66 | 0.2 | −0.3 | −0.9 |
| $m_n$ (mm) | 5.946 | 6.378 | 6.789 | 7.359 | 8.035 | 8.846 |
| $b$ (mm) | 70.0 | 68.4 | 67.0 | 65.8 | 64.0 | 62.2 |
| $x_p$ max (mm) | 291.9 | 291.6 | 291.9 | 291.8 | 291.8 | 291.9 |
| $x_p$ min (mm) | 217.0 | 217.4 | 218.3 | 218.5 | 218.9 | 219.2 |
| $R_p$ max (mm) | 125.8 | 126.1 | 125.2 | 125.8 | 126.4 | 125.2 |
| $x_g$ max (mm) | 137.9 | 139.0 | 138.7 | 140.2 | 142.0 | 144.2 |
| $x_g$ min (mm) | 84.8 | 84.8 | 83.5 | 83.3 | 83.1 | 82.9 |
| $R_g$ max (mm) | 286.8 | 286.1 | 286.1 | 285.8 | 285.2 | 284.6 |
| $R_g$ min (mm) | 211.8 | 211.9 | 212.6 | 212.4 | 212.2 | 211.9 |
| $L_+$m (mm) | 272.32 | 272.32 | 272.32 | 272.32 | 272.32 | 272.32 |
| $\rho_s$ (mm) | 2.3 | 2.4 | 2.6 | 2.7 | 2.8 | 3.0 |
| $\sigma_H$ (MPa) | 1507 | 1491 | 1499 | 1492 | 1496 | 1508 |
| $\sigma_{Fp}$ (MPa) | 685 | 641 | 591 | 563 | 519 | 468 |
| $\sigma_{Fg}$ (MPa) | 671 | 640 | 593 | 567 | 517 | 462 |
| $a_\xi$ (mm) | 22.0 | 22.0 | 22.0 | 21.5 | 21 | 20.3 |
| $a_\eta$ (mm) | 1.07 | 1.08 | 1.09 | 1.12 | 1.16 | 1.21 |

As an example, consider the same gear with the numbers of teeth $z_p = 31$, $z_g = 73$, as in the previous example, but now $m_n = 5.464$ mm, $h_a^* = 0.9537$ and $\beta = 30° 1'$. The direction of the gear spiral is left. The coefficient of change in the calculated thickness of the tooth $x_\tau = 0.054$. The backlash is created by reducing the thickness of the pinion tooth at $\Delta_p = 0.1$ mm and the gear tooth at $\Delta_g = 0.14$ mm.

The load is the torque $M_g = 1.5 \times 10^4$ N m on the gear shaft. Under this load, the distance $\Delta_{ar}$ of bearing contact from the tip should be 0.6 mm, and the distances $\Delta_{er}$, $\Delta_{ir}$ of bearing contact from the heel and the toe are to be equal to 9.0 and 3.0 mm, respectively.

The characteristics of the gears obtained from the initial gear by decreasing the number of pinion teeth and the recalculation of the mean normal module $m_n$ and the face width $b$ while maintaining the values of all other initial design parameters are given in Table 2.

Table 2 shows that the deviation $\Delta u$ of the transmission ratio from the original value does not exceed one percent. The overall dimensions of the modified gears are not much different from the size of the initial transmission.

If you reduce the numbers of teeth, the major semi-axis $a_\xi$ of the instantaneous contact ellipse is slightly reduced, but this increases the length of the smaller semi-axis $a_\eta$. The total area of the ellipse varies little, and therefore the maximum contact pressures are very little. As expected, bending stresses decrease monotonically with

decreasing number of teeth of the pair. When $z_p = 21$, flexural stress is less than at $z_p = 31$ approximately 30%. Due to the fact that a further decrease in the number of teeth is associated with an increase in the sliding speed at the contact of teeth and contact pressures, a further decrease in the number of teeth of the gear, although it leads to a decrease in bending stresses, should be considered impractical. The number of teeth $z_p = 21$, $z_g = 49$ gears and wheels can be considered optimal.

The analysis of the tooth shape made by the algorithm showed that there is no undercutting in the considered range of tooth numbers, so the addendum modification factor can be left unchanged. The point width tooth taper and thickness tooth taper are satisfactory, so the correction of the face angle and the root cone angle is not necessary.

## 5 Conclusion

The proposed algorithm of synthesis of spiral bevel gears of the given dimensions is designed to build the shape of the surfaces of the teeth, providing the minimum contact pressures and bending stresses. The algorithm of shape optimization is implemented in the form of software that has simple enough to understand the source data. The search for the required tooth surfaces and machine-tool settings to ensure the bearing contact, spaced from the edges of the teeth at the given distances, is carried out automatically. It is shown that the software can be used to improve the existing transmission without changing its dimensions. The new gear transmission with decreased stress level and increased longevity may be placed in housing of prior transmission. In the considered examples, this is achieved by choosing the optimal spiral angle and reducing the number of teeth of the gear and the pinion while maintaining gear ratio close to the previous one.

## References

1. Litvin F.L., Fuentes A. (2004) Gear geometry and applied theory. Cambridge University Press, Cambridge
2. Sheveleva GI, Volkov AE, Medvedev VI (2007) Algorithms for analysis of meshing and contact of spiral bevel gears. Mech Mach Theory 129:198
3. Simon V (2007) Load distribution in spiral bevel gears. ASME J Mech Des 129:201
4. Wilcox LE. (1981) An exact analytical method for calculating stresses in bevel and hypoid gear teeth. In: Proceedings of international symposium on gearing and power transmissions, Tokyo, II, p 115
5. Gosselin C, Cloutier L, Nguyen QD (1995) A general formulation for the calculation of the load sharing and transmission error under load of spiral bevel and hypoid gears. Mech Mach Theory 30:433
6. Simon V (2009) Head-cutter for optimal tooth modifications in spiral bevel gears. Mech Mach Theory 44:1420
7. Medvedev VI, Volkov AE (2007) Synthesis of spiral bevel gear transmissions with a small shaft angle. ASME J Mech Des 129:949

8. Wang PY, Fong YH (2006) Fourth-order kinematic synthesis for face milling spiral bevel gears with modified radial motion (MRM) correction. ASME J Mech Des 128:457
9. Zhang J, Fang F, Cao X, Deng X (2007) The modified pitch cone design of the hypoid gear: manufacture, stress analysis and experimental tests. Mech Mach Theory 42:147
10. Argyris J, Fuentes A, Litvin FL (2002) Computerized integrated approach for design and stress analysis of spiral bevel gears. Comput Methods Appl Mech Eng 191:1057
11. Medvedev VI (2001) Programs packet for quality analysis of the conical and hypoid teeth pairs. Problemy Mashinostraeniya i Nadezhnos'ti Mashin 3:77
12. Medvedev VI, Sheveleva GI (2002) Spiral-conical gears synthesis by the contact teeth strength conditions. Problemy Mashinostraeniya i Nadezhnos'ti Mashin 4:75
13. Medvedev VI (1999) Synthesis of generated non-orthigonal bevel and hypoid gear sets. J Mach Manuf Reliab 5:1
14. Medvedev VI, Volkov AE, Volosova MA, Zubelevich OE (2015) Mathematical model and algorithm for contact stress analysis of gears with multi-pair contact. Mech Mach Theory 86:156
15. Volkov AE, Medvedev VI, Skorodumov OI (2008) Increasing the loading capacity of circular-arc teeth of conic gears without a significant change in dimensions. J Mach Manuf Reliab 37:152
16. Volkov AE, Matveenkov DS, Medvedev VI (2010) Optimizing the structural parameters of conical pairs with circular teeth. Russ Eng Res 10:1060

# Idle Milling System Noise Level Dependency from Temperature Conditions of the Machine Working Area


**Artem V. Rasshchupkin, Kirill P. Pompeev and Viktor M. Medunetskiy**

**Abstract** During experimental research, a deviation of milling system noise level measurement was detected in idle running mode during the period of equipment shift operation. A discrepancy of predicted parameters of predicted vibration activity of the milling system compared to the actual numbers during lowering of the spindle module operating frequencies range in the area of steady cutting. Based on the analysis of the obtained data and additional studies, dependency of system vibration and its noise level from the temperature conditions of the machine working area were identified. This dependency is proposed to be used to adjust the values of the predicted vibration of the milling setup by correlating temperature readings of the system with noise factor by taking into account the operating time of the equipment.

**Keywords** Milling system run-out · Noise peak · Noise input · Effective electric signal · Cold source method

## 1 Introduction

In instrument engineering as a branch of precision engineering, fundamental parameter is the quality of manufacturing of parts. Special requirements are imposed on operating area of units and installations properties, which are caused by the structure of its microgeometry [1]. One of the development directions of instrument engineering is the improvement of the manufacturing technology of products and their individual elements by cutting [2]. Technologists should always search for progressive solutions to the challenges of providing the required quality characteristics. Search

A. V. Rasshchupkin · K. P. Pompeev (✉) · V. M. Medunetskiy
ITMO University, Saint-Petersburg, Russia
e-mail: kir-pom@mail.ru

A. V. Rasshchupkin
e-mail: archijoke@mail.ru

V. M. Medunetskiy
e-mail: vm57med@yandex.ru



A. N. Evgrafov (ed.), *Advances in Mechanical Engineering*,
Lecture Notes in Mechanical Engineering,
https://doi.org/10.1007/978-3-030-11981-2_5

for these solutions takes place in conditions of significant limitations imposed on the production process, which in turn force the specialists to look at working environment from a different perspective for a more detailed understanding of thermo-mechanical dependencies [2].

In conditions of declining costs of production simultaneously with increasing requirements to quality of manufactured products, engineers and specialists of research and development enterprises must use existing high-performance tools and equipment. One way to solve this problem is to improve the milling system vibration noise sound analysis method during its idle running, which is being implemented at one of instrument engineering enterprises of Saint Petersburg. When using this method in practice, it became necessary to increase the reliability of predicted results. Solution to this problem was the identification of temperature dependency between the registered milling system noise during idle running and changing of its amplitude–frequency response.

## 2 Perfecting the Method of Sound Analysis of the Vibration Noise of the Milling System During Its Idle Running

The oscillatory motion trajectory of the spindle unit and the milling system in general is a sinusoidal displacement, becoming an ellipse in a cyclic view [3], which can be described by the expression:

$$\frac{x^2}{A^2} - \frac{2xz}{AC}\cos\varphi + \frac{z^2}{C^2} = \sin^2\varphi,$$

where $A$, $C$ and $x$, $z$ are an amplitude and the spindle unit and milling system movement in radial and axial directions, respectively; $\varphi$—oscillation phases difference.

Non-contact measurement method of radial and axial run-out of the milling system in operation modes in the phase of idle (no load) running is performed with use of magnetic sensors [4]. At that effective gap of the horizontal offset, sensor is taken as the value $\delta_x$, and the effective vertical gap will be $\delta_z$. Change of the value of the effective sensor gap is directly connected with the change of the voltage at its output. The voltage at the sensor output horizontal (radial) offset will be equal:

$$U_x = U_0 \pm \Delta U_x = U_0 \pm \delta_x = U_0 \pm \kappa \cdot d,$$

where $U_0$ is voltage at the sensor output in the absence of a spindle axis offset;

$k$—sensor conversion factor; $d$ is the nominal diameter of the outer ring of the spindle unit body.

The voltage at the vertical (radial) offset sensor output will be equal to:

$$U_z = U_0 \pm \Delta U_z = U_0 \pm \delta_z = U_0 \pm \kappa \cdot l,$$

where $U_0$ is the voltage at the sensor output in the absence of a spindle butt end offset; $l$—spindle overrun from the body of the spindle head.

The application of devices using quadratic analyzer allows to get more valid data on the noise level presented in peak form (noise peaks).

In modern devices for sound signals processing the spectrum of the noise significantly exceeds the limits of the audible range, so the indications differ significantly from the values in the perceptible range. Measuring of the noise level, emerging from the milling system, should be performed by isolation of the corresponding frequency band in the signal under investigation.

In order to do that, a filter limiting the frequency band set to the device voltmeter by audio signals in the range from 20 Hz to 20 kHz should be included in the measuring circuit of the noise meter. For adequate noise measurement, a level "A" filter is used. The difference between the change of noise signal values, measured in dB and dBA modes depends on the noise spectrum and in general is unpredictable. At that noise signal values, measured in dBA mode, tend to be smaller, and the range of their change is wider. Therefore, the analysis of the measurements carried out in BA mode will allow to draw conclusions about the mutual dependence of the input and output noise signals, the nature of their origin, and reliability of effective electric signal value.

One of the most important indicators of low-level signals effectiveness is a noise coefficient (factor) $F$, proposed by Harold Friis, representing the signal-to-noise correlation of the source in ($\mathrm{SNR}_i$) operation mode to signal-to-noise of the *cold source* ($\mathrm{SNR}_0$):

$$F \equiv \frac{\mathrm{SNR}_i}{\mathrm{SNR}_0}$$

Reliable comparisons of noise factor require to make measurement under standard temperature using the so-called *cold source method*. Friis proposed to use the reference temperature denoted $T_0$ equal to 290 K (about 62 °F or 17 °C), i.e., the temperature which is significantly below the air temperature of the majority of production facilities.

Factor $F$ characterizes the deterioration of signal-to-noise ratio at the input of the sound analyzer amplifier. In real production conditions, it may not be less than one.

Change of the signal-to-noise value of the input signal, i.e., a change of the factor $F$ allows to register the noise level error sources of the target system.

An important factor in measuring noise activity is the temperature of the noise source itself and the measuring environment. Temperature component has significant impact not as much on the actual measurements results, as on the estimated values of the noise factor; the vibration activity analysis of the whole system is performed on the basis of information about the noise factor. This dependency can be analyzed on the basis of registry actuation mechanism generating its own effects, affecting the nominal indications during measurement regardless of the source temperature. Thus, the measured noise factor will be higher if the source of the noise activity

was hotter and, therefore, noiser. In professional equipment, signal-to-noise ratio is rarely specified, since this value depends on the real operating conditions.

Noise factor is the scanning device own characteristic, in which its own excitements occur. It should be noted that the available noise power appearing at the output of the scanner has two components. One of them is enhanced available noise power of the source at temperature $T_0 = 290$ K, that has a value of:

$$N_{0S} = \kappa T_0 B G_{\alpha v},$$

where $\kappa$ is Boltzmann's constant; $B$ is noise frequency band; $G_{\alpha v}$ is available noise factor on power of the tested device.

Another component of the output noise is the noise with the power $N_\alpha$, added by the measuring device itself, which must be compensated for during the analysis of data obtained during measurements. Then the total available noise power at the output will be calculated by:

$$N_1 = \kappa T_0 B G_{\alpha v} + N_\alpha$$

In view of the fact that the signal-to-noise ($\mathrm{SNR}_0$, $\mathrm{SNR}_i$) is the ratio of the noise value ($S_0$, $S_i$) to its power ($N_0$, $N_i$), can be written as:

$$F = \frac{S_i / N_i}{S_0 / N_0} = \frac{1}{G_{\alpha v}}\left(\frac{N_0}{N_i}\right) = \frac{1}{G_{\alpha v}}\left(\frac{N_1}{N_i}\right) = \frac{N_1}{N_{0S}} = \frac{\kappa T_0 B G_{\alpha v} + N_\alpha}{\kappa T_0 B G_{av}}$$

The noise power measurement is carried out at the temperature of the source $T_h$, which is higher than the reference temperature by $T_{ex}$, then available noise power at the output will be:

$$N_2 = \kappa B G_{\alpha v} T_h + N_\alpha = \kappa B G_{\alpha v}(T_0 + T_{ex}) + N_\alpha$$

Ratio $N_2/N_1$ in [5] is called "$Y$ factor" (noise factor, measured by the method of the two temperatures). Figure 1 shows that the temperature of the cold source is equal to the reference temperature $T_0$, but any temperature other than $T_h$ can be used to calculate the slope ratio.

When the source reaches the temperature $T_{h,}$ available noise power at the output of the source amplifier must be taken into account. However, in real-world conditions, temperature $T_0$, part of $T_h$, will be higher than 290K. Let us denote it as $T_e$. The higher the value $T_e$ is, the greater the available power ($N_a$), which affects the accuracy of the results of the noise measurement. In this case, the value $N_a$ will be determined by the following expression:

$$N_\alpha = \kappa T_e B G_{\alpha v}$$

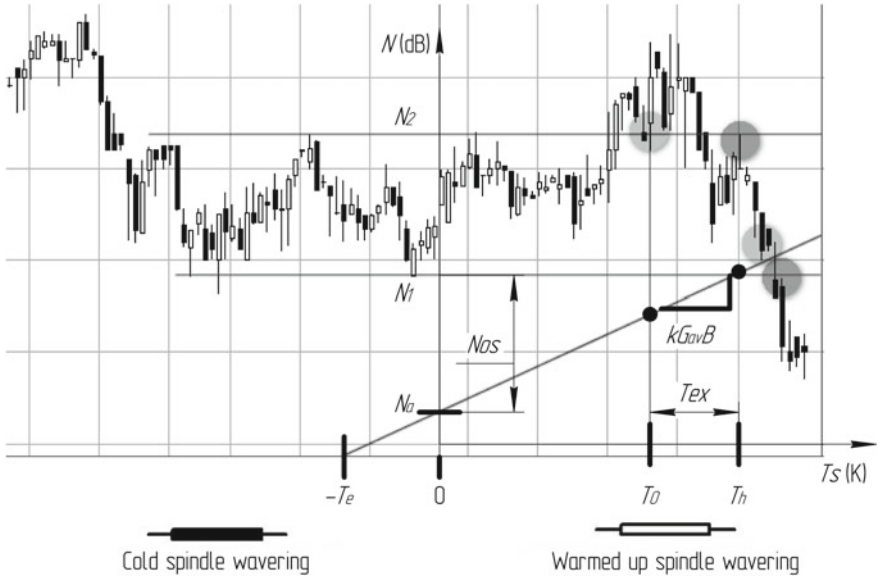


**Fig. 1** Dependency of spindle noise and the front bearing unit run-out in various temperature conditions

The slope ratio determined from the chart (see Fig. 1) at temperature $T_e$ is the more accurate the more noise factor $F$ is closer to one [6].

Let us define the noise factor through the temperature as follows:

$$F = 1 + \frac{T_e}{290}$$

The results of calculation of the noise factor for the above-mentioned dependency are represented in Table 1.

Taking into account the influence of the temperature changes on the milling system run-out value in the process of noise activity measuring, it is necessary to analyze the noise factor values in order to get the refined data [7, 8]. Figure 2 presents charts of the milling setup run-out in conditions of periodic system operation and corresponding noise peaks [9, 10].

Justification of the temperature changes influences on system performance during cutting allowed to get the refined data used to predict values of the milling system run-out [11].

**Table 1** Dependency of the noise factor on temperature readings

| Noise factor $F$ | Noise temperature $T_e$ (K) |
|---|---|
| 1 | 0 (absolute zero) |
| 1.122 | 35.4 |
| 1.148 | 43.0 |
| 1.175 | 50.7 |
| 1.202 | 58.7 |
| 1.230 | 66.8 |
| 1.259 | 75.1 |
| 1.288 | 83.6 |
| 1.318 | 92.3 |
| 2.00 | 290 |
| 10 | 2610 |
| 100 | 28,710 |

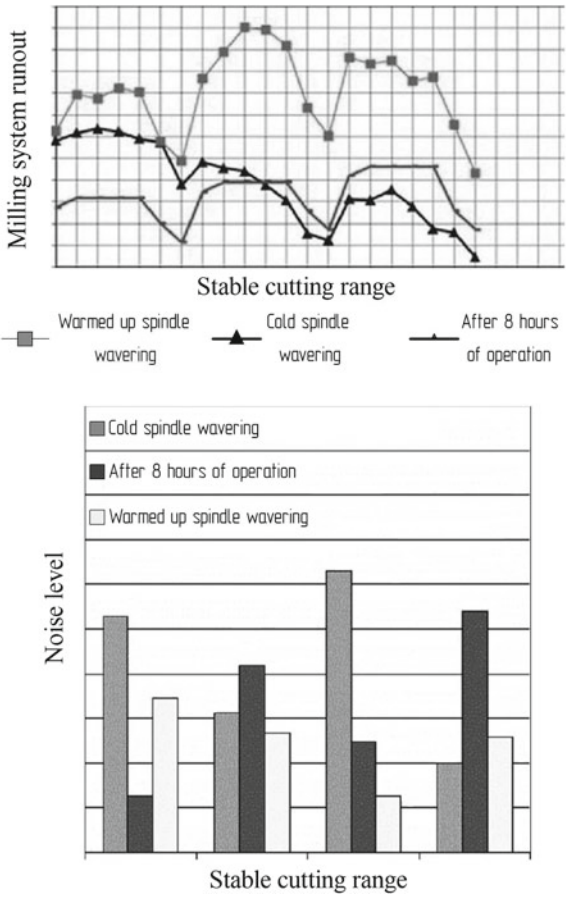


**Fig. 2** Change of the milling system characteristics during the industrial shift

## 3 Conclusion

Thus, the adjustment of predicted cutting parameters when implementing the method used by clarifying the temperature settings and introducing temperature coefficients of measuring environment is allowed to improve the reliability of the applied parameters and values. At that keeping of statistical data made it possible to create a base of frequency characteristics that are applied during implementation of the proposed method, as well to introduce a constant expansion and update of the data to improve the accuracy and reliability of the proposed parameters.

## References

1. Ershov DY (2013) Evaluation of the impact of technological errors of manufacture of the mechanical system on the vibration characteristics of a system during its operation. In: Radkevich MM, Evgrafov AN (eds) Modern machine industry: science and education: materials of the 3rd International research and training conference. Publishing house of the Polytechnic University, St. Petersburg, pp 709–717 (in Russian)
2. Korotkih MT (2014) Structural damping of cutting tools in intermittent machining. . In: Radkevich MM, Evgrafov AN (eds) Modern machine industry: science and education: materials of the 3rd International research and training conference. Publishing house of the Polytechnic University, St. Petersburg, pp 1140–1147 (in Russian)
3. Trofimova TV (1985) Physics studies. Higher School, Moscow, p 380 (in Russian)
4. Goryachev VJ, Gavrina OV, Chapchikov YK, Shatova YA (2013) Analysis of information and measurement system bias error based on the shaft run-out sensor shaft with the running magnetic field. Tech Sci 1, 46–57 (in Russian)
5. Agilent (2004) Noise Figure Measurement Accuracy – The Y-Factor Method. Application note 57–2, pp. 9-10
6. Vondran D (1999) Vector corrected noise figure measurements. Microwave J 22–38
7. Ivanov NI, Nikiforov AS (2000) Basics of vibroacoustics. Polytechnics, St. Petersburg, p 412 (in Russian)
8. Balykov IA, Chukarin AN, Evseev DZ (1996) Influence of cutting processes on milling machines noise. In: New in health and safety, and ecology: volume of conference reports, St. Petersburg, 14–16 Oct 1996, pp. 222–223 (in Russian)
9. Balykov IA (1996) On calculating the noise emitted by the workpiece when milling. Don State Technical University, Rostov on Don, Depositing in All-Union Institute of Scientific and Technical Information (VINITI), 16 Aug 96, no. 2685-B96 (in Russian)
10. Chukarin AN, Balykov IA (1996) Experimental studies of noise and vibration of milling machines. Don State Technical University, Rostov on Don, Depositing in All-Union Institute of Scientific and Technical Information (VINITI), 16 Aug 96, no. 2687-B96 (in Russian)
11. Zharkov IG (1986) Vibration during edge tool processing. Machine Industry, Leningrad, p 184 (in Russian)

# Tribotechnical Properties of Nanostructured Coppernickel Coatings


**Margarita A. Skotnikova, Vladimir P. Artemyev, Svetlana A. Shasherina, Olga V. Paitova and Galina V. Tsvetkova**

**Abstract** The tribotechnical, metallographic, physical, and chemical properties of nanostructured copper–nickel coatings applied on products made of X12M tool steel were investigated. The results showed that a significant increase (2.3 times) in the wear resistance of the coatings was achieved after high plastic deformation under a stress of 3.5 GPa. A structure was formed with a minimum size of coherent scattering regions (CSR) of 23 nm and a maximum crystal lattice microstrain value (CLM) of 1.25%.

**Keywords** Wear · Nanostructure · Coating · Intensive plastic deformation

## 1 Introduction

Improving the wear resistance of the cutting tool during machining is an important task in engineering [1–9]. The edge of the tool must have high wear resistance, adhesive interaction and high thermal conductivity. Copper–nickel coatings satisfy these conditions. They reduce the contact temperature due to the increased thermal conductivity of the surface layer.

In order to effectively increase the serviceability of the instrument, the technology of diffusion metallization from the environment of low-melting liquid metal solutions can be used, which makes it possible to create solid wear- and corrosion-resistant

M. A. Skotnikova (✉) · O. V. Paitova · G. V. Tsvetkova
Peter the Great Saint-Petersburg Polytechnic University, Saint Petersburg, Russia
e-mail: skotnikova@mail.ru

O. V. Paitova
e-mail: olja.stern@gmail.com

G. V. Tsvetkova
e-mail: tsvetkova_gv@mail.ru

V. P. Artemyev · S. A. Shasherina
The Kuban State Technological University, Krasnodar, Russia
e-mail: svetlana111@inbox.ru



A. N. Evgrafov (ed.), *Advances in Mechanical Engineering*,
Lecture Notes in Mechanical Engineering,
https://doi.org/10.1007/978-3-030-11981-2_6

layers on the instrument surface, which have high viscosity and thermal conductivity. The method of diffusion alloying from low-melting liquid metal solutions is used for applying (Cu–Ni) coatings on tools. Coatings were obtained that are characterized by the same thickness, stability of the structure, properties, and high quality [10–14].

## 2 Methods and Materials

The materials for the research were prepared using the technology of the Kuban State Technological University [1]. Figure 1 shows the setup for diffusion metallization in an environment of low-melting liquid metal solutions.

Installation consists of the lower and upper water-cooled chambers. Between the chambers, there is a hermetic shutter, which allows to unite and divide the cavities of these chambers. In the lower chamber, there are heating elements, an object table, on which a bath with a low-melting solution is installed, heat shields, a movable screen, as well as a vacuum line with a stop valve, an inert gas supply line. In the upper chamber, there is a shutter drive mechanism, a movable rod, on which the coated products are fixed. On the side surface of the upper chamber, there is a loading door. A vacuum line with a shutoff valve is mounted in the lower part of the upper chamber, and an inert gas supply line is mounted in the upper part. The vacuum line and the inert gas supply line are interconnected by a pipeline of the inert gas circulation system, which, in addition to the pipelines, contains a heat exchanger and a pump that circulates the inert gas in the upper chamber and the heat exchanger.

A bath with a fusible solution is installed on the stage of the lower chamber. Through the loading hatch in the upper chamber, the products are placed in this chamber and fixed on a movable rod, which serves to move products from one chamber to another. After that, the loading door closes and the upper chamber is sealed and the lower and upper chambers are evacuated. After reaching a given vacuum, the upper and lower chambers are filled with argon. Next is heating the bath with a metal solution for diffusion metallization of the surfaces of products.

Coatings based on copper or nickel were applied on tool from steel X12M. After that the materials were subjected to additional intensive plastic deformation (IPD) at stresses of 3.0, 3.5, 4.0, and 4.5 GPa [10, 11, 15, 16].

The research of the microstructure of steel X12M was performed using a microvisor of reflected light μVizo-MET.

X-ray microanalysis was performed using “Camebax-Micro” microanalyzer, equipped with an INCA ENERGY 350 energy-dispersive spectrometer.

Phase identification in the samples was carried out by X-ray diffraction analysis (XRD) using Bruker D8 diffractometer.

Wear tests were conducted using friction machine SMTs-2 with “block–roller” configuration with frequency of rotation of the bottom roller of 300 rpm.

Tribotechnical tests were carried out on samples of steel X12M before and after applying coatings.

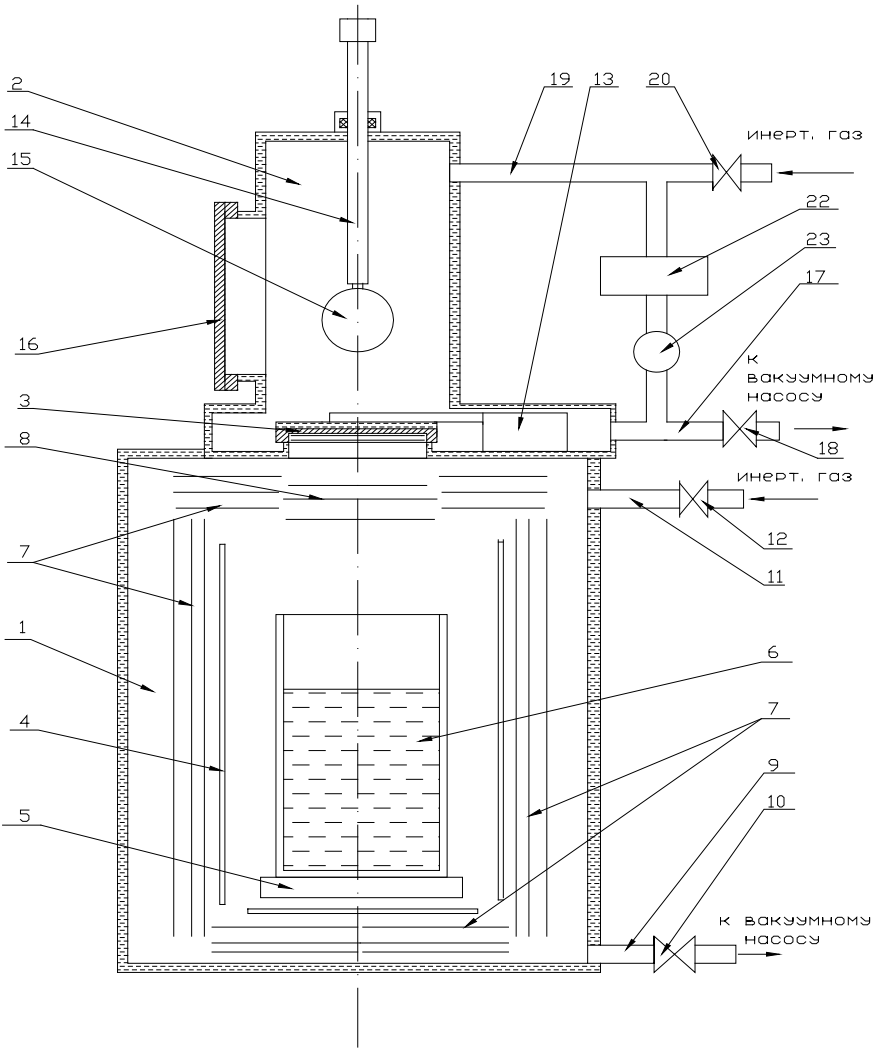


**Fig. 1** Installation for diffusion metallization in an environment of low-melting liquid metal solutions. 1—lower chamber; 2—upper chamber for heat treatment; 3—shutter; 4—heaters; 5—table; 6—bath with melt; 7—screens; 8—movable screen; 9—vacuum line; 10—valve; 11—inert gas supply line; 12—valve; 13—the drive mechanism of the shutter; 14—movable rod; 15—covered items; 16—loading door; 17—vacuum line; 18—valve; 19—inert gas supply line; 20—valve; 21—circulation system; 22—heat exchanger; and 23—pump

# 3 Results of the Research

## *3.1 Optical Metallography and Micro-X-Ray-Spectral Analysis of the Coating in the Initial State*

The results of the study of coatings microstructure and the distribution of alloying elements after diffusion metallization at temperature of 1000 °C, 2 h (initial state) are presented in Figs. 2, 3 and in Table 1. In the boundary layer of the applied coating, we see the crushing of grains, the appearance of particles of secondary phases (carbides and intermetallic compounds).

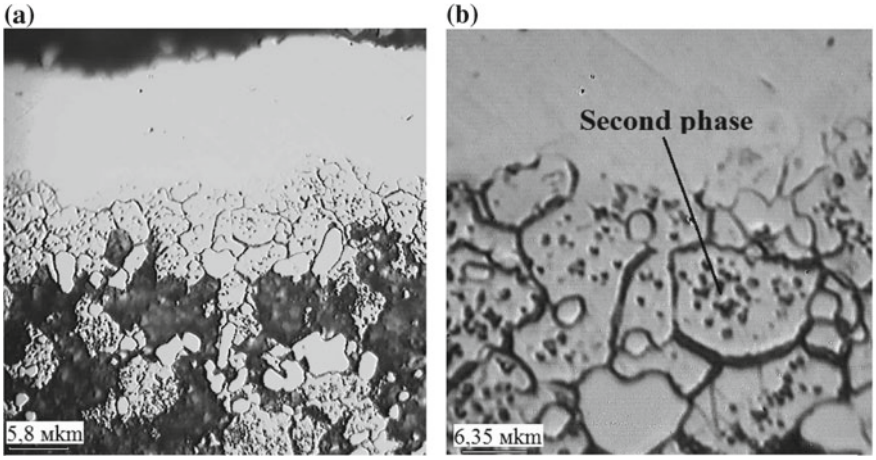


**Fig. 2** Microstructure of X12M coated steel (in the initial state), obtained using an optical microscope μVizo-MET. ×1600 (**a**), ×2500 (**b**)

**Table 1** Distribution of alloying elements in the initial state (weight)

| Analysis | Al | Cr | Fe | Ni | Cu |
|---|---|---|---|---|---|
| 1 | 2.59 | 0.06 | 19.49 | 54.10 | 23.55 |
| 2 | 0.67 | 0.66 | 23.75 | 54.01 | 20.91 |
| 3 | 0.90 | 1.01 | 32.43 | 50.18 | 15.23 |
| 4 | 1.08 | 1.62 | 44.57 | 43.21 | 9.33 |
| 5 | 0.87 | 5.72 | 67.73 | 21.73 | 3.83 |
| 6 | 0.57 | 15.12 | 74.51 | 8.35 | 1.27 |
| 7 | 0.62 | 20.18 | 76.32 | 2.69 | 0 |
| 8 | 0.59 | 14.75 | 83.56 | 0.98 | 0 |
| Max. | 2.59 | 20.18 | 83.56 | 54.10 | 23.55 |
| Min. | 0.57 | 0.06 | 19.49 | 0.98 | 1.27 |

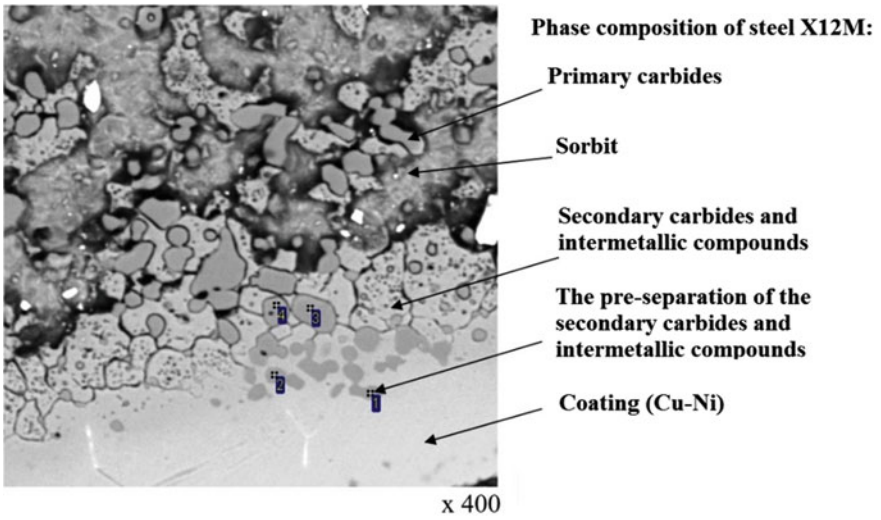


**Fig. 3** Microstructure of the intermediate coating layer of the X12M steel after diffusion alloying at a temperature of 1000 °C, 2 h

**Fig. 4** Photograph of the structure of steel X12M after diffusion alloying (initial state), obtained using "Camebax-Micro" microanalyzer

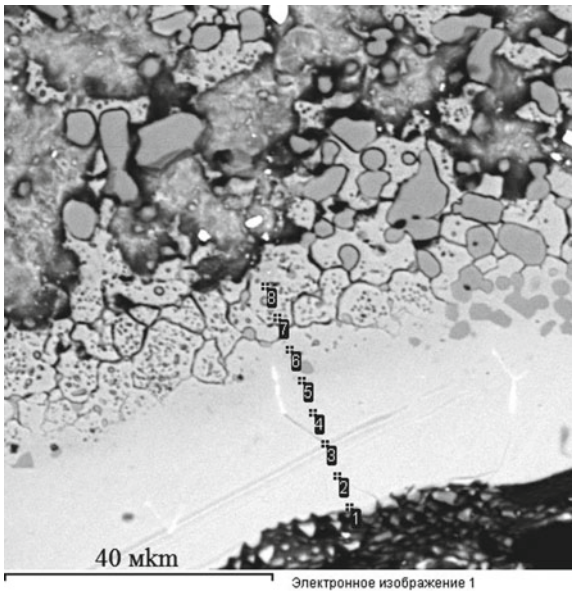


In the initial state in the surface layer of the coating, the content of copper, nickel, and chromium was 23.55, 54.10, and 0.006%, respectively. At a distance of 25 μm from the surface (transition layer), the content of Cu and Ni decreased to 0 and 2.69%, respectively, see Fig. 4 and Table 1.

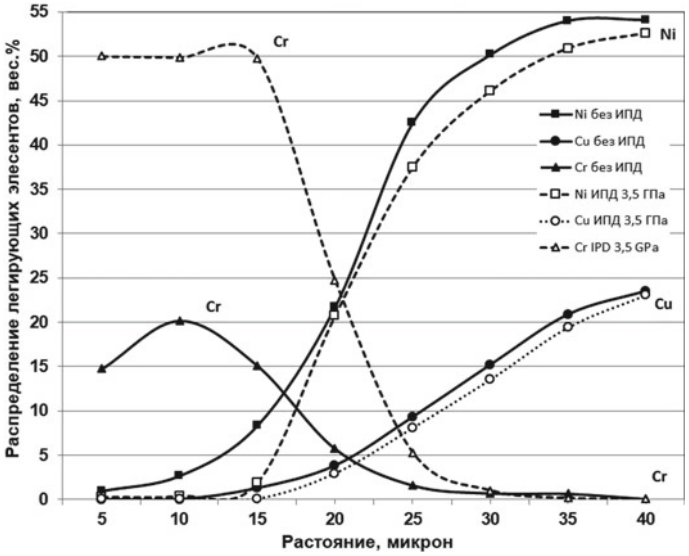


**Fig. 5** Distribution of alloying elements in steel X12M before and after intensive plastic deformation (IPD) under stress of 3.5 GPa (Cu–Ni coating on the right)

On the contrary, the Cr content in the transition layer increased to 20.18%. As shown by X-ray diffraction data, cubic carbide particles M23C6 and sigma-phase FeCr are formed in these transition layers enriched in chromium and iron, Figs. 2b and 4.

Thus, in the process of diffusion alloying of a tool made of X12M steel (initial state), counterflows of alloying elements appear in the surface layer. Copper and nickel penetrate on the surface of the tool from steel X12M. Chromium and iron from steel are redistributed into the (Cu–Ni) coating, especially to its boundary region, where secondary phases precipitate [17–20].

## *3.2 Optical Metallography and Micro-X-Ray-Spectral Analysis of the Coating After Intensive Plastic Deformation*

The results of micro-X-ray-spectral analysis of the distribution of alloying elements in steel X12M before and after intensive plastic deformation (IPD) under the action of a stress of 3.5 GPa are presented in Fig. 5.

As shown by the results, the distribution of the alloying elements after IPD was identical to the graph of the initial state. On a quantitative level, the concentration of Cu and Ni decreased to 1.3…3.4% after IPD in the surface layer and at the depth

of the coating. The Cr concentration increased in the intermediate layer compared with the initial condition, but only after IPD at stress of 3.5 GPa, Fig. 5. Equally distribution of Cr and Fe was observed on the remaining samples in boundary region of coating. In this case, we did not observe precipitation of cubic carbide M23C6 and sigma-phase FeCr.

## *3.3 X-Ray Diffraction Analysis of Steel X12MF Before and After Intensive Plastic Deformation*

We studied the width of diffraction lines, the size of the coherent scattering regions (CSR), and the value of microstrains ($\varepsilon$) of the crystal lattice before and after intense plastic deformation under stresses of 3.0, 3.5, 4.0, and 4.5 GPa. CSR is a part of the grain, separated from neighbor part through the defective wall. For very small grains, CSR determines the grain size. As grain grows, it is divided into a number of coherent scattering regions separated by dislocation walls. The subgrains are deployed relative to each other and therefore they disperse non-coherently.

The formation of cubic carbide M23C6 and the sigma phase of FeCr is represented as a multistage process in the initial state in the intermediate layer of the coating. It includes: 1. formation of segregations of atoms, 2. formation of coherent predispositions, and 3. separation of secondary phases of carbide M23C6 and intermetallic FeCr, having a maximum CSR of 36 nm and a minimum ε of 1.25%.

The size of the CSR and ε changed after IPD at stresses of 3.0, 3.5, 4.0, and 4.5 GPA, as shown in Fig. 6 and in Table 2.

After the IPD under stress of 3.5 GPa, the maximum of diffraction line width *W* (220) was 1.97°, the maximum size of the $\varepsilon$—1.25%, and the minimum size of the CSR was 23 nm.

**Table 2** Diffraction line width (*W*), size of coherent scattering regions (CSR), and crystal lattice microstrain size ($\varepsilon$), depending on the magnitude of stresses for IPD

| Sample №. | Stress IPD (GPa) | Diffraction line width *W* (angle degrees) | | | Size of coherent scatter regions (CSR) (nm) | Crystal lattice microstrain size $\varepsilon$, % |
|---|---|---|---|---|---|---|
| | | CuNi (111) | CuNi (222) | CuNi (220) | | |
| Initial | 0 | – | – | 1.71 | 36 | 1.15 |
| 2 | 3.0 | 0.42 | 0.77 | 1.95 | 34 | 1.17 |
| 1 | 3.5 | 0.53 | 0.91 | 1.97 | 23 | 1.25 |
| 3 | 4.0 | 0.41 | 0.75 | 1.90 | 30 | 1.19 |
| 4 | 4.5 | 0.37 | 0.62 | 1.86 | 32 | 1.15 |

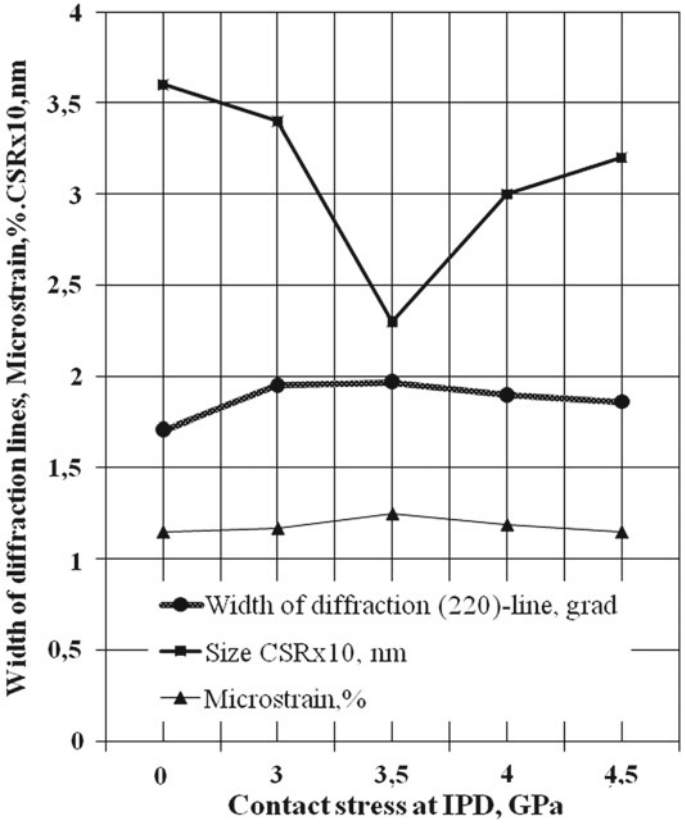


**Fig. 6** Graph of the diffraction line width ($W$), the microstrain of the crystal lattice ($\varepsilon$), and the coherent scattering region (CSR), depending on the value of the stresses at the IPD

## *3.4 Tribological Properties of Materials*

The results of tribological tests are shown in Fig. 7. After applying the Cu–Ni coating, the relative wear resistance significantly increases by 1.5 times, and the surface roughness of the tool decreases by 2.4 times, compared to the surface properties of the uncoated surface.

When abrasion paired with steel X12M, the friction coefficient and relative wear resistance had values of $0.083 \pm 0.028$ and $1.54 \pm 0.21$, respectively. As a result of IPD of Cu–Ni coatings at stresses of 3.0, 3.5, 4.0, and 4.5 GPa; relative wear resistance increased by 2.5, 2.1, 2.6, and 3.5 times, respectively, Fig. 7.

Congruence was observed between the decrease in relative wear resistance after IPD at stress of 3.5 GPa and the decrease in the size of CSR having low-angle dislocation boundaries in an elongated polygonized nanostructure. An increase in

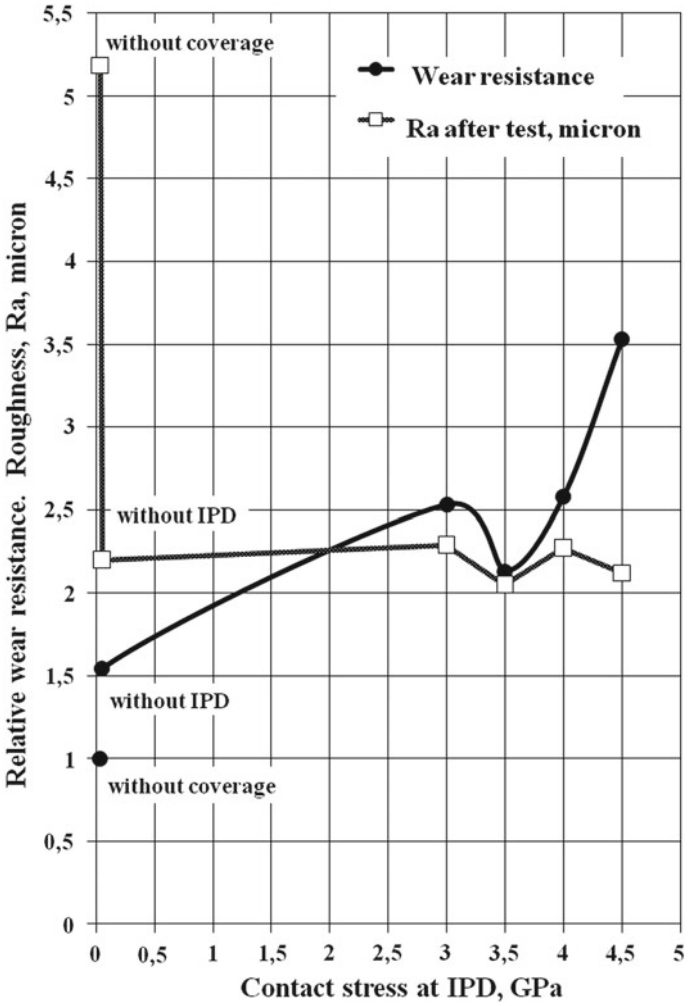


**Fig. 7** Effect of diffusion alloying and IPD on the relative wear resistance and roughness of X12M steel

the Cr concentration was observed compared to the initial state in the transition layer of the coating (Fig. 5; Table 1).

We assume that chromium from steel X12M was redistributed along the dislocation boundaries of subgrains. This causes a hardening change in the chemical and phase composition of the Cu–Ni coating and decrease in its relative wear resistance. This redistribution causes a hardening change in the chemical and phase composition of the coating and decrease in relative wear resistance.

## 4 Conclusion

The conducted studies allowed to conclude that in the process of deposition of copper–nickel (Cu–Ni) coating on a tool made of steel X12M and subsequent intensive plastic deformation at contact stresses 3.0, 4.0, and 4.5 GPa, it was discovered nanostructuring of its surface layer and the corresponding redistribution of alloying elements.

Significant increase in wear resistance and decrease in surface roughness after the application of copper–nickel coating on the instrument correlated with decrease in the size of coherent scatter regions (CSR) with low-angle dislocation boundaries in an elongated polygonized nanostructure at stress of 3.5 GPa. Increase in the concentration of Cr was observed in the transition layer of coating as compared with the initial state.

1. Thus, ultrafine-grained structure is formed in the process of IPD of the copper–nickel coating at contact stresses of 3.0, 3.5, 4.0, and 4.5 GPA in the surface layer. It significantly increases the tribological properties of the surface of steel products X12M.
2. Plastic deformation under the action of external contact stresses from 3.0 to 3.5 GPa causes an increase in internal stresses, broadening of diffraction lines, and microstrain of the crystalline lattice. The minimum size of the CSR 23 nm was achieved with abrasion paired with steel X12M at 3.5 GPA. The coefficient of friction and wear resistance have values of 0.078 and 2.13, respectively.
3. The application of nickel–copper coatings on the cutting tool and the use of IPD reduces the temperature of the cutting edge of the tool due to the high thermal conductivity and heat removal of the coating. This made it possible to increase the wear resistance of the tool during machining.

**Acknowledgements** This work was performed with financial support of the Ministry of Education and Science of the Russian Federation within the grants № 933-2014, № 1972-2014, and № 11.5832.2017/8,9.

## References

1. Flom DG, Komanduri R, Lee M (1994) High-speed machining of metals. Ann Rev Mater Sci 231–278
2. Skotnikova MA, Krylov NA (2016) About nature of dissipative processes at cutting treatment of titanium vanes. In: Proceedings of the 5th international scientific and practical conference “modern engineering: science and education” MMESE-2016. Publishing house of Polytechnical Institute, St. Petersburg, June 30–01 July 2016, pp 530–539
3. Komanduri R, Schroeder T, Hazra J, Von Turkovich BF, Flom DG (1982) On the catastrophic shear instability in high speed machining of an AISI 4340 steel. ASME J Ind 104:121–131
4. Skotnikova MA, Krylov NA, Van Uyin (2016) Structural and phase transformations in VT-23 alloy at high-speed cutting. In: Proceedings of the IV international scientific-practical conference “innovations in transport and mechanical engineering”, vol. III. National Mineral Resources University “Mining”, St. Petersburg, pp. 130–133

5. Skotnikova MA, Kastorsri DA, Krylov NA (2003) Structural and phase transformations in metals at fast-track cutting. Mater Sci Quest SPb. 1(33):214–224
6. Skotnikova MA, Vinogradov VV, Krylov NA (2005) Accounting of the wave theory of a plastic strain at high-speed machining of surfaces of preparations. Metal Work SPb. 11:12–15
7. Ivanov EK, Skotnikova MA, Krylov NA (2012) Structural phase changes in the hardly processed materials as a way of increase of wear resistance of the tool/scientific and technical sheets SPBGPU. Sci Educ 1:41–52
8. Skotnikova MA, Krylov NA, Motovilina GD etc. (2007) Transformation in two phase titanium alloys under high speed mechanical loading. Mater Sci Quest SPb. 4(52):359–365
9. Skotnikova MA, Krylov NA (2017) About the nature of dissipative processes in cutting treatments of titanium vanes. Advances in mechanical engineering. Springer International Publishing, pp. 115–123
10. Sokolov AG, Artemiev VP, Shasherina SA (2009) The Influence of carbon steel and the nature of the coverage elements on the process and mechanism of formation of diffusion coatings from the environment fusible recomedations-cal solutions. Technol Metals 11:40–44
11. Sokolov AG, Artemiev VP, Shasherina SA (2010) Technology and equipment for the diffusion metallization from environment of the fusible liquid metal solutions. Technol Metals 3:30–35
12. Skotnikova M.A, Shasherina S.A., Krylov N.A., Ivanov E.K. Modern metal materials and technologies/collection of materials of the international scientific and technical conference SPbGPU, Saint Petersburg, Russia, 20–21 June 2011, pp 114–115
13. Skotnikova MA, Shasherina SA, Krylov NA, Tsvetkova GV (2014) Research tribology properties nanostructure diffusion layers of metal coverings. In: XII International conference on nanostructured materials (NANO 2014) 13–18 July 2014, Lomonosov Moscow State University, Moscow, Russia, p 332
14. Skotnikova MA, Tsvetkova GV, Krylov NA, Ivanov EK, Medvedeva VV, Bezenkin NV (2015) Features of wear of abrasive grains depending on microcuttings speed of steels. In: Proceedings of the 24th international conference engineering materials & tribology BaltMatTrib—2015, 5–6 Nov 2015, Tallinn, Estonia, pp. 189–194
15. Skotnikova MA, Krylov NA, Tsvetkova GV (2014) Peculiarities of plastic deformation and wear of abrasive grains at high-speed machining. Ferrous Metals 4(988):84–92
16. Skotnikova MA, Tsvetkova, GV, Krylov NA (2016) Features of wear of abrasive grains depending on microcuttings speed of steels. Key Eng Mater 674. The title of the volume is "Engineering Materials and Tribology" pp 358–364
17. Skotnikova MA, Tsvetkova GV, Lanina AA, Krylov, NA Ivanova GV (2015) Structural and phase transformation in material of blades of steam turbines from titanium alloy after technological treatment. Lect Notes Mech Eng 93–101
18. Skotnikova, MA, Krylov, NA, Ivanov, EK, Tsvetkova GV (2016) Structural and phase transformation in material of steam turbines blades after high-speed mechanical effect. Lect Notes Mech Eng 159–168
19. Skotnikova MA, Tsvetkova GV, Krylov NA, Ivanov EK (2016) Features of wear of abrasive grains depending on microcuttings speed of steels. Key Eng Mater 674:358–364
20. Skotnikova MA, Krylov NA (2017) About the nature of dissipative processes in cutting treatments of titanium vanes. In: Advances in mechanical engineering. Selected contributions from the conference "modern engineering: science and education", Saint Petersburg, Russia. Springer, Berlin–Heidelberg, 20–21 June, 2016, pp 115–124

# Kinematic Synthesis of Programmed Motions of Drivers of a Manipulator-Tripod with a Three-Degree Gripper


**Natalia S. Vorob'eva, Victor V. Zhoga, Ivan A. Nesmiyanov and Andrey V. Dyashkin**

**Abstract** The article provides a solution for the task with regard to synthesis of the laws for motion of the slave cylinders in a parallel-serial structure manipulator to realize the predetermined path of an end effector. The set of points characterizing subsequent positions of the actuators is determined by solving an optimization task on the manipulator's configuration. The laws for motion of slave cylinders are established by the method of the fifth-order polynomial interpolation of the first and last sections of the determined path. The intermediate path section is described by a typical polynomial. The polynomial coefficients are determined by the point square approximation method.

**Keywords** Parallel-serial structure manipulator · Programmed motion · Optimization · Gripper · Third- and fourth-order splines

## 1 Introduction

The paper considers a parallel-serial structure manipulator [1] (Fig. 1). Due to high structural rigidity parameters and positioning accuracy, parallel-serial structure mechanisms-based manipulators are nowadays applied as simulators, in measurement systems and metal-cutting equipment to treat surfaces of irregular shape [2–4]. When performing these activities, the manipulator's end effector shall move along complex three-dimensional paths.

Generation of the laws for changes of manipulator's generalized coordinates $l_k(t)$, $(k = 1 - 4)$, $\alpha(t)$, $\psi(t)$, $\beta(t)$ on a real-time basis involves some difficulties because of a large-scale task and restricted computational power of drive-level controllers. As control systems architecture is based on a hierarchical principle, it is

N. S. Vorob'eva (✉) · I. A. Nesmiyanov · A. V. Dyashkin
Volgograd State Agrarian University, Volgograd, Russia
e-mail: vorobva@inbox.ru

V. V. Zhoga
Volgograd State Technical University, Volgograd, Russia



A. N. Evgrafov (ed.), *Advances in Mechanical Engineering*,
Lecture Notes in Mechanical Engineering,
https://doi.org/10.1007/978-3-030-11981-2_7

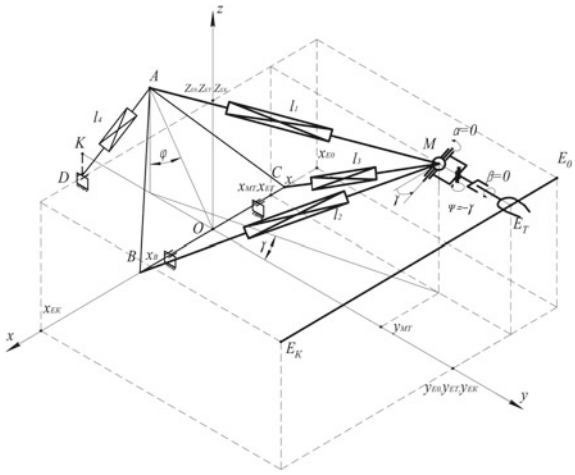


**Fig. 1** Parallel-serial structure manipulator on a swiveling base

deemed to be reasonable to determine in advance the analytical laws for changes of generalized coordinates of the servo drivers.

Spatial position of the manipulator and end effector is determined in the absolute coordinate system $Oxyz$ (Fig. 1). Each link of the gripper is connected to the moving coordinates $O_j x_j y_j z_j$, $(j = 1, 2, 3, 4)$. The manipulator structure ensures relations between actuating links length, point $M$ coordinates $x_M(t)$, $y_M(t)$, $z_M(t)$, and swivel angle $\varphi$ of base $ABC$ [5]

$$
\begin{aligned}
&l_1(t) = \sqrt{x_M^2 + (y_M + OA \cdot \sin\varphi)^2 + (z_M - OA \cdot \cos\varphi)^2},\\
&l_2(t) = \sqrt{(x_M - OB)^2 + y_M^2 + z_M^2}, \quad l_3(t) = \sqrt{(x_M + OB)^2 + y_M^2 + z_M^2},\\
&l_4(t) = \sqrt{(OK - OA \cdot \sin\varphi)^2 + (OA \cdot \cos\varphi + DK)^2}.
\end{aligned} \tag{1}
$$

Parameter $\gamma(t)$ of the manipulator (Fig. 1) is determined through the expression

$$
tg\gamma = \frac{-x_M}{y_M + OA\sin\varphi} \tag{2}
$$

Any process operation includes sequential performance of defined programmed motions of the end effector [6]. Number of generalized coordinates of the manipulator is seven—length of actuating links $l_k(t)$, $(k = 1-4)$ and swivel angles of the gripper links $\alpha(t)$, $\psi(t)$, $\beta(t)$ [7]. Number of generalized coordinates of the end effector is six—Cartesian coordinates of distinguished point $E[x_E(t), y_E(t), z_E(t)]$ and Euler angles [8] specifying its space orientation. Thus, manipulator's movability is equal to one [9]. In this case, the task aimed to generate a law of control movements changes for the actuating links allows for a set of solutions, that is, multiple manipulator's configurations correlate to the set position of the end effector.

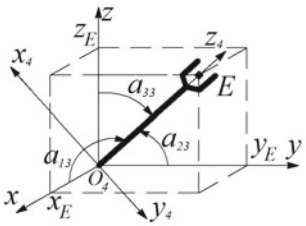


**Fig. 2** Space orientation of manipulator's gripper

For the process operations to be performed efficiently, the manipulator's gripper shall be moved with the set speed along smooth path connecting the target points.

**Task definition**

The laws for movement of the distinguished point of the manipulator's end effector (Fig. 1) $E[x_E(t), y_E(t), z_E(t)]$ and its directional cosines $\alpha_{pq}(t)$ (Fig. 2) are to be defined.

It is required to find the laws for changes of manipulator's generalized coordinates $l_k(t)$, $(k = 1-4)$, $\alpha(t)$, $\psi(t)$, $\beta(t)$ ensuring end effector motion laws are fulfilled. It is accepted that speed and acceleration are equal to zero in initial and terminal path points and continuously vary in intermediate points.

**Solution method**

It is considered that at some reference time, the manipulator's configuration is known, that means, the generalized coordinate values are set $l_k(0) = l_{k0}$, $(k = 1-4)$, $\alpha(0) = \alpha_0$, $\psi(0) = \psi_0$, $\beta(0) = \beta_0$. The end effector position in space is determined by transfer matrix $\mathbf{M_{J-1,J}}$, composition describing the position of gripper link j relative to $(j-1)$ [10]

$$\mathbf{M_{04}} = \mathbf{M_{01}} \times \mathbf{M_{12}} \times \mathbf{M_{23}} \times \mathbf{M_{34}}. \tag{3}$$

Coordinates of points $\mathbf{x_j}$ in $j$ and $\mathbf{x_{j-1}}$ in $(j-1)$ coordinate systems are interrelated through sequential execution of operations $\mathbf{x_{j-1}} = \mathbf{M_{J-1,J}}, \cdot \mathbf{x_j}$, using the transfer matrices [11].

With serial transfer along the chain of gripper-hinged links from coordinate system $O_4x_4y_4z_4$ to system $O_1x_1y_1z_1$, we have

$$\begin{cases} x_E = x_M + b\alpha_{13} - a\cos\alpha\sin\gamma \\ y_E = y_M + b\alpha_{23} + a\cos\alpha\cos\gamma \\ z_E = z_M + b\alpha_{33} + a\sin\alpha \\ \alpha_{33} = \cos\psi\sin\alpha \\ \alpha_{23} = \cos\gamma\cos\psi\cos\alpha - \sin\gamma\sin\psi, \end{cases} \tag{4}$$

where $a$, $b$—geometrical parameters of the gripper (Fig. 2).

The programmed path of point $E$ is split to $n$ areas at regular time intervals $\Delta t$. As coordinate values $x_E(t_i)$, $y_E(t_i)$, $z_E(t_i)$ for point $E$ of the end effector and

directional cosines $\alpha_{pq}(t_i)$ at time $t_i = i \cdot \Delta t, i = 0, 1, 2, 3 \ldots, n$ are known, the values of generalized coordinates (1) $l_k(t_i)$, $(k = 1 - 4)$ of the manipulator-tripod, generalized coordinates $\alpha(t_i)$, $\psi(t_i)$ of the gripper and (2) design angle $\gamma(t_i)$ at time $t_i$ are deduced from the condition for minimum of generalized energy criterion [12]

$$\Phi(\varphi_i) = c_1[l_{1i}(\varphi_i) - l_{10}]^2 + c_4[l_{4i}(\varphi_i) - l_{40}]^2, \tag{5}$$

where $l_{1i}(\varphi_i)$, $l_{4i}(\varphi_i)$—values of the actuating links length at time $t_i$; $c_1, c_4$—weighting factors with values proportional to the actuating links loads (Fig. 1).

Thus, at current time $t_i$, configuration of the manipulator $l_{ki}(t_i)$, $(k = 1 - 4)$, $i = 0, 1, 2, 3 \ldots, n$ and gripper $\varphi_i, \alpha_i, \psi_i$ are completely known (Fig. 2).

Polynomial interpolation is deemed to be the simplest. From the efficiency perspective, it shall be applied when it is required to arrive at an acceptable result based on a small number of set points. However, under polynomial interpolation, the law for changing gripper path velocity contravenes the programmed one that prevents from arranging a control system with velocity feedback. This is due to presence of local extremums of interpolation angular coordinate curve. Increase in number of node points does not allow for steady velocity change. Therefore, the obtained values of the generalized coordinates are approximated by regular m degree polynomial in the set of values $l_{ki}(t_i)$ [13, 14] within the time interval from $t_1 = \Delta t$ to $t_{n-1} = (n-1)\Delta t$

$$Q_k(t) = A_{0k} + A_{1k}t + A_{2k}t^2 + \cdots + A_{mk}t^m. \tag{6}$$

Constant coefficients $A_{mk}$ are defined from the condition minimum of a function represented as a square deviation

$$\delta = \sum_{i=1}^{n-1} [Q_k(t_i) - l_{ki}(t_i)]^2. \tag{7}$$

To ensure the required condition of minimum (7), the partial derivatives from (7) with respect to all variables $A_m$ [15] shall be equal to zero. After transformations, we have a linear equation system $(m + 1)$ respective to $(m + 1)$ unknown $A_m$.

$$\sum_{s=0}^{s=m} A_{sk} \sum_{i=1}^{n-1} t_i^{s+p} = \sum_{i=1}^{n-1} t_i^p l_k(t_i), \quad p = 0, 1, 2, \ldots, m, \tag{8}$$

It is proved that if there are no coinciding points among $t_i$ points and $m < n-1$, the system determinant (8) is not equal to zero; therefore, the system has only one solution [16]. After solving the system (8) for each value $l_k(t_i)$, $(k = 1 - 4)$, we define the polynomials (6) approximating values $l_{ki}(t_i)$, $(k = 1-4)$, $i = 1, 2, 3 \ldots, n-1$ with continuous functions of time of slave cylinders length change $l_k(t) = Q_k(t_i)$, $(k = 1 - 4)$ within time interval from $t_1 = \Delta t$ to $t_{n-1} = (n-1)\Delta t$. Based on Weierstrass

theorem for a continuous function at some segment, it is possible to find a polynomial in which absolute deviation from this function is less than a sufficiently small preset value [16].

In order to satisfy the boundary conditions for position, velocity, and acceleration of the gripper within the time interval from $t_0 = 0$ to $t_1 = \Delta t$ and from $t_{n-1} = (n-1)\Delta t$ to $t_n = n\Delta t$, the required function of actuating link movement is to be interpolated with the fifth-order polynomials.

$$P_k(t) = B_{5k}t^5 + B_{4k}t^4 + B_{3k}t^3 + B_{2k}t^2 + B_{1k}t + B_{0k}, \quad \text{for} \quad \Delta t \geq t \geq 0,$$

$$H_k(t) = C_{5k}t^5 + C_{4k}t^4 + C_{3k}t^3 + C_{2k}t^2 + C_{1k}t + C_{0k}, \quad \text{for} \quad t_n \geq t \geq t_{n-1}. \quad (9)$$

For the first path segment by substituting value $t = 0$, we obtain

$$B_{0k} = l_k(0) = l_{k0}, \quad B_{1k} = \dot{l}_k(0) = 0, \quad B_{2k} = \ddot{l}_{k0} = 0. \quad (10)$$

At $t_1 = \Delta t$ on the right end, we have

$$P_k(t_1) = B_{5k}t_1^5 + B_{4k}t_1^4 + B_{3k}t_1^3 + B_{0k} = Q_k(t_1), \quad (11)$$

$$\dot{P}_k(t_1) = 5B_{5k}t_1^4 + 4B_{4k}t_1^3 + 3B_{3k}t_1^2 = \dot{Q}_k(t_1), \quad (12)$$

$$\ddot{P}_k(t_1) = 20B_{5k}t_1^3 + 12B_{4k}t_1^2 + 6B_{3k}t_1 = \ddot{Q}_k(t_1). \quad (13)$$

For the last path segment by substituting value $t_{n-1} = (n-1)\Delta t$, we obtain

$$H_k(t_{n-1}) = C_{5k}t_{n-1}^5 + C_{4k}t_{n-1}^4 + C_{3k}t_{n-1}^3 + C_{2k}t_{n-1}^2 + C_{1k}t_{n-1} + C_{0k} = Q_k(t_{n-1}), \quad (14)$$

$$\dot{H}_k(t_{n-1}) = 5C_{5k}t_{n-1}^4 + 4C_{4k}t_{n-1}^3 + 3C_{3k}t_{n-1}^2 + 2C_{2k}t + C_{1k} = \dot{Q}_k(t_{n-1}), \quad (15)$$

$$\ddot{H}_k(t_{n-1}) = 20C_{5k}t_{n-1}^3 + 12C_{4k}t_{n-1}^2 + 6C_{3k}t_{n-1} + 2C_{2k} = \ddot{Q}_k(t_{n-1}). \quad (16)$$

At $t_n = n\Delta t$ on the right end, we have

$$H_k(t_n) = C_{5k}t_n^5 + C_{4k}t_n^4 + C_{3k}t_n^3 + C_{2k}t_n^2 + C_{1k}t_n + C_{0k} = l_k(t_n), \quad (17)$$

$$\dot{H}_k(t_n) = 5C_{5k}t_n^4 + 4C_{4k}t_n^3 + 3C_{3k}t_n^2 + 2C_{2k}t + C_{1k} = \dot{l}_k(t_n) = 0, \quad (18)$$

$$\ddot{H}_k(t_n) = 20C_{5k}t_n^3 + 12C_{4k}t_n^2 + 6C_{3k}t_n + 2C_{2k} = \ddot{l}_k(t_n) = 0. \quad (19)$$

From the equation systems (11–13, 14–16) and (17–19), we find polynomial coefficients (9). Thus, the polynomials (6), (9) completely define the analytical laws of changing slave cylinders length through the continuous functions of time

$$l_k(t) = \begin{cases} P_k(t), & 1 \geq t \geq 0, \\ Q_k(t), & 11 \geq t \geq 1, \\ H_k(t), & 12 \geq t \geq 11, \end{cases} \quad k = 1 - 4. \tag{20}$$

In case some extreme points are discovered when calculating polynomials (9), there are methods to ensure monotonicity of path of change in corresponding variable [14].

**Example of method implementation**

As an example of implementation of the proposed method to calculate programmed actuating links motion, we consider translational motion of the gripper along a horizontal line (Fig. 1) parallel to axis $Ox$ from the initial point with coordinates $x_E(0) = -316,36\,\mathcal{MM}$, to the terminal point with coordinates $x_E(T) = 420,05\,\mathcal{MM}$. $y_E(0) = y_E(T) = 1437,65\,\mathcal{MM}.$, $z_E(0) = z_E(T) = 740,49\,\mathcal{MM}$. within $T = 12\,c$.

Reference [9] is the law of coordinate $x_E(t)$ variation ensuring velocity and acceleration to be equal to zero in the initial and terminal points of the path

$$x_E(t) = \left(10 - 15\frac{t}{T} + 6\frac{t^2}{T^2}\right)\frac{t^3}{T^3}L, \quad T \geq t \geq 0, \tag{21}$$

where $L = [x_E(T) - x_E(0)]$—path length.

End effector position in space is specified by directional cosines $\alpha_{23} = 1, \alpha_{33} = 0, \alpha_{13} = 0$ of moving coordinates $O_4x_4y_4z_4$ of the end effector relative to fixed coordinates $Oxyz$ (Fig. 2). It follows from (4) that having selected programmed motion of the end effector within all the time of movement $\alpha = 0, \psi = -\gamma$. Number of the node points to be selected depends on the type of programmed motion of the gripper. In the given example, we divide the entire segment of $L$ length into twelve parts $n = 0 - 12$. At regular intervals $\Delta t = T/12$, we find coordinates $x(t_i)$ of the node points; the coordinates of the initial and terminal points are known (18), $t_i = i \cdot \Delta t, i = 0, 1, 2, 3 \ldots, n$

$$x_E(t_i) = x(t_i) + x_E(0), \quad y_E(t_i) = y_E(0), \quad z_E(t_i) = z_E(0). \tag{22}$$

We determine [10, 17] the manipulator's configuration at initial time $l_k(0) = l_{k0}, (k = 1 - 4), \alpha(0) = 0, \psi(0) = \psi_0 = -\gamma_0$. Then we specify the manipulator's configuration at any specific time $t_i = i \cdot \Delta t$. Therefore, slave cylinders length $l_k(t_i), (k = 1 - 4)$ is known at time $t_i$. The values derived are used to calculate approximating and interpolating polynomials (6), (9) which determine the laws of manipulator's drives motion. Based on the expression (8), we have simultaneous linear algebraic equations relative to coefficients $A_{mk}$ of polynomials of type (6). The coefficients of polynomials (9) are established from Eqs. (11–19). With increasing order m of an approximating polynomial, the squared error (7) reduces, i.e., approximation accuracy becomes higher. A peak value of the square deviation is received for the third link of the manipulator. So, at $m = 3$, mean square deviation is equal to

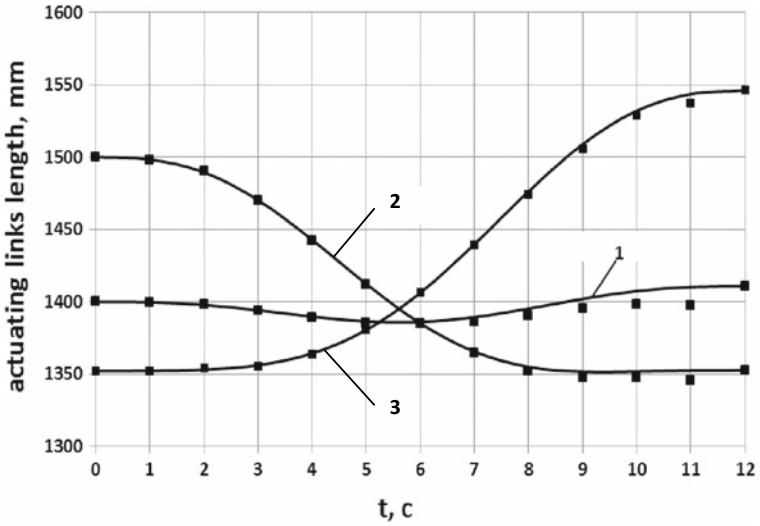


**Fig. 3** Dependence of actuating links length

$\sigma = 11, 3$, at $m = 4$, $\sigma = 2, 95$ and at $m = 5$, $\sigma = 2, 51$. And with further polynomial order growth, mean square deviation slightly reduces. Based on the calculations for the expressions (17), it is received at $m = 5$ for the third actuating link.

$$l_3(t) = \begin{cases} P_3(t) = -22, 01t^5 + 49, 703t^4 - 27, 81t^3 + 1352, 6, 1 \geq t \geq 0, \\ Q_3(t) = 1383, 86 + 23, 30t - 13, 08t^2 + 3, 03t^3 - 0, 227t^4 \\ \qquad + 0, 0052t^5, 11 \geq t \geq 1, \\ H_3(t) = 20, 68t^5 - 1193, 19t^4 + 27520, 51t^3 - 317210, 49t^2 \\ \qquad + 1, 83t - 4, 2, 12 \geq t \geq 11. \end{cases} \tag{23}$$

To evaluate accuracy of the prescribed programmed gripper motion tracked by the manipulator's drives, a path and law of shifting distinguished point $E[x_E(t),\ y_E(t),\ z_E(t)\ ]$ of the end effector (Fig. 1) are established on the basis of the generated (20) laws of changes in slave cylinders length. For this purpose, by solving a direct task on positions, we determine the coordinates of point $M(x_M,\ y_M,\ z_M)$ through manipulator's generalized coordinates $l_k(t)$, $(k = 1 - 4)$ [18].

Then using the expression (4), we find the laws for changing the coordinates of point $E[x_E(t),\ y_E(t),\ z_E(t)\ ]$. Figure 3 shows dependence (20) of actuating links length, and Fig. 4 shows the laws for changing coordinate $x_E(t)$ established on the basis of specified programmed movements (18) and of the laws resulted from the calculations:

– according to the specified program movements
– according to the laws obtained as a result of calculations
– according to the specified program movements

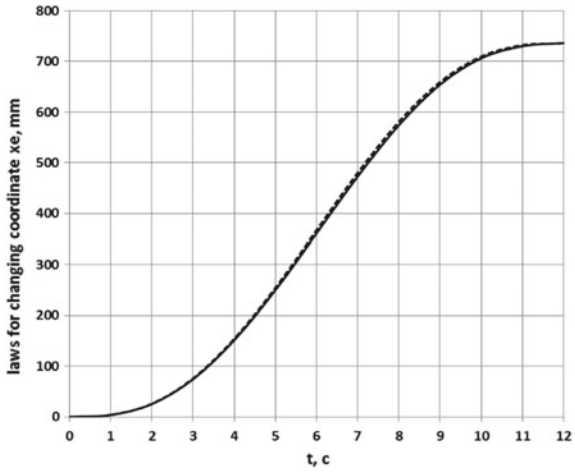


**Fig. 4** Laws for changing coordinate $x_E(t)$

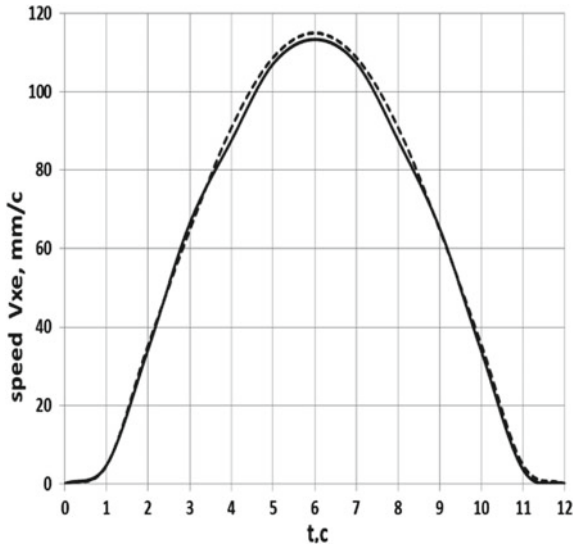


**Fig. 5** Laws for changing velocity of the distinguished point $Vx_E(t)$ of the gripper

– according to the laws obtained as a result of calculations.

Accuracy of approximation of the programmed path (Fig. 4) when forming control movements of the slave cylinders is estimated through the ratio of maximum deviation from the path to the path length [16].

$$\delta = \frac{\Delta z \max}{L}, \quad \text{(in the considered example } \delta = 0.0095\text{)}.$$

If the obtained accuracy fails to meet the requirements of proper process performance, it is required to increase the number of the node points along the programmed path.

Velocity and acceleration of a distinguished point of the gripper along the path are determined as the first and the second derivatives of the generated polynomials (17). Figure 5 shows the laws for changing programmed velocity of coordinate $x_E(t)$ calculated on the expression (18) and velocity of this point retrieved from the method described in this article (20).

## 2 Conclusion

The suggested method to calculate analytical dependence of the laws for changing the control actuating links of the parallel-serial structure manipulator through interpolation polynomials on the initial and terminal path segments and approximation of intermediate path segments allows for generating a drive signal for each actuating link of the manipulator [19] and developing a programmed and position control systems with position and velocity feedback used to follow the programmed paths [20, 21].

## References

1. Glazunov VA, Koliskor ASh, Krajnev AF (1991) Spatial mechanisms of parallel structure. Nauka, Moscow, p 95
2. Afonin VL, Podzorov PV, Sleptsov VV (2006) Processing equipment based on mechanisms of parallel kinematics. Mechanical Engineering, Moscow
3. Bushuev VV, Golyshev IG (2001) Mechanisms of parallel structure in mechanical engineering. STIN 1:3–8
4. RobB FlexBicker IRB 360 robot manipulator from ABB www.abb.com/robotics [Electronic resource]—Access mode: http://www.roboticturnkeysolutions.com/robots/abb/datasheet/IRB_360.pdf
5. Zhoga VV, Djashkin-Titov VV, Djashkin AV, Vorob'eva NS, Nesmiyanov IA, Ivanov AG (2017) Pat. 2616493 Rossijskaja Federacija, MPK V66S 23/44. Manipulator-tripod parallel-serial structure. opubl. 17.04.2017. Bjul. № 11
6. Intelligent robot/ pod obshhej redakciej E.I. Jurevicha/ I.A. Kaljaev, V.M. Lohin, I.M. Makarov i dr. Moscow: Mashinostroenie, 2007. 360 s
7. Dyashkin-Titov VV, Vorob'eva NS, Terekhov SE (2016) Algorithm for positioning the capture of the manipulator-tripod. In: Contemporary Mechanical Engineering: Science and Education: Materials of the 5th Intern. scientific-practical. conference. In: Evgrafova AN, Popovich AA (eds) Publishing house of Polytechnic. Univ., SPb, pp 634–644
8. Kobrinskij AA, Kobrinskij AE (1985) Manipulation systems of robots. Nauka, Moscow, 343 s
9. Kolovskij MZ, Sloushh AV (1998) Bases of dynamics of industrial robots. Nauka. Gl. red. fiz.-mat. Lit., Moscow, 240 s
10. Zhoga VV, Djashkin-Titov VV, Nesmiyanov IA, Vorob'eva NS (2016) The task of positioning the manipulator of a parallel-sequential structure with a controlled gripper. Mech Autom Control, No. 8. 17:525–530

11. Korendyasev AI, Salamandra BL, Tyves LI (2006) Theoretical foundations of robotics: in 2 books. ot. In: Kaplunov CM (ed) Institute of Mechanical Engineering. A.A. Blagonravova RAS. - Science, Book 1, Moscow 383p
12. Jurevicha EI, Kozlov, VV, Makarychev VP (1984) Dynamics of control of robots/ pod redakciej. i dr. Nauka. Glavnaja redakcija fiziko-matematicheskoj literatury, Moscow, 336 s
13. Zenkevich SL, Yushchenko AS (2004) Fundamentals of manipulation robots, MGTU. N.E. Baumana, 449p
14. Modeling, trajectory planning and motion control of the robot manipulator, R. Paul, Transl. with English. The main edition of the physical and mathematical literature of the publishing house "Nauka", Moscow; 1976, 104p
15. Bryson A, Ho Y-s (1972) Applied theory of optimal control. Mir, Moscow, Moscow, 544p
16. Demidovich BP, Maron IA, Shuvalova EZ (1962) Numerical methods of analysis. State publishing house of physical and mathematical literature, Moscow, 367p
17. Zhoga V, Gavrilov A, Gerasun V, Nesmianov I, Pavlovsky V, Skakunov V, Bogatyrev V, Golubev D, Dyashkin-Titov, V, Vorobieva N (2014) Walking mobile robot with manipulator-tripod. In: Proceedings of Romansy 2014 XX CISM-IFToMM symposium on theory and practice of robots and manipulators. Series: Mechanisms and Machine Science, vol 22. Springer International Publishing Switzerland, pp. 463–471
18. Gerasun VM, Zhoga VV, Nesmijanov, IA, Vorob'eva, NS, Djashkin-Titov VV (2013) Determination of the service area of the mobile manipulator-tripod. Mashinostroenie i inzhenernoe obrazovanie 3, 2–8
19. Nesmiyanov I, Zhoga V, Skakunov V, Terekhov S, Vorob'eva N, Dyashkin-Titov V, Ali Hussein Al-hadsha F (2015) Synthesis of control algorithm and computer simulation of robotic manipulator-tripod. In: Communications in computer and information science. Springer International Publishing Switzerland, CIT&DS 2015, CCIS 535, pp 392–404
20. Zhoga V, Gavrilov A, Gerasun V, Nesmianov I, Pavlovsky V, Skakunov V, Bogatyrev V, Golubev D, Dyashkin-Titov V, Vorob'eva N (2014) Walking mobile robot with manipulator-tripod. In: Proceedings of Romansy 2014 XX CISM-IFToMM symposium on theory and practice of robots and manipulators. Series: Mechanisms and Machine Science, vol 22, Springer International Publishing Switzerland, pp 463–471
21. Gayduk AR (2012) Theory and methods of analytical synthesis of automatic control systems (polynomial approach). FIZMATLIT, Moscow, 360 with

# About Implementation Harmonic Impact of the Resonance Method


**P. A. Andrienko, Vladimir I. Karazin, Denis P. Kozlikin and Igor O. Khlebosolov**

**Abstract** This study considers the problem of improving test equipment through the use of resonant modes to reproduce harmonic impacts, and examines the influence of various parameters on the reproduction of a wider range of test impacts, including in transient modes.

**Keywords** Harmonic impact · Combined impact · Resonance excitation of oscillations · Resonance effect

## 1 Introduction

Mechanical tests for harmonic impact are the most common type in the testing of different purpose objects [1–3]. Vibration stands allow conducting such tests in a wide range of amplitudes and frequencies [4]. However, reproduction of combined impact [5–7] requires the source of vibration to be placed on a movable base. In this case, vibrator mass should be minimized.

One way of achieving this is to use the resonance effect [8] in the reproduction of the test impact.

Study [9] shows that using the method of resonance excitation of oscillations for testing purposes significantly reduces energy consumption and substantially extends the range of test impacts. However, in order to confirm the feasibility of reproduction

P. A. Andrienko (✉) · V. I. Karazin · D. P. Kozlikin · I. O. Khlebosolov
Peter the Great Saint-Petersburg Polytechnic University, St.-Petersburg, Russia
e-mail: pavandrienko@spbstu.ru

V. I. Karazin
e-mail: visv05@mail.ru

D. P. Kozlikin
e-mail: kozlikindenis@gmail.com

I. O. Khlebosolov
e-mail: khlebosolov@mail.ru



A. N. Evgrafov (ed.), *Advances in Mechanical Engineering*,
Lecture Notes in Mechanical Engineering,
https://doi.org/10.1007/978-3-030-11981-2_8

of the parameters that have been considered irreproducible, it is necessary to consider the examined models in detail.

Previous studies [10–12] indicate two parameters that play a major role in the testing process: time of the transient process $\tau$ and maximum oscillation amplitude A, changes in which are defined by generalized coordinate $q$ (position of the table with the test object).

This study explores several opportunities for using resonant modes to reproduce harmonic impacts and examines the influence of various parameters on the reproduction of a wider range of test impacts, including in transient modes.

## 2 Single-Mass Model

Let us consider a model of a single-mass oscillatory system (Fig. 1),

where $m$ is the mass of the table; $c$ and $B$ are the stiffness and the damping coefficient of the elastic suspension; $C_n$, $B_n$ are the stiffness and the damping coefficient of the transmitting element; $u(t) = u_0\cos(pt)$ is the vibration impact of the coil of the vibrator with frequency $p$.

In this model, we assume that the adapter between the movable vibrator coil and the table has elastic-dissipative properties.

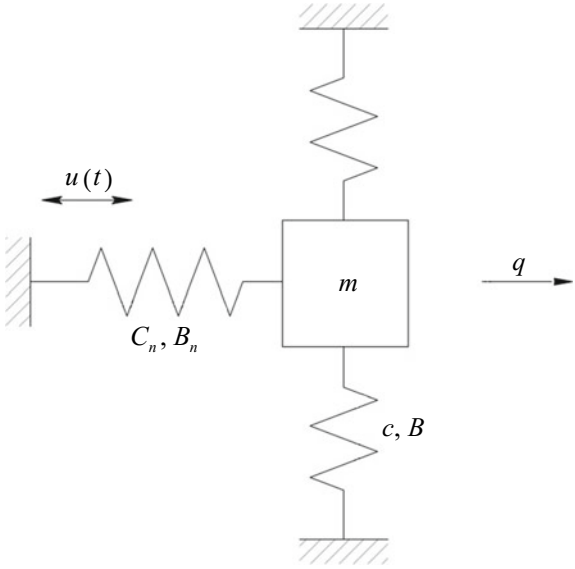


**Fig. 1** Single-mass oscillatory system

Equation of motion:

$$m\ddot{q} + 2B\dot{q} + cq = C_n(u(t) + 2B_n(\dot{u}(t) - \dot{q})); \tag{1}$$

or

$$m\ddot{q} + 2(B + B_n)\dot{q} + (c + C_n)q = \sqrt{C_n^2 + 2B_n k^2}u_0 \cos(pt + \gamma); \tag{2}$$

With $p = k$, we get:

$$q = \left(1 - e^{-\frac{B+B_n}{m}t}\right)\frac{\sqrt{C_n^2 + 4B_n^2k^2}u_0}{2(B + B_n)k}\cos(kt + \beta). \tag{3}$$

where $k$ is the natural frequency.

If stiffness $C_n$ is insignificant and damping is substantial—for example, when a damper is used—then $q_{\max} \approx u_0$ and time of the transient process $\tau = \frac{3m}{B_n}$ is insignificant. If $B_n$ is small, then

$$q\max = \frac{C_n u_0}{2(B + B_n)p}, \tag{4}$$

and the time of the transient process increases.

$$\tau = \frac{3m}{B + B_n}. \tag{5}$$

## 3 Dual-Mass Model

If we consider vibrator coil mass $m_0$, the model becomes a dual-mass model (Fig. 2).

Two degrees of freedom are defined by two generalized coordinates—$q_0$ and $q$; $c_0$, $B_0$ are the characteristics of the suspension of the movable vibrator coil.

Equations of motion:

$$\begin{cases} m_0\ddot{q}_0 = F - C_n(q_0 - q) - 2B_n(\dot{q}_0 - \dot{q}) - C_0q_0 - B_0\dot{q}_0 \\ m\ddot{q} = C_n(q_0 - q) + 2B_n(\dot{q}_0 - \dot{q}) - cq - B\dot{q}. \end{cases} \tag{6}$$

For this model, let us determine the influence of stiffness $C_n$ and the ratio between masses $m_0$ and $m$ on the natural frequencies of the system. In order to calculate the natural frequencies, let us assume that $B = B_n = B_0 = 0$

$$\Delta = \begin{vmatrix} m_0p^2 + C_n + C_0 & -C_n \\ -C_n & mp^2 + C_n + C_0 \end{vmatrix}. \tag{7}$$

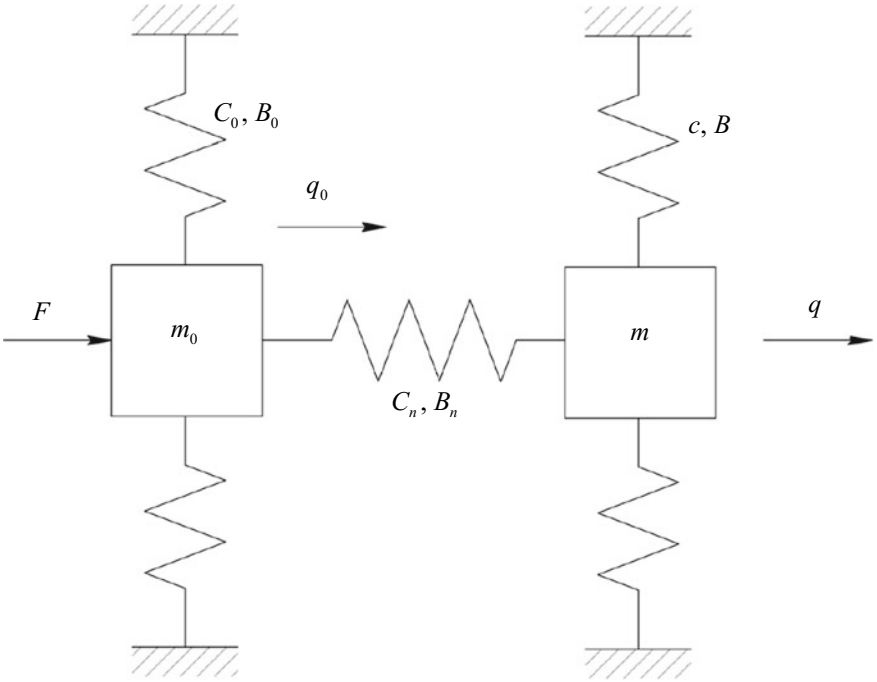


**Fig. 2** Dual-mass model

Now, let us apply $p = ik$ to the determinant and set it to zero

$$\Delta(ik) = m_0 m k^4 - (m + m_0) C_n k^2 - (C_0 m + c m_0) k^2 + C_n (c + C_0) + c C_0 = 0. \tag{8}$$

Finally, let us introduce the notation

$$M = \frac{m \cdot m_0}{m + m_0},$$

then

$$\boxed{k^4 - \left(\frac{C_n}{M} + \frac{C_0}{m_0} + \frac{c}{m}\right) k^2 + \frac{C_n (c + C_0) + c C_0}{m \cdot m_0} = 0.} \tag{9}$$

Normally, the first natural frequency of the vibrator $\left(p_1 = \frac{c_0}{m_0}\right)$ amounts to a few hertz; therefore, $\frac{C_0}{m_0} \ll \frac{c}{m}$. This also applies to stiffness ($c \gg c_0$). Eventually, we get:

$$k^4 - \left(\frac{C_n}{M} + \frac{c}{m}\right) k^2 + \frac{c \cdot C_n}{m \cdot m_0} = 0;$$

$$k_{1,2}^2 = \frac{1}{2}\left[\left(\frac{C_n}{M} + \frac{c}{m}\right) \pm \sqrt{\left(\frac{C_n}{M} + \frac{c}{m}\right)^2 - 4\frac{c \cdot C_n}{m \cdot m_0}}\right]. \tag{10}$$

Let us consider the following special cases:

**Case 1** $m \gg m_0$—the moving mass of the table with the test object is significantly greater than the mass of the vibrator coil.

Let us determine the values of natural frequencies $k_1$ and $k_2$ as well as the amplitude ratio of generalized coordinates $q_0$ and $q$:

$$k_{1,2}^2 = \frac{1}{2}\left[\frac{C_n}{M} + \frac{c}{m} \pm \sqrt{\left(\frac{C_n}{M}\right)^2 + \left(\frac{c}{m}\right)^2 - \frac{2c \cdot C_n}{m \cdot m_0}\left(1 - \frac{m_0}{m}\right)}\right]. \tag{11}$$

Given that $M \approx m_0$, $1 - \frac{m_0}{m} \approx 1$, we get

$$k_1^2 = \frac{c}{m}, \quad k_2^2 = \frac{C_n}{m_0}.$$

Let us determine the value

$$\eta = \frac{|\Delta q_0|}{|\Delta q|}.$$

For this purpose, let us rewrite the system of Eq. (6) in the following form:

$$\begin{cases} q_0\left(\lambda^2 + \frac{2(B_n+B_0)}{m_0}\lambda + \frac{C_n+C_0}{m_0}\right) - q\left(\lambda\frac{2B_n}{m_0} + \frac{C_n}{m_0}\right) = \frac{F}{m_0} \\ -q_0\left(\frac{2B_n}{m}\lambda + \frac{C_n}{m}\right) + q\left(\lambda^2 + \frac{2(B_n+B)}{m}\lambda + \frac{C_n+c}{m}\right) = 0. \end{cases} \tag{12}$$

Let us substitute $\lambda = ik$, then

$$|\Delta q_0(ik)| = \mathrm{mod}\begin{vmatrix} \frac{F}{m_0} & -\left(ik\frac{2B_n}{m_0} + \frac{C_n}{m_0}\right) \\ 0 & k^2 + \frac{2(B_n+B)}{m}ik + \frac{C_n+c}{m} \end{vmatrix}$$

$$= \frac{F}{m_0}\sqrt{\left(\frac{C_n + c}{m} - k^2\right)^2 + 4\left(\frac{B_n + B}{m}k\right)^2};$$

$$|\Delta q(ik)| = \mathrm{mod}\begin{vmatrix} -k^2 + \frac{2(B_n+B_0)}{m_0}ik + \frac{C_n+C_0}{m_0} & \frac{F}{m_0} \\ -\left(\frac{2B_n}{m}ik + \frac{C_n}{m}\right) & 0 \end{vmatrix}$$

$$= \frac{F}{m_0}\sqrt{\left(\frac{C_n}{m}\right)^2 + 4\left(\frac{B_n}{m}k\right)^2}.$$

At the same time, the amplitude ratio of generalized coordinates can be represented as

$$\eta = \frac{|\Delta q_0(ik)|}{|\Delta q(ik)|} = \frac{\sqrt{\left(\frac{C_n+c}{m} - k^2\right)^2 + 4\left(\frac{B_n+B}{m}k\right)^2}}{\sqrt{\left(\frac{C_n}{m}\right)^2 + 4\left(\frac{B_n}{m}k\right)^2}}. \tag{13}$$

With frequency $k^2 = k_1^2 = \frac{c}{m}$

$$\eta(k_1) = \frac{\sqrt{\left(\frac{C_n}{m}\right)^2 + 4\left(\frac{B_n+B}{m} \cdot \frac{c}{m}\right)^2}}{\sqrt{\left(\frac{C_n}{m}\right)^2 + 4\left(\frac{B_n}{m} \cdot \frac{c}{m}\right)^2}} = \frac{\sqrt{m^2\left(\frac{C_n}{c}\right)^2 + 4(B_n + B)^2}}{\sqrt{m^2\left(\frac{C_n}{c}\right)^2 + 4B_n^2}}.$$

Obviously, $\eta \geq 1$, i.e., we cannot achieve amplitude $q$ greater than $q_0$. If $C_n \gg 1$ and $\eta = 1$, the coordinates $q$ and $q_0$ are the same.

With $C_n \ll c$

$$\eta = 1 - \frac{B}{B_n}.$$

For frequency,

$$\eta(k_2) = \frac{\sqrt{\left[-m + m_0\left(1 + \frac{c}{C_n}\right)\right]^2 + 4(B_n + B)^2}}{\sqrt{m_0^2 + 4B_n^2}}. \tag{14}$$

The minimum value of $\eta$ is achieved when

$$m = m_0\left(1 + \frac{c}{C_n}\right). \tag{15}$$

However, if we work at frequency $k_2$, it will be necessary to change stiffness $C_n$ or mass $m_0$ in order to switch to another operating frequency, which is rather difficult in terms of design. Therefore, let us take frequency $k_1$, which is defined through variable stiffness $C_0$, as the operating frequency.

**Case 2** $m \ll m_0$—the mass of the vibrator coil is significantly greater than the mass of the moving table with effective load.

For this ratio, on condition that $m \to 0$,

$$k_{1,2}^2 = \frac{1}{2m}\left[\left(C_n\frac{m}{M} + c\right) \pm \sqrt{\left(C_n\frac{m}{M} + c\right)^2 - 4C_n c\frac{m}{m_0}}\right] \tag{16}$$

Since $\frac{m}{m_0} \ll 1$, let us take the last item in the expression under the radical as the small quantity. With accuracy up to the small quantity of the first order, let us write:

$$\sqrt{\left(C_n\frac{m}{M}+c\right)^2-4C_nc\frac{m}{m_0}}=C_n\frac{m}{M}+c-\frac{2C_nc}{C_n+c}\cdot\frac{m}{m_0}. \tag{17}$$

As long as $\frac{m}{M} \approx 1$, then

$$k_1 \approx \sqrt{\frac{C_nc}{(C_n+c)m_0}}, \quad k_2 \approx \sqrt{\frac{C_n+c}{m}}. \tag{18}$$

It should be noted that $k_1 \ll k_2$.

For different $C_n$ and $c$ ratios, we get:

(1) $C_n \gg c \Rightarrow k_1 \approx \sqrt{\frac{c}{m_0}}, k_2 \approx \sqrt{\frac{C_n}{m}}$.
Operating frequency $k_1$ (can be changed by changing stiffness $c$), $\eta_1 \approx 1$.

(2) $C_n \ll c \Rightarrow k_1 \approx \sqrt{\frac{C_n}{m_0}}, k_2 \approx \sqrt{\frac{c}{m}}$.
In this case, operating frequency $k_2$, amplitude ratio $\eta_2 < 1$.

(3) $C_n = c \Rightarrow k_1 \approx \sqrt{\frac{c}{2m_0}}, k_2 \approx \sqrt{\frac{2c}{m}}, \eta_1 > 1, \eta_2 < 1$.

In this case, frequency $k_2$ is preferable because $\eta_2 < 1$ and both the first and the second frequency can be changed.

The amplitude ratio of the generalized coordinates on the first and the second natural frequency:

$$\eta_1=\frac{\sqrt{\left(\frac{C_n+c}{m}\right)^2+4\left(\frac{B_n+B}{m}k_1\right)^2}}{\sqrt{\left(\frac{C_n}{m}\right)^2+2\left(\frac{B_n}{m}k_1\right)^2}} \geq 1, \quad \eta_2=\frac{2\frac{B_n+B}{m}k_2}{\sqrt{\left(\frac{C_n}{m}\right)^2+4\left(\frac{B_n}{m}k_2\right)^2}} < 1. \tag{19}$$

## 4 Conclusion

Comparison of the above two cases shows that with $m \gg m_0$ even "soft" connection of the movable vibrator coil to the table with the test object cannot generate amplitude $q_1$ greater than $q_0$ ($\eta \geq 1$). With $m \ll m_0$, it is possible to achieve $\eta < 1$, but the time of the transient process will increase.

## References


1. Batuev GS, Bolshikh AS, Golubkov VS et al (1982) Test equipment: reference book: in 2 books. Under the editorship of V. V. Klyuev. Mashinostroenie, Moscow, 528p (rus.)
2. Evgrafov AN, Karazin VI, Smirnov GA (1999) Rotary stands for motion variables simulation. Sci Tech Rep SPbGTU 3(17):89–94 (rus.)
3. Evgrafov AN, Karazin VI, Khlebosolov IO (2003) Playing motion parameters on rotary stands. Theory Mech Mach 1(1):92–96 (rus.)
4. Chernyshev AV (1983) Design of test benches for testing and control of aircraft onboard systems. Mashinostroenie, Moscow, p 384 (rus.)
5. Karazin VI, Kozlikin DP, Sloushch AV, Khlebosolov IO (2007) Dynamic model of vibratory stand. Theory of mechanisms and machines. Period Sci Method J 1(9):38–44 (rus.)
6. Karazin VI, Kozlikin DP, Khlebosolov IO (2006) Dynamic stands for vibro-rotary tests. Sci Tech Rep SPbGPU. 3(45):44–49. (rus.)
7. Karazin VI, Kozlikin DP, Khlebosolov IO (2007) On balancing the inertial forces in vibrotsentrifugal. Theory Mech Mach Period Sci Method J 2(10):63–71 (rus.)
8. Astashev VK, Babitsky VI (2007) Ultrasonic processes and machines. Dynamics, control and applications. 330p. Springer
9. Ksenofontov VI, Nikolaev VN, Chernokrylov SYu (1992) Multifunctional dynamic stand. Testing and Control Stands. LGTU, Leningrad, pp 29–32 (rus.)
10. Evgrafov AN, Karazin VI, Kozlikin DP, Khlebosolov IO (2017) Centrifuges for variable accelerations generation. Int Rev Mech Eng (IREME) 11(5):280–285
11. Evgrafov AN, Karazin VI, Kozlikin DP, Khlebosolov IO (2018) Some characteristics of linear acceleration reproduction with flexible harmonical component. Lect Notes Mech Eng 71–82
12. Antipov VI, Astashev VK (2004) Principles of creating the energy-saving vibration machines. Problemy Mashinostraeniya i Nadezhnos'ti MashinIssue 4:3–8

# Determination of Conjugated Profiles of Teeth in Cylindrical Gears, Knowing Meshing Line in Face Section


**Dmitry T. Babichev, Sergey Yu. Lebedev and Denis A. Babichev**

**Abstract** To identify the gears, tooth shape that ensures optimal gearing quality indicators is a crucial design problem. The authors suggest a new optimization synthesis concept based on the determination of an optimized meshing line to address this issue. The synthesis algorithm including its key and the largest (as concerns calculations) blocks is described in the article. The article introduces derivation of formulae for determination of the tooth profiles with a known meshing line. According to the formulae, profiles for various types of meshing lines (a straight line, a curve, etc.) were obtained. The conclusions were made, and further fields for research were determined.

**Keywords** Theory of gearing · Cylindrical gears · Analysis · Optimization synthesis

## 1 Introduction

In recent years, the issue of determining tooth surfaces (profiles) with maximum load capacity (high contact and bending stiffness) and wear resistance of working surfaces is getting more relevant. The reasons are the rapid development of computer modeling and the advent of advanced materials and manufacturing technologies such as:

– tooth surfacing on numeric-controlled machine tools;
– 3D printing;

D. T. Babichev (✉) · S. Yu. Lebedev · D. A. Babichev
Industrial University of Tyumen, Tyumen, Russia
e-mail: babichevdt@rambler.ru

S. Yu. Lebedev
e-mail: lebedevsergey1995@gmail.com

D. A. Babichev
URL: http://www.nipingp.ru



A. N. Evgrafov (ed.), *Advances in Mechanical Engineering*,
Lecture Notes in Mechanical Engineering,
https://doi.org/10.1007/978-3-030-11981-2_9

– manufacturing by means of pressing and sintering synthetic materials and powders, in particular, reinforced with high-tenacity yarn.

Thus, modern technologies enable to obtain a variety of complex tooth shapes which creates the issue of determining an optimal shape that ensures maximum tooth strength. In this article, the authors suggest a new method to address the issue.

Define research subject and objectives. The subject of the research is conjugated $\Sigma_1$ and $\Sigma_2$ profiles *in plane gearing*. The meshing is considered "*ideal*": Transverse sections of mutual envelope surfaces meet at the point K, while surfaces of $\Sigma_1$ and $\Sigma_2$ meet the line L; manufacture and installation deviations and deformations in meshing components are excluded; there is no $\Sigma_1$ and $\Sigma_2$ modifications in order to reduce tooth collision; and gearwheels in meshing contact rotate with constant angular velocity $\omega_1$ and $\omega_2$. Developed models and algorithms may be partially used for the research of gears with non-circular wheels and for design and analysis of camshaft mechanisms.

Figure 1 demonstrates the main elements of the plane gearing: $\Sigma_1$ and $\Sigma_2$—pinion and gearwheel teeth profiles. *The main contact parameters* of $\Sigma_1$ and $\Sigma_2$: $K$—contact point; $\Sigma$—meshing line segment, which ends are at points a and b.

*Points and lines in meshing*: $P_1$ and $P_2$—centroids; W—relative velocities instantaneous center; $r_{w1}$ and $r_{w2}$—radii of curvature $P_1$ and $P_2$ at the point $W$; and $O_1$ and $O_2$—centers of curvature of centroids at the contact point $W$. If $O_1$ and $O_2$—centers of rotation for gearwheels with $i_{12} = \text{const}$, then $P_1$ and $P_2$—pitch circles with radii $r_{w1}$ and $r_{w2}$. *Vectors and meshing angles*: $\boldsymbol{n}$—common contact normal for $\Sigma_1$ and $\Sigma_2$, passing through the point W; meshing angle $\alpha$—angle between $\boldsymbol{n}$ and common tangent of $P_1$ and $P_2$ (at the pitch point $W$).

Figure 2 shows four quadrants (pole at the point W) and two ML ($\Sigma$ and $\Sigma^*$) corresponding right and left tooth halves. The main coordinate system is $XWY$, its axes $WX$ and $WY$ cross at the point $W$. If $W$ moves (for example, in gears with non-circular wheels), then the coordinate system $XWY$ will also move.

Figure 3 demonstrates four types of meshing, which can be designed according to the methods described in the article. Among these types are three "ordinary" mechanisms: toothed mechanisms, camshaft mechanisms and rotary pneumatic and hydraulic machines. One-parametric molded gearings are also related to the considered types. In these mechanisms, one of the surfaces is an initial surface of a cutting tool, and another is a shaped tooth surface.

*Research subject summary: The key subject of the research is the plane gearing with rotating meshing links.* Spur gears with gear ratio $i_{12} = const$ and with smooth mutual envelopes $\Sigma_1$ and $\Sigma_2$ meeting at a point are primarily considered in the article. Additional reasons that determine the choice of the research object are the following: (**a**) cylindrical gears are the most common; (**b**) helical gears are generally designed based on transverse sections of tooth profile; (**c**) before determining teeth shapes according to the parameters of a known meshing line in tridimensional gears, the same (and more simple) task for plane gears should be completed; (**d**) Tyumen Industrial University has gained ample experience in cylindrical gears optimization synthesis and has accumulated data on the association between $\Sigma_1$, $\Sigma_2$ geometry

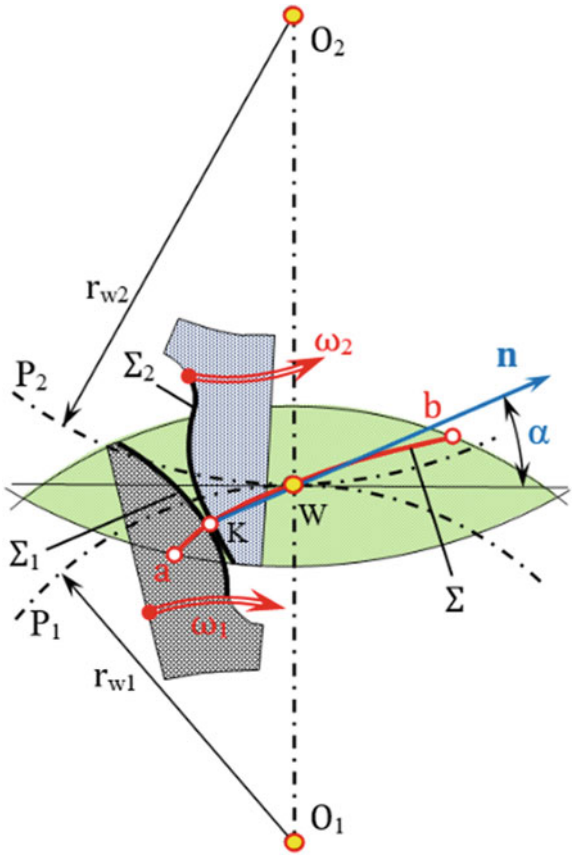


**Fig. 1** Main elements of plane gearing

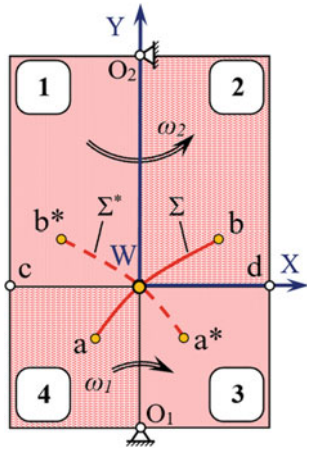


**Fig. 2** Main *XWY* coordinate system

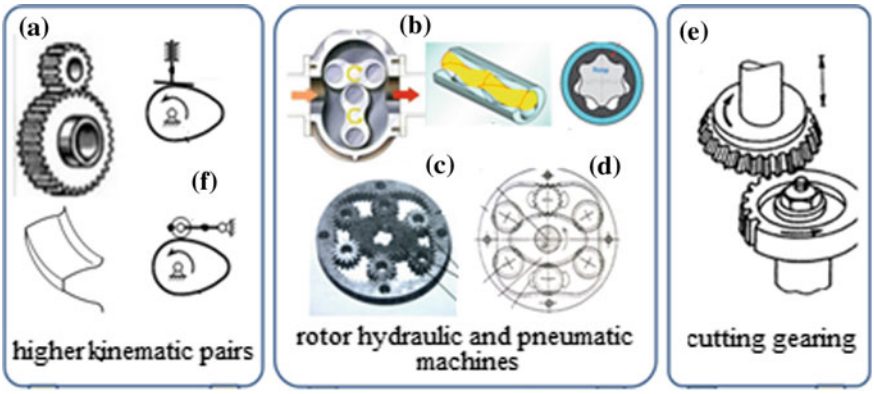


**Fig. 3** Types of plane gearing

parameters and ML form with gear load capacity [1, 2]. The data can be used in plane gearing design.

1. ***The main objectives of the classical meshing theory***.

In the meshing theory [3], there are two fundamental tasks that significantly affect meshing analysis and synthesis:

*Task 1*—using the known teeth profile $\Sigma_1$ of one of the meshing links, find another meshing link teeth profile $\Sigma_2$ and also its contact point (surface or meshing line $\Sigma$).

*Task 2*—using the known teeth profiles of two sliding meshing links, find the motion law of driven link.

In addition to meshing links synthesis and analysis, the following task should be completed:

*Task 3*—using the known $\Sigma_1$, $\Sigma_2$, $\Sigma$ surfaces, and links positions, and its motion laws, find meshing line quality indicators (local and global).

As is shown in the study [4], the following task is becoming more relevant:

*Task 4*—using the known meshing line $\Sigma$, find teeth profiles $\Sigma_1$ и $\Sigma_2$.

It is suggested in the article [4] that task 4 "synthesis of teeth surfaces according to the parameters of a known meshing line" should also be related to the fundamental tasks of the meshing theory.

From the mathematical point of view, task 4 substantially differs from task 1. Thus, task 1 involves solving the algebraic equation of meshing $\mathbf{N}\cdot\mathbf{V}_{12}=0$ [5], while task 4 involves solving the differential equation of meshing [6, Sect. 6.8].

2. ***Optimization synthesis objectives***

The solution to task 4 which is complicated enough from the mathematical point of view may be obtained by means of: (**1**) nonlinear programming: the classical problem that consists in determining parameters values of the vector x at which the objective function (load capacity) with nonlinear restrictions $F(\mathbf{x}) \rightarrow max.$ (**2**) or solving variational problem of determining the control function $f(u)$ or $f(u,v)$—tooth

profile $\boldsymbol{r}=\boldsymbol{r}(u)$ or surface $\boldsymbol{r}=\boldsymbol{r}(u,v)$—wherein the objective function $F(f(u)) \rightarrow max$ or $F(f(u,v)) \rightarrow max$ [2]. In both cases, optimal synthesis is recommended to conduct *based on determining optimal meshing curves or surfaces instead of optimal teeth profiles*. The truth of this assertion is not sufficiently based on the framework of the article. The described approach can critically reduce the number of calculations and, moreover, increase design reliability, and simplify the process of optimization synthesis. One of the reasons for increasing reliability is that the significant change of ML causes only minor modification of $\Sigma_1$ and $\Sigma_2$. For instance, for a similar reason synthesis of camshafts does not require a tappet motion law $S = S(\varphi)$ (as a function of rotational angle). Instead, the acceleration variation law is required $a = a(\varphi)$.

## 2 Fundamentals of Optimization Synthesis Approach

Based on the works [7–18] and the authors' experience [1, 4, 19, 20], the design algorithm of cylindrical gears with high load capacity (Fig. 4) was developed.

There are two types of leader lines in Fig. 4. Single lines show the sequence of calculations. Double lines show the direction of data transfer between blocks and external devices. Calculation blocks are numbered.

Considering the number of calculations required, block 2 and block 4 are critical. These blocks are described further.

*Block 2* requires thousands of iterations. In order to fasten the process, *the simple basic formula* for determining the radius of curvature of one of the conjugated profiles (using ML parameters and coordinates) should be obtained. *Establishing a link between the synthesizing profiles degree of curvature and ML parameters* appears to be a significant meshing theory problem that is not solved yet. *The first principal research goal* of the article is to obtain that formula and to create on that basis the method of all the radii of curvature determination in plane gearings ($\rho_1$—pinion profile, $\rho_2$—gearwheel profile, $\rho_\Sigma$—radius of relative curvature).

*Block 4* also requires iterations. A large number of calculations should be done due to the necessity of solving the differential ME while determining conjugated $\Sigma_1$ and $\Sigma_2$ profiles. To fasten the process, *the method of $\Sigma_1$ and $\Sigma_2$ determination without numerical solving of the differential equation* should be developed. The development of that method is also a significant meshing theory problem that is not solved. That *is the second principal research goal* of the article.

*Research objectives summary: The development of the methodology, method, and algorithm to complete task 4 (determining $\Sigma_1$ and $\Sigma_2$ teeth profiles according to the parameters of a known meshing line $\Sigma$)* is the key objective. Therefore, it is essential to solve two following theoretic problems:

(1) To be able to calculate all radii of curvature in teeth profiles contact through parameters of ML (without determining teeth profiles).—*It is a block 2 theory*.

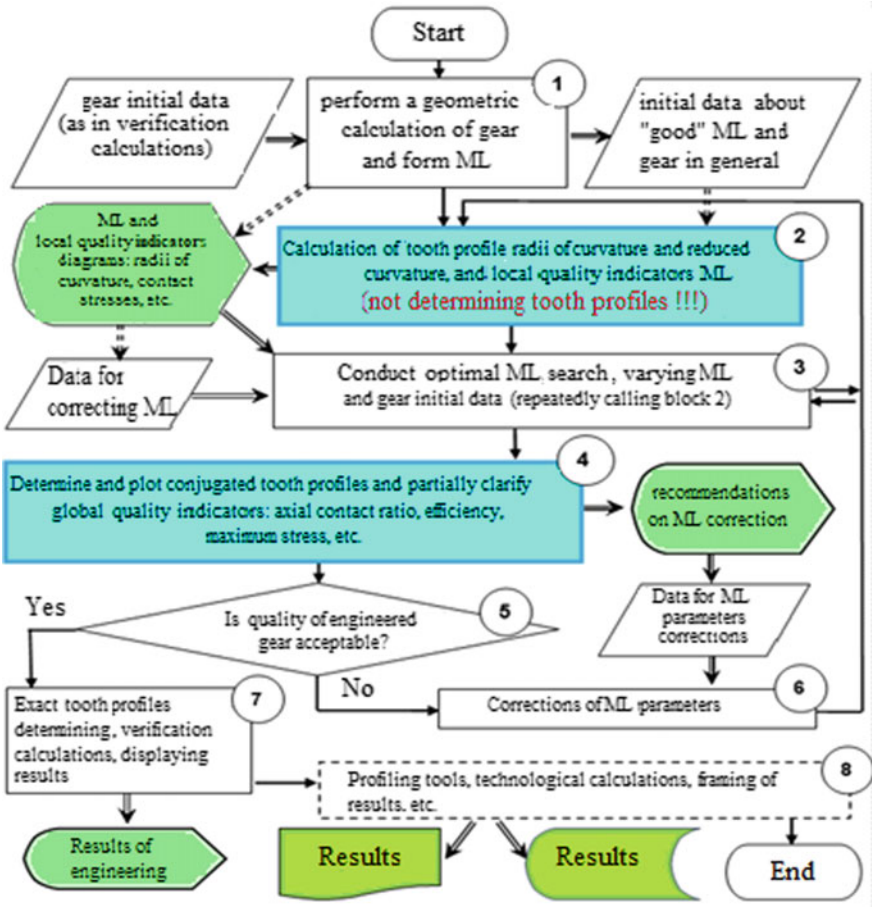


**Fig. 4** Concept and algorithm of optimization synthesis of cylindrical gears with high load capacity

(2) To be able to determine $\Sigma_1$ and $\Sigma_2$ profiles through coordinates of a point on ML and through profiles radii of curvature that cross at the contact points.—*It is a block 4 theory*.

Other "routine," however, significant issues are testing of methods and algorithms, and also assessing the accuracy of developed calculation methods described in blocks 2 and 4. Consideration of the rest blocks is within the framework of the article.

## 3 Calculation of All Radii of Curvature in Teeth Contact Through Parameters of ML (*Block 2 Theory*)

The review of a large number of works [21, 22] devoted to meshing theory and geometry shows that the works, where the radii of curvature $\rho_1$, $\rho_2$, or $\rho_\Sigma$ in gears with known ML were determined analytically, were absent. In the reviewed works, ρ was determined only numerically which involves *numerical solving* of the differential ME and the preliminary determination of $\Sigma_1$ and $\Sigma_2$.

The task of meshing curves analytical determination may be considered completed if the formula for one of the meshing links radius of curvature $\rho$ is obtained. According to the first principle of conjugated gearings formation (the principle of Olivier [3]), there are three meshing links: a cutting tool with working edge surface $\Sigma_0$ and two links with meshing profiles $\Sigma_1$ and $\Sigma_2$. There are also three gearings: two molded gearings $\{(\Sigma_0 + \Sigma_1$ и $\Sigma_0 + \Sigma_2)\}$ and one meshing gearing $\{\Sigma_1 + \Sigma_2\}$. It is recommended to consider the gearing that is simpler from the mathematical point of view. The simplest gearings are the plane gearings with a translatory moving gearing rack. In these gearings, the equation of meshing is linear in gearing rack S movement [23]. Thus, the formula for determining $\rho$ of a *translatory moving* gearing rack $\Sigma_0$ was derived. According to the first Olivier principle: (1) the meshing surface $\Sigma$ is the same for three mentioned above gearings; ($s_2$) the surface $\Sigma_0$ on a translatory moving rack may be assigned generating. In cylindrical gears, meshing surfaces of both molded gearings coincide, and in meshing gearings, teeth contact surface is the line L as in both molded gearings. This allows considering cylindrical gears as the plane meshing of $\Sigma_1$ and $\Sigma_2$ *profiles* (not surfaces) in transverse section.

According to the foregoing, the following plan of calculating cylindrical gears radii of curvature was adopted:

Stage 1 is to derive a basic formula for calculating $\rho_0$ of generating rack tooth profile $\Sigma_0$ at transverse sections by analyzing rack gearing through ML characteristics at the contact point.

This stage was completed and described in the article [24, 25]. The basic formulae:

$$\rho = -\mathrm{WK}_0 \cdot \left(1 + \frac{\tan \alpha_o}{\tan(\lambda)}\right) \tag{1a}$$

$$k = \frac{1}{\rho} = -\frac{\mathrm{tg}\lambda}{WK \cdot (\mathrm{tg}\lambda + \mathrm{tg}\alpha)} \tag{1b}$$

*WK—distance between the pitch point and e contact point;* $\lambda = (\theta – \alpha)$ $\alpha$—meshing angle, i.e., slope angle of contact normal passing through the point W; and $\theta$—slope angle of normal to $\Sigma_0$ at the current contact point $\mathrm{K}_0$.

Stage 2 is to develop an algorithm for calculating all radii of curvature in meshing of two profiles at cylindrical gear transverse sections: $\rho_1$, $\rho_2$, $\rho_\Sigma$—radii of curvature of $\Sigma_1$, $\Sigma_2$ and relative curvature profile. The base of the algorithm—Euler-Savary equation and the value $\rho_0$ of $\Sigma_0$ calculated by the basic formula.

This stage was completed and described in the article [19]. The resulting formulae:

$$\rho_1 = \frac{r_{w1} \cdot sin\alpha \cdot (\rho_0 + sign(x_K) \cdot WK)}{(\rho_0 + sign(x_K) \cdot WK) - r_{w1} \cdot sin\alpha} + sign(x_K) \cdot WK \quad (2)$$

$$\rho_2 = \frac{r_{w2} \cdot sin\alpha \cdot (\rho_0 - sign(x_K) \cdot WK)}{(\rho_0 - sign(x_K) \cdot WK) - r_{w2} \cdot sin\alpha} - sign(x_K) \cdot WK \quad (3)$$

Stage 3 is to calculate other local characteristics in teeth contact. After calculating all radii of curvature in meshing, all characteristics necessary for calculating objective function should be determined in order to optimize gear parameters. The main characteristic is a contact stress $\sigma_{h\text{-}}$, which can be found using common Hertz equation:

$$\boldsymbol{\sigma}_H = \sqrt{\frac{\boldsymbol{F} \cdot (\boldsymbol{\rho}_1 + \boldsymbol{\rho}_2) \cdot \boldsymbol{E}_1 \cdot \boldsymbol{E}_2}{\boldsymbol{\pi} \cdot \boldsymbol{b}_2 \cdot \boldsymbol{\rho}_1 \cdot \boldsymbol{\rho}_2 \cdot \left[\boldsymbol{E}_1 \cdot \left(1 - \boldsymbol{\nu}_2^2\right) + \boldsymbol{E}_2 \cdot \left(1 - \boldsymbol{\nu}_1^2\right)\right]}} \quad (4)$$

or using partial Hertz equation (for steel wheels):

$$\sigma_H = 0.418 \cdot \sqrt{\frac{F \cdot E}{b_2 \cdot \rho_\Sigma}} \quad (5)$$

Other characteristics are not considered in this article.

## 4 Determination of Conjugated Profiles Through Contact Points Coordinates on ML (*Block 4 Theory)*

As it was mentioned earlier, three conjugated profiles are to be determined. Profile $\Sigma_0$ is better to be determined first. Then, $\Sigma_1$ and $\Sigma_2$ can be determined in a relatively simple and reliable way with the help of gearing theory methods by analyzing two molded gearings: $\{(\Sigma_0 + \Sigma_1)$ and $(\Sigma_0 + \Sigma_2)\}$. In this case, *linear* meshing equation is to be solved relatively to rack displacement *S* for each molded gearing [5]. The next significant feature of gearings with translatory moving link: all vector projections on fixed coordinate axes and on coordinate axes related to the rack are *equal*, which simplifies determination of $\Sigma_0$ through ML parameters.

The stages of determination of all conjugated profiles are described below.

**Stage 1. Determination of rack tooth profile**. Figure 5 demonstrates meshing line *ab*, passing through *W* and on which multiple contact points $K_i$ are located. The points are indexed from 0 to *k*. The point $K_0$ coincides with the initial point of ML *a*, the point $K_k$—with the terminal point *b*. The set of coordinates $x_i$, $y_i$ of points $K_i$ ($i = 0...k$) is formed in block 1 (Fig. 4) in coordinate system $X_W WY_W$. Unit normal vectors $\mathbf{n}_i$ passing through W are shown at points $K_i$. These vectors are determined in block 2 (Fig. 4) in coordinate system $X_W WY_W$. Also radii of curvature ρ of $\Sigma_0$ and curvature of $k_i$ ($i = 0, \ldots k$) at all points $K_i$ on ML are calculated in block 2 according to the Formula 1a, 1b.

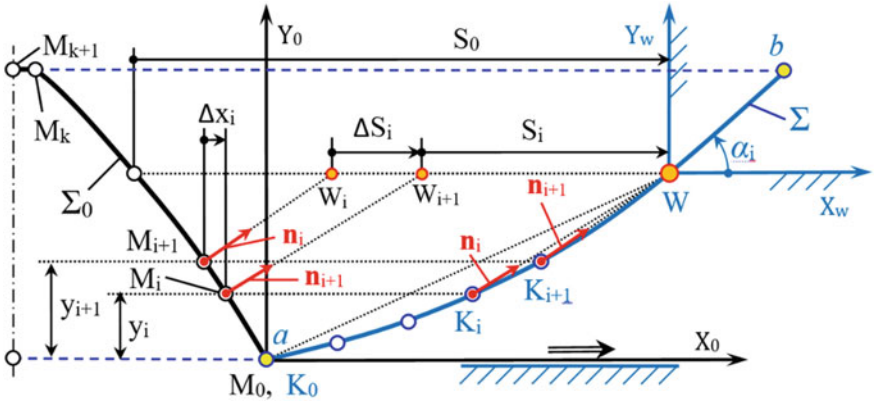


**Fig. 5** Rack $\Sigma_0$, shaping pinion, and gear wheel (the meshing line $\Sigma$ is determined)

Figure 5 shows profile $M_0M_K$ on $\Sigma_0$ where points $M_i$ are located; this points contact with $\Sigma_1$ and $\Sigma_2$ at points $K_i$ (ML $\Sigma$) in molded gearings. This article considers only determination of the working section of $\Sigma_0$ (line $M_0M_K$ on $\Sigma_0$) and sections on $\Sigma_1$ *и* $\Sigma_2$, formed by the line $M_0M_K$.

Figure 5 demonstrates two coordinate systems—fixed system $X_WWY_W$ on a base and moving system $X_0M_0Y_0$ on a rack. Also displacements $S_0$, $\Delta S_i$, and $\Delta S_W$ are shown. $S_0$—trajectory of the rack from the initial position where rack contacts $M_0$ at the point $a$ to the position where rack profile $M_0M_K$ contacts the point $W$. $\Delta S_i = \Delta S_W$—displacement of the rack while the contact point is moving from $K_i$ to the next point $K_{i+1}$.

The chosen approach of determination of $\Sigma_0$ is described further. The profile $\Sigma_0$ is a polyarc, i.e., multiple short arcs of circles, which are located consistently one after another and have different radii of curvature $\rho_{oi}$ $(i = 1\ldots k)$ in the common case. The points of contact $M_i$ $(i = 1\ldots k-1)$ of adjacent arcs touch ML $\Sigma$ at specified points $K_i$ $(i = 1\ldots k-1)$. This states the following requirement: The points $M_i$ are to contact with $\Sigma$ at specified points $K_i$.

Figure 6 demonstrates a design scheme for determination of the next point $M_{i+1}$, when the previous point $M_i$ is determined. Besides, in coordinate system $X_0M_0Y_0$ the following criteria are known: coordinates $\{x_{0i}, y_{0i}\}$ of the point $M_i$; unit normal vectors projections $\{n_{xi}, n_{yi}\}$; and rack profile radii of curvature $\{\rho_i, \rho_{i+1}\}$ at the points $M_i$ and $M_{i+1}$.

In a common case, ME for plane rack gearing is the following:

$$S_i = -y_i \cdot \frac{n_{xi}}{n_{yi}} \tag{6}$$

if $n_{xi}$, $n_{yi}$, $y_i$ occurred in (6) are determined in the system $X_wWY_w$ (Fig. 5) with the center $W$.

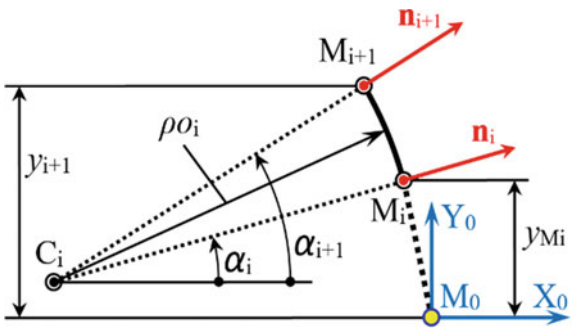


**Fig. 6** Design scheme for determination of the next point on generating rack teeth profile

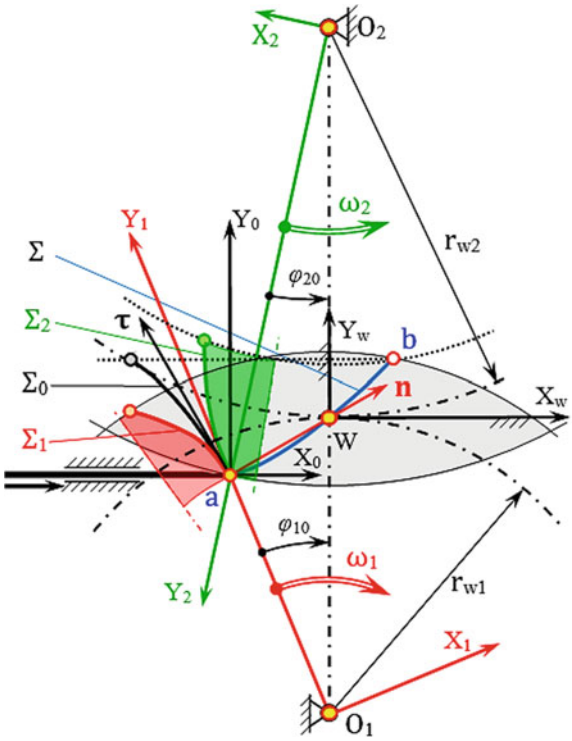


**Fig. 7** Coordinate system and the motion in three gearings: $\{\Sigma_0 + \Sigma_1\}$, $\{\Sigma_0 + \Sigma_2\}$, $\{\Sigma_1 + \Sigma_2\}$ with the same meshing line $\Sigma$

**Stage 2. Determination of pinion and gear wheel teeth profiles.** Figure 7 demonstrates a design scheme of three gearings: (1) molded $\{\Sigma_0 + \Sigma_1\}$—a pinion is shaped; (2) molded $\{\Sigma_0 + \Sigma_2\}$—a gear wheel is shaped; and (3) meshing $\{\Sigma_1 + \Sigma_2\}$—cylindrical gear.

The scheme includes three moving links: (1) a rack with determined profile $\Sigma_0$ and coordinate axes $X_0Y_0$ moving horizontally with the velocity $V$; (2) a pinion with sought profile $\Sigma_1$ and coordinate axes $X_1Y_1$ rotating with the velocity $\omega_1 = V/r_{\omega 1}$; and (3) a gear wheel with sought profile $\Sigma_2$ and coordinate axes $X_2Y_2$ rotating with

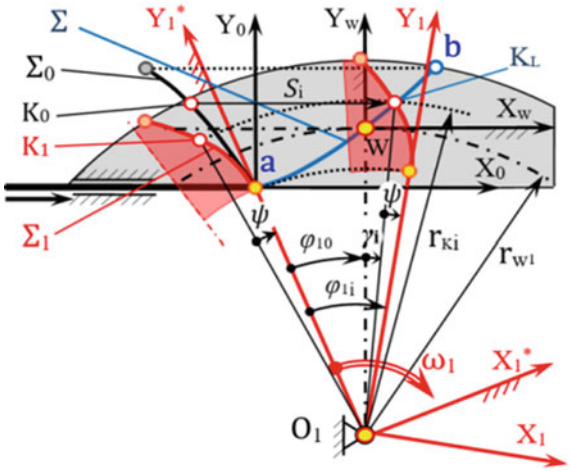


**Fig. 8** Design scheme for determination of the pinion tooth profile $\Sigma_1$ (the rack profile is determined)

the velocity $\omega_2 = V/r_{\omega 2}$. All the moving coordinate systems are shown in Fig. 12 at their initial positions. In this case, $Y$ axes pass through the ML initial point $a$. Thus, coordinates of all profiles at initial points $x = 0$.

Figure 8 demonstrates the initial position of a rack profile $\Sigma_0$ (at the initial point of ML) and two positions of $\Sigma_1$—initial and current (after rotating by the angle $\varphi_{1i}$, counted from initial position). The formulae for calculating parameters demonstrated in Figs. 11–13 are given further.

In the process of formulae derivation, the point $K_{0i}$ was moved from $\Sigma_0$ to $\Sigma_1$ (distance $S_i$); meanwhile, coordinate system $X_1Y_1$ rotated by the angle $\varphi_{1i}$ from its initial position $X_1^*Y_1^*$ (Fig. 8). The movement process can be mathematically described with the formulae below (7–15). The calculation can be made for every point on ML or rack profile; ME solvation is not necessary. Movement of the point from one coordinate system to another is required. The sequence of determining the point $K_1$ in pinion coordinate system $X_1Y_1$ (which is also the point $K_L$ in coordinate system $X_1^*Y_1^*$) is the following:

1. Pinion angle of rotation $\varphi_1$:

$$\varphi_{1i} = \frac{(S_i - S_0)}{r_{\omega 1}} \tag{7}$$

gear wheel angle of rotation $\varphi_2$:

$$\varphi_{2i} = \frac{(S_i - S_0)}{r_{\omega 2}} \tag{8}$$

2. Distance between the points a, K$i$ and the center $\Sigma_1$ (point $O_1$):

$$O_1 a = \sqrt{x_0^2 + (r_{\omega 1} + y_0)^2} \tag{9}$$

$$r_{K1} = \sqrt{x_i^2 + (r_{\omega 1} + y_i)^2} \tag{10}$$

where $x_0$ and $y_0$—coordinates of point a in $X_W W Y_W$

3. Angles $\varphi_{10}$ and $\gamma_i$ (Fig. 13):

$$\varphi_{10} = -\frac{x_0}{O_1 a} \tag{11}$$

$$\gamma_i = asin\left(\frac{x_i}{r_{K1}}\right) \tag{12}$$

4. Angle $\psi$ (Fig. 8):

$$\psi = \varphi_{1i} - \varphi_{10} - \gamma_i \tag{13}$$

5. Coordinates of $K_L$ in $X_1^* Y_1^*$ (and of $K_1$ in $X_1 Y_1$):

$$x_{1i} = -r_{K1} \cdot \sin\psi \tag{14}$$

$$y_{1i} = r_{K1} \cdot \cos\psi - r_{w1} \tag{15}$$

Algorithm for calculating coordinates of points $M_i$ on the rack tooth profile is demonstrated in Fig. 9. The figure also shows all initial data and calculation results.

Formulae for determination of coordinates of the points on $\Sigma_2$ in system $X_2 O_2 Y_2$ (Fig. 7) are similar to formulae (7–15) for $\Sigma_1$. These formulae are universal, as they can be used for any $\Sigma_0$.

Figure 10 shows the fragment of three gearings (the analog of Fig. 7) created by one of the key procedures while testing and debugging optimization design system for cylindrical gears. Calculations were made for the involute gear with following parameters: $z_1 = 14$, $z_2 = 29$, $m = 6$ mm, $x_1 = 0.3$, $x_2 = 0.4$, $\alpha = 20^\circ$, $h_a^* = 1$, $h_l^* = 1$ при $a_w = 106.219$ mm. An example of linear ML is chosen to compare the obtained working sections of all three profiles with profiles determined in accordance with existing reliable programs for involute gears.

Figure 10 shows the four meshing links ($\Sigma$, $\Sigma_0$, $\Sigma_1$, $\Sigma_2$) and $OY$ axes for $\Sigma_1$ and $\Sigma_2$ in two positions: initial $i = 0$ (profiles are marked with a dotted line) and current $i = 3$ (profiles are marked with a solid line). All the lines and point are obtained with the help of the computer program; the text is typed in the graphic editor by one of the authors. The image is an "action" image: Now it allows to observe only current contact position of reference points in motion.

Figure 11 demonstrates the rack profile obtained for the meshing line in the form of an arc of a circle. Red lines correspond to normal lines to profile. In a contact point, the normal line passes through the pitch point—it represents the accuracy of obtained formulae and algorithms.

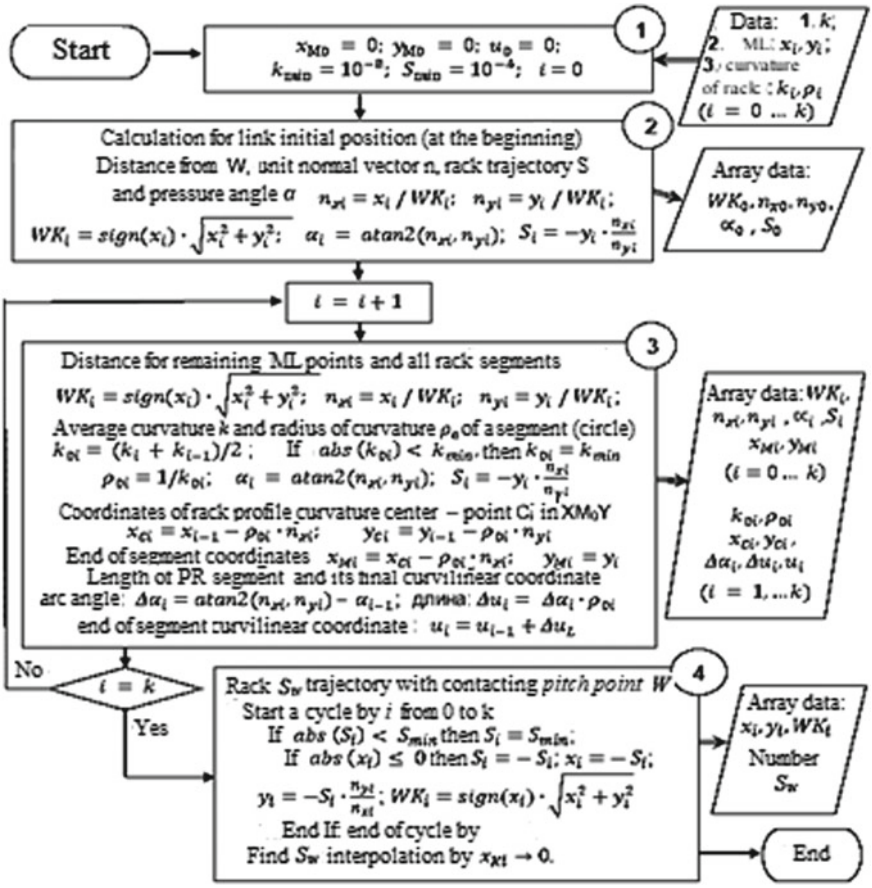


**Fig. 9** Algorithm for calculating generating rack profile

Figure 12 shows the fragment of three gearings made for ML in the form of an arc of a circle. Figure 12 is obtained with the help of the program used for Fig. 10.

Figure 13 represents the rack (Figs. 11, 12) profile radii of curvature diagram.

Further planes include setting ML in the form of an involute section and determining rack, pinion, and gearwheel teeth profiles.

## 5 Assessment of the Developed Calculation Methods and Algorithms Accuracy

Calculation accuracy of rack profile coordinates depends on real rack profile approximation errors; the approximation is realized by the set of arcs. Teeth profiles opti-

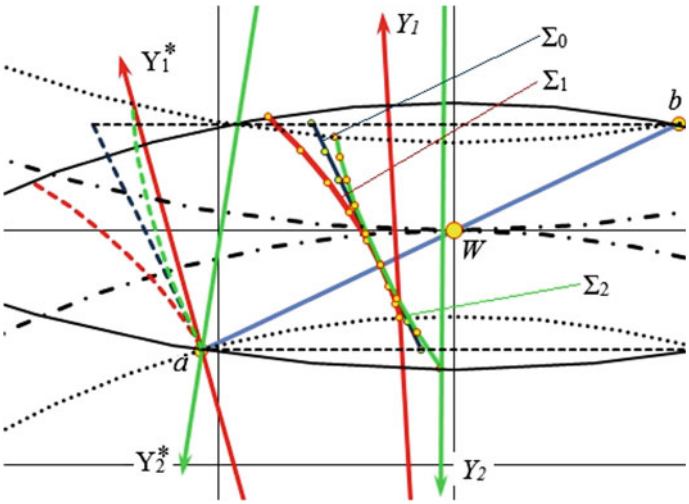


**Fig. 10** Gear conjugated profiles, in which ML is a line segment passing through a pitch point

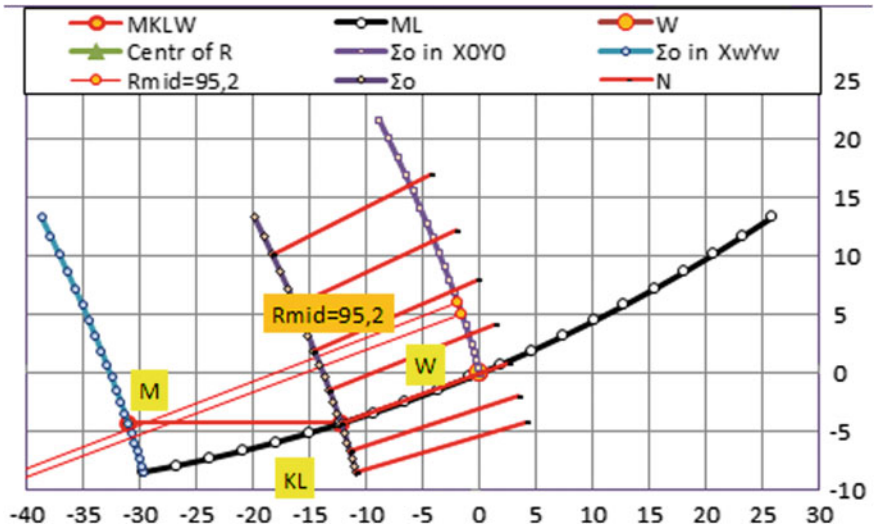


**Fig. 11** Rack profiles with normals

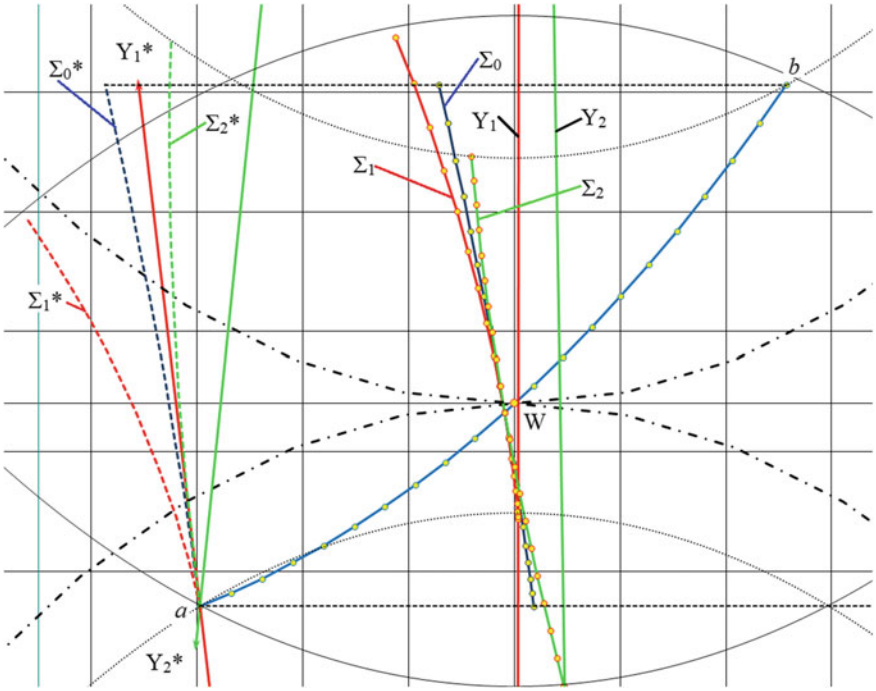


**Fig. 12** Gear conjugated profiles, in which ML is a line segment passing through a pitch point

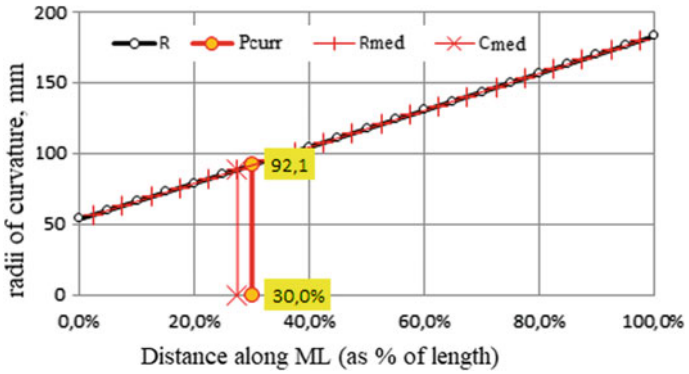


**Fig. 13** Rack profile radii of curvature

mization synthesis requires iterations. On this account, it is recommended to pick a small number of points on ML. Computational errors at ML $\Sigma$ reference points are almost equal to zero ($\approx 10^{-15}$)—the method is theoretically accurate. Computational errors between reference points require further investigation to pick a minimal number of reference points that ensure acceptable calculation accuracy on a reasonable basis.

## 6 Conclusion

1. The theory and method for *all types of cylindrical gears* that allow direct determining (without necessity to solve trigonometric and algebraic equations) conjugated profiles and its any local quality indicators are developed.
2. Research mathematical models, algorithms, and computer programs are developed. The conducted calculations prove the efficiency of the methods and demonstrate perspectives of gears analysis and synthesis *oriented on primarily ML setting instead of* setting curve type of wheel teeth or shaping edges of the cutting tool *profiles*.
3. The development of the new method of gears design make a certain contribution in the meshing theory (MT) that consists of:

- Development of an effective method for addressing the new basic MT problem—*determination of teeth profiles* $\Sigma_1$ *u* $\Sigma_2$ *according to the parameters of a known meshing line* $\Sigma$;
- Development of universal optimization *design system for cylindrical gears of various types and purposes* that is based on optimal meshing lines determination.

**Acknowledgements** This work was supported by grant (project N9.6355.2017/БЧ) of government order of Ministry of education and science of Russia Federation for the period 2017–2019 in Industrial University of Tyumen.

## References

1. Babichev D, Storchak M (2015) Synthesis of cylindrical gears with optimum rolling fatigue strength. Production Engineering. Res Develop 9(1), Springer, pp. 87–97 ISSN 0944-6524
2. Babichev DT, Lebedev SY, Babichev DA (2018) Fundamentals of the design of cylindrical gears during the initial synthesis of the optimal gearing line in the end section. Mod Eng Sci Educ, pp 681–692 (in Russian)
3. Lytvyn FL (1968) Theory of gearing. Science 584 (in Russian)
4. Babichev DT (2017) The main tasks of the classical theory of gearing and the problem of the optimization synth:esis of tooth profiles, 20(2): 71–74 (in Russian)
5. Pavlov AI (2005) The modern theory of gearing, (in Russian)
6. Shishov VP, Nosko PL, Fil PV (2006) The theoretical basis of the synthesis of gearing, p 408 (in Russian)

7. Evgrafov A, Khisamov A, Egorova O (2014) Experience of modernization of the curriculum TMM in St. Petersburg state polytechnical university. Mech Mach Sci 19: 239–247 https://doi.org/10.1007/978-3-319-01836-2_26 (in Russian)
8. Egorova O, Evgrafov A, Rayushkina V (2014) Modern view on "History of science" teaching at technical universities. Mech Mach Sci 19: 137–144. https://doi.org/10.1007/978-3-319-01836-2_15 (in Russian)
9. Semenov YA, Semenova NS (2017) Analysis of machine tool installation on the base. Lecture notes in mechanical engineering, pp 105–114. https://doi.org/10.1007/978-3-319-53363-6_11 (in Russian)
10. Evgrafov AN, Petrov GN (2017) Computer simulation of mechanisms. Lecture notes in mechanical engineering, pp 45–56. https://doi.org/10.1007/978-3-319-53363-6_6
11. Didikov R, Dobretsov R, Galyshev Y (2018) Power Distribution Control in the Transmission of the Perspective Wheeled Tractor with Automated Gearbox. Adv Intell Syst Comput 692:192–200. https://doi.org/10.1007/978-3-319-70987-1_21
12. Vetyukov Y, Oborin E, Krommer M, Eliseev V (2017) Transient modelling of flexible belt drive dynamics using the equations of a deformable string with discontinuities. Math Comput Modell Dyn Syst 23(1):40–54. https://doi.org/10.1080/13873954.2016.123228
13. Borina A, Tereshin V (2017) Stability of walking algorithms. Lecture notes in mechanical engineering, pp 19–25. https://doi.org/10.1007/978-3-319-53363-6_3
14. Evgrafov AN,. Petrov GN (2016) Drive selection of multidirectional mechanism with excess inputs. Lecture notes in mechanical engineering, pp 31–37 https://doi.org/10.1007/978-3-319-29579-4_4
15. Evgrafov AN, Petrov GN (2013) Calculation of the geometric and kinematic parameters of a spatial leverage mechanism with excessive coupling. J Mach Manuf Reliab 42(3):179–183. https://doi.org/10.3103/S1052618813030035
16. Eliseev KV (2018) Contact forces between wheels and railway determining in dynamic analysis. Numerical simulation. Lecture notes in mechanical engineering, pp 61–70 https://doi.org/10.1007/978-3-319-72929-9_8
17. Borina A, Tereshin V (2016) Mathematical modelling of interaction of the biped dinamic walking robot with the ground. Lecture notes in mechanical engineering, pp 127–133 https://doi.org/10.1007/978-3-319-29579-4_13
18. Manzhula KP, Shlepetinskii AY (2016) Stress and strain concentration in weld-joint flaws. Russ Eng Res 36(9):722–726. https://doi.org/10.3103/S1068798X16090148
19. Babichev DT., Babichev DA, Lebedev SY (2018) Calculation of tooth profile radiuses of curvature into line of contact parameters. IOP Conf. Series: Mater Sci Eng (KOD 2018). 393: 681–692 http://iopscience.iop.org
20. Lebedev SY, Babichev DT (2018) Development of the program complex for analysis and optimization synthesis of cylindrical gears. Modern engineering: science and education, pp 710–719 (in Russian)
21. Babichev DT, Volkov AE (2015) The history of the development of the theory of gearing. Bul Sci Techn Develop 5(93): 25–42 www.vntr.ru (in Russian)
22. Babichev DT, Lagutin SA, Barmina NA (2016) Review of the works of the Russian school of theory and geometry of gearing. part 1. Sources of the theory of gearing and the period of its heyday in the years 1935–1975. Theory Mech Mach. 14(3) (31). (in Russian)
23. Babichev DT (2017) Theorems on linear and quadratic gearing equations and their solution. Mod Mech Eng Sci. Educ 80–90 (in Russian)
24. Babichev Dmitry T, Babichev Denis A, Lebedev Sergey Yu (2018) Concept of gear synthesis based on assignment of instant contact areas for loaded teeth. Int Rev Mech Eng (IREME) 12(5):420–429

25. Babichev DT, Lebedev SY, Babichev DA (2018) Theoretical fundamentals of spur and helical gear synthesis based on assignment of meshing lines at face section. Mech Eng Res Educ 4: IREME
26. Isai's K-K, Jürgen Z (2010) Contribution to the geometric synthesis of gears. Special Edition Publication series of the Georg Simon Ohm University Nuremberg, Vol. 46, p 45

# Modeling and Simulation of Dynamic Contact Atomic Force Microscope


**Mohammad Reza Bahrami and A. W. Buddimal Abeygunawardana**

**Abstract** The aim of this article is modeling of the atomic force microscope as a lumped parameter system in its dynamic contact mode of operation. The Derjaguin—Muller–Toporov (DMT) force is considered as the interaction of the cantilever tip with the sample surface, and it introduces the nonlinearity to the model. The frequency response equation of the model is obtained by the method of multiple scales. As the results, effects of the nonlinearity, amplitude of excitation, and the damping coefficient on the frequency response are investigated.

**Keywords** AFM · Modeling · Contact mode · Vibration · Lumped parameter model

## 1 Introduction

The atomic force microscope (AFM) [1] utilizes to amplify surface properties. With the help of the AFM, it is conceivable to scan an object surface topography with to a great degree high amplification; up to million *X*. By AFM, scanning of an object surface is done in three dimensions, *X*, *Y,* and *Z* directions. This feature, scanning in three dimensions, is one of the most significant properties of an AFM.

Figure 1 shows the schematic of a typical AFM which consists of:

- Microcantilever with a sharp tip,
- Piezoscanner,
- Photodetector,
- Control unit.

M. R. Bahrami (✉)
Innopolis University, Innopolis, Russia
e-mail: mo.bahrami@innopolis.ru

A. W. B. Abeygunawardana
Peter the Great Saint-Petersburg Polytechnic University, Saint-Petersburg, Russia
e-mail: awbuddimal@gmail.com



A. N. Evgrafov (ed.), *Advances in Mechanical Engineering*,
Lecture Notes in Mechanical Engineering,
https://doi.org/10.1007/978-3-030-11981-2_10

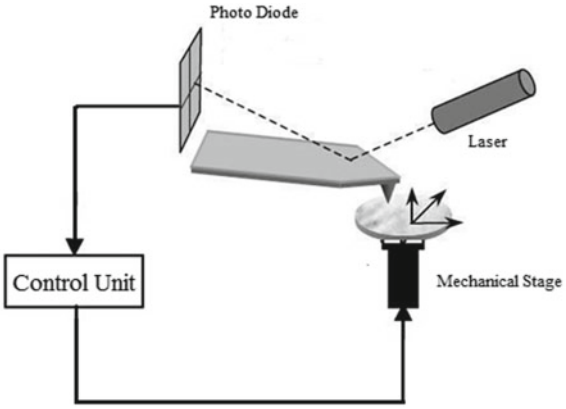


**Fig. 1** Schematic of a conventional AFM [2]

Three modes of working exist in which AFM works. These modes are namely: the contact, non-contact, and dynamic contact or tapping mode. Between the tip and sample, nonlinear forces exist which change the amplitude, phase, and frequency of oscillation. Comparing these changes in cantilever vibration with respect to the external excitation plays the key role to create a topography of the sample surface. Therefore, studying the dynamic behavior of the cantilever is a key role in a different mode of AFM operations [2].

A lot of books and articles [2–16] are devoted to obtain a mathematical model of dynamic systems, especially for the AFM in a different mode of operations by different methods.

In this paper, we consider the nonlinear vibration of AFM cantilever in the dynamic contact mode. In order to get the frequency response and analyze the problem, the method of multiple scales has been used.

## 2 Modeling of AFM Cantilever

For modeling the cantilever, in this article, the lumped parameter model of the cantilever has been used. This model consists of an effective mass $m_e$ at the end of a massless spring with the stiffness of $K$ and a massless damper with the coefficient $b$ (Fig. 2).

The equation of motion is known as

$$m_e \ddot{Z}(t) + \frac{m_e \omega_0}{Q} \dot{Z}(t) + K Z(t) = F_{\text{EXT}} - P(Z(t)) \tag{1}$$

In (1), the position of the cantilever tip is designated by $Z(t)$, the fundamental resonance frequency of the cantilever is designated by $\omega_0 = \sqrt{K / m_e}$, the quality factor is designated by $Q$, the external exciting force is $F_{\text{EXT}} = F_0 \cos(\Omega t)$, and

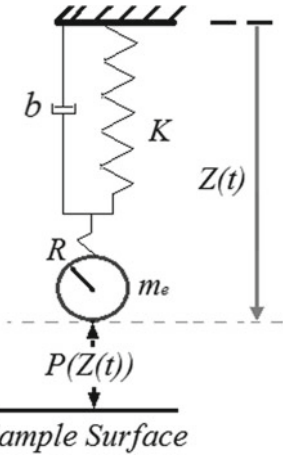


**Fig. 2** AFM lumped parameter model

$P(Z(t))$ is the force acting on the tip as the result of interaction between the tip and the sample surface. For the dynamic contact AFM, DMT sphere–plane interaction force is used as

$$F_{\mathrm{DMT}}(Z(t)) = -\frac{A_H R}{6a_0^2} + \frac{4}{3}E^*\sqrt{R}(a_0 - Z_0 + Z)^{3/2}, \tag{2}$$

where $A_H$, $R$, and $Z_0$ are the Hamaker constant, the tip apex radius, and the distance from the fixed base frame coordinate to the sample, respectively (Fig. 2).

Defining $A_0 = F_0/m_e$, and $b = 1/Q$, substituting (2) into (1), we get

$$\ddot{Z}(t) = A_0\cos(\Omega t) + \frac{A_H R}{6a_0^2 m_e} - \frac{4}{3}\frac{E^*\sqrt{R}}{m_e}(a_0 - Z_0 + Z)^{3/2} - b\omega_0\dot{Z}(t) - \omega_0^2 Z(t) \tag{3}$$

Setting

$$\zeta_1 = Z, \quad \zeta_2 = \dot{Z} \tag{4}$$

state-space form of Eq. (3) will be

$$\dot{\zeta}_1 = \zeta_2 \tag{5}$$

$$\dot{\zeta}_2 = A_0\cos(\Omega t) + \frac{A_H R}{6a_0^2 m_e} - \frac{4}{3}\frac{E^*\sqrt{R}}{m_e}(a_0 - Z_0 + \zeta_1)^{3/2} - b\omega_0\zeta_2 - \omega_0^2\zeta_1 \tag{6}$$

The equilibrium point of the unexcited system can be obtained by setting $\dot{\zeta}_1$, $\dot{\zeta}_2$, and $A_0$ to zero in Eqs. (5) and (6), from

$$\frac{A_H R}{6a_0^2 m_e} - \frac{4}{3}\frac{E^*\sqrt{R}}{m_e}(a_0 - Z_0 + Z_s)^{3/2} - \omega_0^2 Z_s = 0 \tag{7}$$

Introducing the dimensionless variables

$$x = \frac{Z}{Z_s} \tag{8}$$

$$\tau = \omega_0 t \tag{9}$$

$$p = \frac{A_0}{Z_s \omega^2} \tag{10}$$

$$\eta = \frac{a_0 - Z_0}{Z_s} \tag{11}$$

$$q = \frac{A_H R}{6a_0^2 m_e Z_s \omega_0^2} \tag{12}$$

$$w = \frac{E^*\sqrt{R}}{m_e \omega_0^2 Z_s^{1/3}} \tag{13}$$

and setting

$$\Omega = \omega_0 + \varepsilon\sigma \tag{14}$$

where $\sigma$ is a detuning parameter which describes the nearness of $\Omega$ to $\omega_0$ and $\varepsilon$ is a small parameter, the dimensionless equation of motion is obtained as

$$\frac{\mathrm{d}^2 x}{\mathrm{d}\tau^2} + b\frac{\mathrm{d}x}{\mathrm{d}\tau} + x = p\cos((1+\varepsilon\sigma)\tau) + q - w(\eta + x)^{3/2} \tag{15}$$

## 3 Method of multiple scales

Instead of a single variable to create uniformly valid approximate solutions for perturbation problems, one can write the response as a function of multiple independent variables. This is the principle of the method of multiple scales [9–12].

In order to utilize the method of multiple scales, it is needed to rewrite Eq. (15) as

$$\frac{\mathrm{d}^2 x}{\mathrm{d}\tau^2} + x = \varepsilon p\cos((1+\varepsilon\sigma)\tau) + \varepsilon\left[q - w(\eta + x)^{3/2} - b\frac{\mathrm{d}x}{\mathrm{d}\tau}\right] \tag{16}$$

In the method of multiple scales, the timescales are defined as

$$T_n = \varepsilon^n \tau, n = 0, 1, 2, \ldots \tag{17}$$

In the next step, we can express the derivatives with respect to $\tau$ in terms of the partial derivatives with respect to $T_n$, i.e.,

$$\begin{aligned} \frac{\mathrm{d}}{\mathrm{d}\tau} &= D_0 + \varepsilon D_1 + 2\varepsilon D_2 + \cdots \\ \frac{\mathrm{d}^2}{\mathrm{d}\tau^2} &= D_0^2 + 2\varepsilon D_1 D_0 + \varepsilon^2 (D_1^2 + 2D_0 D_2) + \cdots \end{aligned} \tag{18}$$

where

$$D_n = \frac{\partial}{\partial T_n} \tag{19}$$

An approximate solution of Eq. (16) is

$$x(t, \varepsilon) = x_0(T_0, T_1) + \varepsilon x_1(T_0, T_1) + O(\varepsilon^2) \tag{20}$$

From Eq. (16) considering that $T_0 = \tau$ and $T_1 = \varepsilon\tau$, the first term on the right-hand side of (16) is expressed in terms of $T_0$ and $T_1$ as

$$\varepsilon\zeta \cos(T_0 + \sigma T_1) \tag{21}$$

Using Maclaurin series expansion, the second term on the right-hand side of (16) is approximated.

Equating the coefficients of $\varepsilon^0$ and $\varepsilon^1$ on both sides of equation obtaining by substituting (18) and (20) into (16) yields

$$D_0^2 x_0 + x_0 = 0 \tag{22}$$

$$\begin{aligned} D_0^2 x_1 + 2D_0 D_1 x_0 + x_1 &= p\cos(T_0 + \sigma T_1) - bD_0 x_0 \\ &+ \cdots + q - w\eta^{3/2} - \frac{3}{2} w\eta^{1/2} x_0 - \frac{3}{8} w\eta^{-1/2} x_0^2 + \frac{3}{48} w\eta^{-3/2} x_0^3 \end{aligned} \tag{23}$$

The solution of (22) may be expressed as

$$x_0 = A(T_1)\exp(iT_0) + \overline{A}(T_1)\exp(-iT_0) \tag{24}$$

Substituting (24) into (23), we obtain

$$D_0^2 x_1 + x_1 = \exp(iT_0)\left\{\frac{1}{2} p\exp(\sigma T_1) - ibA(T_1)\right.$$

$$+\cdots+\frac{9}{48}w\eta^{-3/2}A(T_1)^2\overline{A}(T_1)-\frac{3}{2}w\eta^{1/2}A(T_1)-2iA'(T_1)\Big\}$$
$$+\cdots+\frac{3}{48}w\eta^{-3/2}A(T_1)^3\exp(3iT_0)+q$$
$$-w\eta^{3/2}-\frac{3}{8}w\eta^{-1/2}A(T_1)^2\exp(2iT_0)+cc \tag{25}$$

The complex conjugate of preceding terms in (25) showed by *cc*.
From the particular solution of (25), one can omit secular terms. It yields

$$\frac{1}{2}p\exp(\sigma T_1)-ibA(T_1)+\frac{9}{48}w\eta^{-3/2}A(T_1)^2\overline{A}(T_1)-\frac{3}{2}w\eta^{1/2}A(T_1)-2iA'(T_1)=0 \tag{26}$$

Writing $A(T_1)$ in the form of $A(T_1)=\frac{1}{2}a\exp(i\beta)$ where $a$ and $\beta$ are real variables, substituting into (26), and separating the real and imaginary parts, it yields

$$\frac{1}{2}p\sin(\sigma T_1)-\frac{1}{2}ab\cos(\beta)-a'\cos(\beta)$$
$$-\cdots-\frac{3}{4}w\eta^{1/2}a\sin(\beta)+\frac{a^3}{128}w\eta^{-3/2}\sin(\beta)+a\beta'\sin(\beta)=0 \tag{27}$$
$$\frac{1}{2}p\cos(\sigma T_1)+\frac{1}{2}ab\sin(\beta)+a'\sin(\beta)$$
$$-\cdots-\frac{3}{4}w\eta^{1/2}a\cos(\beta)+\frac{a^3}{128}w\eta^{-3/2}\cos(\beta)+a\beta'\cos(\beta)=0 \tag{28}$$

Solving (27) and (28) for $a'$ and $\beta'$, one obtains

$$a'=\frac{1}{2}p\sin(\sigma T_1-\beta)-\frac{1}{2}ab$$
$$\beta'=\frac{1}{128}\frac{96w\eta^2a+wa^3-32p\eta^{3/2}\cos(\sigma T_1-\beta)}{a\eta^{3/2}} \tag{29}$$

Introducing $\gamma=\sigma T_1-\beta$, (29) is rescaled as

$$a'=\frac{1}{2}p\sin(\gamma)-\frac{1}{2}ab$$
$$\gamma'=\sigma-\frac{1}{128}\frac{96w\eta^2a+wa^3-32p\eta^{3/2}\cos(\gamma)}{a\eta^{3/2}} \tag{30}$$

Setting $a'=\gamma'=0$ yields to

$$\sin(\gamma)=\frac{ab}{p}$$

$$\cos(\gamma) = -\frac{\frac{2}{9}a^3 + \frac{4}{27}\eta^2 a + \eta^4 a\sigma}{\frac{1}{2}p\eta^4} \tag{31}$$

Squaring and adding equations from (31) yields to

$$\frac{a^2b^2}{p^2} + \left(\frac{\frac{2}{9}a^3 + \frac{64}{3}\eta^2 a - \eta^{3/2}a\sigma}{4p\eta^{3/2}}\right)^2 = 1 \tag{32}$$

Equation (32), the frequency response equation, states the response amplitude as a function of the detuning parameter, the amplitude of excitation, and the tip-sample distance. From (32), we can find $\sigma$

$$\sigma = \frac{2}{9}\frac{\eta^{3/2}a^3 + 96\eta^{7/2}a \pm 18\sqrt{\eta^6(p^2 - a^2b^2)}}{\eta^{3/2}a} \tag{33}$$

## 4 Results

The effect of the nonlinearity, amplitude of excitation, and damping on the behavior of the cantilever can be investigated through Eq. (33).

The linear and nonlinear response graphs are compared, shown in Fig. 3. By setting $\eta = 5$ in (33), the linear response occurs. As illustrated in Fig. 3, the amplitude peak is independent of the value of $\eta$. In the linear case, the response graph is symmetric but in the nonlinear cases depending on the sign of $\eta$, the graph bends to the right or left.

The influence of the excitation amplitude on the frequency response is shown in Fig. 4. Increase in the excitation amplitude leads to the growth of the bending and the peak of the amplitude of the response.

Figure 5 indicates the effect of the damping coefficient on the frequency response. As it is expected by decreasing the damping coefficient, the peak increases, and of course in the absence of damping, the amplitude of the response goes to infinity.

As mentioned above, multivalued areas are formed because of the effect of nonlinearity on the frequency response. The multivaluedness of response yields to jump phenomenon [8, 9] as shown in Fig. 6 by arrows. By increasing the excitation frequency, i.e., $\sigma$, the amplitude of response varies very slowly until it reaches to the point 1 on the curve. Because of a further increase in $\sigma$, a jump occurs from point 1 to point 2. Then, the amplitude decreases through the curve by increasing the value of $\sigma$. If $\sigma$ slowly decreases from the right-hand side of the curve, the amplitude increases until point 3 on the curve, then a jump takes place from point 3 to point 4.

In summary, by increasing the excitation frequency, the amplitude of the response would jump to a higher amplitude, and by decreasing the excitation frequency, the amplitude of the response would jump to a lower amplitude. In nonlinear systems with soft springs, such a well-known phenomenon often occurs [9, 13].

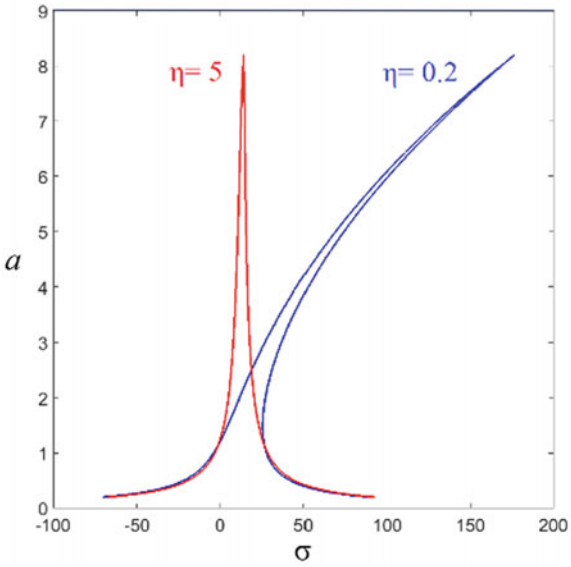


**Fig. 3** Linear and nonlinear response graphs

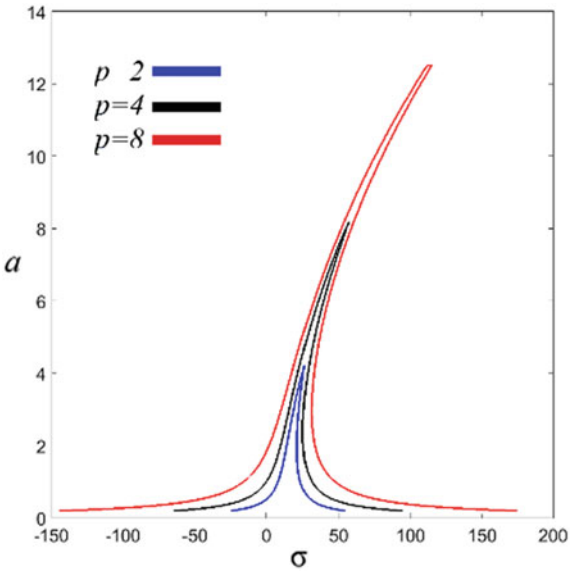


**Fig. 4** Amplitude of excitation vs frequency response

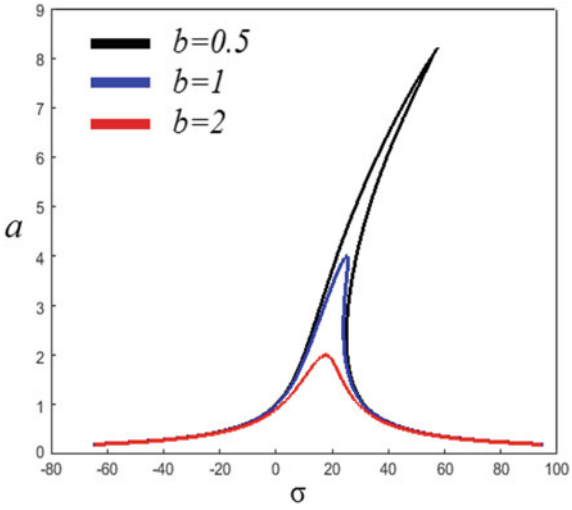


**Fig. 5** Effect of the damping on the frequency response graphs

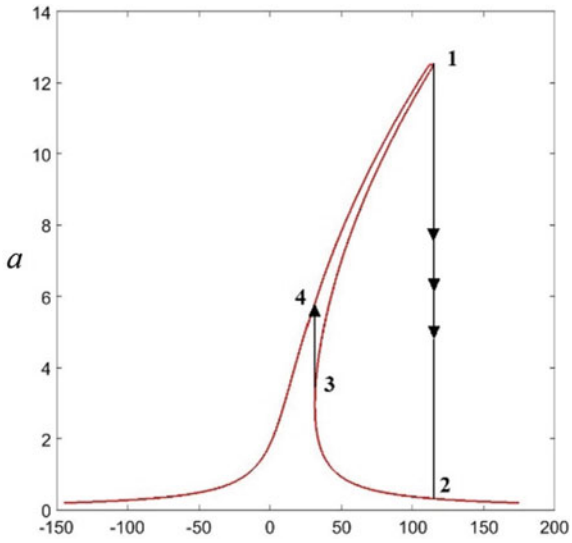


**Fig. 6** Jump phenomenon

## 5 Conclusion

In this paper, the atomic force microscope in the dynamic contact operation mode has been studied. The lumped parameter model has been used. The DMT force is considered as the tip-sample interaction, which makes the model nonlinear. The method of multiple scales is used to obtain the frequency response equation. As the results, the effects of the nonlinearity, amplitude of excitation, damping coefficient, on the frequency response are studied.

## References


1. Binnig G, Quate CF, Geber Ch (1986) Atomic Force Microscope Phys Rev Lett 56(9):930
2. Bahrami MR, Ramezani A, Osgouie K (2010) Modeling and simulation of non-contact atomic force microscope. In: Proceedings of the ASME 2010 10th conference on engineering system design and analysis, ESDA 2010. Vol. 5. pp 565–569
3. Materassi D, Basso M, Genesio R (2004) Frequency analysis of atomic force microscopes with repulsive-attractive interaction potentials. In: Proceedings of IEEE conference on decision and control. pp 3059–3061
4. Sebastian A, Salapaka MV, Chen DJ, Cleveland JP (2003) Harmonic analysis based modeling of tapping-mode AFM. In: Proceedings of American control conference. pp 232–236
5. Wang L (1998) Analytical descriptions of the tapping-mode atomic force microscopy response. Appl Phys Lett 73(25):3781–3783
6. Gauthier M, Tsukada M (2000) Damping mechanism in dynamic force microscopy. Phys Rev Lett 85(25):5348–5351
7. Belikov S, Magonov S (2009) Classification of dynamic atomic force microscopy control modes based on asymptotic nonlinear mechanics. In: Proceedings of American control conference. pp 979–984
8. Bahrami MR, Abeygunavardana VB (2018) Modeling and simulation of atomic force microscope through bond graph. Lecture notes mechanical engineering: advances in mechanical engineering, pp 9–15. Springer ISBN: 978-3-319-72928-2. 2018. PartF5
9. Nayfeh, AH, Mook DT (1995) Nonlinear oscillations, pp. 161–224. A Wiley-Interscience publication, New York
10. Bender CM, Orszag SA (1999) Advanced mathematical methods for scientists and engineers, pp 544–568. Springer
11. Kevorkian J, Cole JD (1996) Multiple scale and singular perturbation methods, Springer
12. Evgrafov AN, Petrov GN (2017) Computer simulation of mechanisms. Lecture notes in mechanical engineering. pp 45–56
13. Manzhula KP, Naumov AV (2017) Influence of flections' radius value to local buckling of box-shaped beams with non-linear walls. Int Rev Mech Eng 11(5):326–331
14. Egorova OV, Shcherbinin DY (2015) 3D documents in the field of history of science and technology. In: 2015 IFToMM World Congress Proceedings, IFToMM
15. Eliseev KV (2018) Contact forces between wheels and railway determining in dynamic analysis. Numerical simulation. Lecture Notes in Mechanical Engineering pp. 61–70. PartF5
16. Eliseev VV (2006) Mechanics of a deformable solid. p 231. Publishing house Polytechnic University

# Analysis of the Self-braking Effect of Linkage Mechanisms


**Alexander N. Evgrafov, Vladimir I. Karazin and Gennady N. Petrov**

**Abstract** When structural groups of linkage mechanisms approach singular positions, a self-braking effect may occur due to friction forces. By the example of structural groups with revolute kinematic pairs, conditions that ensure the absence of such undesirable effects are shown. The concept of a structural group with equivalent ideal kinematic pairs is introduced. Getting such a group into a singular position indicates the occurrence of the self-braking effect.

**Keywords** Structural group · Assur group · Mechanism · Self-braking · De-braking · Equivalent ideal kinematic pair · Friction

## 1 Introduction

In some cases, friction forces cause such a phenomenon as self-braking, when movement is impossible under any forces. Researchers study this effect in order to either avoid it or use it in a rational way. For example, paper [1] proposes to use the self-braking mode to determine mechanical losses during bench tests of the mechanical part of a hydraulic transmission. Paper [2] discusses advanced driver assistance systems (ADAS) using the self-braking system. Paper [3] presents the results of designing, implementing, and testing self-braking piezo-drive mechanisms. Paper [4] considers a method for calculating and analyzing the electromagnetic holding forces of self-braking electric motors. Paper [5] shows that the traction efficiency of a self-braking drive is two times higher than of a drive with a self-braking worm transmission. A miniature mechanism for robotic applications using the self-braking

A. N. Evgrafov (✉) · V. I. Karazin · G. N. Petrov
Peter the Great Saint-Petersburg Polytechnic University, St.-Petersburg, Russia
e-mail: a.evgrafov@spbstu.ru

V. I. Karazin
e-mail: visv05@mail.ru

G. N. Petrov
e-mail: gnpet@mail.ru



A. N. Evgrafov (ed.), *Advances in Mechanical Engineering*,
Lecture Notes in Mechanical Engineering,
https://doi.org/10.1007/978-3-030-11981-2_11

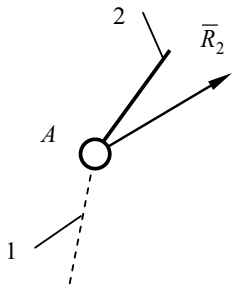


**Fig. 1** Model of an ideal *RKP*

effect is considered in paper [6]. Paper [7] studies the dynamics of a space robot manipulator using various friction models: Coulomb friction, LuGre friction, Wojewoda friction, and a hybrid model of friction. The influence of the size of the gap, the static friction coefficient, and the coefficient of sliding friction on the dynamics of the manipulator are also analyzed. Paper [8] considers the dynamic behavior of a slider-crank mechanism with a gap in one or two joints. The general theory of the motion of mechanical systems with Coulomb friction is considered in book [9]. Papers [10, 11] show computer 3D models of mechanisms of various types. Many papers present computer models of the behavior of linkage mechanisms: actuator mechanism of an excavator [12], mechanisms with redundant links [13], and redundant inputs [14]. The conditions for the occurrence of self-braking and de-braking modes for one of the Assur groups are considered in paper [15].

This paper studies the conditions under which a mechanism in certain positions enters the self-braking mode, when the reactions in kinematic pairs do not give the possibility to make program motion, i.e., the mechanism becomes "wedged." Let us consider the models of a revolute kinematic pair (RKP) without taking into account friction forces and with it.

## 2 Model of a Revolute Kinematic Pair (RKP)

We will consider planar mechanisms and reactions that occur in the plain of motion of the links. Figure 1 shows an RKP with the axis of relative rotation at point $A$, connecting links 1 and 2. Overall reaction $\bar{R}_2$, acting on the second link from the side of the first one in an ideal RKP passes through point $A$:

$$\bar{R}_2 = -\left(\bar{\Phi}_2 + \bar{P}_2^a + \bar{R}_2^e\right) = -\bar{P}_2, \tag{1}$$

where $\bar{\Phi}_2$, $\bar{P}_2^a$, $\bar{R}_2^e$ are main vectors of inertia forces, active forces, and external reactions, acting on the second link; $\bar{P}_2$ is the total force.

When allowing for friction forces, we consider that a moment occurs (Fig. 2a):

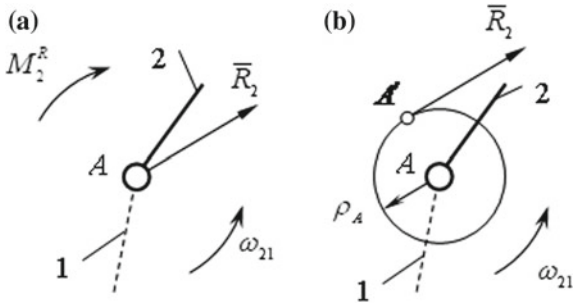


**Fig. 2** Model of a non-ideal *RKP* **a** moment of friction and **b** friction circle radius

$$M_2^R = -\varepsilon^V \rho_A R_2 = -\left(M_2^\Phi + M_2^a + M_2^e\right) = -M_2, \tag{2}$$

where $\varepsilon^V = sign\omega_{21} = \pm 1$ is the sign of the angular velocity of the second link relative to the first one; $\rho_A$ is the friction circle radius;

$R_2 = \left|\bar{R}_2\right|$ is the modulus of reaction $\bar{R}_2$;

$M_2^\Phi$, $M_2^a$, $M_2^e$ are moments of active forces and external reactions acting on the second link;

$M_2$ is the total moment relative to point $A$.

In statics (in the absence of the relative motion in the links, connected by the RKP), the moment strength is in the range

$0 \le \left|M_{2S}^R\right| < \left|M_2^R\right|$.

It is possible to present the overall reaction in a non-ideal RKP as a tangent to a $\rho_A$ radius circumference (Fig. 2b).

Similarly, with the equivalent mechanism in which the links carry out the same movements as in the original one at a given time, the term "equivalent ideal kinematic pair" (EIKP) can be introduced. In this ideal kinematic pair, the same reactions will occur as in the original KP with allowance for the friction forces. It is obvious that in our case, the axis of the EIKP is located at (•) $A'$ (Fig. 2b), since overall reaction $\bar{R}_2$ should pass through the axis of relative rotation of the IKP. Many such EIKPs are inside the friction circle in the absence of the relative motion of the links or on the circumference of radius $\rho_A$ with $\omega_{21} \neq 0$.

## 3 One-Bar One-Degree-of-Freedom Structural Group

Let us consider a structural group consisting of crank 1 attached to the rack of the active RKP. In an ideal RKP, similar to (1), a reaction emerges from the side of the rack to the crank and the driving moment (Fig. 3a):

$\bar{R}_1 = -\bar{P}_1$, $Q = -M_1$,where $\bar{P}_1$, $M_1$ are total force and moment (except for the driving moment) relative to (•) O, acting on the crank.

When taking into account friction forces in this structural group (Fig. 3b), the driving moment is the only element that will be changed by the value of the moment of friction (2):

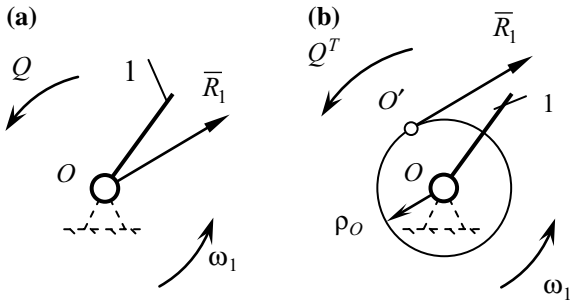


**Fig. 3** Crank ($Q$—driving moment) **a** ideal RKP and **b** determination of the equivalent ideal RKP taking friction into account

$$Q^T = Q - M_1^R = Q + \varepsilon^V \rho_O R_1.$$

With $\omega_1 \neq 0$, the center of the EIKP will be located at (•) $O'$. In statics ($\omega_1 = 0$), it is located on line $O\,O'$ inside the friction circle.

In such a model, there is no self-braking effect.

Let us substitute driving moment Q with driving force $\bar{P}$ which acts on the crank at the distance $h$ (Fig. 4). Let us introduce a system of coordinates, directing axis x in the direction of positive force $\bar{P}$. Let us denote with $\alpha$ the angle between axis $x$ and reaction $\bar{R}_1$ in the ideal RKP. Let us determine addition to the driving force $\Delta\bar{P}$ and reaction $\bar{R}_1^T$ in the RKP allowing for the friction forces:

$$\begin{cases} \bar{R}_1^T = \bar{R}_1 - \Delta\bar{P} \\ h \cdot \Delta P = \varepsilon^V \rho_O R_1^T \end{cases}$$

where

$R_1^T = \left|\bar{R}_1^T\right|$, $\Delta P = \varepsilon^V \left|\Delta\bar{P}\right|$.

It is worth noting that $\text{sign}(\Delta P) = \varepsilon^V$, which means $\Delta P > 0$ with $\omega_1 > 0$ and $\Delta P < 0$ with $\omega_1 < 0$. In the projections on the axis, we obtain the following system of equations:

$$\begin{cases} R_{1X}^T = R_1 \cos\alpha - \Delta P \\ R_{1Y}^T = R_1 \sin\alpha \\ h \cdot \Delta P = \varepsilon^V \rho_O R_1^T. \end{cases} \tag{3}$$

Let us square the third equation of system (3) and substitute $R_1^T$ from the first two equations into it:

$(h \cdot \Delta P)^2 = \rho_O^2 \left(R_1^2 + \Delta P^2 - 2R_1 \cdot \Delta P \cdot \cos\alpha\right)$.

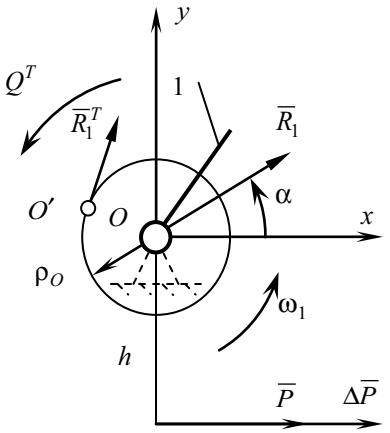


**Fig. 4** Crank ($Q$—driving force), determination of the equivalent ideal RKP with allowance for friction

Denoting $\mu = \Delta P / R_1$, $\lambda = h / \rho_O$, it is possible to obtain the equation to determine $\mu$:

$$\mu^2(\lambda^2 - 1) + 2\mu\cos\alpha - 1 = 0. \tag{4}$$

Roots of the equation

$$\mu_{1,2} = \frac{-\cos\alpha \pm \sqrt{\cos^2\alpha + \lambda^2 - 1}}{\lambda^2 - 1} = \frac{-\cos\alpha \pm \sqrt{\lambda^2 - \sin^2\alpha}}{\lambda^2 - 1}$$

with $\varepsilon^V = 1$ (counterclockwise rotation of the crank).

In this case, $\Delta P > 0$, $\mu > 0$. Let us determine the solution to Eq. (4) for different values of $\lambda$.

$\lambda > 1$, we obtain the only positive solution$\mu = \frac{-\cos\alpha + \sqrt{\lambda^2 - \sin^2\alpha}}{\lambda^2 - 1} > 0$.

$\lambda < |\sin\alpha|$, the self-braking mode occurs since there are no valid solutions.

$|\sin\alpha| \le \lambda < 1$, the real roots of $\mu_{1,2}$ have the same sign; therefore, both the self-braking mode ($\mu_{1,2} < 0$) and the de-braking mode are possible ($\mu_{1,2} > 0$).

The main conclusion is that the de-braking and self-braking modes are only possible when $\lambda \le 1$, that is, when the line of action of the driving force crosses the friction circle.

Now, let us consider the Assur group with three revolute kinematic pairs.

## 4 Assur Group RRR

For dyad RRR (Fig. 5a), in the case of ideal kinematic pairs, the reactions in joints $A$, $B$, $C$ may tend to infinity when approaching a singular position (Fig. 5b), when

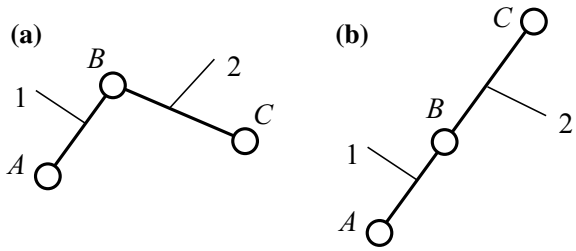


**Fig. 5** Assur group RRR **a** current position and **b** singular position

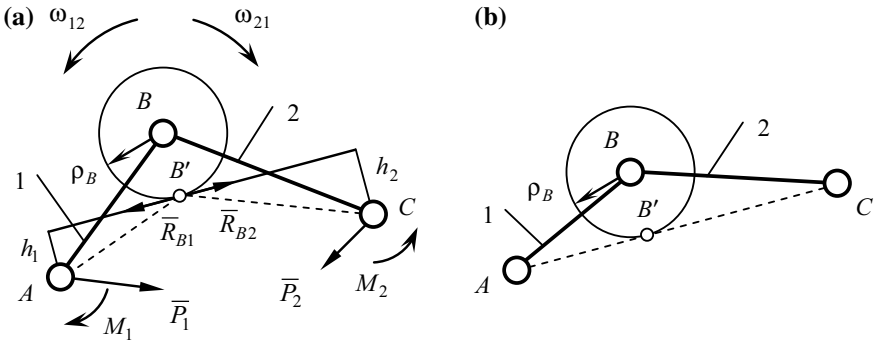


**Fig. 6** Taking into account the friction in joint B of group BBB **a** current position and **b** self-braking mode

three joints are in one line. Allowing for the friction forces in central joint $B$, it is feasible to determine in which position of the group the self-braking mode can occur.

Let the links be acted upon by total forces $\bar{P}_1$ , $\bar{P}_2$ and moments $M_1$ , $M_2$ relative to points $A$ and $C$, respectively. For definiteness, let $M_1 < 0$ and $M_2 > 0$. The angular velocity of the first link relative to the second one $\omega_{12} > 0$. In this case (as shown in Fig. 6a), the reaction in internal joint B acting on the first link $\left(\bar{R}_{B1}\right)$ creates a positive moment relative to (•) $A$ and a negative moment relative to (•) $B$. Reaction $\bar{R}_{B2} = -\bar{R}_{B1}$ acting on the second link creates a negative moment relative to (•) $C$ and a positive one relative to (•) $B$. The line of action of the reaction in joint B should be tangent to a $\rho_B$ radius circumference, and the distances from points $A$ and $C$ to this line are inversely proportional to moments $|M_1|$ and $|M_2|$:

$$\frac{h_1}{h_2} = \frac{|M_2|}{|M_1|}.$$

The value of the internal reaction is determined from the expression:

$$R_{B1} = R_{B2} = \frac{|M_1|}{h_1} = \frac{|M_2|}{h_2}.$$

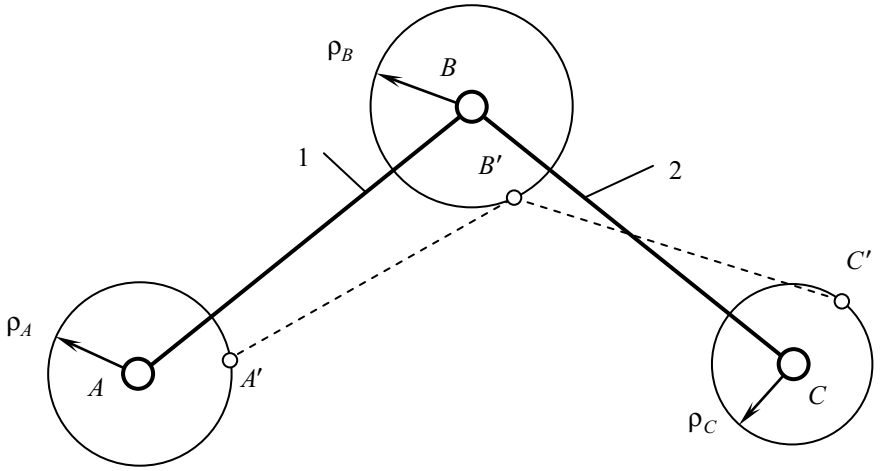


**Fig. 7** Determination of equivalent IKPs for dyad RRR

Point $B'$ corresponds to the equivalent IKP. This means that when considering dyad $AB'C$ with ideal kinematic pairs, we obtain the same reactions in the joints as in the original dyad with allowance for friction. When moments $M_1$, $M_2$ and the sign of relative angular velocity $\omega_{12}$ change, we have many equivalent IKP lying on the $\rho_B$ radius circumference. Obviously, if none of the dyads with equivalent IKPs is in a singular position, the reactions in joints $A$, $B$, and $C$ will be terminal. Figure 6b shows the position in which the equivalent IKP is located on line $AC$; therefore, the self-braking mode may occur.

Similar conclusions can be drawn when considering friction in all the RKPs (Fig. 7). If among the many dyads with equivalent IKPs $A'B'C'$, the centers of which lie on circumferences of radii $\rho_A$ , $\rho_B$ , $\rho_C$, it is impossible to find any dyad in the singular position, the self-braking mode cannot occur. In the case that there are equivalent IKPs $A'B'C'$, located on the same line on the circumferences of the friction circles or inside them, at certain values of the relative angular velocities in the joints and the loads on the links, the self-braking effect may occur (Fig. 8).

## 5 Conclusion

Judging by the above-stated issues, it can be concluded that in order to determine the presence or absence of the self-braking mode in structural groups, it is enough to determine the areas in which equivalent IKPs can be located.

If among many structural groups with equivalent IKPs there is at least one group in a singular position, the self-braking mode is possible, when the reactions emerging in the joints will not provide the desired movement of the links.

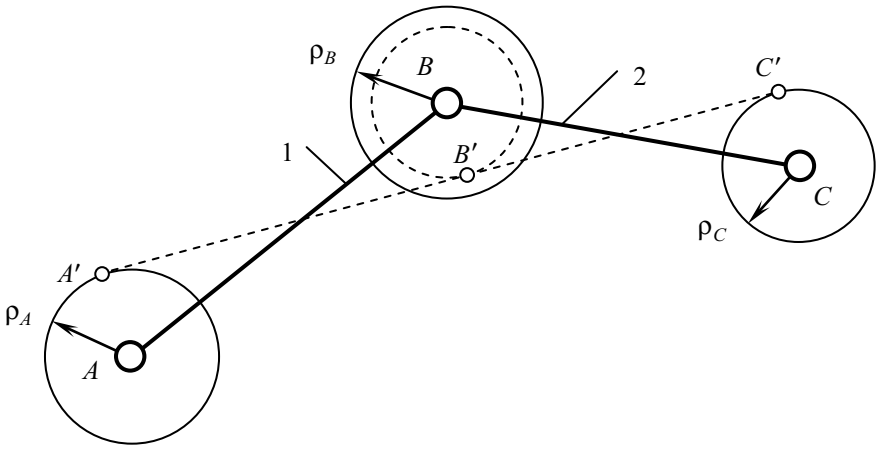


**Fig. 8** Self-braking mode for dyad RRR

## References


1. Bodnar B, Ochkasov O, Bobyr D, Korenyuk R, Bazaras Z (2018) Using the self-braking method when the post-overhaul diagnostics of diesel-hydraulic locomotives. In: 2018 Transport means-proceedings of the international conference 2008-October, pp 914–919
2. Mullett GJ (2017) Smart, connected, and autonomous automobiles—The impact on two-year college technical education. In: 2017 ASEE annual conference and exposition, conference proceedings. 2017-June
3. Navarro R, Elswijk E, Tromp N, Kragt J, Kroes G, Hanenburg H, de Haan M, Schuil M, Teuwen M, Janssen H, Venema L.: Precision mechanisms for optics in a vacuum cryogenic environment. In: 2017 Proceedings of SPIE—the international society for optical engineering
4. Burulko LK, Korolev VE (2016) Calculation and analysis of electromagnetic forces in a self-braking electric motors. In: Proceedings of International siberian conference on control and communications, SIBCON 2016
5. Kargin AP (2011) High-efficiency self-braking drive for hoists. Russ Eng Res 31(5): 451–453
6. Controzzi M, Cipriani C, Carrozza MC (2010) Development of self-braking nozzle for steel slab continuous casting process. Mech Mach Theory 45(10): 1395–1406
7. Xiang W, Yan S, Wu J (2018) Dynamic analysis of planar mechanical systems considering stick-slip and Stribeck effect in revolute clearance joints. Nonlinear Dyn
8. Tan H, Hu Y, Li L (2017) A continuous analysis method of planar rigid-body mechanical systems with two revolute clearance joints. Multibody Syst Dyn 40(4): 347–373
9. Anh LX (2003) Dynamics of mechanical systems with Coulomb friction. IV p 272, Springer
10. Evgrafov AN, Petrov GN (2017) Computer simulation of mechanisms. Lecture notes in mechanical engineering, pp 45–56. https://doi.org/10.1007/978-3-319-53363-6_6
11. Vukolov A, Egorova O (2015) New perspectives of real and virtual mechanisms models in theory of mechanisms and machines. In: 2015 IFToMM World Congress Proceedings, IFToMM 2015. https://doi.org/10.6567/iftomm.14th.wc.os7.006
12. Semenov YA, Semenova NS (2018) Features of calculating the working mechanism of an excavator. Lecture notes in mechanical engineering, pp 129–142. PartF5 https://doi.org/10.1007/978-3-319-72929-9_14
13. Evgrafov AN, Petrov GN (2013) Calculation of the geometric and kinematic parameters of a spatial leverage mechanism with excessive coupling J Mach Manuf Reliab 42(3): 179–183. https://doi.org/10.3103/s1052618813030035

14. Evgrafov AN, Petrov GN (2016) Drive selection of multidirectional mechanism with excess inputs (2016). Lecture notes in mechanical engineering, pp 31–37. https://doi.org/10.1007/978-3-319-29579-4_4
15. Evgrafov AN, Petrov GN (2018) Self-braking of planar linkage mechanisms (2018). Lecture notes in mechanical engineering, PartF5, pp 83–92

# To the Question of the Synthesis of Modifications Bennett's Mechanism

**Fanil F. Khabibullin, Ildar H. Saitov and Ilyas Z. Bagautdinov**

**Abstract** The dependences of the values of angular velocities and angular accelerations of the driven crank on the leading crank are investigated. The methods of synthesis of modifications of Bennett's mechanism according to the degree of nonuniformity of rotation of the driven crank, according to the positions of the driving and driven units are considered. Formulas are obtained that allow tracing the influence of the geometric parameters of the links of the mechanism on the kinematics of the cranks. The calculation results are displayed in the form of graphs.

**Keywords** Bennett's mechanism · Parallelogram · Antiparallelogram · Irregularity coefficient · Synthesis

## 1 Introduction

The study of the kinematic chains of a parallelogram and Bennett's antiparallelogram is considered on the example of two-moving high-performance disintegrator drives [1, 2]. The structural diagram and the photograph of the industrial disintegrator model are presented in Fig. 1.

The disintegrator drive mechanism consists of 1—leading crank, 2—connecting rod, 3—driven crank of Bennett's parallelogram, 4—internal cone, 5—leading crank, 6—connecting rod, 7—driven crank Bennett's antiparallelogram, and 8—external cone [3–5].

F. F. Khabibullin (✉) · I. H. Saitov
National Research Technical University Named After a.N. Tupolev—KAI, Kazan, Russia
e-mail: fanil_arsk@mail.ru

I. H. Saitov
e-mail: saitovildar@yandex.ru

I. Z. Bagautdinov
Research Laboratory of "Physical and Chemical Processes in Power Engineering" Kazan State Power Engineering University, Kazan, Russia
e-mail: ilyas_81992@mail.ru



A. N. Evgrafov (ed.), *Advances in Mechanical Engineering*,
Lecture Notes in Mechanical Engineering,
https://doi.org/10.1007/978-3-030-11981-2_12

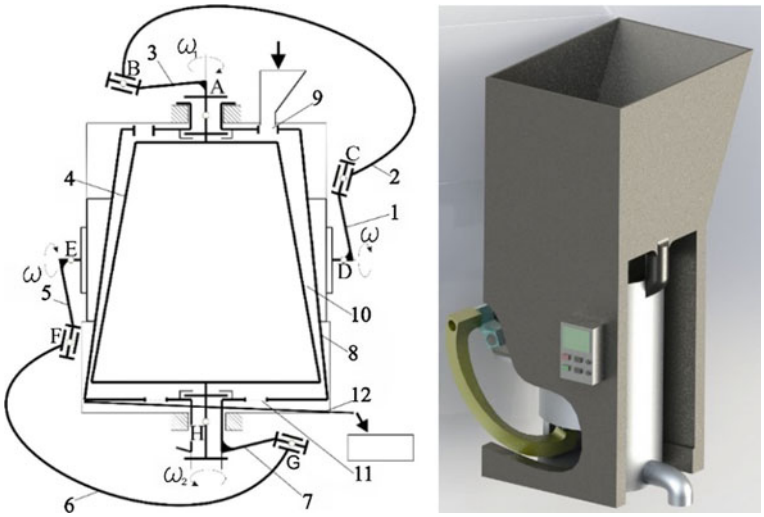


**Fig. 1** Structural diagram and a photograph of a model of an industrial disintegrator with drives based on Bennett's mechanisms

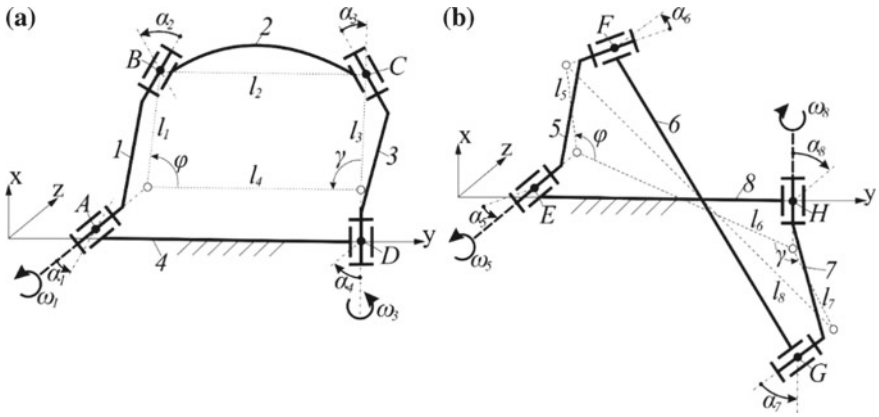


**Fig. 2** Closed kinematic chains: **a** Bennett's parallelogram; **b** Bennett's antiparallelogram

The purpose of research is to determine the dependence of the angle of rotation of the driven crank $\gamma$, the angular velocity $\omega_3$, and angular acceleration depending $\varepsilon_1$ on the angle of rotation, angular velocity, and angular acceleration of the driving crank and explore the methods of synthesis according to the provisions of the master and slave units, synthesis according to the degree of uneven rotation of the slave crank (see Fig. 2) [6, 7].

Figures 2a, b shows the structural diagrams of Bennett's parallelogram and Bennett's antiparallelogram, where $\alpha_1$, $\alpha_3$—the installation angles of the driving and

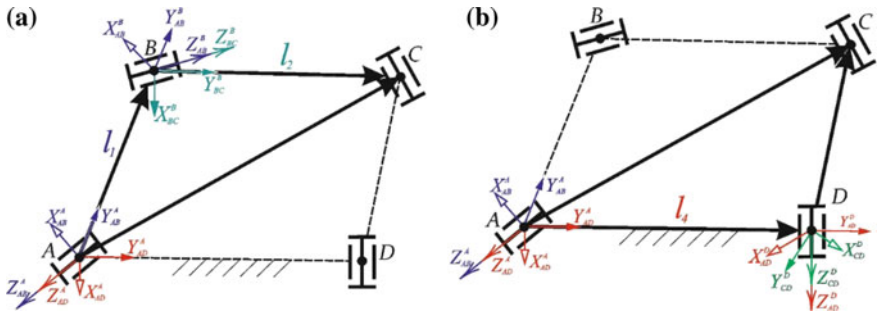


**Fig. 3** Structural diagram of Bennett parallelogram **a** vector contour ABCA, **b** vector contour ADCA

driven crank, $\alpha_2$, $\alpha_4$—the installation angles of the connecting rod and the frame, and $l_1$, $l_2$, $l_3$, $l_4$—theoretical lengths of the corresponding links.

## 2 The Study of the Kinematics of the Driven Crank

The structural diagram of Bennett's parallelogram in the form of the ABCDA contour is given in Fig. 3. The position of the driven crank (angle $\gamma$) is determined by the projections of the radius vector $AC$ of the axis $X^A_{AD}$, $Y^A_{AD}$, and $Z^A_{AD}$. The resulting vector contours ABCA and ADCA are considered separately before obtaining the equations of displacements in the projections on the coordinate axes [8, 9].

The ABCA contour is schematically represented in Fig. 3a, and from the ABCA vector contour, you can determine the value of the radius vector of the $AC$ by the equation:

$$\overline{AC} = \overline{AB} + \overline{BC}, \tag{1}$$

Equality (1) in projections on the $X$, $Y$, $Z$ axes is the following [9, 10]:

$$AC: \begin{cases} AC^X = AB \cdot K^{Y^A_{AB}}_{X^A_{AD}} + BC \cdot K^{Y^B_{BC}}_{X^A_{AD}} \\ AC^Y = AB \cdot K^{Y^A_{AB}}_{Y^A_{AD}} + BC \cdot K^{Y^B_{BC}}_{Y^A_{AD}} \\ AC^Z = AB \cdot K^{Y^A_{AB}}_{Z^A_{AD}} + BC \cdot K^{Y^B_{BC}}_{Z^A_{AD}}, \end{cases} \tag{2}$$

where $K^{Y^A_{AB}}_{X^A_{AD}}$ is the projection of the coordinate system $X^A_{AD}$ into the coordinate system $Y^A_{AB}$.

Using the transition matrices and taking into account the direction cosines, one can obtain the equation of displacement in projections onto three coordinate axes.

$$AC: \begin{cases} AC^X = AB \cdot (-\sin\varphi) + BC \cdot (-\cos\alpha_1 \cdot \cos\gamma \cdot \sin\varphi + \cos\gamma \cdot \sin\varphi) \\ AC^Y = AB \cdot (\cos\varphi) + BC \cdot (\cos\alpha_1 \cdot \sin\gamma \cdot \sin\varphi + \cos\gamma \cdot \sin\varphi) \\ AC^Z = AB \cdot (0) + BC(\sin\alpha_1 \cdot \sin\varphi) \end{cases} \tag{3}$$

Considering that $BC = AD = l_2$, $AB = DC = l_1$, you can get the following equation:

$$\begin{cases} AC^X = l_1 \cdot (-\sin\varphi) + l_2 \cdot (-\cos\alpha_1 \cdot \cos\gamma \cdot \sin\varphi + \cos\gamma \cdot \sin\varphi) \\ AC^Y = l_1 \cdot (\cos\varphi) + l_2 \cdot (\cos\alpha_1 \cdot \sin\gamma \cdot \sin\varphi + \cos\gamma \cdot \sin\varphi) \\ AC^Z = l_2 \cdot (\sin\alpha_1 \cdot \sin\varphi) \end{cases} \tag{4}$$

Vector contour ADCA is schematically represented in Fig. 3b, and from the vector contour, you can determine the value of the radius vector $AC$ by the equation [10, 11]:

$$\overline{AC} = \overline{AD} + \overline{DC}, \tag{5}$$

Equality in projections on the X, Y, Z axis

$$\begin{cases} AC^X = AD \cdot K^{Y^D_{AD}}_{X^A_{AD}} + CD \cdot K^{Y^D_{DC}}_{X^A_{AD}} \\ AC^Y = AD \cdot K^{Y^D_{AD}}_{Y^A_{AD}} + CD \cdot K^{Y^D_{DC}}_{Y^A_{AD}} \\ AC^Z = AD \cdot K^{Y^D_{AD}}_{Z^A_{AD}} + DC \cdot K^{Y^D_{DC}}_{Z^A_{AD}}, \end{cases} \tag{6}$$

Taking into account the direction cosines, one can obtain the equation of displacement in the coordinate axes $x$, $y$, $z$ of the projections of the vector radius.

$$AC: \begin{cases} AC^X = AD \cdot (0) + CD \cdot (\sin\gamma) \\ AC^Y = AD \cdot (1) + CD \cdot (\cos\gamma) \\ AC^Z = AD \cdot (0) + CD(0), \end{cases} \tag{7}$$

Given that $AB = DC = l_1$, $BC = AD = l_2$, we get:

$$AC: \begin{cases} AC^X = l_2 \cdot (\sin\gamma) \\ AC^Y = l_1 + l_2 \cdot (\cos\gamma) \\ AC^Z = 0, \end{cases} \tag{8}$$

The obtained Eqs. (4) and (8) represent the projection of vector contours on the coordinate axes, equating the right sides of Eqs. (4) and (8), we obtain:

$$\begin{cases} l_2 \cdot (\sin\gamma) = l_1 \cdot (-\sin\varphi) + l_2 \cdot (-\cos\alpha_1 \cdot \cos\gamma \cdot \sin\varphi + \cos\gamma \cdot \sin\varphi) \\ l_1 + l_2 \cdot (\cos\gamma) = l_1 \cdot (\cos\varphi) + l_2 \cdot (\cos\alpha_1 \cdot \sin\gamma \cdot \sin\varphi + \cos\gamma \cdot \sin\varphi) \\ 0 = l_2 \cdot (\sin\alpha_1 \cdot \sin\varphi), \end{cases} \quad (9)$$

Solving Eq. (9) for $\sin\gamma$ and $\cos\gamma$, you can get

$$\cos\gamma = \frac{l_1(\cos\varphi - \cos\alpha_1 \cdot \sin\varphi - 1)}{l_2 \cdot 1 + (\sin)^2 \cdot (\cos\alpha_1 - 1) - \sin\varphi}, \quad (10)$$

$$\sin\gamma = \frac{l_1(\cos\varphi - \cos\alpha_1 \cdot \sin\varphi - 1) \cdot \sin\varphi - \cos\alpha_1 - \sin\varphi \cdot 1 + (\sin)^2 \cdot (\cos\alpha_1 - 1) - \sin\varphi}{l_2 \cdot 1 + (\sin)^2 \cdot (\cos\alpha_1 - 1) - \sin\varphi} \quad (11)$$

In the Maple program, formula (11) is simplified and differentiated, and an equation is obtained to determine the angular velocity of the driven crank:

$$\omega_3 = \frac{-\omega_1 \cdot \cos\alpha_1}{1 - \sin\alpha_1 \cdot \cos\varphi}. \quad (12)$$

From Eq. (12), it can be seen that when $\omega_1 = \text{const}$, the angular speed of the driven crank $\omega_3$ is not a constant value, depending on the position of the driving crank. Analysis of Eq. (12) shows that $\omega_3$ reaches the maximum value in absolute value at 4 and the minimum value in absolute value at $\varphi = 180°$, has the form

$$\omega_{3\max} = \frac{\omega_1 \cdot \cos\alpha_1}{1 - \sin\alpha_1}, \omega_{3\min} = \frac{\omega_1 \cdot \cos\alpha_1}{1 + \sin\alpha_1}, \quad (13)$$

The coefficient of unevenness is determined by the formula

$$\delta = \frac{\omega_{3\max} - \omega_{3\min}}{(\omega_{3\max} + \omega_{3\min})/2}. \quad (14)$$

Differentiating by time, the expression (13) is obtained the angular acceleration of the driven crank

$$\varepsilon_3 = \frac{\omega_1^2 \cdot \sin\alpha_1 \cdot \cos\alpha_1 \cdot \sin\varphi}{(1 - \sin\alpha_1 \cdot \cos\varphi)^2}. \quad (15)$$

## 3 Synthesis According to the Provisions of the Master and Slave Units

Let the parameters of the frame $l_4$ and $\alpha_4$, as well as the position of the leading crank $\varphi$ and the driven cranks $\gamma$, be given, it is necessary to find the parameters $\alpha_1$ and $l_1$ considering that $l_1/l_2 = \sin\alpha_1/\sin\alpha_2$ is at $l_1 = l_3, \alpha_1 = \alpha_3, l_2 = l_4, \alpha_2 = \alpha_4$ [12, 13].

To determine the value of the installation angle of the leading crank $\alpha_1$, we make the equation of the weighted difference

$$\Delta q = (X_B - X_C)^2 + (Y_B - Y_C)^2 + (Z_B - Z_C)^2 - l_2^2 = 0 \tag{16}$$

Taking into account that

$$\begin{aligned} X_B &= AB \cdot K_{X_{AD}^A}^{Y_{AB}^A} = -l_1 \sin\varphi \\ Y_B &= AB \cdot K_{Y_{AD}^A}^{Y_{AB}^A} = l_1 \cos\varphi \\ Z_B &= AB \cdot K_{Z_{AD}^A}^{Y_{AB}^A} = 0 \end{aligned} \tag{17}$$

$$\begin{aligned} X_C &= X_{AD} \cdot K_{X_{AD}^A}^{Y_{AD}^D} + X_{DC} \cdot K_{X_{AD}^D}^{Y_{BC}^D} = -l_1 \cos\alpha_2 \sin\gamma \\ Y_C &= Y_{AD} \cdot K_{Y_{AD}^A}^{Y_{AD}^D} + Y_{DC} \cdot K_{Y_{AD}^D}^{Y_{BC}^D} = l_2 + l_1 \cos\gamma \\ Z_C &= Z_{AD} \cdot K_{Z_{AD}^A}^{Y_{AD}^D} + Z_{DC} \cdot K_{Z_{AD}^D}^{Y_{BC}^D} = -l_1 \sin\alpha_2 \sin\gamma \end{aligned} \tag{18}$$

Substituting (17) and (18) into Eq. (16), we obtain

$$\begin{aligned} q = {} & ((-l_1 \sin\varphi) + (l_1 \cos\alpha_2 \sin\gamma))^2 + ((l_1 \cos\varphi) - (l_2 + l_1 \cos\gamma))^2 \\ & + (l_1 \sin\alpha_2 \sin\gamma))^2 - l_2^2 = 0 \end{aligned} \tag{19}$$

Solve the equation for $l_1/l_2$

$$\begin{aligned} & \frac{l_1}{l_2}(1 - 2\sin\varphi\cos\alpha_2\sin\gamma + \cos\alpha_2^2\sin\gamma^2 - 2\cos\varphi\cos\gamma + \cos\gamma^2 + \sin\alpha_2^2\sin\gamma^2) \\ & = (2\cos\varphi - 2\cos\gamma) \end{aligned} \tag{20}$$

After transformations we get:

$$\frac{\sin\alpha_1}{\sin\alpha_2}(1 - \sin\varphi\cos\alpha_2\sin\gamma - \cos\varphi\cos\gamma) = \cos\varphi - \cos\gamma \tag{21}$$

Where do we get:

$$\alpha_1 = \arcsin\frac{(\cos\varphi + \cos\gamma)\cdot\sin\alpha_2}{1 - \sin\varphi\cos\alpha_2\sin\gamma - \cos\varphi\cos\gamma} \tag{22}$$

Based on the obtained Eq. (22), which allows synthesizing modifications of the Bennett mechanism according to the positions of the driving crank and driven cranks, graphs are obtained.

Figure 4a shows a graph of possible values of $\alpha_1$, $\alpha_2$ when $\varphi = 15°$, $\gamma_1 = 16°$, $\gamma_2 = 30°$, $\gamma_3 = 120°$, $\gamma_4 = 180°$, $\gamma_5 = 344°$. Figure 4b presents a graph of possible

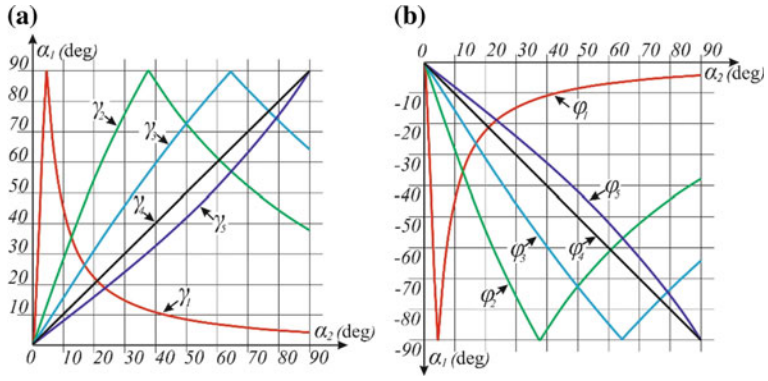


**Fig. 4** Graph of possible values $\alpha_1$, $\alpha_2$ **a** at $\varphi = 15°$, $\gamma = 16° \ldots 344°$; **b** at $\gamma = 15°$, $\varphi = 16° \ldots 344°$

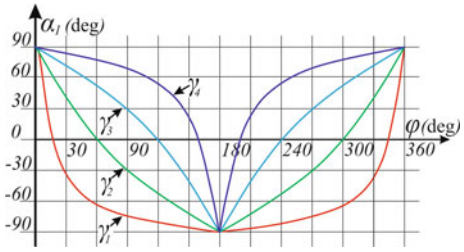


**Fig. 5** Graph of possible values of $\alpha_1$, $\varphi$ at $\alpha_2 = 90°$ and $\gamma = 15° \ldots 160°$

values of $\alpha_1$, $\alpha_2$ when $\gamma = 15°$, $\varphi_1 = 16°$, $\varphi_2 = 30°$, $\varphi_3 = 120°$, $\varphi_4 = 180°$, $\varphi_5 = 344°$.

Analysis of the graph shows that the convergence of the values of the initial positions of the leading crank $\varphi$ and slave $\gamma$ cranks leads to an increase in the difference of the values of the installation angles of the leading crank $\alpha_1$ (driven crank $\alpha_3$) and connecting rod $\alpha_2$ (frame $\alpha_4$) [14].

Thus, under condition $\varphi > \gamma$ and at $\varphi + \gamma > 360°$, the value of the installation angle of the driving crank $\alpha_1$ takes a positive value.

From the graph, it is seen that at $\alpha_1 = 90°$, the installation angle of the second link $\alpha_2$ takes some value (for example, at $\varphi = 30°$, $\alpha_1 = 90°$, therefore, $\alpha_2 = 37°$, 66°), after which the schedule starts to decrease when $\alpha_2 = 90°$, then $\alpha_1$ takes the same value ($\alpha_2 = 37°$, 66°).

Figure 5 shows a graph of possible values of $\alpha_1$, $\varphi$ at $\alpha_2 = 90°$ and $\gamma_1 = 15°$, $\gamma_2 = 60°$, $\gamma_3 = 120°$, $\gamma_4 = 160°$, and the data values of the angle of rotation of the leading crank $\gamma$ are selected to provide an overall picture of the relationship of the starting position of the leading crank depending on the installation angle of the first link and the third link.

From Fig. 5, it can be seen that the graph intersects with the axis of the angle of rotation of the driving crank $\varphi$ in precisely those values that are equal to the value of the angle of rotation of the driven crank $\gamma$.

Based on this, it can be said that increasing the value of the rotation angle of the driven crank $\gamma$ results in the installation angle of the leading crank and the driven crank with a positive sign, and therefore, $180° - \gamma = x$ is obtained, then $180° \pm x$, therefore, we get the installation angle of the leading crank and the driven crank negative sign $(-\alpha_1, -\alpha_3)$.

## 4 Synthesis According to the Degree of Uneven Rotation of the Driven Crank

Suppose that using the Bennett mechanism, it is required to transfer the rotation with a given degree of unevenness $\delta$ from the motor shaft to the working body, the geometric axes of which intersect at an angle of $\alpha_2(\alpha_4)$ and are separated from each other at a distance of $l_2(l_4)$, where it is necessary to find parameters $\alpha_1$ and $l_1$, considering that $l_1 = l_3$, $\alpha_1 = \alpha_3$, $l_2 = l_4$, $\alpha_2 = \alpha_4$ [15–17].

To do this, we use formula (14), taking into account that $(\omega_{3\max} + \omega_{3\min})/2 = +\omega_1$ for parallelogram and antiparallelogram $(\omega_{3\max} + \omega_{3\min})/2 = -\omega_1$, respectively, we get

$$\delta = \pm 2\frac{\sin\alpha_1 \sin\alpha_2}{\cos\alpha_2 - \cos\alpha_1} \tag{23}$$

After several transformations, Eq. (23) will have:

$$\cos\alpha_1 = \frac{\delta^2 \cos\alpha_2 \pm 2\sqrt{\delta^2 \sin^2\alpha_2 + 4\sin^4\alpha_2 - \sin^2\alpha_2\delta^2\cos^2\alpha_2}}{\delta^2 + 4\sin^2\alpha_2} \tag{24}$$

For convenience of calculations, we simplify Eq. (24), we get:

$$\cos\alpha_1 = \frac{\delta^2 \cos\alpha_2 \pm 2 \cdot \sin^2\alpha_2\sqrt{4 + \delta^2}}{\delta^2 + 4\sin^2\alpha_2} \tag{25}$$

Based on the obtained Eq. (25), we plotted the possible values of $\alpha_1, \alpha_2$ at $\delta = 0$, 5; $\delta = 1$; $\delta = 2$; $\delta = 3$ for the Bennett parallelogram (see Fig. 6a) and the Bennett antiparallelogram (see Fig. 6b).

Analysis of the graph shows that when synthesizing the Bennett parallelogram according to the degree of uneven rotation of the driven crank, it is necessary to take into account that the value of the installation angle of the first (third) link will be relatively larger compared to the installation angle of the second (fourth) link.

When analyzing the graphs, it is possible to determine the optimum installation angles of the cranks by the required values of the coefficients of the rotation non-uniformity. It can be said that the greatest non-uniformity for case $\delta = 3$ can be achieved under condition $\alpha_1 = \alpha_2 + 15° \ldots 30°$.

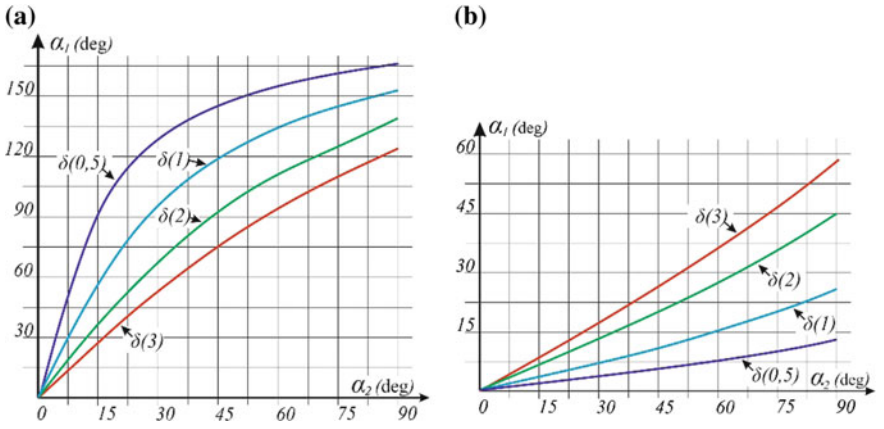


**Fig. 6** Graph of possible values of $\alpha_1$, $\alpha_2$ at $\delta = 0.5 \ldots 3$ for **a** Bennett's parallelogram, **b** for Bennett's antiparallelogram

From the graph, it can be seen that during the synthesis of the Bennett antiparallelogram by the degree of uneven rotation of the driven crank, it is necessary to take into account that the value of the installation angle of the second (fourth) link will be relatively larger compared to the installation angle of the first (third) link.

## 5 Conclusion

In practice, it is necessary to develop new mechanisms for existing devices in connection with a breakdown, lack of picking parts, and the emergence of new requirements for existing installations. The formulas obtained make it possible to synthesize modifications of the Bennett mechanism according to the positions of the links and according to the degree of irregularity of rotation of the driven crank. However, when synthesizing new mechanisms, the following features must be considered:

– With an increase in the values of the installation angles $\alpha_1(\alpha_3)$ and $\alpha_2(\alpha_4)$ to 90° and with their approach, the degree of unevenness of the rotation of the driven crank increases.
– With the same parameters of the installation angles of the links ($\alpha_1 = 45°$, $\alpha_2 = 30°$), the degree of non-uniformity of the antiparallelogram ($\delta = 2.224$) will be higher compared to the parallelogram ($\delta = 0.224$).

## References


1. Yarullin MG, Khabibullin FF (2017) Theoretical and practical conditions of Bennett mechanism workability. Lect Notes Mech Eng, 145–153
2. Borodin VM, Lustin AD, Khairov LS, Shcherbakov AV (2017) The six-link mechanism as a topological phenomenon of Mobius symmetry. In: Proceedings of Akademenergo, № 3, pp 79–87 (in Russian)
3. Lee CC, Herve JM (2014) Oblique circular torus, Villarceau circles, and four types of Bennett linkages. Proc IMechE, Part C J Mech Eng Sci. 228(4):742–752
4. Yarullin MG, Isyanov IR (2018) Structural study of a two-mobility five-link space mechanism with a double crank. Lect Notes Mech Eng 2018, PartF5, pp 187–194
5. Yarullin MG, Faizov MR (2018) Synthesis of spherical four-links rotational pairs in the solidworks program. Lect Notes Mech Eng 2018, PartF5, pp 177–185
6. Husty M, Pfurner M, Schrocker H-P, Brunnthaler K (2007) Algebraic methods in the analysis and synthesis. Robotica. Cambridge University Press, Cambridge, pp 661–675
7. Yarullin MG, Khabibullin FF (2017) Geometry of the kinematic chain and links of the Bennett mechanism. In: Modern mechanical engineering: science and education: Materials of the 6th International scientific-practical. conference. Ed. A.N. Evgrafova and A.A. Popovich. - SPb .: Publishing house of Polytechnic. Univ., pp 262–274 (in Russian)
8. Sakhapov RL, Nikolaeva RV, Gatiyatullin MH, Makhmutov MM (2017) Mathematical model of highways network optimization. J Phys Conf Ser 936(1):012032. https://doi.org/10.1088/1742-6596/936/1/012032
9. Fen H, Kang R, Chen Y (2016) Workspace analysis of a reconfigurable mechanism generated from the network of Bennett linkages. Mech Mach Sci 36:153–163
10. Gabsattarov RM, Konoplev YG, Sachenkov OA, Egorov SV, Lustin AD (2015) Defining relations of vibrations of vehicle suspension with the mass and rigidity design deviations. Int J Appl Eng Res 10(24):44629–44635
11. Ding H, Cao W, Chen Z (2015) Structural synthesis of two-layer and two-loop spatial mechanisms with coupling chains. Mech Mach Theor 92:289–313
12. Evgrafov AN, Petrov GN (2018) Self-braking of planar linkage mechanisms. Lecture Notes in Mechanical Engineering PartF5, pp 83–92
13. Sakhapov RL, Nikolaeva RV, Gatiyatullin MH, Makhmutov MM (2016) Modeling the dynamics of the chassis of construction machines. J Phys: Conf Ser 738(1):012119. https://doi.org/10.1088/1742-6596/738/1/012119
14. Guo H, Song X, Li L, Deng Z, Liu R, Geng J (2018) Type synthesis of deployable single-loop overconstrained linkages based on Bennett linkages. Mech Mach Theor 120:1–29
15. Evgrafov AN, Petrov GN (2017) Computer simulation of mechanisms. Lecture Notes in Mechanical Engineering, pp 45–56
16. Roshchin VV, Yerakhmadov SN (2017) Method for calculating the thermal conditions of gas cylinders heated from the outside GTD. Bulletin of the Kazan State Technical University. A.N. Tupolev. vol 73, no 2, pp 102–106 (in Russian)
17. Qu H, Fang Y, Guo S (2013) Bennett motion analysis based on specific regulus. Int J Mech Rob Syst 1(2/3):170–184

# Test Centrifuge Arrangement Analysis


**Arkady N. Popov, Mikhail N. Polishchuck and Nikolay Ye. Pulenets**

**Abstract** Comparative analysis of configurations of test centrifuges designed for mechanical testing of devices and instruments has been performed. Schemes of centrifuges, rotor-balancing devices, have been considered. Recommendations for rotor aerodynamic casings design have been given.

**Keywords** Mechanical tests · Centrifuge · Configuration · Rotor · Balancing · Aerodynamic casing

## 1 Introduction

Mechanical tests of devices, instruments, and machine assemblies are an important part of a technological process of critical products' quality control [1, 2]. Tests on constant accelerations effect [3], as well as those on effect of accelerations, being changed according to different functional rules, are to be carried out with centrifuges. A technological machine that provides such an effect is a centrifuge. Issues of configuration, mating, and coordination of centrifuge assemblies have always been important in design engineering, and now, when a unification level is particularly high, these issues have become even more urgent [4].

A. N. Popov · M. N. Polishchuck (✉) · N. Ye. Pulenets
Peter the Great St. Petersburg Polytechnic University, St. Petersburg, Russia
e-mail: polishchuck@mail.ru

A. N. Popov
e-mail: porka.n@mail.ru

N. Ye. Pulenets
e-mail: virus80@mail.ru



A. N. Evgrafov (ed.), *Advances in Mechanical Engineering*,
Lecture Notes in Mechanical Engineering,
https://doi.org/10.1007/978-3-030-11981-2_13

## 2 Centrifuges with Classic Gear Drive

All tests of one-axis centrifuges have a vertical axis of rotation [5, 6]. Depending on rotation velocity, the centrifuge rotors can be configured according to two schemes: with direct drive (when a motor shaft is connected directly to a rotor or a rotor shaft) and according to a reduction scheme. In this case, a reducing element, in the form of a gear or a belt drive, is to be installed between a drive motor and a rotor. Schemes of centrifuges with a gear drive are shown in Fig. 1a, b; in Fig. 1c, SY31 series centrifuge, manufactured by DONLING Technologies (China), with a gear drive, is presented [7].

Schemes with a gear reducer are considered classical and allow to realize a kinematic scheme that is optimum for the motor and to use the electric drive motor in the best way, providing its operation at nominal frequency, significantly reducing the moment of inertia of a massive centrifuge rotor adjusted to the motor shaft. This approach is typical for low-speed centrifugal benches with high load capacity, low accuracy, and not intense dynamics.

The schemes shown in Fig. 1 have a number of configuration constraints associated with a great number of mating elements that shall ensure the shafts' alignment. The gear reducer, as a rule, does not suppose operation in an "acceleration-deceleration"

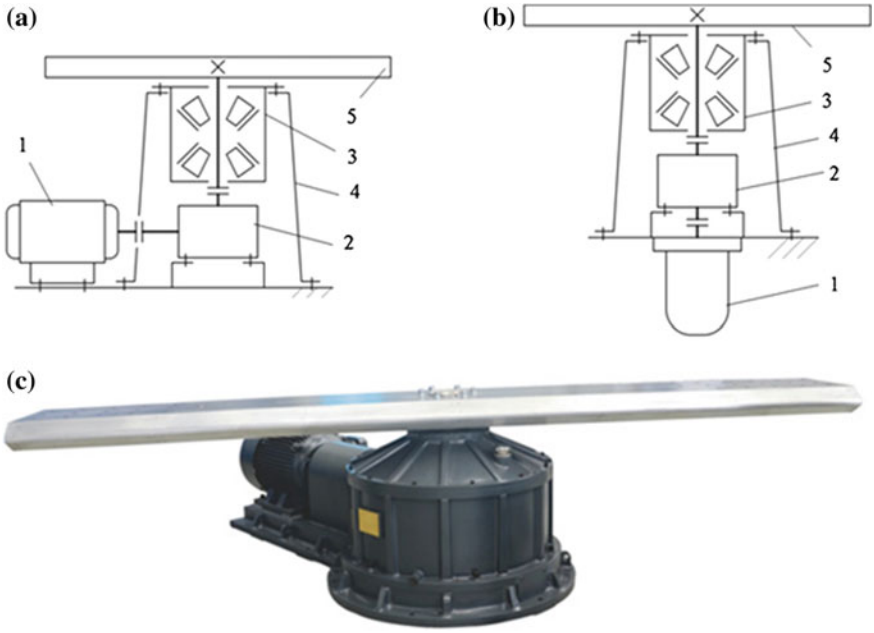


**Fig. 1** Configurations of centrifuges with classic gear drive: **a** with a motor in a radial position; **b** with a motor in a axial position; **c** SY31 series centrifuge (manufacturer: DONLING Technologies); 1 electric motor, 2 gear reducer, 3 spindle, 4 housing, 5 rotor

mode, typical for centrifugal benches, due to a shift of gaps in gears occurring in this case. Besides, a gear reducer itself is a source of increased noise and vibration.

## 3 Centrifuges with Belt Drive

Recently, centrifuges using belt drives with V-ribbed and tooth belts as a reducing element have become widespread (Fig. 2).

Schemes with a drive belt have a number of advantages against "traditional" gear drives: Centrifuge configuration is significantly simplified, and the size is reduced, reduced requirements for connecting a motor to a rotor spindle; at the same time, a motor operation mode is close to optimal, without noise and vibration.

In the scheme shown in Fig. 2a, one drive motor on legs mounted vertically is used. The next two diagrams in Fig. 2b, c show what effect can be reached when using a drive with two motors. We can see that height and radial size of the base are now reduced; the centrifuge becomes more compact. The minimum dimensions are obtained in the scheme shown in Fig. 2c. Of course, a drive with two motors is more expensive and requires additional resources for control. At the same time, a significant configuration advantage has led to the fact that most of the benches, manufactured

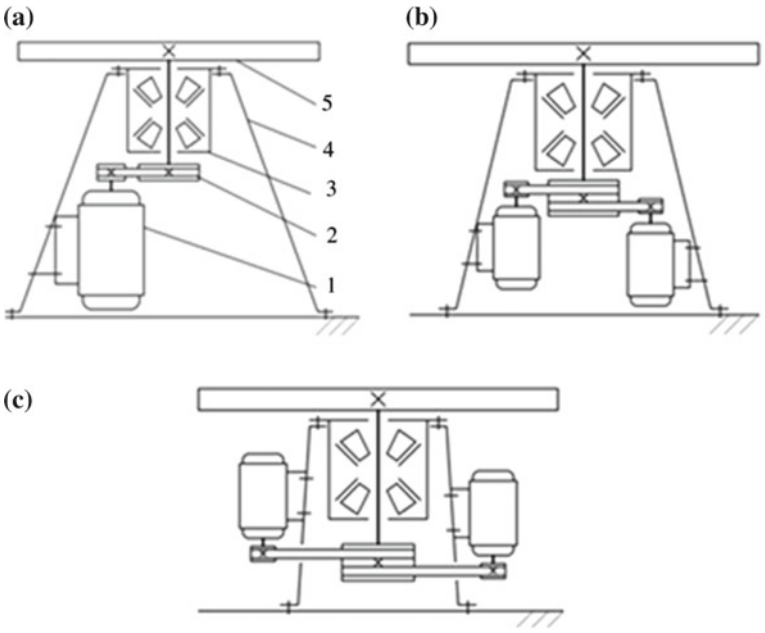


**Fig. 2** Configurations of centrifuges with belt drive: **a** with one drive motor; **b**, **c** with two drive motors; 1 electric motor, 2 belt drive, 3 spindle, 4 housing, 5 rotor

**Fig. 3** BD66 centrifugal benches, manufactured by Acutronic (USA)

by Active Dynamics (France) [8], are designed according to this scheme. Figure 3 shows BD66 series centrifugal bench, manufactured by Acutronic (USA), with a belt drive [9].

At strict requirements to centrifugal acceleration accuracy or at high rotation velocities of a rotor, gears are a source of additional disturbances and reduce a level of achievable angular velocities. In this case, a direct drive is used in centrifuges (Fig. 4).

## 4 Centrifuges with Direct Drive

The configuration of a centrifuge with a "high" rotor (Fig. 4a) is determined by a series connection of a standard motor, a standard spindle, and a special rotor [10]. There occur two problems with this configuration. First, an operation area of the centrifuge (rotor area) is located too high, so it becomes inconvenient to maintain the centrifuge. Second, due to a high center of gravity of the structure, the vibration activity of the bench increases.

In these cases, a motor is often lowered into a pit under the centrifuge, which is also inconvenient, as it is difficult to maintain the motor and protect it from dust, and when water leaks—from moisture.

In a number of designs, a motor is positioned over the rotor (Fig. 4b), but then the centrifuge's support structure becomes much more complicated, and the motor hides a part of the rotor's operating area. The second problem is the connection of a motor shaft to a centrifuge spindle shaft. It is almost impossible to achieve an ideal shaft alignment, and in case of misalignment, the rotor motion disturbances appear. The coupling connecting the shafts shall have a high torsional stiffness and a stable gear ratio equal to one, but these conditions are not met in a standard coupling. As a result, mainly test centrifuges that do not provide high accuracy are designed according to the schemes with a "high" rotor and a motor located above the spindle.

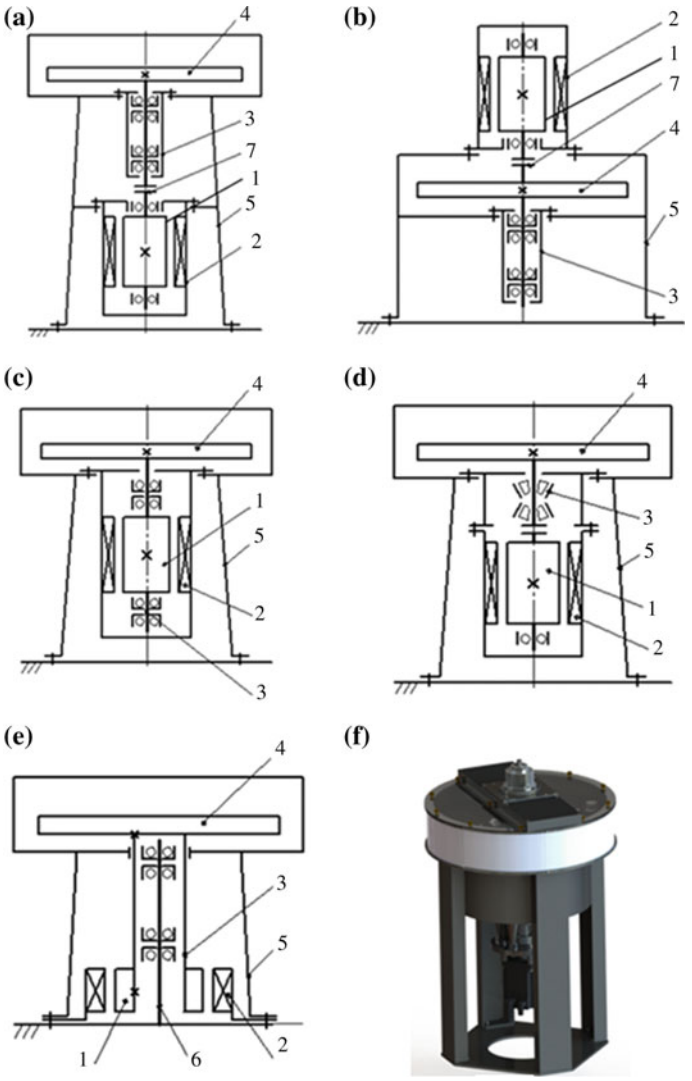


**Fig. 4** Configurations of centrifuges with direct drive: **a** with "high" rotor; **b** with a motor located above a rotor; **c** with a motor spindle; **d** with a modernized motor; **e** with a motor spindle on a column; **f** PC18 centrifuge, manufactured by Deltamec (RF); 1 motor rotor, 2 motor stator, 3 spindle, 4 centrifuge rotor, 5 support structure, 6 column, 7 coupling

The best solution to these problems is usage of motor spindles in centrifuges. To realize it, a motor and a spindle are assembled in the form of a mono-block, and the motor has no own supports (Fig. 4c). Another option is to replace standard motor supports with special spindle supports (Fig. 4d). Unfortunately, this solution leads to necessity to manufacture special electric motors, which, firstly, is expensive and, secondly, in case of a motor failure, eliminates an opportunity of its replacement by a serial production machine.

Centrifuge configurations are often determined by particular design traditions of a particular company. Figure 4e shows a scheme of the centrifuge, designed on the basis of a motor spindle mounted on the column. The centrifuge support is made in the form of fixed column 6 and hollow spindle 3, onto which motor rotor 1 and centrifuge rotor 4 are installed. Column 6 and motor stator 2 are mounted to support structure (frame) 5. This scheme, unlike the previous ones, requires development of a special motor or usage of a purchased ring unsupported motor. Figure 4f represents PC18 centrifuge, manufactured by Deltamec Company [10], with a "high" rotor.

## 5 Typical Scheme of Centrifuge Rotors

There are two typical schemes of centrifuge rotors: with a disk "rigid" rotor and a swinging rod (or beam) rotor (Fig. 5). The scheme with disk rotor 1 (Fig. 5a) provides a stable position of products 2 in relation to an axis of rotation of drive shaft 3. In addition, the disk, having a large moment of inertia, levels down the motor torque pulsations. Therefore, these rotors are widely used for the production of centrifugal benches, which shall meet strict requirements to acceleration accuracy.

The second feature of this design is the ability of the disk rotor to perceive ultra-large overloads, when exposed to centrifugal forces, which is important for high-speed centrifuges. The main drawback of the scheme is necessity to carry out a thorough balancing of a rotor with products and a large moment of inertia, which negatively affects dynamics of centrifuges designed for acceleration gradients reproduction.

The scheme with a swinging rotor (Fig. 5b) actually represents the scheme of scales (a weighing device). Rotor 1 of such centrifuges is usually of rod type. Swinging rotors are used in test benches, when it is allowed not to take into account an error due to swinging. The main advantage of the scheme is convenience and easiness of balancing.

## 6 Rotor with Counterweight

A counterweight for balancing shall be installed on the smallest possible radius $R_2 < R_1$ (Fig. 6), increasing accordingly its mass $m$ with respect to the mass of a tested product $m_0$. This makes it possible to reduce the rotor's axial moment of inertia $J$ and

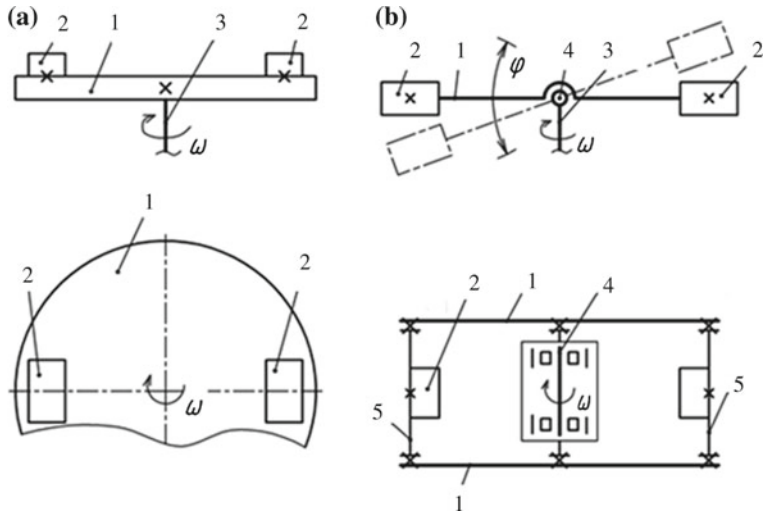


**Fig. 5** Typical scheme of centrifuge rotors: **a** scheme with a disk "rigid" rotor; **b** scheme with a swinging rotor; 1 rotor, 2 product, 3 drive shaft, 4 hinge, 5 traverse

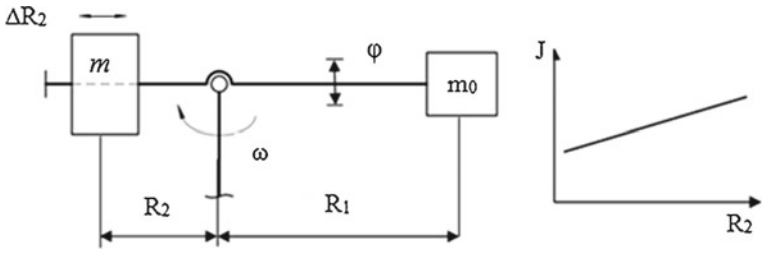


**Fig. 6** Scheme of swinging rotor with counterweight

to install motors with less torque (power) onto the centrifuges, which is especially important for large-radius centrifuges.

Static balancing of a rotor is achieved due to dislocation $\Delta R_2$ of counterweight $m$ along the radius relative to the swinging pin. The swinging pin is typically designed with rolling supports to reduce a friction torque. Dynamic balancing of a rotor is not required and is performed automatically, when the rotor deflects from the horizon by $\varphi$ angle due to centrifugal forces. The deflection angle depends on imbalance and velocity $\omega$ of the rotor rotation.

In centrifuges, various schemes of counterweight installation and methods of their balancing are used [11, 12]. Figure 7 shows a diagram of installation of a counterweight and the tested product, widely used by Active Dynamics (France) [8]. The design allows the rod rotor to move and to be fixed relative to a rotation axis; thus, both goals are achieved: balancing and changing a base radius of the tested product installation.

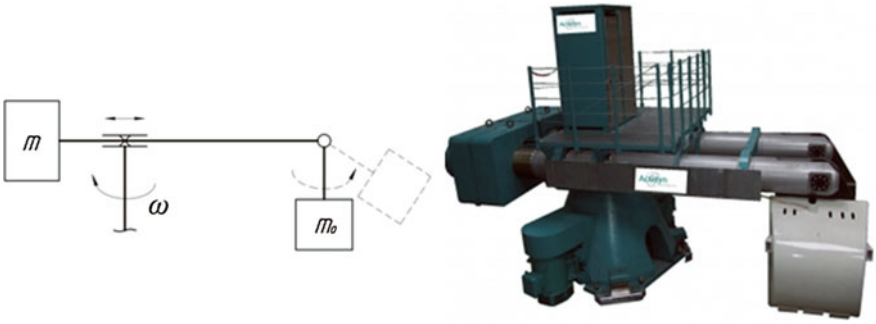


**Fig. 7** Diagram of installation of counterweight and product on rod rotors manufactured by Active Dynamics (France)

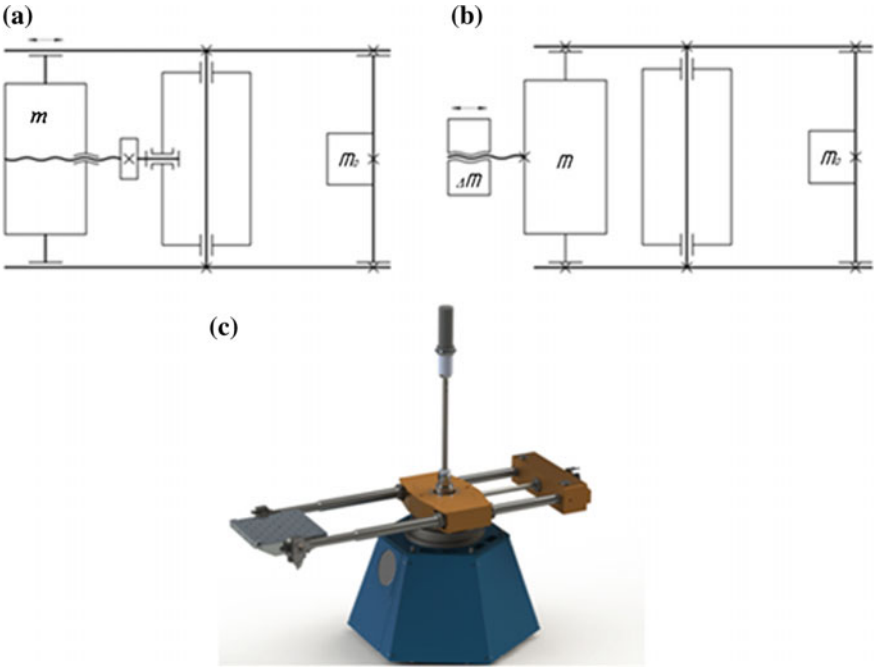


**Fig. 8** Devices for manual balancing of rod swinging rotors with screw mechanisms: **a** balancing using a large counterweight; **b** diagram of accurate balancing with a small counterweight; **c** PC19 centrifuge with a swinging rotor, manufactured by Deltamec (RF)

Scheme with a swinging rotor allows you to easily automate the balancing process, when the centrifuge is equipped with drive balances and force sensors (or position switches) that contact with the rotor in case of a static imbalance (Fig. 8a, b). Figure 8c shows a model of PC19 centrifuge with a swinging rotor, manufactured by Deltamec (RF).

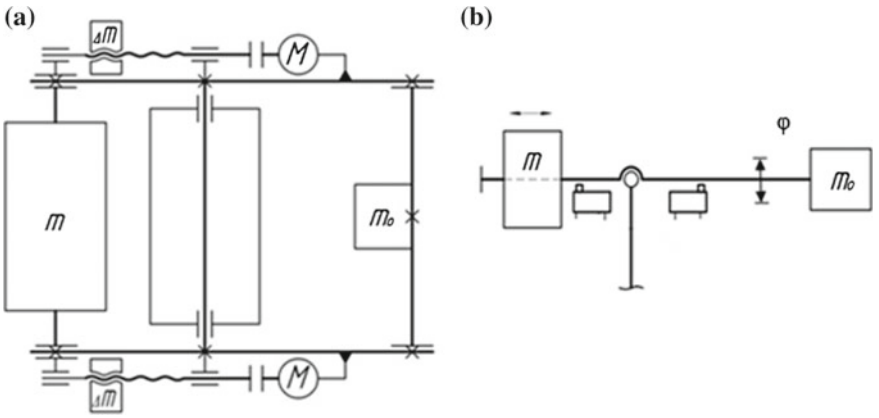


**Fig. 9** Device for automatic balancing of rod swinging rotors with screw mechanisms: **a** automatic balancing using counterweights drive $\Delta m$; **b** diagram of limit switches installation at automatic balancing

**Fig. 10** Centrifuge with swinging rotor and drive counterweights

Two schemes of balancing devices with mobile counterweights and swinging rotors are shown in Fig. 9 [6].

The scheme shown in Fig. 9a, in addition to automatic static balancing, allows you to additionally limit the dynamic imbalance (Fig. 9b), since during rotation of a dynamically unbalanced rotor, the former declines from its horizontal position, which is fixed by the position switch. HPC-4-7-600 centrifuge, manufactured by Acuitas (Switzerland), with automatic balancing, is shown in Fig. 10 [13].

## 7 Design of Centrifuge Casing

One of the tasks in the development of centrifugal benches is a casing design. As a rule, in centrifuges of small radius (for example, up to 1 m, Fig. 11a), the casing design is technological and relatively easy to manufacture. Therefore, it is quite reasonable that such a centrifuge has a casing, and a designing engineer always has a desire to locate a rapidly rotating element of a machine, the rotor, inside a protective screen (Fig. 11).

In this case, casing 1 has another important function: It is a support structure, rotary-motion feedthrough (electric, hydraulic, pneumatic, optical, etc.) can be mounted on it.

At low power, a centrifuge motor can be located on base 3 in full, in accordance with ergonomics rules in relation to height $H$ of the rotor servicing area. In this case, base 3 is to be fixed to the power floor of test box 4.

Figure 12 presents photographs of centrifuges with protective casings.

In medium-radius centrifuges [14], for example, from 1 … 1.5 m or more, the casing shall be assembled from different segments, and for installation of the tested products onto the rotor, the casing is to be made with an opening part. In that, all the casing elements shall be sufficiently rigid, while the door itself shall be securely locked, since when the rotor rotates, significant air cores arise, leading to vibrations and excessive pressure acting onto a cylindrical part of the casing [15, 16]. In this case, the casing turns out to be too complex, expensive, and non-technological in manufacture. Therefore, rotors of centrifugal benches designed for simulation of accelerations up to $(1 \ldots 1.5) \times 10^3$ m/s$^2$ often has no casings, and centrifuges are installed in separate premises—boxes (Fig. 11b). Rotary-motion feedthrough is to

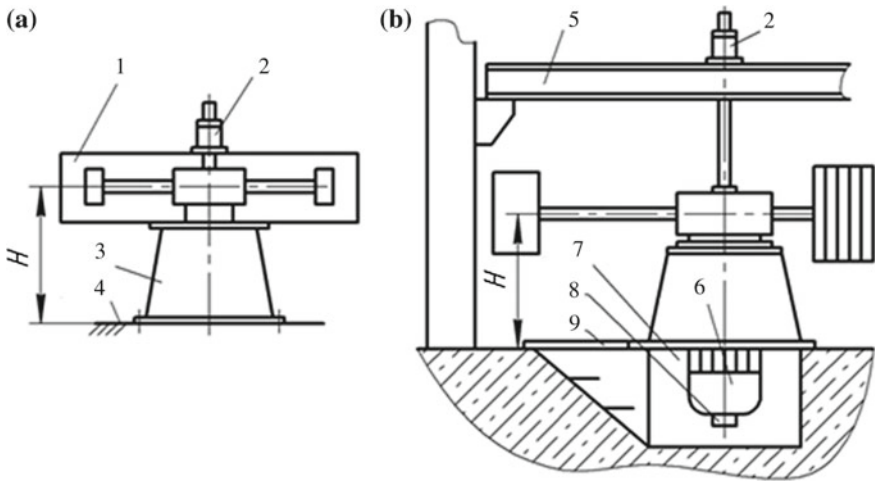


**Fig. 11** Scheme of centrifuge with casing: 1 casing, 2 rotary-motion feedthrough, 3 base, 4 power floor (**a**); 5 traverse, 6 drive motor, 7 pit, 8 engine sensor, 9 manhole (**b**)

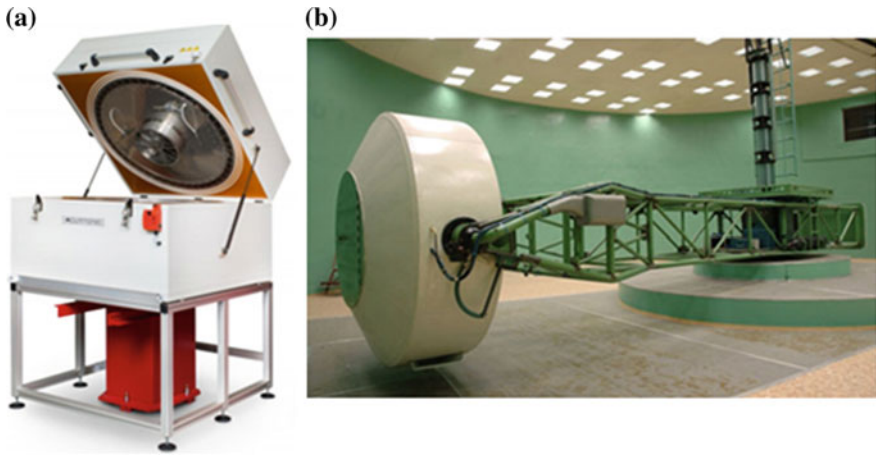


**Fig. 12** Centrifuges with protective casings: **a** AC66 centrifuge, manufactured by Acutronic (USA); **b** CF-7 medium-radius centrifuge (RF)

be mounted onto traverse 5, supported by construction structures of the building. At large driving capacities, the centrifuge height dimension becomes significant, and for the location of the rotor service area at a required height, a part of motor 6 has to be placed below the test box floor level, in pit 7, and to get access to motor sensor 8, it is necessary to use manhole 9. The second solution option is to build a protruding base with steps around the centrifuge.

There are also intermediate solutions for medium-radius centrifuges, such as installation of a protective screen only on the periphery (with free upper part) or installation of a centrifuge into a pit with an upper overlap and manhole providing access to the rotor operating area. The latter solution is the most non-ergonomic.

At high accelerations $(0.5 \ldots 5) \times 10^4$ m/s$^2$ and more, centrifuge rotors are always to be placed into casings, the main purpose of which is to reduce aerodynamic losses caused by air turbulence. The casing allows to reduce the drive power more than twice, which for high-speed centrifugal benches can be hundreds of kilowatts [15, 16].

Large-radius centrifuges are mounted in special boxes with radius walls [17, 18]. In this case, rotary-motion feedthrough shall be installed on the higher floor, and the motors occupy a part of the lower floor.

## 8 Conclusion

Considerable attention paid by the authors to configuration of centrifuges is due to significant influence of the configuration on all the test centrifuge characteristics. At the same time, when designing machines and, in particular, centrifuges, design

solutions are always compromised, largely associated both with design traditions and with cost and technological constraints.

We draw the following conclusions.

1. In practice, the leading designing companies use different schemes of test centrifuge configurations. Each scheme has its own advantages, disadvantages, and a designated area.
2. Centrifuges with a classic gear drive should be attributed to outdated technical solutions.
3. For low-speed benches with low requirements for dynamics and accuracy, belt-driven centrifuges (with one motor or two motors) are the best solution.
4. At high requirements for accuracy or high rotation velocities, a direct (gearless) drive shall be used.
5. There are two typical schemes of centrifuge rotors: disk and swinging (rod or beam) ones. The scheme with a disk rotor is rational at increased requirements for accuracy and high overloads in high-speed centrifuges. The main advantage of the schemes with a swinging rotor is easy balancing.
6. Particular attention, when handling high-speed test centrifuges, shall be paid to design of protective casings that reduce aerodynamic resistance to the rotor rotation.
7. Large-radius centrifuges shall be mounted in special cylindrical boxes.

## References

1. Lalanne C (2009) Mechanical shock: monography. ISTE Ltd.,Wiley, p 367
2. Harris CV, Piersol AG (eds) (2002) Harris shock and vibration handbook, 5th edn
3. GOST 2057.406-81 (1982) Electronic, quantum electronic and electro-technical components. Test methods. IPK Standards Publishing House, Moscow, p 139
4. Pavlyuchenko SV et al (2013) Design of mechatronic systems. Schemes of technological machines: training manual. SPb: Publishing House of Polytechnical University, p 167
5. Popov AN, Polishchuck MN, Timofeev AN (2016) Benches for mechanical tests—training manual. SPb: Publishing House of Polytechnical University, p 200
6. Popov AN, Polishchuck MN (2017) Testing machines. Monography. Uralsky Rabochy Publishing House, Yekaterinburg, p 217
7. Test centrifuges [electronic resource]. Access mode: http://www.technoprist.ru. Reference date: 04 Apr 2018
8. Products—Actidyn. Geotechnical modeling. Basket centrifuges [electronic resource]. Access mode: http://www.actidyn.com. Reference date: 04 Apr 2018
9. The driving force in motion simulation. Centrifuges [electronic resource]. Access mode: http://www.acutronic.com. Reference date: 04 Apr 2018
10. Mechanical test benches. Centrifugal benches [electronic resource]. Access mode: http://www.deltamec.ru. Reference date: 08 Apr 2018
11. Karazin VI, Kozlikin DP, Sukhanov AA, Tereshin VA, Khlebosolov IO (2017) Some ways of stable counterbalancing in respect to moving masses on centrifuges. Lecture notes in mechanical engineering, pp 73–85. https://doi.org/10.1007/978-3-319-53363-6_9

12. Karazin VI, Kozlikin DP, Sukhanov AA, Khlebosolov IO (2016) One stable scheme of centrifugal forces dynamic balance. Lecture notes in mechanical engineering, none, pp 75–85. https://www.scopus.com/inward/record.uri?eid=2-s2.0-84961239856&doi=10.1007%2f978-3-319-29579-_8&partnerID=40&md5=d0b01a4e394a9dc0d4d4229efa03c28f, https://doi.org/10.1007/978-3-319-29579-4_8
13. Centrifuges [electronic resource]. Access mode: http://www.acuitas.ch. Reference date: 26 Nov 2018
14. Popov AN, Polishchuck MN, Pulinets NY, Vasiliev AK (2017) PC25 centrifugal bench. In: Modern mechanical engineering. Science and education, vol 6, pp 515–526
15. Nazarov AV, Popov AN, Chernova YA (2013) Bench for simulation aerodynamic losses in test centrifuges. In: Modern mechanical engineering. Science and education, vol 3, pp 210–216
16. Chernova YA, Chelpanov IB, Popov AN (2014) Experimental study of aerodynamic losses in test centrifuges. In: Kokorin MS et al (eds) Week of science at SPbSPU. Materials of scientific-practical conference with international attendees. Editorial Board, pp 10–13
17. CF17 centrifuge—40 years of service to Russian manned space navigation (2013). Manned flights into outer space. Sci J 1(6). Yu. A. Gagarin Research & TEST Cosmonaut Training Center, FSBI, p 116
18. Experiments to support long-distance flights into outer space and activities on surface of mars and moon (2013). Manned flights into outer space. Sci. J. 1(6), Yu. A. Gagarin Research & TEST Cosmonaut Training Center, FSBI, pp 114–115

# Perspective Planetary-Layshaft Transmissions with Three Power Flows


**Konstantin Salamandra**

**Abstract** The most effective way to reduce fuel consumption by the vehicle equipped with internal combustion engine is to increase the number of speed ratios in the transmission. It leads to design complication and increasing the number of gear trains used. Here is proposed to make combinations of planetary gear sets and gears with fixed axles for obtaining simple designs of multi-speed transmissions with a small number of shifting elements used. The aim of the paper is to analyze compound transmission structures consisting of three simple gear trains with fixed axles and two planetary differential gear sets which forms three parallel power flows (three-stream transmissions). The possible structures of combined transmissions with planetary gears and gears with fixed axles are considered in the article. Such transmissions have a great perspective because of utilization simple gears and a small number of clutches, while these transmissions allow obtaining a significantly larger number of different speed ratios than the transmissions made up of the identical gears type. The possible three-stream transmissions structures were analyzed and classified, and a general expression is obtained for calculating the number of speeds in such transmission. A technique for synthesizing kinematic diagrams of transmissions with three power flows is described, using which new transmissions designs are obtained for each possible structure.

**Keywords** Power flows · Gearbox · Transmission · Synthesis · Planetary-layshaft transmission · Differential

K. Salamandra (✉)
Mechanical Engineering Research Institute of the Russian Academy of Sciences (IMASH RAN), Moscow, Russia
e-mail: ksalamandra@yandex.ru



A. N. Evgrafov (ed.), *Advances in Mechanical Engineering*,
Lecture Notes in Mechanical Engineering,
https://doi.org/10.1007/978-3-030-11981-2_14

## 1 Introduction

An increase in the number of speed ratios in transmissions is the most effective way to reduce fuel consumption and improve the efficiency of automotive vehicles equipped with internal combustion engines [1–3]. The increase in the number of speed ratios leads to complicated designs and increasing the number of gear trains used. These factors lead to an increase in overall dimensions, mass, and cost of the transmission. One of the methods to solve these problems is to use combined (planetary-layshaft) gearbox arrangements containing simple gears with fixed axles and planetary gear sets. Such designs perform a greater number of speeds with fewer gear trains used. For example, in transmissions of trucks and tractors, gears with a planetary splitter and/or an additional gear [4, 5] are used to change the ranges of the main 3-speed or 4-speed gearbox consisting of layshaft gears. This increases the number of obtained speed ratios in 4 times.

As is known [4–7], the planetary gear set consisting of three parts, in dependence on the linkages of its parts, has three operation modes:

1. Differential drive—converts the motion of two input links into the motion of one output link (summing gear) or the motion of one input link into the motion of two output links (differential gear).
2. Reducer or multiplier—when one gear is fixed.
3. Blocked, rotates as a single unit with direct gear when any two gears connected with each other.

In the transmissions of trucks and tractors, the planetary gear of the splitter or the additional gear operates only in modes 2 and 3. Mode 1 is used in planetary transmissions and in hybrids to divide or sum up the power flows of the internal combustion engine and electric motor [4, 5, 8, 9].

At the same time, the possibilities of planetary differential gears in conventional transmissions are not fully used. As shown in [10], the use of the planetary gear set as a differential drive in transmissions with fixed-axle gears makes it possible to obtain transmissions with simple design, high efficiency and a greater number of speed ratios than transmissions consisting of one type of gear trains. A greater number of speeds is achieved by changing the mode of operation of the planetary gear set and gears with fixed axles, which allows the latter to work both separately in the one-stream mode of operation of the planetary gear set (reducer or multiplier) and in parallel with other layshaft gears in two-stream mode. Using the terminology [11], the obtained transmissions are called two-stream by the number of parallel power flows from the input shaft to the output one. A method for the synthesis of kinematic diagrams was developed in [10], with the help of which a number of new designs of two-stream transmissions were obtained [12, 13].

With the use of two planetary gear sets operating as differential drives, the number of parallel power flows increases to three, which makes it possible to further improving the functionality of the multi-stream transmissions. In addition, if in a two-stream transmission, the 50–60% of the input flow is transmitted by two paths,

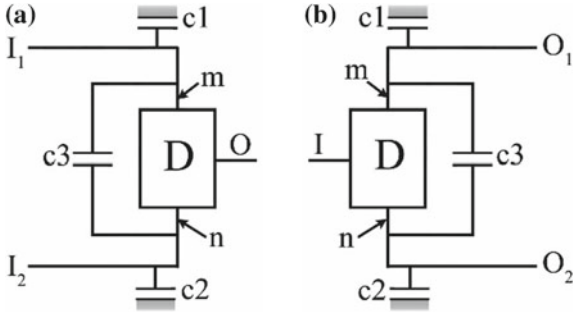


**Fig. 1** Generalized schemes of the planetary gear set: **a** summing gear; **b** differential gear. I, O—the input and output links, respectively; *m* and *n* are the parts of the differential D; c1 and c2—brakes which, respectively, fix the parts *m* and *n* with the frame; and c3—clutch which connects the parts *m* and *n* for differential blocking and rotation on direct gear

then in three-stream transmissions this percentage decreases by a factor of 1.5 or 2 [11]. Therefore, the loads on internal gears in multi-stream transmissions are much lower, so the gear trains used can be smaller in weight, overall dimensions, and also less complicated. The purposes of this paper are analysis possible structural schemes of the couplings of planetary-layshaft transmissions with three power flows, determination of their general properties, and the synthesis method for obtaining kinematic diagrams of these transmissions.

## 2 Structural Schemes and Classification of Planetary-Layshaft Transmissions with Three Power Flows

The generalized symbols of the gear trains involved in [14, 15] were used for a visual representation of the planetary-layshaft transmission structures. The planetary gear set and one or several gears with fixed axles can be represented by means of generalized symbols.

The planetary gear set can be represented in the general case by only two generalized schemes (Fig. 1) with shifting elements added to the generalized symbol of planetary gear set that provides external couplings on its parts. The schemes differ in the locations of the input and output links, and at switched-off c1, c2, and c3 determine the planetary gear set, as a summing gear (Fig. 1a) or differential gear (Fig. 1b). Two shifting elements c1, c2, c3 of the differential D cannot be switched-on at the same time.

Similarly, by the symbol GB (Fig. 2) was represented the internal gearbox with fixed axles which has one or more gears and shifting elements built into them per-

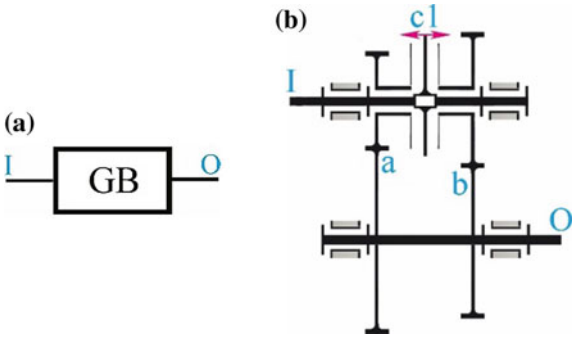


**Fig. 2** Generalized symbol (**a**) and kinematic diagram (**b**) of a two-speed gearbox with fixed axles of gears. I, O—the input and output links, respectively; c1—shifting element (clutch or synchronizer) which has three working positions

forming different gear ratios from input shaft I to output shaft O. Figure 2b shows an example of a kinematic diagram of a two-speed GB.

It is necessary to make three kinematic connections on the parts of the differentials to realize a gearbox made up of two differentials connected in parallel, and three closed circuits are obtained as a result. The differential parts can be connected to the internal links of the gearbox, with the input or output shafts. The number of possible permutations of two differentials (inside the transmission, at the input, or at the output) gives $2^2 = 4$ possible structures. We install internal layshaft gearboxes GB in each closed loop formed by the parts of the differentials. Thus, only four different structures of planetary-layshaft transmissions with three power flows were obtained as a result of structural synthesis (Fig. 3).

The following notation for four obtained structures depending on the location of the differentials, input and output links introduced:

- DD shown in Fig. 3a—the structure in which the planetary gear sets locate on the input and output.
- DDO shown in Fig. 3b—the structure in which first planetary gear set locates at the input, the second one in the internal circuit, and the power flows are summarizing on the output link O.
- IDD shown in Fig. 3c—the structure in which planetary gear set locates at the output, the second one in the internal circuit, and the power flow is distributing by the input link I.
- IDDO shown in Fig. 3d—the structure in which both planetary gear sets locate in internal circuits and the power flows is distributing by the input I and summarizing on the output O.

Each closed circuit in the structures (Fig. 3) on one side has a differential and on the other the node point (A or B) in which the power flows are distributing or summarizing. There are two possible variants of an internal circuit in the DD structure (Fig. 3a), i.e., connections between the links of internal GB2 and differentials parts:

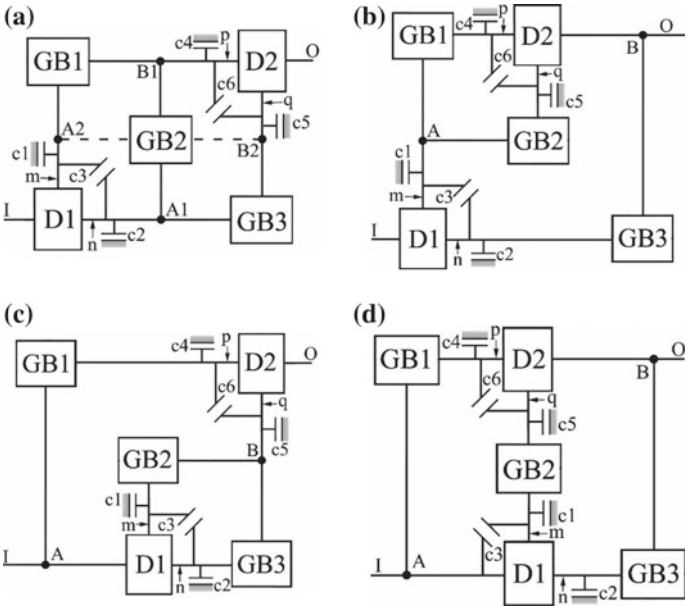


**Fig. 3** Structures of planetary-layshaft transmissions with three power flows: **a** DD structure; **b** DDO structure; **c** IDD structure; and **d** IDDO structure. I, O—the input and output links, respectively; *m* and *n* are the parts of the differential D1; *p* and *q* are the parts of the differential D2; c1, c2 and c4, c5 are brakes which, respectively, fix parts *m*, *n* and *p*, *q* with a frame, respectively; and c3 and c6 are the blocking clutches of the differentials D1 and D2, respectively

either with parts *m* and *q* of differentials (dashed lines) or with parts *n* and *p* (solid lines). There is only one possible connection between internal links for forming three parallel power flows from input I to output O in other structures.

The shifting elements in the internal gearboxes GB must be switched-on at switched-off shifting elements of the differentials for power distribution in three paths on the three-stream mode. Thus, three-stream transmissions generally have four degrees of freedom, i.e., three shifting elements must be switched-on each speed. But the DDO and IDD structures have one, and the IDDO structure has two internal gearboxes GB, for which only two shifting elements are switched-on in one-stream mode: one in the corresponding GB and one shifting element of one of the differentials D1 or D2. For example, in the DDO structure by shifting brake c1 or blocking clutch c3, one-stream mode via GB3 is possible. The property can be used to preselect the shifting element of the next speed, as it does in dual-clutch transmissions [16]. In addition, the third shifting element can be switched-on to minimize the idling loss on these speeds.

The maximum number of differentials' shifting elements (brakes c1, c2, c4, c5 and blocking clutches c3, c6) is presented in the structures (Fig. 3). The shifting elements determine possible two- and one-stream operation modes and may be absent in the specific kinematic diagrams of the transmissions, and then, the number of operating

modes of such transmission will accordingly decrease. Up to 4 one-stream modes for each internal GB and up to 2 two-stream modes through each pair of internal GBs are possible in each structure. In general, the number of speeds performed by a three-stream transmission is defined by Eq. (1).

$$N = N_{GB1} \cdot l_1 + N_{GB2} \cdot l_2 + N_{GB3} \cdot l_3 + N_{GB1} \cdot N_{GB2} \cdot l_4 + N_{GB1} \cdot N_{GB3} \cdot l_5 + N_{GB2} \cdot N_{GB3} \cdot l_6 + N_{GB1} \cdot N_{GB2} \cdot N_{GB3} \quad (1)$$

where $N_{GB1}$, $N_{GB2}$, $N_{GB3}$—number of speeds in GB1, GB2, GB3, respectively; $l_4$, $l_5$, $l_6$—number of one-stream modes via GB1, GB2, GB3, respectively; $l_4$, $l_5$, $l_6$—number of two-stream modes via GB1 and GB2, GB1 and GB3, GB2 and GB3, respectively.

## 3 Synthesis the Kinematic Diagrams of Planetary-Layshaft Transmissions with Three Power Flows

Synthesis of the kinematic diagrams of transmissions with three power flows is proposed by replacing generalized symbols with the diagrams of gear trains in the selected structure (Fig. 3).

Various diagrams of the gear trains used and combinations of their connections with input, output, and internal links determine a vast array of permissible kinematic diagrams. The limitations must be introduced for a substantial cutting down of this array. The limitations must determine the predominance of multi-flow modes in the synthesized transmission designs, the specified direction of rotation of the output shaft for the forward and reverse gears, etc. The type of planetary gear sets and gears with fixed axles must be also defined in order to simplify the design of the transmission. The list of limitations adopted in this paper for the synthesis of kinematic diagrams of planetary-layshaft transmissions with three power flows is presented below.

1. The simple epicyclic gear sets consisting of sun pinion, ring gear, and carrier holding the planets will be used as D1 and D2.
2. The layshaft gearboxes with one or two speeds (Fig. 2b) will be used as internal GBs.
3. The D1 differential input link will be connected with the sun gear in order to increase the transmission ratio from gear to gear because the gear ratio from the sun gear to the ring gear and carrier is greater than 1. The rotation direction of the carrier will coincide with the rotation direction of the sun gear in this case, and the ring gear will rotate in the opposite direction. All parts of the D1 gear set will rotate in the same direction as the sun gear if the planetary gear set will be blocked by the clutch c3.
4. The internal gearbox GB connected to the ring gear of D1 must have two gears. The first one with a parasitic gear for unidirectional rotation of all transmission

gears at three-stream mode and two-stream mode at c6 clutch switched-on, and for obtaining reverse gear when c3 and c6 clutches switched-on. The second one consists of two gear wheels and works when the c3 clutch is switched-on and D1 planetary gear set is blocked.

5. The output link of D2 will be connected with the carrier of the planetary gear set. The carrier rotates in the same direction as sun gear or ring gear at such arrangement.
6. The following notation for the parts of differentials are introduced to match the resulting kinematic diagrams with parent structures (Fig. 3): ring gear of D1—*m*; carrier of D1—*n*; sun gear of D2—*p*; and ring gear of D2—*q*.
7. Above mentioned that two- and three-stream modes could significantly reduce the loads on the internal gears. So, increasing the proportion of multi-stream speeds in the total number of speeds of the transmission recommended at the stage of kinematic diagrams synthesis. Therefore, the brakes c1, c2, c4, and c5 that mainly switched-on at one-stream modes excluded from the consideration. Thus, the blocking clutches c3 and c6 for implementation the two-stream and the remaining one-stream modes will be used. Then, according to point 2 in the synthesized transmissions, there will be no more than five shifting elements, and the parameters of one-stream modes for all internal GBs are $l_1 = l_2 = l_3 = 1$.
8. The transmission shifting elements will placed on the driver links in order to reduce the torques acting on them.

The limitations stated assume a positive gear ratio from the planetary gear sets to the transmission links, except the ring gear of D1, where the gear ratio is negative, and the parasitic gear is set to change the direction of its rotation in the corresponding GB (point 4 of the limitations). The internal GBs (Fig. 2b) have gear pairs and a negative gear ratio from the GB input link to the output one. Therefore, the total transmission speed ratio from input I to output O will also be negative. The countershafts must be added inside transmission or after the output shaft if needed unidirectional rotation I and O.

The formulation of limitations is the main goal of the proposed method for synthesizing kinematic diagrams of transmissions. The more limitations, the less variants of the connections between the gear trains in the design and easier to perform synthesis. Also, should note that the specification, experience, and intuition of the designer largely determine the set of limitations adopted. Allocating potentially commercially available transmission designs with required functions from the whole variety of diagrams for further consideration and analysis is the main goal of the proposed synthesis methodology.

### 3.1 *Synthesis the Kinematic Diagram According to the Structure DD with Nodes A1 and B1 (Fig. 3a)*

In accordance with the structure (Fig. 3a) and point 6 of the adopted limitations the GB1 input shaft connected with the ring gear of D1, the GB2 and GB3 input shafts—with the carrier of D1, the GB1 and GB2 output shafts—with the sun gear of D2, and the GB3 output shaft—with the ring gear of D2. In accordance with point 4 of the limitations, GB1 has two gears, one of which with a parasitic gear. The parameters of the two-stream modes via GB1, GB2 and via GB2, GB3 are $l_4 = l_6 = 1$ and the parameter of two-stream modes via GB1 and GB3, respectively, $l_5 = 2$. The two-stream mode occurs via GB1, GB2 and via GB1, GB3 through a parasitic gear in GB1 when clutch c6 switched-on. The two-stream mode occurs via GB1 and GB3 through the gear without parasitic gear wheel when clutch c3 switched-on. If GB2 fitted up with one speed and GB3 has two speeds, then by Eq. (1) one gets 14 speeds in the synthesized transmission including one reverse gear. For unidirectional rotation of the input shaft I and output shaft O at forward speeds, there installed the countershafts between the internal GBs and the input parts of the differential D2. The kinematic diagram of the transmission is presented in Fig. 4.

The operating modes ("−"—one-stream; "="—two-stream; "≡"—three-stream) and overall gear ratios $i_{IO}$ implementing by the transmission (Fig. 4) depending on the states of shifting elements (switched-on shown with the "x" symbol) are shown in Table 1, R—reverse gear.

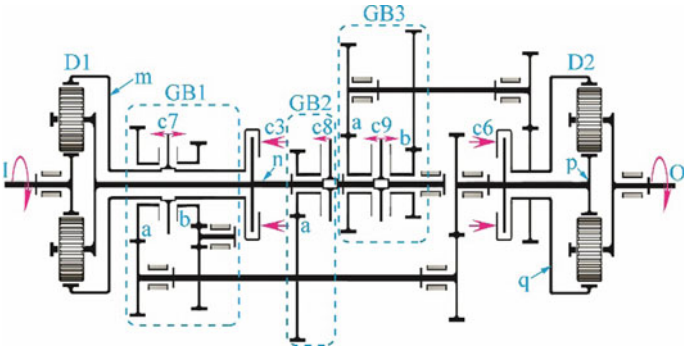


**Fig. 4** Kinematic diagram of the 14-speed transmission according to the DD structure

**Table 1** Operating modes and overall gear ratios implementing by the transmission shown in Fig. 4

| Speed and mode | s7 | | s8 | s9 | | c3 | c6 | $i_{10}$ |
|---|---|---|---|---|---|---|---|---|
| | a | b | | a | b | | | |
| 1 = | | x | X | | | | x | 5.753 |
| 2 = | | x | | x | | | x | 4.099 |
| 3 ≡ | | x | X | x | | | | 4.013 |
| 4 – | x | | | | | x | x | 3.483 |
| 5 = | | x | | | x | | x | 2.911 |
| 6 ≡ | | x | X | | x | | | 2.371 |
| 7 – | | | X | | | x | x | 1.657 |
| 8 = | x | | | x | | x | | 1.324 |
| 9 = | | | x | x | | x | | 1.156 |
| 10 – | | | | x | | x | x | 0.995 |
| 11 = | x | | | | x | x | | 0.738 |
| 12 = | | | x | | x | x | | 0.683 |
| 13 – | | | | | x | x | x | 0.52 |
| R – | | x | | | | x | x | −1.074 |

## 3.2 *Synthesis the Kinematic Diagram According to the Structure DDO (Fig. 3b)*

The GB1 and GB2 input shafts connected with ring gear of D1; the GB3 input shaft—with the carrier of D1, the GB3 output shaft—with the output shaft O; the GB1 output shaft—with the sun gear of D2, and the GB2 output shaft—with the ring gear of D2. Each of the GB1 and GB2 has two gears, and one gear at both GBs has a parasitic gear wheel, in accordance with point 4. Parameters of two-stream modes for all GBs are $l_4 = l_5 = l_6 = 1$. Two- and three-stream modes via GB1 and GB2 occur through the gears with parasitic gear wheels. If GB3 has two speeds, then by Eq. (1) one gets 14 speeds in synthesized transmission and three of which are reverse gears. The kinematic diagram (Fig. 5) is obtained assuming an opposite rotation direction of the input shaft I and output shaft O at forward speeds.

The operating modes and speed ratios implementing by the transmission (Fig. 5) depending on the states of shifting elements are shown in Table 2.

## 3.3 *Synthesis the Kinematic Diagram According to the Structure IDD (Fig. 3c)*

The power flow distribution occurs on the transmission input shaft I in the IDD structure, and the power flows summation occurs on the output shaft in the DDO

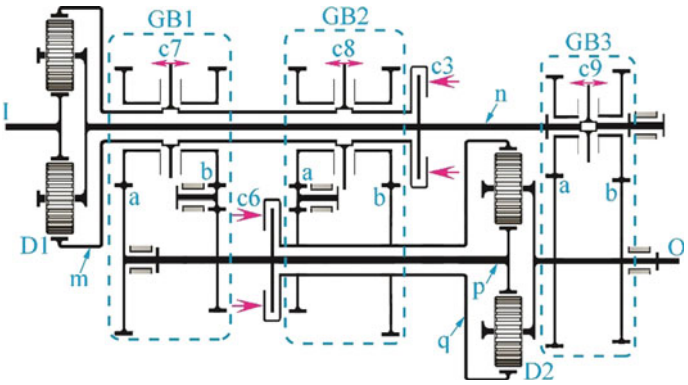


**Fig. 5** Kinematic diagram of the 14-speed three-stream transmission according to the DDO structure

**Table 2** Operating modes and overall gear ratios implementing by the transmission shown in Fig. 5

| Speed and mode | s7 | | s8 | | s9 | | c3 | c6 | $i_{10}$ |
|---|---|---|---|---|---|---|---|---|---|
| | a | b | a | b | a | b | | | |
| 1 = | | x | | | x | | | x | −4.346 |
| 2 = | | x | | | | x | | x | −3.846 |
| 3 − | x | | | | | | x | x | −3.0 |
| 4 ≡ | | x | x | | x | | | | −2.603 |
| 5 = | | | x | | x | | | x | −2.336 |
| 6 ≡ | | x | x | | | x | | | −2.103 |
| 7 = | | | x | | | x | | x | −1.836 |
| 8 = | x | | | x | | | x | | −1.322 |
| 9 − | | | | x | | | x | x | −0.963 |
| 10 − | | | | | x | | x | | −0.695 |
| 11 − | | | | | | x | x | | −0.495 |
| R1 − | | x | | | | | x | x | 1.74 |
| R2 = | | x | x | | | | x | | 0.578 |
| R3 − | | | x | | | | x | x | 0.4 |

structure. Therefore, it is always possible to obtain the IDD diagram from the DDO diagram if one changes the input and output links. The speed ratios in such case will have inverse values.

There is another way to synthesis the kinematic diagram according to the IDD structure where the power flow at the input will be divided after the differential D1. The GB1 input shaft connected with the input shaft I in accordance with the structure (Fig. 3c). The GB1 output shaft connected with the sun gear of D2, and the ring gear of D1—with GB2 input shaft. The GB2 has two gears, one of which with a parasitic gear. The GB3 input shaft connected with the carrier of D1. The GB2 and GB3

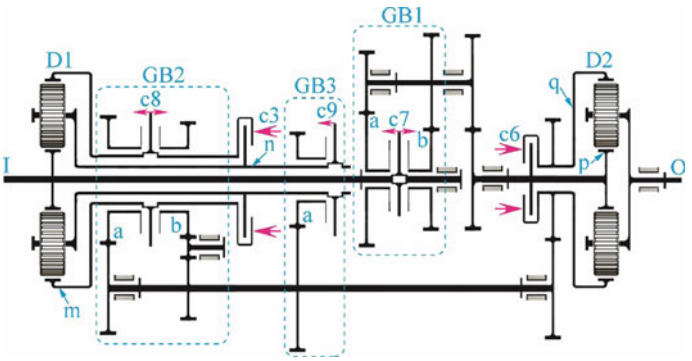


**Fig. 6** Kinematic diagram of the 12-speed three-stream transmission according to the IDD structure

**Table 3** Operating modes and overall gear ratios implementing by the transmission shown in Fig. 6

| Speed and mode | s7 | | s8 | | s9 | c3 | c6 | $i_{10}$ |
|---|---|---|---|---|---|---|---|---|
| | a | b | a | b | | | | |
| 1 = | | | | x | x | | x | 5.328 |
| 2 ≡ | x | | | x | x | | | 4.214 |
| 3 − | x | | | | | | x | 3.21 |
| 4 = | x | | | | x | x | | 2.255 |
| 5 − | | | | | x | x | x | 1.88 |
| 6 = | x | | x | | | x | | 1.272 |
| 7 ≡ | | x | | x | x | | | 0.976 |
| 8 − | | | x | | | x | x | 0.907 |
| 9 = | | x | | | x | x | | 0.813 |
| 10 = | | x | x | | | x | | 0.636 |
| 11 − | | x | | | | | x | 0.439 |
| R − | | | | x | | x | x | −0.254 |

output shafts connected with one shaft, which connects with the ring gear of D2. The parameters of two-stream modes of all internal gearboxes are $l_4 = l_5 = l_6 = 1$. Two-stream mode via GB2 and GB3 occurs through a parasitic gear, and two-stream mode via GB1 and GB2 occurs through a gear without a parasitic gear wheel. If there are two speeds in GB1 and one in GB3, then by Eq. (1) one gets 12 speeds in the synthesized transmission including one reverse gear ratio. There are installed the countershafts between the internal GBs and the input parts of the differential D2 for unidirectional rotation of the input shaft I and output shaft O at forward speeds. The kinematic diagram of the transmission is presented in Fig. 6.

The operating modes and speed ratios implementing by the transmission (Fig. 6) depending on the states of shifting elements are shown in Table 3.

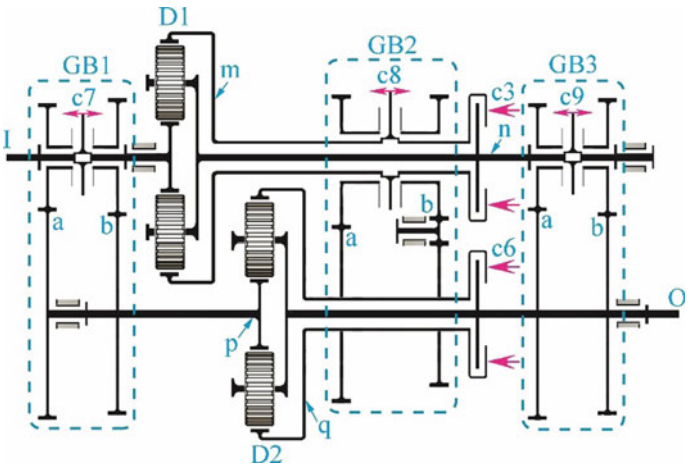


**Fig. 7** Kinematic diagram of the 14-speed three-stream transmission according to the IDDO structure

### *3.4 Synthesis the Kinematic Diagram According to the Structure IDDO (Fig. 3d)*

The input power flow divides between GB1 and D1 in the IDDO structure. The GB1 output shaft connected with the sun gear of D2 in accordance with point 6 of adopted limitations, and the ring gear of D1—with GB2 input shaft, in which there are two gears, one of them with a parasitic gear. The GB2 output shaft connected with the ring gear of D2. The planetary gear set D2 sums the power flows from GB1 and GB2. The carrier of D1 connected with the GB3 input shaft, the output shaft of which connected with the transmission output shaft. Two-stream modes via GB1 and GB3 in the IDDO structure are not possible. The parameters of the other two-stream modes will be $l_4 = l_6 = 1$. If each GB has two speeds, then in accordance with Eq. (1) one gets a 14-speed transmission including one reverse gear ratio. The kinematic diagram (Fig. 7) obtained assuming an opposite rotation direction of the input shaft I and output shaft O at forward speeds.

The operating modes and speed ratios implementing by the transmission (Fig. 7) depending on the states of shifting elements are shown in Table 4.

## 4 Gear Ratios Determination

The problem arises of gear ratios calculation after the synthesis of the transmission kinematic diagram. The problem consists in the search for gear ratios of gear pairs of internal gearboxes GB1, GB2, GB3 and planetary gear sets D1, D2. The gear

**Table 4** operating modes and overall gear ratios implementing by the transmission shown on Fig. 7

| Speed and mode | s7 | | s8 | | s9 | | c3 | c6 | $i_{10}$ |
|---|---|---|---|---|---|---|---|---|---|
| | a | b | a | b | a | b | | | |
| 1 = | | | | x | x | | | x | −4.677 |
| 2 = | | | | x | | x | | x | −3.807 |
| 3 ≡ | | x | | x | x | | | | −3.515 |
| 4 ≡ | | x | | x | | x | | | −3.033 |
| 5 − | | x | | | | | | x | −2.07 |
| 6 = | | x | x | | | | x | | −1.648 |
| 7 − | | | x | | | | x | x | −1.451 |
| 8 ≡ | x | | | x | x | | | | −1.229 |
| 9 ≡ | x | | | x | | x | | | −1.06 |
| 10 − | | | | | x | | x | | −0.872 |
| 11 = | x | | x | | | | x | | −0.707 |
| 12 − | | | | | | x | x | | −0.524 |
| 13 − | x | | | | | | | x | −0.4 |
| R − | | | | x | | | x | x | 1.664 |

**Table 5** Results of gear ratios optimization for synthesized transmissions

| Kinematic diagram | | DD (Fig. 4) | DDO (Fig. 5) | IDD (Fig. 6) | IDDO (Fig. 7) |
|---|---|---|---|---|---|
| GB1 | c7a | −3.0 | −3.0 | −2.885 | −0.4 |
| | c7b | 0.925 | 1.74 | −0.395 | −2.07 |
| GB2 | c8a | −1.427 | 0.4 | −1.429 | −1.451 |
| | c8b | – | −0.963 | 0.4 | 1.664 |
| GB3 | c9a | −1.175 | −0.695 | −2.964 | −0.872 |
| | c9b | −0.614 | −0.495 | – | −0.524 |
| Countershaft gear ratios | $i_p$ | −1.161 | – | −1.113 | – |
| | $i_q$ | −0.847 | – | −0.634 | – |
| D1 | $i_{Im}^{(n)}$ | −1.5 | −1.5 | −1.615 | −1.5 |
| D2 | $i_{pq}^{(O)}$ | −1.877 | −1.5 | −1.496 | −1.5 |

ratios must provide a set of speed ratios $i_{IO}$ that is closest to the assigned set. The proximity criteria can be different. The methodology [17] was adopted in this paper for demonstration the sequence of speed changes.

The optimization results presented for all synthesized transmissions in Table 5 and the gear ratios from input shaft I to output shaft O ($i_{IO}$) obtained with these parameters are in the right columns of Tables 1, 2, 3 and 4.

DDO (Fig. 5) and IDD (Fig. 6) transmissions have two, and the IDDO transmission (Fig. 7) has four speeds, on which only two shifting elements are switched-on. Any

unused shifting elements can also be switched-on at these speeds. Then the next speed, if necessary, can be prepared in advance. For example, if the 11th speed enabled in the DDO transmission (Fig. 5), the clutch c6 can also be switched-on and the transition to the 2nd or the 7th speed could be done by switching-off the clutch c3 and switching-on c7b or c8a, respectively. Thus, the DDO, IDD, and IDDO transmissions have additional features.

The synthesized transmissions (Figs. 4, 5, 6 and 7) equipped with simple mechanisms and five shifting elements, three of which switched-on each speed, which reduces energy losses in the unused shifting elements. A small number of gear trains allow stating that the synthesized transmissions have high efficiency.

## 5 Summary

To obtain simple designs of vehicles transmissions that realize more than 10 speeds proposed to use combined planetary-layshaft arrangement consisting of two planetary differential gear sets and gears with fixed axles. The structures of such arrangement named three-stream transmissions by the number of parallel power flows. The possible structures of three-stream planetary-layshaft transmissions were obtained, the structures were classified according to the location of input and output links and planetary gear sets. The possible operation modes of the three-stream transmissions were analyzed, and the expression for calculation the speeds total number has been obtained. The structures which have additional functional capabilities for control system designing were determined. The methodology for the synthesis of kinematic diagrams of planetary-layshaft transmissions was proposed. Four kinematic diagrams of three-stream transmissions with 12 and 14 speeds were obtained by means of the method. Each obtained design has only five shifting elements, consists of simple mechanisms, has lower loads on internal links on multi-power flow modes, and has high efficiency. Thus, proposed designs have better characteristics than known multi-speed planetary transmissions [3].

The gear ratios for each transmission design were calculated just for demonstration without taking into account single transition shifts between nearby speeds which is that only one pair of clutches is involved in gearshifting process. Ratios calculated need an addition optimization with elimination double transition shifts between nearby speeds.

**Acknowledgements** The research was supported by Russian Science Foundation (project No. 17-79-10493).

## References


1. Wagner G, Naunheimer H, Scherer H et al (2007) Achtgang-automatikgetriebe zur reduzierung des kraftstoffverbrauchs. ATZ Automob Z 109(6):512–519. https://doi.org/10.1007/BF03221894
2. Ota H, Nozaki K, Honda A et al (2007) Toyota's world first 8-speed automatic transmission for passenger cars. SAE technical paper 2007-01-1101. https://doi.org/10.4271/2007-01-1101
3. Dong P, Liu Y, Tenberge P et al (2017) Design and analysis of a novel multi-speed automatic transmission with four degrees-of-freedom. Mech Mach Theory 108:83–96. https://doi.org/10.1016/j.mechmachtheory.2016.10.013
4. Förster H (1991) Automatische fahrzeuggetriebe. Springer, Berlin. https://doi.org/10.1007/978-3-642-84118-7
5. Naunheimer H, Bertsche B, Ryborz J et al (2011) Automotive transmissions. Springer, Berlin. https://doi.org/10.1007/978-3-642-16214-5
6. Volkov DP, Kraynev AF (1974) Transmissii stroitelnikh i dorojnikh mashin. Spravochnoye posobie (Transmissions of Building and Road Machines. Reference Manual). Mashinostroenie, Moscow
7. Müller HW (1982) Epicyclic drive trains. Analysis, synthesis, and applications. Wayne State University Press, Detroit
8. Zhang X, Li C, Kum D et al (2012) Prius(+) and volt(−): configuration analysis of powersplit hybrid vehicles with a single planetary gear. IEEE Trans Veh Technol 61(8):3544–3552. https://doi.org/10.1109/TVT.2012.2208210
9. Yang H, Kim B, Park Y et al (2009) Int J Automot Technol 10:381. https://doi.org/10.1007/s12239-009-0044-y
10. Kraynev A, Salamandra K, Raghavan M (2013) Synthesis of the two-stream transmissions. In: Dobre G (eds) Power transmissions. Mechanisms and machine science, vol 13. Springer, Dordrecht. https://doi.org/10.1007/978-94-007-6558-0_25
11. Antonov AS (1975) Silovie peredachi kolesnikh i gusenichnikh mashin. Teoriya i raschet (Power transmission of wheeled and caterpillar vehicles. Theory and calculation), 2nd edn. Mashinostroenie. Leningrad
12. Krajnev AF, Astashev VK, Salamandra KB et al (2010) Gearbox. RU Patent 2391588, 10 Jun 2010
13. Kraynev AF, Astahev VK, Salamandra KB et al (2013) Multi-speed transmission. US Patent 8,360,919, 29 Jan 2013
14. Wolf A (1958) Die Grundgesetze der Umlaufgetriebe. Vieweg, Braunschweig
15. Kirdyashev YuN (1969) Mnogopotochnie peredachi differentsialmogo tipa (Multistreamed differential type transmissions). Mashinostroenie, Leningrad
16. Matthes B (2005) Dual clutch transmissions—lessons learned and future potential. SAE technical paper 2005-01-1021. https://doi.org/10.4271/2005-01-1021
17. Salamandra K (2018) Static analysis and parameters synthesis of planetary-layshaft transmissions with three power flows. In: MATEC Web of conferences, p 224. https://doi.org/10.1051/matecconf/201822402040

# Study of Mechanisms with Allowance for Friction Forces in Kinematic Pairs


**Yuri A. Semenov and Nadezhda S. Semenova**

**Abstract** Friction forces emerge in kinematic pairs of mechanisms; in many cases, these forces significantly affect the movement of the links of the mechanisms and should be taken into account in force calculations. Introduction of friction forces leads to an increase in the number of unknown components of the reactions of the pair while the number of kinetostatic equations does not increase. In order for the problem of force analysis to remain solvable, it is necessary to introduce additional conditions, the number of which is equal to the number of additional unknowns. Usually, additional conditions are selected allowing for the design features of the elements of kinematic pairs, which allow making some a priori assumptions about the nature of the normal forces distribution. The paper considers the formation of such conditions, i.e., essentially, the examples of constructing computational models of kinematic pairs with friction. A force calculation of the mechanism with allowance for friction is shown, which is reduced to the joint solution of the kinetostatic equations and additional equations describing the models of kinematic pairs. It is also shown that for the given kinematic parameters of motion, the system of force calculation equations has one solution, several solutions, or no solution at all.

**Keywords** Friction force · Dry friction · Models of kinematic pairs · The Painleve paradox

Y. A. Semenov (✉) · N. S. Semenova
Peter the Great Saint-Petersburg Polytechnic University, St.-Petersburg, Russia
e-mail: tmm-semenov@mail.ru

N. S. Semenova
e-mail: tmm-nss@yandex.ru



A. N. Evgrafov (ed.), *Advances in Mechanical Engineering*,
Lecture Notes in Mechanical Engineering,
https://doi.org/10.1007/978-3-030-11981-2_15

# 1 Introduction

The assumption of ideality for kinematic pairs is widely used in the theory of mechanisms and machines. When analyzing the motion of mechanisms, it allows using the D'Alembert–Lagrange equation and the Lagrange equation of the second kind which does not contain the reactions in kinematic pairs as unknowns.

However, some cases have to allow for friction forces. The most important are the forces of sliding friction occurring on the contact surfaces forming kinematic pairs. Let us separate out on the contact surface of two bodies (links) elementary area d$S$ in the vicinity of a certain point $A$ (Fig. 1). The interaction forces which occur in this area and applied to one of the links of the kinematic pair can be reduced to the main vector and the main moment of these forces. Let us decompose the main vector into two components: normal force d$\mathbf{N}$, directed along the normal to surface $S$, and force d$\mathbf{F}$, lying in the tangent plane. The main moment relative to point $A$ is also decomposed into normal d$\mathbf{M}_\mathrm{p}$ and tangential d$\mathbf{M}_\mathrm{r}$ components.

Force d$\mathbf{F}$ is called the sliding friction force; moment d$\mathbf{M}_\mathrm{r}$ is the rolling friction moment, and moment d$\mathbf{M}_\mathrm{p}$ is the frictional moment of pivoting. By their physical nature, friction forces are motion resistance forces; it follows that force d$\mathbf{F}$ is opposite to the vector of relative velocity $\mathbf{v}_\mathrm{sl}$ (sliding velocity) at point A, and vectors d$\mathbf{M}_\mathrm{r}$ and d$\mathbf{M}_\mathrm{p}$ are opposite in the direction of tangential $\boldsymbol{\omega}_\tau$ and normal $\boldsymbol{\omega}_\mathrm{n}$ components of the vector of relative angular velocity, respectively.

The sliding friction force in the general case can be represented in the form of

$$\mathrm{d}\mathbf{F} = -|\mathrm{d}F|(|v_\mathrm{sl}|, |\mathrm{d}N|) \cdot \frac{\mathbf{v}_\mathrm{sl}}{|v_\mathrm{sl}|}. \tag{1}$$

The dependence of the force or the friction moment on the normal force and velocity is called the friction law. Various frictions laws are considered.

If there is a lubricating fluid between the contacting links, we speak of fluid friction. In this case, the friction force changes according to Newton's law:

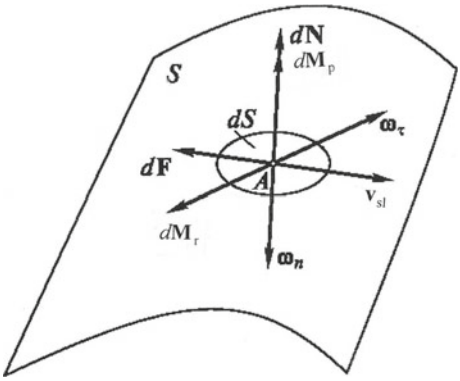


**Fig. 1** Friction forces in the kinematic pair

$$\mathrm{d}\mathbf{F} = -\eta \mathrm{d}S \frac{\mathrm{d}\mathbf{v}_{\mathrm{sl}}}{\mathrm{d}y}, \tag{2}$$

where $\eta$ is the viscosity coefficient; $\mathrm{d}S$ is the contact surface; and $\mathrm{d}\mathbf{v}_{\mathrm{sl}}/\mathrm{d}y$ is the velocity gradient, i.e., the velocity variation in height.

In dissipative devices (dampers), the law of viscous friction is usually considered:

$$\mathrm{d}\mathbf{F} = -b\,\mathrm{d}\mathbf{v}_{\mathrm{sl}}, \tag{3}$$

where $b$ is the resistance coefficient.

If the layer of lubricant, placed between two contacting surfaces, only partially separates them, then there is semifluid friction.

Numerous experimental studies have shown that during the force analysis of mechanisms, it is possible in the majority of cases to rely on the dry friction law, known in physics as the Amontons–Coulomb law. According to this law, the modulus of sliding friction force $\mathrm{d}F$ is taken proportional to the modulus of normal component of the reaction $\mathrm{d}N$:

$$|\mathrm{d}F| = f(v_{\mathrm{sl}})|\mathrm{d}N|, \tag{4}$$

where $f(v_{\mathrm{sl}})$ is the dimensionless coefficient of sliding friction determined experimentally; it depends on many factors: properties of the material, of which the contacting elements of kinematic pairs are made: surface finish characteristics, lubricant and the lubricant properties, and finally, on the value of the relative velocity. In the theory of mechanisms and machines, the value of this coefficient is assumed to be given and constant.

From (4) and the above-stated assumption about the force direction results into the following vector relation:

$$\mathrm{d}\mathbf{F} = \left\{ -f|\mathrm{d}N|\frac{\mathbf{v}_{\mathrm{sl}}}{|v_{\mathrm{sl}}|} = -f|\mathrm{d}N|\operatorname{sign}\mathbf{v}_{\mathrm{sl}} \quad \text{and } \mathbf{v}_{\mathrm{sl}} \neq 0, \right. \tag{5}$$

where $\operatorname{sign}\mathbf{v}_{\mathrm{sl}}$ is the sign function.

Formula (5) becomes inapplicable if the sliding velocity at the contact point equals to zero, i.e., if the links which form the kinematic pair are in the state of relative rest. In this case, the friction force in the kinematic pair can be determined from the equilibrium conditions of the links; they turn out to be dependent not on normal reactions but directly on the applied external forces.

The Amontons–Coulomb law can be extended to the rolling and spinning friction:

$$\mathrm{d}\mathbf{M}_{\mathrm{r}} = -k|\mathrm{d}N|\operatorname{sign}\boldsymbol{\omega}_{\tau}; \quad \mathrm{d}\mathbf{M}_{\mathrm{p}} = -k_{\mathrm{p}}|\mathrm{d}N|\operatorname{sign}\boldsymbol{\omega}_{n}, \tag{6}$$

where $k$ and $k_{\mathrm{p}}$ are the coefficients of the rolling and pivoting friction.

Formulae (5) and (6) can be directly used to determine friction forces in a higher kinematic pair with point contact. In the case of a lower kinematic pair and a higher

kinematic pair with contact along the line, the main vector and the main moment of friction forces are determined by integrating the forces and moments occurring in elementary areas along the surface of the line of contact. Thus, for example, the total sliding friction force in the lower kinematic pair can be determined by the formula

$$\mathbf{F} = \int_S \mathrm{d}\mathbf{F} = -\int_S f|\mathrm{d}N|\operatorname{sign}\mathbf{v}_{\mathrm{sl}}, \tag{7}$$

where $S$ is the contact surface.

General information on friction forces in the kinematic pairs of mechanisms was considered in [1–3].

## 2 Models of Prismatic Kinematic Pairs with Friction

In order to use formula (7), it is necessary to know the law of distribution of normal reactions over surface $S$. Determination of this law is a complex task, the solution of which requires considering a dynamic model of a kinematic pair, allowing for the presence of gaps, a lubricating layer, etc. To avoid this, some reliable assumptions about the nature of normal forces distribution over the surface are made, and based on them, the friction forces are expressed through the remaining components of the reactions [4, 5].

The simplest model of a prismatic kinematic pair is given in Fig. 2a. It is assumed that normal interaction forces are reduced to concentrated force $N$, applied at some point $A$ of the slider, if its contact occurs with the bottom rail. When the acting forces change, relocation of the gaps is possible, i.e., transition to the contact with the top rail. In this case, the direction of the normal reaction changes to the opposite one ($N'$) and the point of application passes to point $A'$. Friction force F is directed against movement speed $\dot{x}$. Projecting the forces on the axes and determining their moments relative to origin $O$, we obtain the components of reactions, lying in the motion plane:

$$R_x = -f|N|\operatorname{sign}\dot{x}, \quad R_y = N, \quad M^R = Ne - fhN\operatorname{sign}\dot{x}\,. \tag{8}$$

A more complex model, allowing for the possibility of skewing of the glider and its simultaneous contact with both rails, is given in Fig. 2b. Here, normal reactions are reduced to two forces $N_1$ and $N_2$, applied to points $A$ and $B$. In this case, we obtain:

$$\left.\begin{aligned} R_x &= -f(|N_1| + |N_2|)\operatorname{sign}\dot{x}, \quad R_y = N_1 + N_2, \\ M^R &= (N_2 - N_1)a - fh(N_1 + N_2)\operatorname{sign}\dot{x}. \end{aligned}\right\} \tag{9}$$

In the model shown in Fig. 2c, it is supposed that the forces of normal interaction are distributed according to the linear law.

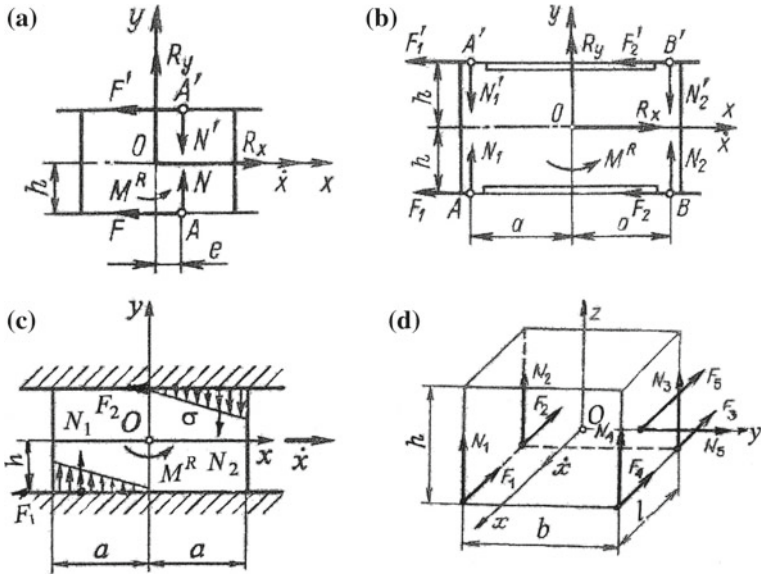


**Fig. 2** Models of friction of the prismatic pair

In Fig. 2d, a slider of a spatial prismatic pair, which can move along axis $x$, is shown. Assuming that normal reactions $N_1$, $N_2$, $N_3$, $N_4$ are applied along the edges and force $N_5$—at the center of the lateral edge, we obtain one of the possible models of a prismatic pair which leads to the following relations:

$$\left.\begin{aligned}
&R_x = -f(|N_1| + |N_2| + |N_3| + |N_4| + |N_5|)\operatorname{sign}\dot{x},\\
&R_y = N_5, \qquad R_z = N_1 + N_2 + N_3 + N,\\
&M^R_{O_x} = 0.5b\,(N_3 + N_4 - N_1 - N_4),\\
&M^R_{O_y} = 0.5l\,(N_2 + N_3 - N_1 - N_2) + 0.5fh(N_1 + N_2 + N_3 + N_4)\operatorname{sign}\dot{x},\\
&M^R_{O_z} = 0.5fb\,(|N_3| + |N_4| + |N_5| - |N_1| - |N_2|)\operatorname{sign}\dot{x}.
\end{aligned}\right\} \tag{10}$$

## 3 Force Calculation of a Sine Mechanism with Allowance for Friction

The calculation of mechanisms allowing for friction forces comes down to the joint solution of kinetostatic equations which contain friction forces as additional unknowns and the equations describing the models of kinematic pairs [6, 7]. In the given position of crank $q$, let us determine normal reactions in the kinematic pairs of the slotted link of a Scotch yoke mechanism (Fig. 3a), if the slotted link mass is $m_3$,

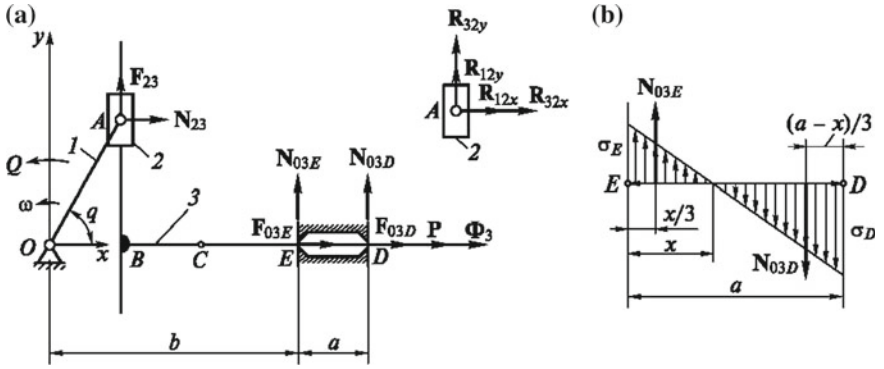


**Fig. 3** Models of friction of the Scotch yoke mechanism

the sliding friction coefficient between the slotted link and the rack is $f$, the friction coefficient between the slotted link and crosshead $f_1$, angular velocity of the crank is $\omega = \text{const}$, the crank length is $l_1$, and the rack size: $a$; $b$. The working load, acting on the connecting link, varies according to the law $P = -P_0 \text{sign}\, v_{30}$, where $P_0$ is the force amplitude, and $v_{30} = \dot{x}_{C3}$ is the slotted link's velocity relative to the rack.

Friction in revolute pairs and gravity are not taken into account. In prismatic pair 0–3, let us bring normal forces to two concentrated forces $N_{03E}$ and $N_{03D}$, and pair 2–3 to one force $N_{23}$. Let us solve the problem by the method of successive approximations and the exhaustive sign search.

Using the assumed models of prismatic pairs with friction, let us write the kinetostatic equations for structural group 2–3:

$$\left.\begin{aligned} \textstyle\sum F_{2,3x} &= P + \Phi_3 + R_{12x} + F_{03E} + F_{03D} = 0, \\ \textstyle\sum F_{2,3y} &= N_{03E} + N_{03D} + R_{12y} = 0, \\ \textstyle\sum M_B &= N_{03E}(b - x_A) + (b + a - x_A) - R_{12} y_A = 0, \end{aligned}\right\} \tag{11}$$

where $x_A = l_1 \cos\, q = l_1 \cos \omega t, \quad y_A = l_1 \sin\, \omega t$.

From the kinetostatic equations of the second link (crosshead):

$$\begin{aligned} \textstyle\sum F_{2x} &= R_{12x} + R_{32x} = 0, \\ \textstyle\sum F_{2y} &= R_{12y} + R_{32y} = 0 \end{aligned}$$

it follows that

$$R_{12x} = -R_{32x} = R_{23x} = N_{23}, \quad R_{12y} = -R_{32y} = R_{23y} = F_{23}.$$

Allowing for these forces from Eq. (11), we obtain

$$N_{23} = -\Phi_3 - P - F_{03E} - F_{03D}, \tag{12}$$

$$N_{03D} = a^{-1}[N_{23} l_1 \sin \omega t + (b - l_1 \cos \omega t) F_{23}], \tag{13}$$

$$N_{03E} = -N_{03D} - F_{23}, \tag{14}$$

where the inertial force of the slotted link

$$\Phi_3 = -m_3 \ddot{x}_{C3} = -m_3 (l_1 \cos \omega t + BC_3)^{\cdot\cdot} = m_3 l_1 \omega^2 \cos \omega t, \tag{15}$$

working load is

$$P = -P_0 \text{sign}\, v_{30} = -P_0 \text{sign}\, [(l_1 \cos \omega t + BC_3)^{\cdot}] = P_0 \text{sign}(\sin \omega t), \tag{16}$$

friction forces are

$$F_{03E} = -f |N_{03E}| \text{sign}\, v_{30} = f |N_{03E}| \text{sign}(\sin \omega t), \tag{17}$$

$$F_{03D} = -f |N_{03D}| \text{sign}\, v_{30} = f |N_{03D}| \text{sign}(\sin \omega t), \tag{18}$$

$$F_{23} = -f_1 |N_{23}| \text{sign}\, v_{32} = -f_1 |N_{23}| \text{sign}[-(l_1 \sin \omega t)^{\cdot}] = f_1 |N_{23}| \text{sign}(\cos \omega t). \tag{19}$$

Assuming that the friction forces are small, we will obtain the recurrence relations based on formulae (12)–(19):

$$\left.\begin{aligned} N_{23}^{(k)} &= -m_3 l_1 \omega^2 \cos \omega t - P_0 \text{sign}(\sin \omega t) - f\left(\left|N_{03E}^{(k-1)}\right| + \left|N_{03D}^{(k-1)}\right|\right)\text{sign}(\sin \omega t), \\ N_{03D}^{(k)} &= a^{-1}[N_{23}^{(k)} l_1 \sin \omega t + f_1 (b - l_1 \cos \omega t)\left|N_{23}^{(k-1)}\right| \text{sign}(\cos \omega t)], \\ N_{03E}^{(k)} &= -N_{03D}^{(k)} - f_1 \left|N_{23}^{(k-1)}\right| \text{sign}(\cos \omega t), \qquad k = 0, 1, 2, \ldots. \end{aligned}\right\} \tag{20}$$

These relations enable finding unknown forces $N_{23}$, $N_{03D}$, and $N_{03E}$ by the method of successive approximations. In this case, the reactions in kinematic pairs without friction are determined first. Then, using the obtained normal reactions, friction forces are found. At the next stage of the calculation, these forces are considered as given forces, and normal components of the reactions are calculated again but taking them into account; then, improved values of friction forces are determined, etc. If this process converges to a certain limiting solution, it is the solution of the force analysis [8–10].

The values of the normal reactions can also be determined from the system of Eq. (11) by the exhaustive sign search:

$$\left.\begin{aligned} &\varepsilon_S \varepsilon_E f N_{03E} + \varepsilon_S \varepsilon_D f N_{03D} + N_{23} = -U, \\ &N_{03E} + N_{03D} + \varepsilon_C \varepsilon_A f_1 N_{23} = 0, \\ &(b - l_1 \cos \omega t) N_{03E} + (b + a - l_1 \cos \omega t) N_{03D} - l_1 \sin \omega t \, N_{23} = 0. \end{aligned}\right\}$$

The desired forces will be determined by Cramer's rule

$$N_{03E} = \frac{\Delta_E}{\Delta}, \quad N_{03D} = \frac{\Delta_D}{\Delta}, \quad N_{23} = \frac{\Delta_A}{\Delta},$$

where

$$\Delta = a - f\varepsilon_S(\varepsilon_E - \varepsilon_D)(\sin\omega t - f_1\varepsilon_A|\cos\omega t|)l_1 + ff_1\varepsilon_S\varepsilon_C\varepsilon_A[b\varepsilon_D - (b+a)\varepsilon_E]$$
$$\Delta_E = U[(\sin\omega t - f_1\varepsilon_A|\cos\omega t|)l_1 + f_1\varepsilon_C\varepsilon_A(b+a)],$$

$$\Delta_D = -U[(\sin\omega t - f_1\varepsilon_A|\cos\omega t|)l_1 + f_1\varepsilon_C\varepsilon_A b], \quad \Delta_A = -Ua,$$
$$\varepsilon_S = \text{sign}(\sin\omega t), \quad \varepsilon_C = \text{sign}(\cos\omega t), \quad \varepsilon_E = \text{sign}(N_{03E}),$$
$$\varepsilon_D = \text{sign}(N_{03D}), \quad \varepsilon_A = \text{sign}(N_{23}), \quad U = m_3 l_1\omega^2\cos\omega t + P_0\varepsilon_S.$$

Given the values $\varepsilon_A = \text{sign}(N_{23}) = \pm 1$, $\varepsilon_D = \text{sign}(N_{03D}) = \pm 1$, $\varepsilon_E = \text{sign}(N_{03E}) = \pm 1$, we obtain $2^3 = 8$ linear systems of equations. Solving them, we compare the obtained signs of reactions $N_{23}$, $N_{03D}$, and $N_{03E}$ with previously specified $\varepsilon_A, \varepsilon_D, \varepsilon_E$. If the signs of forces coincide with $\varepsilon_A, \varepsilon_D, \varepsilon_E$, the found values of the reactions can be considered suitable, otherwise they should be discarded.

Having preserved the original data of the previous problem, we determine the normal reactions in the kinematic pairs of the slotted link of the Scotch yoke mechanism if in prismatic pair 0–3 the normal forces are distributed according to the linear law.

For the normal forces per unit length of the contact line (Fig. 3b), with the linear distribution law, the following relation is true: $\sigma_E/x = \sigma_D/(a-x)$, from which $\sigma_E = x\sigma_D/(a-x)$.

Resultants of the normal forces are

$$N_{03E} = \frac{\sigma_E x}{2} = \frac{x^2}{2(a-x)}\sigma_D, \quad N_{03D} = \frac{a-x}{2}\sigma_D.$$

The friction force acting from the side of stone 2 on connecting link 3,

$$F_{23} = -f_1|N_{23}|\text{sign}(v_{23}) = f_1|N_{23}|\text{sign}(\cos\omega t) = f_1\varepsilon_A\varepsilon_C N_{23},$$

where $\varepsilon_A = \text{sign}(N_{23})$, $\varepsilon_C = \text{sign}(\cos\omega t)$.

From the equilibrium equation

$$\sum F_y = F_{23} + N_{03E} - N_{03D} = 0$$

we will obtain

$$\sigma_D = \frac{2f_1\varepsilon_A\varepsilon_C(a-x)}{a(a-2x)},$$

$$N_{03E} = \frac{x^2}{2(a-x)}\sigma_D = \frac{f_1\varepsilon_A\varepsilon_C x^2}{a(a-2x)}N_{23},$$
$$N_{03D} = \frac{a-x}{2}\sigma_D = \frac{f_1\varepsilon_A\varepsilon_C (a-x)^2}{a(a-2x)}N_{23}.$$

From the moment equilibrium equation

$$\sum M_B = N_{03E}\left(b + \frac{x}{3} - l_1\cos\omega t\right) - \left(b + a - \frac{a-x}{3} - l_1\cos\omega t\right) - N_{23}l_1\sin\omega t = 0$$

we will find

$$x = \frac{a}{3}\cdot\frac{3[f_1\varepsilon_A\varepsilon_C(b - l_1\cos\omega t) + l_1\sin\omega t] + 2f_1\varepsilon_A\varepsilon_C a}{2[f_1\varepsilon_A\varepsilon_C(b - l_1\cos\omega t) + l_1\sin\omega t] + f_1\varepsilon_A\varepsilon_C a}.$$

Here, it is taken into account that the resultants of normal forces $N_{03E}$ and $N_{03D}$ are spaced away from extreme points $E$ and $D$ at distances $x/3$ and $(a-x)/3$, respectively.

Since

$$\sum F_x = P + \Phi_3 + N_{23} + F_{03E} + F_{03D} = 0,$$

then moduli of normal forces

$$N_{23} = -\frac{P + \Phi_3}{1 + f_1 f\varepsilon_S\varepsilon_C\varepsilon_A[\varepsilon_E x^2 + \varepsilon_D(a-x)^2][a(a-2x)]^{-1}};$$
$$N_{03E} = \frac{f_1\varepsilon_A\varepsilon_C x^2}{a(a-2x)}N_{23};\ N_{03D} = \frac{f_1\varepsilon_A\varepsilon_C(a-x)^2}{a(a-2x)}N_{23}.$$

Let us estimate the reactions in the kinematic pairs of the Scotch yoke mechanism (see Fig. 3a) if the mass of the slotted link is $m_3 = 25$ kg. The coefficient of sliding friction between the slotted link and the rack is $f = 0.105$; the coefficient of friction between the slotted link and the crosshead is $f_1 = 0.105$. Angular velocity of the crank is $\omega = 14\ \mathrm{s}^{-1} = \text{const.}$; the length of the crank is $l_1 = 0.6$ m; and the distances are $a = 0.1$ m; $b = 0.7$ m. The working load acting on the slotted link changes according to the law $P = -P_0\,\mathrm{sign}\,v_{30}$, where $P_0 = 430$ N is the force amplitude, and $v_{30}$ is the velocity of the slotted link relative to the rack. The friction in revolute pairs and gravity are not taken into account.

The results of calculating the normal forces for 12 positions of the crank are given in the following table:

| $q$, deg | $N_{03E}$, N | $N_{03D}$, N | $N_{23}$, N |
|---|---|---|---|
| 0 | −520.2 | 255.1 | −2430 |
| 30 | 19,135.4 | −19,878 | −7072.5 |
| 60 | 1,104,842 | −1,129,678 | −236,524.6 |
| 90 | No solution | | |
| 120 | −2260 | 2318.7 | 559.2 |
| | 20,467 (lateral solution) | −20,129 | −3222.6 |
| 150 | −2530.5 | 2695 | 1567.4 |
| 180 | 2843.3 | −2640.2 | 1934.2 |
| 210 | 144,942 | −141,472 | 33,049.6 |
| 240 | No solution | | |
| 270 | No solution | | |
| 300 | −2716.4 | 2666.5 | −474.8 |
| 330 | −4147.6 | 4015.4 | −1259 |

## 4 Conclusion

As it can be seen from the table above, in some positions of the mechanism with given kinematic parameters of motion and given friction coefficients, the system of equations of force calculation does not have a solution at all. From the physical point of view, this means that the movement under study for this mechanism with friction is impossible at any values of driving forces. In this case, we usually imply jamming of the mechanism. A special case of jamming is the self-braking effect: The mechanism cannot be put out of the state of rest, no matter what force is applied to its input link. An increase in the driving force causes in such a mechanism an increase in friction forces, balancing its action.

In fact, the obtained result means that a system with the corresponding parameters cannot be analyzed on the basis of the assumed model of a rigid mechanism and Coulomb friction in the prismatic pair without a gap. The self-braking effect should be analyzed on the basis of the refined model [11–16].

In another position $\left(q = 120^{\circ}\right)$, the system of nonlinear equations has two solutions; in other words, with the same active forces, the mechanism can carry out a given movement with different driving forces and different values of the reactions. It usually happens in such positions of the mechanism, in which self-braking is possible, but the active forces and inertial forces have positive power, i.e., "help" the driving force, causing the "de-braking" effect. It is possible to find out which solution will correspond with the additional values of the reactions and driving forces if we attract additional conditions or develop a new model of the mechanism.

The phenomenon of nonexistence and non-uniqueness of solutions of the dynamic equations of systems with friction has been called the Painleve paradoxes [17], illustrated in the paper under consideration.

## References


1. Kolovsky MZ (1989) Dynamics of machines-L.: mechanical engineering, 263 p
2. Vulfson II, Kolovsky MZ (1968) Nonlinear problems of dynamics of machines. L.: mechanical engineering, 282 p
3. Anh LX (1999) The dynamics of systems with coulomb friction, Theory and Experiment Publishing House of Polytechnical Institute. 300 p
4. Kolovsky MZ, Evgrafov AN, Semenov YA, Slousch AV (2000) Advanced theory of mechanisms and machines. Springer, Berlin, 394 p
5. Dresig H, Holzweißig F (2010) Dynamics of Machinery. Springer, Berlin, 554 p
6. Semenov YA, Semenova NS (2016) Theory of mechanisms and machines in examples and problems. part 2. Publishing House of Polytechnical Institute, 282 p
7. Persson NJ (2000) Sliding friction, Springer, Berlin, 497 p
8. Otsuki M, Matsukawa H (2013) Systematic breakdown of Amontons' law of friction for an elastic object locally obeying Amontons' law, p 1586
9. Evgrafov AN, Kolovsky MZ, Petrov GN (2015) Theory of mechanisms and machines, textbook for university students. Publishing House of Polytechnical Institute. University, with it's, 248 p
10. Evgrafov AN, Petrov GN (2017) Self-braking of planar linkage mechanisms. In: Advances in mechanical engineering. In: Selected contributions from the conference modern engineering: science and education, pp 83–92
11. Ann LX (2011) Dynamics of mechanical systems with coulomb friction. Springer, Berlin, p 272. (Foundations of engineering mechanics)
12. Durango S, Calle G, Ruiz O Analytical method for kinetostatic analysis of the second-class RRR, assur group, allowing for friction in kinematic pairs. J Braz Sos Mech Sci Eng. 200–207
13. Pennestri E, Valenti PP, Vita L (2007) Multibody dynamics simulation of planar linkages with friction. Multibody Syst Dyn 17:321–347
14. Timofeev GA, Panyukhin VV, Yaminsky AV (2017) Analysis of self-braking criteria, news of higher educational institutions. Mech Eng 2:12–18
15. Bowden FP, Tabor D (2007) The friction and lubrication of solids, Oxford University Press, Oxford, 554 p
16. Nosonovsky M (2013) Friction-induced vibrations and self-organization mechanics. Oxford University Press, Oxford, p 244
17. Painlivé P (1895) Lecons sur le frottement, Paris

# Size of a Zone Dangerous by Damage at the Root of Cruciform Weld Joint


**Anton Y. Shlepetinskiy and Konstantin P. Manzhula**

**Abstract** The results of research mode of the "dangerous" pre-destruction zones at the root of cruciform weld joint are presented. A technique for determining the areas of "dangerous" zones in numerical simulation is proposed. The engineering equation to determine the area of the danger zone as a result of numerical modeling of the elastoplastic problem is received.

**Keywords** Pre-destruction zone · Fatigue failure · Lack of fusion · Cruciform weld joint · Scale effect

Lack of fusion in welded joints with fillet welds is stress and strain concentrators and may be due to an imperfect technology of their manufacture or the constructive impossibility of welding the root of the seam. Under cyclic loading, lack of fusion is the source of fatigue crack initiation.

The metal at the tip of the lack of fusion may be in an elastoplastic $\varepsilon_{max} > \varepsilon_{0.2}$ or cyclically inelastic $\sigma_{0.2} > \sigma_{max} > u$ state [1], depending on the level of nominal stress. Here, u is the lower threshold of dangerous fatigue damage stress. In the presence of a plastic zone, there is always an adjacent cyclically inelastic zone $\sigma_{max} > u$ at the tip, which is also dangerous due to damaging effects. These pre-fracture zones are characterized by a volume that is different in laboratory samples and real structures, which determine the manifestation of the scale effect. The study of the scale effect in the fatigue strength of welded joints is devoted to the work [2–7 and others].

In [4, 5], to determine the volumes of metal of «dangerous» (calculated) zones near radius transitions, the configuration of zones is taken as part of a circle in a section the formulas are used:

A. Y. Shlepetinskiy (✉)
Engineering Centre JSC «REP Holding», Saint-Petersburg, Russia
e-mail: A.Shlepetinskiy@reph.ru

K. P. Manzhula
Peter the Great Saint-Petersburg Polytechnic University, Saint-Petersburg, Russia
e-mail: conpaman@gmail.com



A. N. Evgrafov (ed.), *Advances in Mechanical Engineering*,
Lecture Notes in Mechanical Engineering,
https://doi.org/10.1007/978-3-030-11981-2_16

$$V_\sigma = S_u \cdot L = \frac{\pi \cdot r_{f\sigma}^2}{2} L \tag{1}$$

$$V_\varepsilon = S_{\varepsilon 0.2} \cdot L = \frac{\pi \cdot r_{f\varepsilon}^2}{2} L \tag{2}$$

where $S_u$ is the area of the stress zone exceeding $u$, $S_{\varepsilon 0.2}$ is the area of the strain zone exceeding $\varepsilon_{0.2}$, $L$ is the weld length, and $r_{f\sigma}$, $r_{f\varepsilon}$ are the radii of the «dangerous» stress and strain zones determined by formulas:

$$r_{f\sigma} = \frac{\sigma\max - u}{tg\theta_2} = \frac{\sigma\max - u}{G_\sigma} \tag{3}$$

$$r_{f\varepsilon} = \frac{\varepsilon\max - \varepsilon_{0.2}}{tg\theta_1} = \frac{\varepsilon\max - \varepsilon_{0.2}}{G_\varepsilon} \tag{4}$$

where $\theta_2$ is the angle of slope of the line drawn through $\sigma_{\max}$ and $u$, and $\theta_1$ is the angle of slope of the line drawn through $\varepsilon_{\max}$ and $\varepsilon_{0.2}$. The designations used are applied in the schemes of Figs. 1a, b and 2. For the tip of the lack of fusion, the radii of the «dangerous» zones will correspond to the lengths of the segments OA (Fig. 1a) and OB (Fig. 1b), i.e., $r_{f\sigma} = a_B'$ and $r_{f\varepsilon} = a_A'$.

Dependencies for determining stress gradients $G_\sigma$ and strain gradients $G_\varepsilon$ in a cruciform weld joint are given in [8].

The metal volume determination of the computational zone at the tip of the lack of fusion by formulas (1, 2) through the radii of the zones of «dangerous» stresses and strains is approximate. To study the size and configuration of «dangerous» zones, a

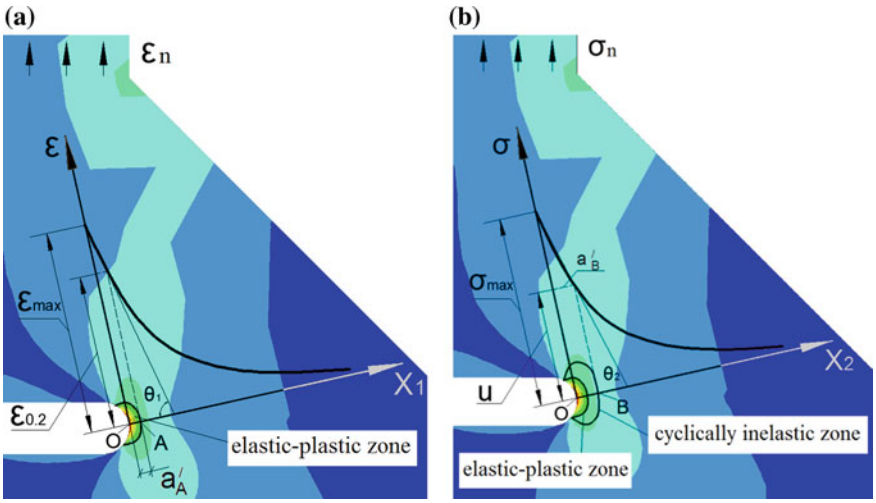


**Fig. 1** Scheme for the definition of strain gradients (**a**) and stresses (**b**) (shown in the loaded model with von Mises stress and strain distributions) [8]

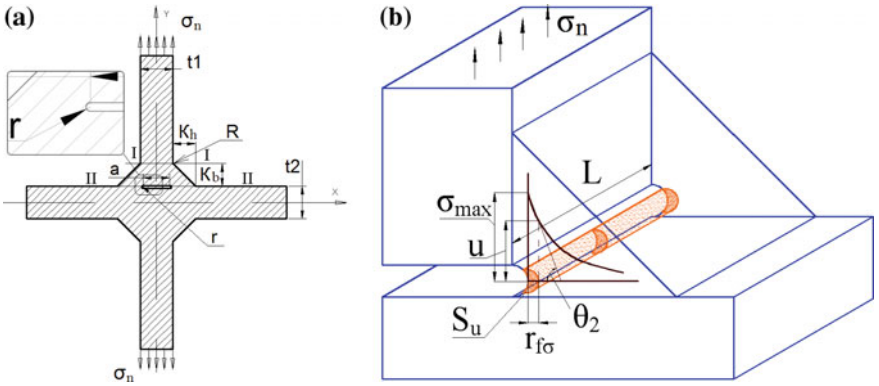


**Fig. 2** Geometric parameters and the cruciform weld joint loading scheme (**a**), scheme for defining the «dangerous» stresses zone (**b**)

numerical simulation of a cruciform weld joint in a finite element modeling environment was carried out with the solution of an elastoplastic problem under loading according to the scheme shown in Fig. 2. The diagram of elastic–plastic deformation of low-alloy 09G2S steel was used [9]

$$\sigma = \sigma_{0.2} \cdot \left(\varepsilon \big/ \varepsilon_{0.2}\right)^{0.114} \tag{5}$$

where $\sigma_{0.2} = 365$ MPa, $\varepsilon_{0.2} = 0.002$.

As a method for determining $S_u$ and $S_{\varepsilon 0.2}$, an analysis can be made of the areas occupied by a sample of nodes from a finite element model with stress values exceeding $u$ and strain values exceeding $\varepsilon_{0.2}$, followed by visualization in Mathcad [10]. The contour is enclosed by a closed polyline for which the area is determined. The error in traversing the sampling contour is no more than 5%. An example of such a sample is shown in Figs. 3 and 4.

Figure 3 shows how the shape of the «dangerous» zone changes with increasing load. With a developed zone of plasticity (calculated case 3c), its shape is significantly different from a circular arc; the error in the calculation according to (2) may exceed twice the value.

Table 1 presents the values $S_{\varepsilon 0.2}$ obtained as a result of numerical modeling of an elastoplastic problem. The «app» index denotes the values obtained from the approximated dependence in the form of a second-order polynomial by the method [11, 12]. The approximation error is estimated as a percentage of the dependence (6) and is included in Table 1

$$\delta_S = \frac{S_{\varepsilon 0.2\,\mathrm{app}} - S_{\varepsilon 0.2}}{S_{\varepsilon 0.2}} \tag{6}$$

**Table 1** Numerical values obtained from the simulation

| $r$ (mm) | $K_b$ (mm) | $K_h$ (mm) | $a/t$ | $t$ (mm) | $\sigma_n/\sigma_{0,2}$ | $S_{\varepsilon 0.2}$ (mm$^2$) | $S_{\varepsilon 0.2\text{app}}$ (Eq. 7) (mm$^2$) | $\delta_S$ (%) | $S_{\varepsilon 0.2\text{app}}$ (Eq. 8) (mm$^2$) | $\delta_S$ (%) |
|---|---|---|---|---|---|---|---|---|---|---|
| 0.5 | 10 | 10 | 1 | 10 | 0.411 | 0.1219 | – | – | 0.111 | 9.15 |
| | | | | | 0.5479 | 0.2976 | 0.242 | 18.68 | 0.464 | −55.93 |
| | | | | | 0.6849 | 1.3192 | 1.529 | −15.90 | 1.411 | −6.98 |
| 0.75 | 10 | 10 | 1 | 10 | 0.411 | 0.1464 | – | – | 0.124 | 15.54 |
| | | | | | 0.5479 | 0.3793 | 0.246 | 35.14 | 0.518 | −36.61 |
| | | | | | 0.6849 | 1.1935 | 1.479 | −23.92 | 1.576 | −32.03 |
| 1 | 10 | 10 | 1 | 10 | 0.411 | 0.1605 | 0.082 | 48.91 | 0.134 | 16.68 |
| | | | | | 0.5479 | 0.4842 | 0.249 | 48.57 | 0.560 | −15.72 |
| | | | | | 0.6849 | 1.1287 | 1.428 | −26.52 | 1.704 | −50.98 |
| 0.25 | 7 | 7 | 0.7 | 10 | 0.411 | 0.082 | 0.027 | 67.07 | 0.094 | −15.08 |
| | | | | | 0.5479 | 0.4077 | 0.503 | −23.38 | 0.395 | 3.01 |
| | | | | | 0.6849 | 1.9893 | 1.991 | −0.09 | 1.203 | 39.55 |
| 0.5 | 7 | 7 | 0.7 | 10 | 0.411 | 0.1234 | 0.126 | −2.11 | 0.114 | 7.66 |
| | | | | | 0.5479 | 0.3501 | 0.548 | −56.53 | 0.477 | −36.39 |
| | | | | | 0.6849 | 2.1621 | 1.983 | 8.28 | 1.452 | 32.84 |
| 0.75 | 7 | 7 | 0.7 | 10 | 0.411 | 0.15 | 0.225 | −50.00 | 0.127 | 15.18 |
| | | | | | 0.5479 | 0.4079 | 0.593 | −45.38 | 0.533 | −30.71 |
| | | | | | 0.6849 | 2.1367 | 1.974 | 7.61 | 1.621 | 24.11 |
| 1 | 7 | 7 | 0.7 | 10 | 0.411 | 0.172 | 0.323 | −87.79 | 0.138 | 20.00 |
| | | | | | 0.5479 | 0.4765 | 0.637 | −33.68 | 0.577 | −21.00 |
| | | | | | 0.6849 | 2.3038 | 1.964 | 14.75 | 1.753 | 23.89 |

(continued)

**Table 1** (continued)

| $r$ (mm) | $K_b$ (mm) | $K_h$ (mm) | $a/t$ | $t$ (mm) | $\sigma_n/\sigma_{0,2}$ | $S_{\varepsilon 0.2}$ (mm$^2$) | $S_{\varepsilon 0.2\text{app}}$ (Eq. 7) (mm$^2$) | $\delta_S$ (%) | $S_{\varepsilon 0.2\text{app}}$ (Eq. 8) (mm$^2$) | $\delta_S$ (%) |
|---|---|---|---|---|---|---|---|---|---|---|
| 0.5 | 7 | 7 | 0.4 | 10 | 0.411 | 0.048 | 0.036 | 25.00 | 0.031 | 35.76 |
| | | | | | 0.5479 | 0.1338 | – | – | 0.129 | 3.44 |
| | | | | | 0.6849 | 0.3315 | 0.651 | −96.38 | 0.393 | −18.53 |
| 0.5 | 7 | 5 | 0.4 | 10 | 0.411 | 0.0249 | – | – | 0.038 | −51.01 |
| | | | | | 0.5479 | 0.078 | – | – | – | – |
| | | | | | 0.6849 | 0.167 | – | – | – | – |
| 0.5 | 7 | 7 | 1 | 10 | 0.411 | 0.29 | 0.562 | −93.79 | 0.262 | 9.61 |
| | | | | | 0.5479 | 1.9421 | 1.605 | 17.36 | 1.098 | 43.44 |
| | | | | | 0.6849 | – | – | – | – | – |
| 0.5 | 10 | 10 | 0.7 | 10 | 0.411 | 0.0653 | – | – | 0.048 | 26.28 |
| | | | | | 0.5479 | 0.1647 | – | – | 0.202 | −22.48 |
| | | | | | 0.6849 | 0.4164 | 0.501 | −20.32 | 0.613 | −47.32 |
| 0.5 | 10 | 10 | 0.4 | 10 | 0.411 | 0.023 | – | – | 0.013 | 43.37 |
| | | | | | 0.5479 | 0.0774 | – | – | 0.055 | 29.48 |
| | | | | | 0.6849 | 0.1581 | – | – | 0.166 | −4.99 |
| 0.5 | 10 | 7 | 1 | 10 | 0.411 | 0.1467 | 0.089 | 39.33 | 0.137 | 6.84 |
| | | | | | 0.5479 | 0.407 | 0.509 | −25.06 | 0.573 | −40.71 |
| | | | | | 0.6849 | 1.9363 | 1.942 | −0.29 | 1.742 | 10.05 |

(continued)

**Table 1** (continued)

| $r$ (mm) | $K_b$ (mm) | $K_h$ (mm) | $a/t$ | $t$ (mm) | $\sigma_n/\sigma_{0,2}$ | $S_{\varepsilon 0.2}$ (mm$^2$) | $S_{\varepsilon 0.2\text{app}}$ (Eq. 7) (mm$^2$) | $\delta_S$ (%) | $S_{\varepsilon 0.2\text{app}}$ (Eq. 8) (mm$^2$) | $\delta_S$ (%) |
|---|---|---|---|---|---|---|---|---|---|---|
| 0.5 | 10 | 10 | 0.7 | 20 | 0.411 | 0.6489 | 0.633 | 2.45 | 0.862 | −32.90 |
| | | | | | 0.5479 | 3.9722 | 4.007 | −0.88 | 3.614 | 9.02 |
| | | | | | 0.6849 | – | – | – | – | – |
| 0.5 | 15 | 15 | 0.7 | 20 | 0.411 | 0.2826 | – | – | 0.324 | −14.58 |
| | | | | | 0.5479 | 1.1706 | 1.771 | −51.29 | 1.357 | −15.92 |
| | | | | | 0.6849 | 4.9218 | 4.879 | 0.87 | 4.127 | 16.16 |
| 1 | 15 | 15 | 0.7 | 20 | 0.411 | 0.4183 | – | – | 0.391 | 6.52 |
| | | | | | 0.5479 | 1.1125 | 1.956 | −75.82 | 1.638 | −47.28 |
| | | | | | 0.6849 | 5.3493 | 4.956 | 7.35 | 4.983 | 6.85 |
| 0.5 | 15 | 10.5 | 0.7 | 20 | 0.411 | 0.3146 | – | – | 0.400 | −27.03 |
| | | | | | 0.5479 | 1.3364 | 2.116 | −58.34 | 1.675 | −25.31 |
| | | | | | 0.6849 | 5.6594 | 5.442 | 3.84 | 5.093 | 10.01 |
| 0.5 | 15 | 15 | 1 | 20 | 0.411 | 0.6886 | 1.121 | −62.79 | 0.745 | −8.18 |
| | | | | | 0.5479 | 4.1993 | 3.837 | 8.63 | 3.122 | 25.67 |
| | | | | | 0.6849 | – | – | – | – | – |
| 0.5 | 15 | 10.5 | 1 | 20 | 0.411 | 0.9826 | 1.547 | −57.44 | 0.919 | 6.44 |
| | | | | | 0.5479 | 5.1163 | 4.481 | 12.42 | 3.852 | 24.70 |
| | | | | | 0.6849 | – | – | – | – | – |
| 0.5 | 10.5 | 15 | 0.7 | 20 | 0.411 | 0.5516 | 0.485 | 12.07 | 0.621 | −12.60 |
| | | | | | 0.5479 | 3.4671 | 3.513 | −1.32 | 2.603 | 24.93 |
| | | | | | 0.6849 | – | – | – | – | – |

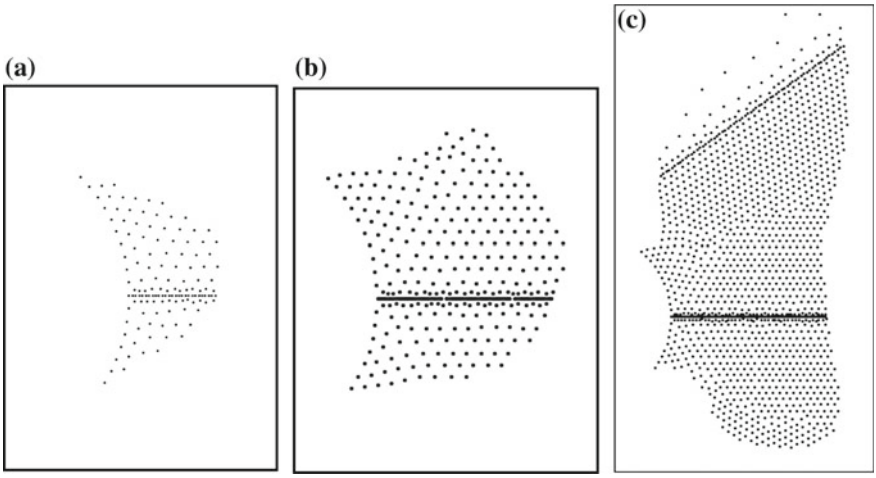


**Fig. 3** Sample of nodes of the finite element model, in which $\varepsilon_{max} > \varepsilon_{0.2}$, at different loading levels **a** $\sigma_n = 150$ MPa, **b** $\sigma_n = 200$ MPa, and **c** $\sigma_n = 250$ MPa (shown for model r = 0.5 mm, $K_b = K_h = 7$ mm, $a/t = 0.7$, $t = 10$ mm)

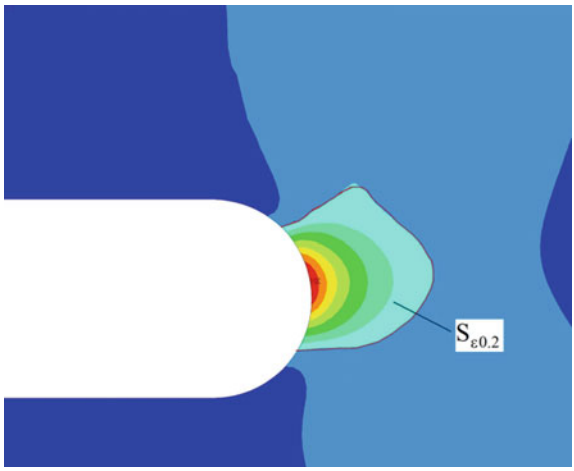


**Fig. 4** Example of the strain distribution at the tip of the lack of fusion at $\sigma_n =$ 200 MPa in the model $r =$ 0.5 mm, $K_b = K_h = 7$ mm, $a/t = 0.7$, $t = 10$ mm, $S_{\varepsilon 0.2}$—the deformation zone exceeding $\varepsilon_{0.2}$

The equation for determining $S_{\varepsilon 0.2}$ depending on the influence of the geometrical parameters of the compound in the range of variation of parameters according to Table 1 in a simplified form, has the form

$$S_{\varepsilon 0.2} = -207.47 + r\left(33.99 + 5.38K_b - 1.287K_h - 41.49\frac{a}{t} - 3.256t - 0.0043\sigma_n\right) + 0.05K_b \cdot \left(-31.81 - 0.073K_h - 9.97\frac{a}{t} - 0.347t - 0.083\sigma_n + 0.074K_b\right) + 0.05K_h \cdot \left(20.86 - 4.44\frac{a}{t} - 0.072t - 0.0194\sigma_n\right)$$

$$+\frac{a}{t}\cdot\left(8.65+0.913t+1.92\frac{a}{t}+0.0414\sigma_n\right)+0.05t$$
$$\cdot(620.74+0.14883\sigma_n-20.61t)$$
$$+0.004\sigma_n\cdot(-31.96+0.0506\sigma_n) \quad (7)$$

By approximating the obtained numerical modeling results in the form of an exponential function, similarly as in [8], we obtain the equation:

$$S_{\varepsilon 0.2}=\frac{0.2011\left(\frac{r}{t}\right)^{0.272}\left(\frac{a}{t}\right)^{2.3358}\left(\frac{K_b}{K_h}\right)^{0.5898}(t)^{2,0192}\left(\frac{\sigma_n}{\sigma_{0.2}}\right)^{0.5898}}{\left(\frac{K_b}{t}\right)^{2.4158}} \quad (8)$$

The obtained dependence (7) and (8), which determines the size of the plastic zone at the tip of the lack of fusion, depending on the geometric parameters and the level of loading, can be used to assess the manifestation of the scale effect during fatigue failure from the lack of welding in the cruciform weld joint.

## References

1. Troshchenko VT (ed) (1985) Tsiklicheskie deformatsii i ustalost' metallov (Cyclic Deformation and Fatigue of Metals). Naukova Dumka, Kiev, in 2 vols (Rus.)
2. Trufiakov VI (ed) (1990) Prochnost' svarnykh soyedineniy pri peremennykh nagruzkakh (Strength of welded joints at variable loads). Naukova Dumka, Kiev, 256 p (Rus.)
3. Yushkevich VN (1988) Teoriya i metody rascheta kharakteristik soprotivleniya ustalosti elementov stal'nykh konstruktsiy kranov (Theory and methods of calculating fatigue resistance characteristics of steel structure elements of cranes). Leningrad, LPI, 681 p (Rus.)
4. Manzhula KP (1997) Teoriya i metody rascheta soprotivleniya ustalosti metallicheskikh konstruktsiy gruzopod"yemnykh mashin (Theory and methods for calculating fatigue resistance of metal structures of lifting machines). PhD thesis. St-Petersburg, 356 p (Rus.)
5. Manzhula KP (2003) Parametry zon ustalostnogo povrezhdeniya v soyedineniyakh s uglovymi shvami pri rastyazhenii-szhatii (Parameters of the zones of fatigue damage in joints with angular seams at tension-compression). In: Proceedings of the Tula State University. Vol. 4 Hoisting-and-transport machines and equipment. Tula, Publishing House of the Tula State University, pp 207–212 (Rus.)
6. Manzhula KP (2005) Analiz masshtabnogo effekta pri perenose rezul'tatov ustalostnykh ispytaniy laboratornykh obraztsov na svarnyye konstruktsii (Analysis of the scale effect in transferring the results of fatigue testing of laboratory samples to welded structures). In: Proceedings of the Tula State University. Vol. 5 Hoisting-and-transport machines and equipment. Tula, Publishing House of the Tula State University, pp 107–114 (Rus.)
7. Manzhula KP (2005) Khuan Pin Parametry zon ustalostnogo povrezhdeniya v soyedineniyakh s uglovymi shvami pri szhatii c izgibom (Parameters of zones of fatigue damage in joints with angular seams during compression with a bend). In: Proceedings of the Tula State University. Vol. 5 Hoisting-and-transport machines and equipment. Tula, Publishing House of the Tula State University, pp 98–108 (Rus.)
8. Manzhula KP, Shlepetinski AY (2016) Stress and strain concentration in weld-joint flaws. Russ Eng Res 36(9):722–726 (Allerton Press, Inc.)

9. Shlepetinskii AY, Manzhula KP (2013) Evaluation of stress-deformed of the state of the lack of fusion top in welded joint crusade, Mater. 3-i mezhd. nauchnoprakt. konf. “Sovremennoe mashinostroenie. Nauka i obrazovanie”. In: Proceedings of the 3rd International Sci.-Pract. Conference “Modern Engineering Industry. Science and Education”. S.-Peterb. Politekh. Univ., St. Petersburg, pp 1073–1081
10. Shlepetinskii AY (2012) Metodika raschetnoy otsenki dolgovechnosti metallokonstruktsiy gruzopod”yemnykh i stroitel’nykh mashin s neprovarami v svarnykh elementakh (The method of calculating the durability assessment of the steel construction lifting and building machines with lack of fusion in welded elements). PhD thesis. St-Petersburg, 176 p (Rus.)
11. Adler YP, Markova EV, Granovskiy YV (1976) Planirovaniye eksperimenta pri poiske optimal’nykh usloviy (Planning an experiment when searching for optimal conditions). Nauka Publishers, Moscow, 279 p (Rus.)
12. Brandt S (2014) Data analysis. Statistical and computational methods for scientists and engineers. Springer International Publishing, 523 p

# Vibractivity of Cycle Machinery Drives in the Accounting of the Space Distribution of Working Bodies Characteristics


**Iosif I. Vulfson**

**Abstract** The paper deals with new problems related to the excitation of oscillations in the drives of cyclic machines, taking into account the spatial distribution of the characteristics of the working elements and the force closure of systems. Dynamic models based on aggregation and general representations of systems with complex structure are proposed. An original method for studying systems with variable parameters is presented, in which the method of the conditional oscillator is applied to variable spatial and temporal arguments. The paper deals with new problems related to the excitation of oscillations in the drives of cyclic machines, taking into account the spatial distribution of the characteristics of the working elements and the force closure of systems with gaps. Dynamic models based on aggregation and general display of systems with complex structure are proposed. The original method of studying systems with variable parameters is presented, in which the conditional oscillator method is applied to the joint consideration of the variability of spatial and temporal characteristics.

**Keywords** Vibrations · Cyclic machines · Gaps · Force closure

## 1 Introduction

The solution of modern problems of machine dynamics is often connected with the analysis of so-called regular oscillatory systems. The term "regularity" means the coincidence of the dynamic structure and parameters of individual subsystems (modules). The theory of regular oscillatory systems is reflected in the works of many prominent scientists. First, a one-dimensional lattice, consisting of the point particles, was studied by Newton, while determining the speed of sound. Further studies are associated with the works of Daniel and Johann Bernoulli, Cauchy, Kelvin, Born,

I. I. Vulfson (✉)
Saint Petersburg State University of Industrial Technologies and Design, Bolshaya Morskaya Str.18, 191186 Saint Petersburg, Russia
e-mail: jvulf@yandex.ru



A. N. Evgrafov (ed.), *Advances in Mechanical Engineering*,
Lecture Notes in Mechanical Engineering,
https://doi.org/10.1007/978-3-030-11981-2_17

Karman, Debye, Brillouin, and others [1, 2]. These works formed the basis of a number of methods, that help to carry out an analytical description of systems with a large number of degrees of freedom, based on the analysis of one structural element of the system. The objects for using the apparatus of the theory of chains were crystal lattices and a number of other problems of theoretical physics.

Among the technical problems of analysis of such class of systems, we can mention the theory of electrical lines, as well as some problems arising in the calculation of deformations and oscillations in frames, girders, etc. In cyclic action machines and automatic lines, one has to deal with regular oscillating systems in connection with the wide spread of dynamically identical modules used for the increased length of the technological process zone, and for the implementation of the same type of technological and transport operations. In such cases, in view of the «natural» desire for unification and interchangeability of individual components or entire units of the machine, arises the certain repeatability of blocks of the dynamic model of the drive. This situation is particularly common in textile machinery, light industry, food, printing, and several other industries [3–6].

The complexity of modern machines and the large dynamic coupling of individual nodes lead to the need to consider vibrational systems with a large number of degrees of freedom. In the analysis, and especially in the dynamic synthesis of such systems, because of the large array of generalized coordinates and variable parameters, certain difficulties arise, for the overcoming of which in mechanics, automatic control, economics, etc., the method of aggregation of the system are used. Applied to the problems of the dynamics of machines in the development of such approaches, continual models were proposed in which the kinematic, elastic, and inertial properties of the mechanisms are displayed by some "pseudo-medium." This allows to operate with a generalized representation of a group of variables and substantially reduce the number of characteristics describing the oscillatory system [3–7].

As a result, the dynamic analysis and synthesis of the system may be simplified, and in many cases to present the solution in analytical form. Note that the use of models with distributed parameters is very effectively combined with the methods of aggregation and decomposition, widely used in solving modern problems of increased complexity in different scientific directions [8, 9]. In this paper, the solution of problems of the dynamics of cyclic machines, considered in a number of works by the author, which are generalized and described in detail in monographs [4, 6], was further developed. As applied to the dynamics of machines, in developing such approaches, continual models are used in which the kinematic, elastic, and inertial properties of mechanisms are replaced by a certain "pseudo-medium". The results of the research make it possible to substantially reduce the vibration activity of the drive and improve the accuracy of reproduction of the specified program movements of the working organs.

The rational dynamic synthesis of oscillating systems in this case plays a special role because of the clearances that can lead to large distortions in the programmed motion of the operating organs, as well as to noise, dynamic loads and vibratory activity of the drive. The clearances, as a rule, are the concomitant factor of any kinematic pair that carries out the connection of the links of the mechanism. Often it

is the size of the clearances that ultimately limits the performance and performance characteristics, which makes it essential to tighten the precision requirements for their manufacture and assembly. Essentially, the kinematic pair should be considered a non-retentive bond, which is usually referred to as mobile connections of units with one-sided contact. Indeed, although the kinematic pair as a whole realizes a two-way coupling, it performs only partially in the gaps, since in the case of a rearrangement, local discontinuities of the kinematic chain, characteristic of systems with non-retentive bonds, take place in the gap. Such relationships can be characterized as pseudo-restraints.

## 2 Dynamic Models. Frequency Analysis Technique

Figure 1 a shows a fragment of the kinematic scheme, which consists of the engine M, the transmission mechanism 1(reducer), the main shaft 2, and drives of the actuators with the ring structure 3. Figure 1b presents a dynamical model with discretely specified elements and its modification in the transformation of this model after transition to a system with distributed parameters (continuum model, Fig. 1c). We accept the following conventions: $J_0$, $J_1$, $J_2$ are moments of inertia; $c$, $\psi$ are the reduced coefficients of torsional stiffness and drive dissipation, $u$—gear ratio; and $\Pi(\varphi)$ is the position function.

The differential equation of free oscillations without taking into account the characteristics of the engine, the forces of resistance, and the force closure is

$$G\frac{\partial}{\partial x}\left[I(x)\frac{\partial \varphi}{\partial x}\right] - \rho(x)\frac{\partial^2 \varphi}{\partial t^2} = 0, \tag{1}$$

where $x$ is the coordinate of shaft axis; $\rho(x) = \partial J/\partial x$ is the change intensity of the moment of inertia along the shaft axis; and $G$ is the shear modulus.

At uniform distribution of the moment of inertia $\rho = J\big/\ell = \text{const.}$, where $\ell$ is the length of a shaft. Then

$$GI\frac{\partial^2 \eta}{\partial x^2} - \rho\frac{\partial^2 \eta}{\partial t^2} - \rho\bar{\omega}^2\frac{\mathrm{d}^2\Pi}{\mathrm{d}\varphi^2} = 0.$$

Here $\eta = \varphi_2(x,t) - \Pi(\varphi)$ is the dynamic error in the section $x$.

The characteristic of the pseudo-medium of one module is the modified transition matrix

$$\tilde{\mathbf{\Gamma}}_* = \prod_s^1 \tilde{\mathbf{\Gamma}}_i = \begin{bmatrix} A(p) & B(p) \\ C(p) & D(p) \end{bmatrix} \quad (i = \overline{1,s}), \tag{2}$$

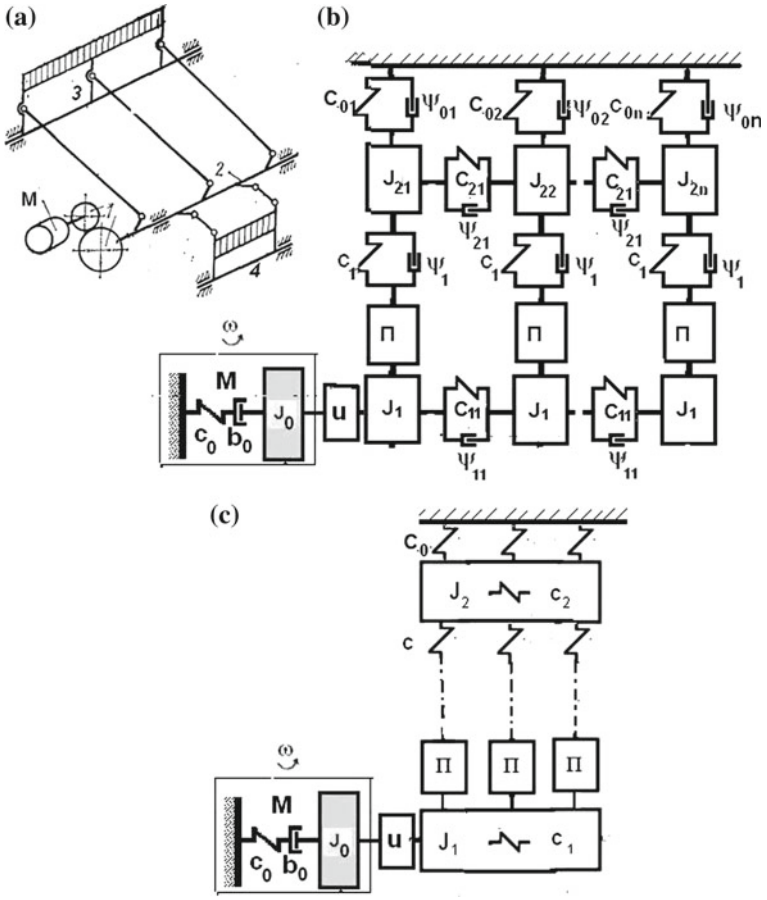


**Fig. 1** Kinematic scheme and modifications of the dynamic drive models of the regular structure: **a** 1—reducer; 2—main shaft; 3, 4—mechanisms of drive of working bodies

where $s$ is the number of elements of the mechanism, $\tilde{\mathbf{\Gamma}}_i$ is the transition matrix of the element $i$.

So, in particular, if the module is formed by a combination of inertial, elastic, and kinematic elements, then

$$\tilde{\mathbf{\Gamma}}_J = \begin{bmatrix} 1 & 0 \\ -p^2 J_*/\ell & 1 \end{bmatrix}; \quad \tilde{\mathbf{\Gamma}}_c = \begin{bmatrix} 1 & \ell/(cn) \\ 0 & 1 \end{bmatrix};$$
$$\tilde{\mathbf{\Gamma}}_\Pi = \begin{bmatrix} \Pi'(\varphi_1^*) & 0 \\ 0 & \Pi'(\varphi_1^*)^{-1} \end{bmatrix}. \tag{3}$$

Here, $\Pi'(\varphi^*) = \mathrm{d}\varphi_2^*/\mathrm{d}\varphi_1^*$ is the first geometric transfer function (below we will take $\Pi' = h_0 \sin\varphi_1$); $J_* = nJ$.

With reference to the analysis and dynamic synthesis of oscillatory systems of the working organs of knitted machines, the problem in question is partially reflected in the work [10].

## 3 Analysis of Oscillations with Variable Intensity of the Spatial Distribution of Characteristics

In contrast to the above case $\rho(x) \neq \text{const}$. Further, following the Fourier method, we seek the solution in the form

$$\varphi(x,t) = X(x,\tau)T(t), \tag{4}$$

where $\tau$ is "slow time".

After substituting (4) into (3) and some transformations, we obtain

$$\begin{aligned} &X'' + 2P(x,\tau)X' + K^2X(x,\tau) = 0;\\ &\ddot{T} + p^2(\tau)T = 0. \end{aligned} \tag{5}$$

Here it is customary:

$$P(x) = 0,5\gamma'(x)/\gamma(x);\ K^2(x,\tau) = p^2(\tau)a(x,\tau)^{-2}\gamma(x)^{-1};$$

$$\begin{aligned} &a^2(x,\tau) = GI(0)/\rho(x,\tau);\ \gamma(x) = I(x)/I(0);\\ &()' = \partial/\partial x;\ (\dot{}) = \partial/\partial t. \end{aligned}$$

On the basis of the method of the conditional oscillator, we have

$$\exp\left\{-\int_0^x P(\xi)\mathrm{d}\xi - 0,5[z(x) - z(0)]\right\}(C_1\cos\Phi + C_2\sin\Phi), \tag{6}$$

where $\Phi(\tau) = \int_0^\ell U(\xi,\tau)\mathrm{d}\xi$; $U(x,\tau) = \sqrt{K^2 - P^2 - P'}$; $C_1$, $C_2$ are the arbitrary constants.

The function is a particular solution (exact or approximate) of the equation of the conditional oscillator [11], which in this case is defined as

$$z'' - 0,5z'^2 + 2U(0,\tau)^2\mathrm{e}^{2z} = 2U(x,\tau)^2. \tag{7}$$

For definiteness, we assume that on the end of the shaft is located a disk (the rotor of the motor, the flywheel), the moment of inertia of which considerably exceeds the reduced moment of inertia of the main shaft, i.e., $J_0 \gg J^*_{\max}$ (see Fig. 1b, model 2). In this case, the boundary conditions for frequency analysis coincide with the conditions for embedding. Then $X(0) = 0;\ X'(\ell) = 0$. In addition, when $I = \text{const.}$ we have $\gamma = 1;\ P = 0;\ U(x,\tau) = K(x,\tau) = p^2/a^2(x,\tau)$. On the basis of (6) and (7), we find that for a slow change in the parameters, the solution coincides with the WKB approximation of the first order [12] and has the form

$$X \approx A\sqrt{a(x,\tau)/a(0,\tau)}\,\sin[p\int_0^x \frac{\mathrm{d}x}{a(x,\tau)} + \alpha]. \tag{8}$$

Hence, after substituting the boundary conditions, we obtain the frequency equation

$$\tan[p\int_o^\ell \mathrm{d}x/a(x,\tau)] + 2p/a'(\ell) = 0. \tag{9}$$

If there is a sufficiently compliant element between the motor and the main shaft (for example, a belt drive, an elastic coupling, etc.), then the following boundary conditions are valid:

$$GIX'(0) = cX(0);\ \ X'(\ell) = 0. \tag{10}$$

Here, $c$ is the stiffness coefficient of the intermediate elastic element.

On the basis of (9) and (10), we obtain

$$\tan\left[p\int_0^\ell \frac{\mathrm{d}x}{a(x,\tau)}\right] - \left[\frac{0,5a' + (a\sigma - 0,5a')}{p - 0,5a'p^{-1}(a\sigma - 0,5a')}\right]_{x=\ell} = 0, \tag{11}$$

where $\sigma = c/GI$.

If the assumption that the function is slow is not right-dimensional, we can use the following modification of the conditional oscillator method. We take as an approximating function

$$a = a_0\big(\zeta x/\ell + 1\big). \tag{12}$$

Here, $\zeta$ is some constant determined by concrete conditions [3–6].

It is easy to see that Eq. (7) is satisfied when substituting (12) and

$$z = \ln\frac{b}{\beta\tau + 1}, \tag{13}$$

where $\beta = \zeta/\tau_*$; $\tau_* = pl/a_0$; $\tau = px/a_0$; $b = \sqrt{1 - 0,25\beta^2}$.

Further, using the boundary conditions and eliminating the trivial solution from consideration $A \neq 0$, we write the frequency equation

$$\tan\left[\frac{b}{\beta}\ln(1+\zeta)\right] = -\frac{2b}{\beta}. \tag{14}$$

On the basis of (14) we find, after which we define $b/\beta$, $\beta$ and $\tau_* = \zeta/\beta$. The required eigenfrequencies are found as

$$p_r = a_0\tau_{*r}/\ell \quad (r = 1, 2, 3, \ldots). \tag{15}$$

## 4 Force Closure

The method considered above can be applied with a change in the stiffness coefficient of the closing spring as a function of the coordinate, as well as in the study of forced oscillations. It should, however, be taken into account that in solving this problem, the Fourier method cannot be directly applied, since the boundary conditions are not homogeneous. This difficulty is eliminated by using a substitution

$$X(x, \tau) = X_1(x, \tau) + w(x, \tau),$$

where $w(x, \tau) = X(0, \tau) + [X(\ell, \tau) - X(0, \tau)]x/\ell$.

Now for the new variable, we have zero boundary conditions: $X_1(0, \tau) = 0$; $X_1(\ell, \tau) = 0$. In the framework of this article, we confine ourselves to an analysis of some qualitative results illustrating the effectiveness of the rational use of force closure in relation to the oscillation system under consideration. For definiteness, let us take the ideal law of motion (without taking into account vibrations and gaps), described by the geometric characteristics given in Fig. 2. Dynamic models (see Fig. 1) do not show operators that display gaps, since by force closure their effect is eliminated. However, in the case of force closure and taking into account the elastic-dissipative characteristics, distortions of the given motion law arise (Fig. 3).

In the general case, the static deformation consists of a constant component due to the preload tention and a variable component proportional to the position function. Curves 2 * and 3 * correspond to two levels of rigidity. Since these curves simultaneously display a slowly varying equilibrium position, order to avoid impactsic excitation the additional inertia force (curves 1, 2, 3), counted from this position, should not cross the gap zone (curves 2, 3). Violation of this condition leads to the excitation of intense oscillations (Fig. 3b, curve 1). When the conditions corresponding to the curves 2 *, 2 are fulfilled (see Fig. 3a, curve 2), the amplitude of the oscillations is substantially reduced. At the same time, the force closure can be lead to additional dynamic errors due to force and parametric vibrations of drive. This

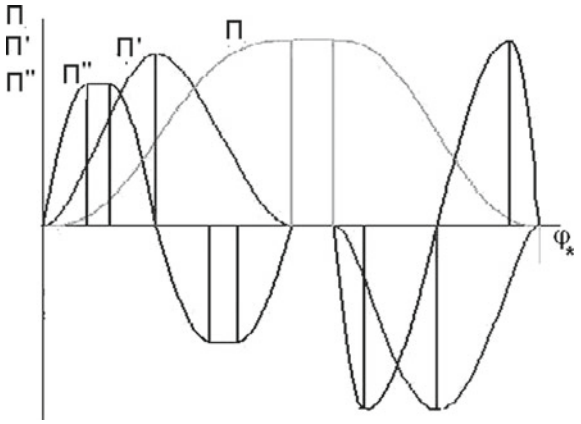


**Fig. 2** Geometric characteristics of the law of motion

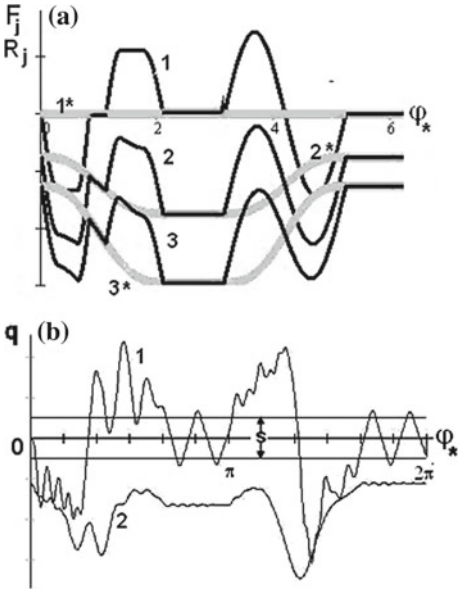


**Fig. 3** To the analysis of the force closure in the case of kinematic excitation

problem, the study of which requires a joint consideration of the characteristics of the engine and the mechanical system of the cyclic machine, is partially reflected in works [13–17], that requires further study.

## 5 Conclusion

The article explores a number of issues related to the further improvement of high-speed cyclic machines, widely used in the textile, light, polygraphic, and a number

of other industries. One of the important tasks in this area is to reduce the vibroactivity of machines, with which the accuracy of reproduction of the laws of program movement of working bodies and the quality of output are directly related. A feature of many machines is the large length of the processing zones. This requires increased attention to the spatial distribution of the dynamic characteristics and suppression of oscillations caused by the collisions in the gaps. In the development of known works in this field, new dynamic models and methods for solving this class of problems are proposed.

## References


1. Brillouin L, Parodi M (1959) Propagation of waves in periodic structures. M Izd Inostr lit
2. Mandelstam LI (1972) Lectures on the theory of oscillations. Nauka, Moscow (in Russian)
3. Vul'fson II (1990) Oscillations of machines with the mechanisms of a cycle action. Mashinostroenie, Leningrad (in Russian)
4. Vul'fson II (2013) Dynamics of cyclic machines. St. Petersburg: Polytechnics (in Russian)
5. Dresig H, Vulfson II (1989) Dynamik der mechanismen. Springer, New York
6. Vulfson I (2015) Dynamics of cyclic machines. Springer, New York, p 2013 (Trans. From Russian, Politechnika, 2013)
7. Palmov VA (1976) Oscillations of elastic-plastic bodies. Moscow. Science (in Russian)
8. Pervozvansky AA (1979) Gaitsgory VG Decomposition, aggregation and approximate optimization. Nauka, Moscow (in Russian)
9. Banakh L, Kempner M (2010) Vibrations of mechanical systems with regular structure. Springer, New York
10. Vul'fson II, Levit VL (1988) Distribution of dynamic loads in closed drives with allowance for gaps and phase mismatches. Machinovedenie 1:75–81
11. Vul'fson II On oscillations of systems with parameters that depend on the time. Appl Math Mech T 33(2): 331–337
12. Freman N, Freman P (1967) JWKB-approximation. North Holland Publ. Com, Amsterdam
13. Veits VL, Kolovsky MZ, Kochura AE (1984) Dynamics of controlled machine aggregates. Nauka, Moscow (in Russian)
14. Kolovsky MZ (1989) The dynamics of machines.—L, Mechanical Engineering
15. Vulfson II (2016) To the problem of the dynamic interdependence of an electric motor and the mechanical drive of a cyclic machine. Theory Mech Mach 32(4):173–182
16. Vulfson I (2017) J Mach Manuf Reliatibility 46(4):322–329
17. Vulfson II (2008) Some peculiarities of the electric drive influence on cyclic dynamics in Mechanical Engineering. In: Selected Contributions from the Conference Modern Engineering: Science and Education, Springer, Saint Pe-tersburg, Russia, Berlin-Heidelberg, 2017, pp 2–14

# Kinematics of the Connecting Rod of a Two-Mobility Five-Link Space Mechanism with a Double Crank


**Munir G. Yarullin, Ilnur R. Isyanov and Alexander P. Mudrov**

**Abstract** The article presents a mathematical model of the kinematics of angular velocities and accelerations of the connecting rod of a two-movable five-link spatial mechanism with a double crank. Based on the analysis of kinematics studies, the nature of the influence of the input parameters of the basic mechanism of the device on the kinematics of the simulator chair is established. The results of analytical calculations are presented in the form of graphs.

**Keywords** Five-link mechanism · Kinematics of the connecting rod · Bennett's mechanism · Two-movement · Double crank · Simulator

## 1 Introduction

Full implementation of the tactical and technical capabilities of modern and advanced fighter aircraft is associated with the emergence of flight overloads +GZ. On advanced aircraft, lateral ±GY and transverse +GX overloads are also expected. At the same time, the currently existing devices for special physical training with the aim of increasing resistance to aerobatic overloads are not effective enough and do not meet modern requirements.

We have developed a simulator based on the spatial five-link mechanism with a double crank [1]. Figure 1 shows a block diagram of a simulator and an experimental laboratory setup.

The main basic component of the simulator is a spatial five-link lever mechanism, obtained based on the Bennett mechanism [2]. In our work [3], the method of

M. G. Yarullin · I. R. Isyanov (✉) · A. P. Mudrov
Kazan National Research Technical University n.a. A.N. Tupolev, Kazan, Russia
e-mail: isyanov1993@mail.ru

M. G. Yarullin
e-mail: isyanov1993@mail.ru

A. P. Mudrov
e-mail: mudrov.alex@yandex.ru



A. N. Evgrafov (ed.), *Advances in Mechanical Engineering*,
Lecture Notes in Mechanical Engineering,
https://doi.org/10.1007/978-3-030-11981-2_18

obtaining a two-moving five-link spatial mechanism with a double crank is considered in detail. Because the geometric axes of the links are crossed in space [4–7], the simulator chair describes a complex spatial trajectory when moving. Analysis of the computer 3D model [8] of the simulator shows that the trajectory of the chair movement contributes to the modeling of loads on the human body. Therefore, it is very important to study the kinematics of angular velocities and accelerations of the chair (connecting rod) of the simulator.

The purpose of the study is to obtain a mathematical model of the kinematics of angular velocities and accelerations, as well as to determine the dependence of the kinematic parameters of the simulator's chair on the input parameters of the leading links.

## 2 The Kinematics of the Connecting Rod

The kinematic parameters of the connecting rod (chair 2) of the simulator are the factors affecting the effectiveness of training in general. They are necessary to justify the optimal training regime. Kinematics of the simulator chair is characterized by its angular velocity and angular acceleration [9–13].

The two-mobility five-star spatial mechanism with a double crank, as the basic mechanism of the simulator, has two input links, a leading crank 1, and a driving rod 4. They are installed on a common axis $O_1$ (Fig. 1) with the possibility of rotation relative to each other and the rack. The angular velocity of the input links is given according to the formulas:

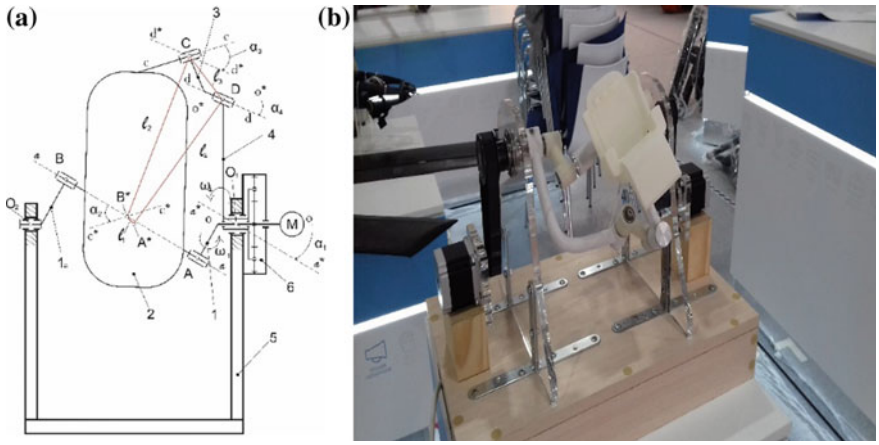


**Fig. 1** Simulator based on two-mobility five-link spatial mechanism with double crank **a** structural diagram, **b** laboratory and experimental setups

$$\omega_1 = \frac{\partial \varphi_1}{\partial t} = \text{const}, \quad \omega_4 = \frac{\partial \varphi_4}{\partial t} = \text{const}, \tag{1}$$

where $\omega_1$—the angular velocity of the leading crank relative to the frame 5; $\omega_4$—the angular velocity of the leading rod relative to the frame 5.

The angular velocity of the connecting rod 2 is determined according to the equation:

$$\overrightarrow{\omega_2} = \overrightarrow{\omega_1} + \overrightarrow{\omega_{3/4}} + \overrightarrow{\omega_4}, \tag{2}$$

where $\omega_2$ is the angular speed of the connecting rod, and $\omega_{3/4}$ is the angular speed of the driven crank 3 relative to the driving rod 4.

The projection of this equation on the fixed axes $X_{O_1}, Y_{O_1}, Z_{O_1}$, rigidly connected with the rack have the form:

$$\begin{cases} \omega_2^{X_{O_1}} = -\omega_{3/4} \sin\alpha_1 \cos(\varphi_1 - \varphi_4); \\ \omega_2^{Y_{O_1}} = -\omega_{3/4} \sin\alpha_1 \sin(\varphi_1 - \varphi_4); \\ \omega_2^{Z_{O_1}} = \omega_1 + \omega_4 + \omega_{3/4} \cos\alpha_1. \end{cases} \tag{3}$$

The module of the angular velocity vector of the chair of the simulator is according to the formula:

$$\omega_2 = \sqrt{\left(\omega_2^{X_{O_1}}\right)^2 + \left(\omega_2^{Y_{O_1}}\right)^2 + \left(\omega_2^{Z_{O_1}}\right)^2} \tag{4}$$

Differentiating expression (3) by time and taking into account that the angular velocities $\omega_1$ and $\omega_4$ are constant values, we obtain the projections of the angular velocities on the coordinate axes $X_{O_1}, Y_{O_1}, Z_{O_1}$:

$$\begin{cases} \varepsilon_2^{X_{O_1}} = -\varepsilon_{3/4} \sin\alpha_1 \cos(\varphi_1 - \varphi_4) + (\omega_1 + \omega_4)\omega_{3/4} \sin\alpha_1 \sin(\varphi_1 - \varphi_4) \\ \varepsilon_2^{Y_{O_1}} = -\varepsilon_{3/4} \sin\alpha_1 \sin(\varphi_1 - \varphi_4) - (\omega_1 + \omega_4)\omega_{3/4} \sin\alpha_1 \cos(\varphi_1 - \varphi_4) \\ \varepsilon_2^{Z_{O_1}} = -\varepsilon_{3/4} \cos\alpha_1. \end{cases} \tag{5}$$

Here $\omega_{3/4}$ and $\varepsilon_{3/4}$ are the angular velocity and acceleration of the driven crank 3 when rotating it relative to the crank 4 around the axis of the hinge D. The values $\omega_{3/4}$ and $\varepsilon_{3/4}$ are defined as the first- and second derivatives of the angle $\gamma$ of rotation of link 3 relative to link 4:

$$\begin{cases} \gamma = \arctan \frac{(\cos\alpha_2 - \cos\alpha_1)\sin(\varphi_1 - \varphi_4)}{(1 - \cos\alpha_1 \cos\alpha_2)\cos(\varphi_1 - \varphi_4) - \sin\alpha_1 \sin\alpha_2}; \\ \omega_{3/4} = \frac{\partial \gamma}{\partial t} = \frac{(\cos\alpha_2 - \cos\alpha_1)(\omega_1 - \omega_4)}{1 - \cos\alpha_1 \cos\alpha_2 - \sin\alpha_1 \sin\alpha_2 \cos(\varphi_1 - \varphi_4)}; \\ \varepsilon_{3/4} = \frac{\partial^2 \gamma}{\partial t^2} = \frac{\sin(\varphi_4 - \varphi_1)(\cos\alpha_2 - \cos\alpha_1)(\omega_1 - \omega_4)^2}{(1 - \cos\alpha_1 \cos\alpha_2 - \sin\alpha_1 \sin\alpha_2 \cos(\varphi_1 - \varphi_4))^2}. \end{cases} \tag{6}$$

From the angle of rotation $\gamma$ of the driven crank 3, pivotally mounted on the driving rod 4, depends on the speed and acceleration of the connecting rod 2. In turn,

the value of $\gamma$ depends on the angles $\alpha_1$, $\alpha_2$ of the crossing of the axes of the hinges of the links, and the angles of rotation $\varphi_1$, $\varphi_4$ of the leading links. As can be seen from the obtained formulas (4) and (5), the chair of the simulator performs a complex spatial movement with variable angular velocities and accelerations.

## 3 Analysis of the Results of Analytical Studies of Kinematic Parameters

The structural parameters of the two-mobility five-link spatial mechanism with a double crank are by determined by the following ratio [14–18]:

$$\frac{l_1}{\sin\alpha_1} = \frac{l_2}{\sin\alpha_2}, \tag{7}$$

where

$l_1 = l_3$ the length of the shortest distance of the leading double crank and the driven crank;

$\alpha_1 = \alpha_3$ the angles of crossing of the axes of the hinges of the leading double crank and the driven crank;

$l_2, = l_4$ the shortest distance lengths of the leading rod and connecting rod (armchair);

$\alpha_2 = \alpha_4$ the angles of crossing of the axes of the hinges of the leading rod and connecting rod (armchair).

The main kinematic calculations of the mechanism were carried out with the following structural parameters: $l_2, = l_4 = 120$mm; $\alpha_2 = \alpha_4 = 90°$; $l_1 = l_3 = 41,042$ mm; $\alpha_1 = \alpha_3 = 20°$.

The leading links of the two-mobility five-link spatial mechanism with a double crank can rotate in one and in different directions and can also be stopped alternately. To study the angular velocities of the connecting rod, we assume that the leading links rotate in one direction with different input parameters.

Figure 2 shows the graphs of the angular velocity of the connecting rod (chair) as a function of time for different values of the angular velocity $\omega_1$ and $\omega_4$ of the leading links of the simulator.

Figure 3 shows the characters of changes in the maximum, minimum, and average values of the angular velocity from the angular velocity of the leading links.

Figure 4 shows a graph of the dependence of the angular velocity of the connecting rod on time at different ratios of the leading links $k = \omega_1/\omega_4$ and graphs of the dependence of the extreme and average angular velocities of the connecting rod on the ratio.

Based on the analysis of the graphs obtained (Fig. 2–4), we can draw the following conclusions:

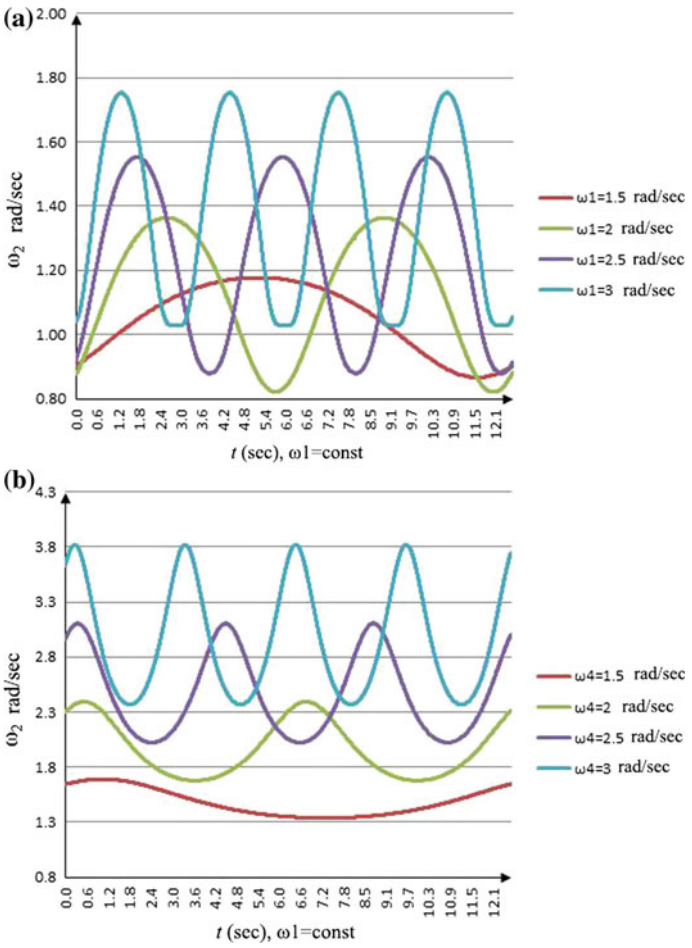


**Fig. 2** Dependence of the angular velocity of the connecting rod on time at **a**—$\omega_4$ = const, **b**—$\omega_1$ = const

1. The uniform rotational movement of the leading links of the simulator is converted into an uneven rotational movement of the connecting rod (chair) relative to the fixed coordinates.
2. The angular velocity of the leading $\omega_1$ and $\omega_4$ links have a great influence on the change in the angular velocity $\omega_2$ of the connecting rod (chair). With an increase in the angular velocity of 1.5 rad/s $\leq \omega \leq$ 3 rad/s, one leading link is an increase in the angular velocity of the connecting rod mechanism.
3. Extreme and average values of the angular velocity of the connecting rod of the mechanism increase with increasing values of the angular velocities of the driving crank and driving rod.

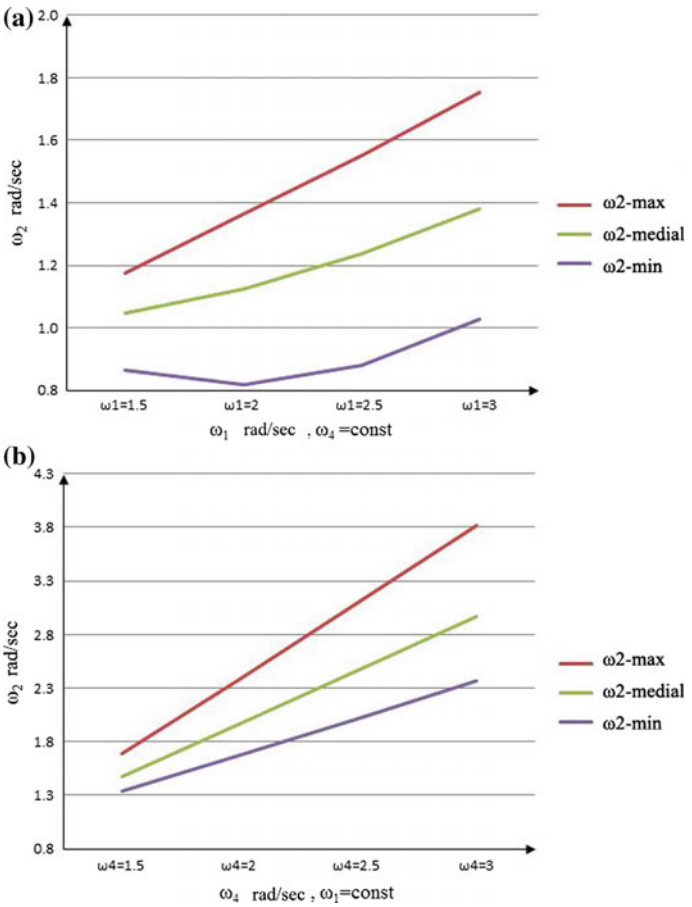


**Fig. 3** Dependence of extreme and average values of the angular velocity of the connecting rod on the angular velocity of the leading links at **a**—$\omega_4 = \text{const}$, **b**—$\omega_1 = \text{const}$

4. According to Fig. 4, the angular velocity values of the connecting rod decrease when the ratio of the angular velocities of the leading links tends to unity $k = 1$.

## 4 Conclusion

Based on the analysis of kinematics research, the nature of the influence of the input parameters of the basic mechanism of the device on the kinematics of the simulator chair is established. From the graphs, it can be seen that the kinematic parameters of the connecting rod are sinusoidal and regular.

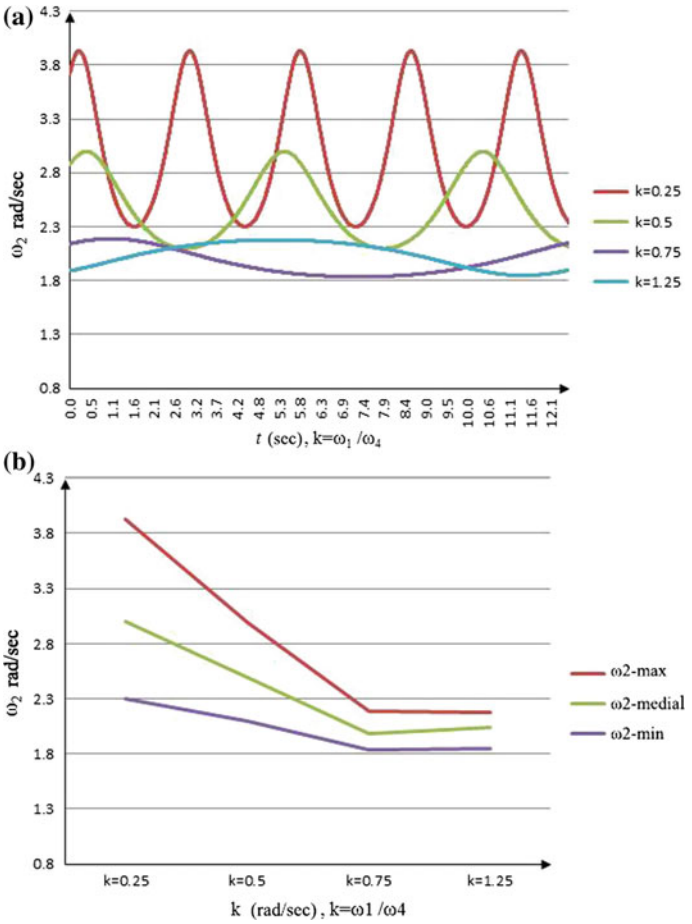


**Fig. 4** Dependence of the angular velocity values of the connecting rod on **a**—time, **b**—ratio coefficient

The obtained equations of angular velocity and angular acceleration of the connecting rod (chair) of the simulator are universal and suitable for determining the kinematic parameters of the connecting rod with different structural parameters of the links of the basic mechanism.

Thus, it can be assumed that the use of a two-mobility five-link spatial mechanism with a double crank as the basic mechanism of the simulator makes it possible to effectively simulate the overload on the human body. Due to the complex spatial motion with variable angular velocity and acceleration, it is possible to simulate the conditions of high and low gravity.

## References


1. Yarullin MG, Isyanov RI, Mingazov MR, Khabibullin FF (2017) Pat. 2639062 RU IPC A63B 23/02 the Device for surface dimensionless machining of parts. publ. 19.12.2017 bull. No. 35 (rus.)
2. Yarullin MG, Mudrov AG, Mingazov MR, Galiullin IA (2015) The 1DOF and 2DOF spatial mechanisms with revolute pairs p 175. Kazan: KNITU-KAI Press
3. Yarullin MG, Isyanov IR (2017) Structural study of a two—mobility five-link space mechanism with a double crank. In: Radkevich MM, Evgrafova AN (eds) Modern machine building. Science and Education: materials of the 6th Intern. Scientific-practical. Conference. SPb .: Publishing house of Polytechnic. Univ., p 239–249, ISSN 2223-0807 https://doi.org/10.1872/mmf-2017-20 (rus.)
4. Bennett, GT (1903) A new mechanism. «Engineering» vol. 76, pp 777–778 London
5. Evgrafov AN, Petrov GN (2014) Selection of drives of a multimotor mechanism with redundant inputs. Modern machine building. In: Radkevich MM, Evgrafova AN (eds) Science and education: materials of the 4th Intern. Scientific-practical. Conference, pp 184–191. SPb: Publishing house of Polytechnic. Univ., ISSN 2223-0807(rus.)
6. Semenov YA, Semenova NS (2014) Static analysis of flat lever mechanisms Modern machine building. In: Radkevich MM, Evgrafova AN (eds) Science and Education: materials of the 4th International Scientific-practical. Conference. SPb: Publishing house of Polytechnic. Univ, pp 107–118. ISSN 2223-0807 (rus.)
7. Mudrov PG (1976) Spatial mechanisms with rotational pairs, Kazan Agricultural Institute named after M.Gorky, 1976. 11(rus.)
8. Evgrafov AN, Petrov GN (2016) Computer modeling of mechanisms. In: Evgrafova AN, Popovich AA (eds) Modern machine building: science and education: materials of the 5th International Scientific-practical. Conference. SPb: Publishing house of Polytechnic. Univ, pp 203–215. ISSN 2223-0807.1(rus.)
9. Nigmatullina FR, Tereshin VA Kinematic study of the telescope. In: Radkevich MM, Evgrafova AN (2014) Modern machine building. Science and Education: materials of the 4th Intern. Scientific-practical. Conference. pp 237–246. SPb: Publishing house of Polytechnic. Univ. ISSN 2223-0807
10. Yarullin MG, Khabibullin FF, Isyanov IR (2016) Nonlinear crushing dynamics in two-degree of freedom disintegrator based on the Bennett's linkage. Vibroengineering PROCEDIA, vol. 8, p 477–482, ISSN 2345-0533
11. Yarullin MG, Isyanov IR, Mudrov AP (2016) Kinematics of a flat two-link five-link lever mechanism. In: Radkevich MM, Evgrafova AN (eds) Contemporary mechanical engineering: science and education: materials of the 5th International Scientific-practical. Conference. pp 297–305. SPb .: Publishing house of Polytechnic. Univ ISSN 2223-0807(rus.)
12. Yarullin MG, Isyanov IR (2015) Two—mobility five-linkage mechanism. In: Tupolev AN (ed) Bulletin of KSTU 2015. Vol. 2. ISSN 2078-6255(rus.)
13. Mudrov AP (2004) Use of spatial five- and six-link differential mechanisms in mixing technology. 100 years of Bennett's mechanism. In: Materials of the international conference on the theory of mechanisms and machines. pp 117–124. Kazan: RIC "School", (rus.)
14. Yarullin MG, Khabibullin FF (2017) Theoretical and practical conditions of bennett mechanism workability, advances in mechanical engineering, Lecture notes in mechanical engineering, Springer, International Publishing AG 2017, pp. 145-153. ISSN 2195-4356, https://doi.org/10.1007/978-3-319-53363-6
15. Yarullin MG, Khabibullin FF (2017) Geometry of the kinematic chain and links of the Bennett mechanism. In: Radkevich MM, Evgrafova AN (eds) Modern machine building. Science and Education: materials of the 6th Intern. Scientific-practical. Conference, pp 262–274. SPb .: Publishing house of Polytechnic. Univ, ISSN 2223-0807 (rus.)

16. Yarullin MG, Faizov MR (2017) Synthesis of spherical quadruplets with rotational pairs in the SOLIDWORKS program. In: Radkevich MM, Evgrafova AN (eds) Modern machine building. Science and Education: materials of the 6th International Scientific-practical, pp 250–261. Conference. SPb: Publishing house of Polytechnic. Univ, ISSN 2223-0807 (rus.)
17. Yarullin MG, Faizov M.R (2017) Kinematics of the balancer of a spherical quadruple. XXIII Tupolev readings (school of young scientists): International youth scientific conference, November 8–10, Conference proceedings. Collection of reports: in 4 volumes—Kazan: Publishing House of the Academy of Sciences of the Republic of Tatarstan, p 763.—T. 3. P.258-262 ISBN 978-5-9690-0395-8 (rus.)
18. Mingazov MR, Yarullin MG (2014) Kinematics of the characteristic points of the working links of the spatial 4R mechanism as an activator of the mixing processes. Bulletin of Izhevsk State Technical University named after M. Kalashnikov. Izhevsk: Publishing house of IzhSTU named after M.T. pp 34–38. Kalashnikov,—T. 3. (rus.)

# Calculation of Equivalent Stiffness of Corrugated Thin-Walled Tube


**Tatiana V. Zinovieva**

**Abstract** The problem of calculation of the stiffness of a rod equivalent to corrugated thin-walled tube is considered. Tensile stiffness, bending stiffness, and shear stiffness are found from solving static problems for a corrugated shell. A version of the classical theory of thin shells is used. The equivalent stiffness found was used to calculate the statics and stability of corrugated tube as a rod.

**Keywords** Equivalent stiffness · Corrugated tube · Corrugated shell · Elastic rod · Statics · Stability

## 1 Introduction

At present, steel-corrugated tubes are actively used in engineering practice. The popularity of such tubes is due to their high strength characteristics and low metal consumption. Large-diameter corrugated tubes (1–15 m) are used in the construction of tunnels and water-flow tubes; the main area of application for small-diameter tubes is heating and water systems, protection of electrical wiring [1, 2].

The peculiarity of corrugated tubes is small relative wall thickness, as a result of which their behavior under load is best investigated with the help of a shell model. However, the equations corresponding to it can lead to an excessively complex problem for engineering evaluations.

As an alternative, it is proposed to use the equivalent rod model to calculate thin wall tubes. At the end of the nineteenth century, Engesser, solving problems of stability, conditionally replaced a composite rod of the type of a lattice rack with an equivalent solid one with effective stiffness [3]. The aim of this study is to calculate the stiffness of the rod equivalent to corrugated tube. Tensile stiffness, bending stiffness, and shear stiffness are calculated.

T. V. Zinovieva (✉)
Institute for Problems in Mechanical Engineering Russian Academy of Sciences, St.-Petersburg, Russia
e-mail: tatiana.zinovieva@gmail.com



A. N. Evgrafov (ed.), *Advances in Mechanical Engineering*,
Lecture Notes in Mechanical Engineering,
https://doi.org/10.1007/978-3-030-11981-2_19

The tube is modeled by a corrugated elastic shell, and equivalent stiffness is found from the solution of static problems for the shell. A variant of the classical theory of shells, built on the basis of Lagrangian mechanics [4–6], was used in this paper. The displacements of a corrugated tube under static load are found numerically, a shell model and two rod models (with equivalent and axial-dependent stiffness) are used. The problem of stability of the corrugated tube under axial force was also solved, and a comparison was made with the results obtained by the finite element method in the Ansys Program.

The presented results continue the studies carried out in [7, 8] papers, where the calculations of the statics and dynamics of the shells of rotation of an arbitrary meridian were considered.

1. Corrugated tube as a shell
   To determine the equivalent stiffness of the tube, we consider a series of linear static problems for a corrugated shell and find its displacements under a given load. Then, we define the necessary stiffness by comparing the results with the solutions found using the rod model.
   Let us consider a shell, and the surface is formed by the revolution of a meridian around the axis $x$. The meridian is defined by a relation between cylindrical coordinates and the arc coordinate: $x = x(s)$, $\rho = \rho(s)$, and its position on the surface is defined by an angle $\theta$ (Fig. 1).
   The radius vector of any surface point is defined by the equality

$$\boldsymbol{r}(\theta, s) = x(s)\boldsymbol{i} + \rho(s)\boldsymbol{e}_\rho(\theta), \quad \boldsymbol{e}_\rho = \boldsymbol{j}\cos(\theta) + \boldsymbol{k}\sin(\theta),$$

   where $\boldsymbol{i}, \boldsymbol{j}, \boldsymbol{k}$ are the unit vectors of the Cartesian frame of reference along the axes, respectively. The unit vector of the tangent to the parallel is $\boldsymbol{e}_\theta =$

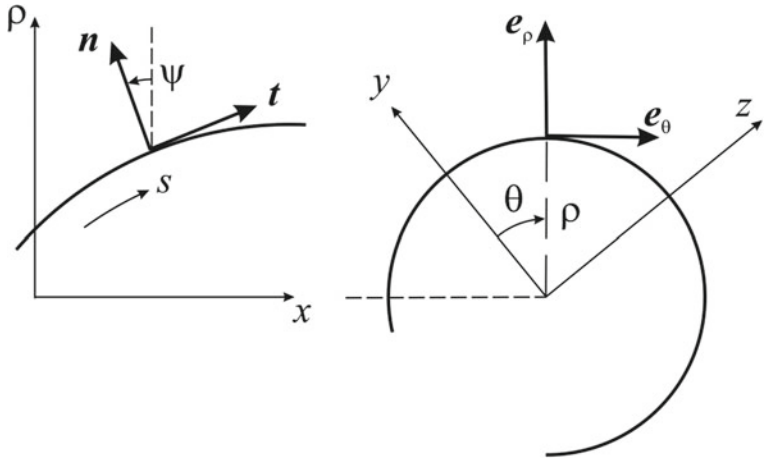


**Fig. 1** Revolution surface

$-\boldsymbol{j}\sin(\theta)+\boldsymbol{k}\cos(\theta)=\boldsymbol{e}'_\rho$. For the unit vectors of the tangent and the normal to the meridian in its plane, it holds

$$\begin{aligned}&\boldsymbol{t}=\partial\boldsymbol{r}/\partial s=x'(s)\boldsymbol{i}+\rho'(s)\boldsymbol{e}_\rho(\theta),\quad x'=\cos\psi,\ \rho'=\sin\psi,\\&\partial\boldsymbol{t}/\partial s=\omega\boldsymbol{n},\quad \omega\equiv\psi'(s),\ \boldsymbol{n}\equiv-\boldsymbol{i}\sin\psi+\boldsymbol{e}_\rho\cos\psi,\end{aligned}\tag{1}$$

where $\omega$ is the curvature of the meridian, and $\rho^{-1}$ of the parallel.
The external load on the shell is given by the vectors of the force $\boldsymbol{q}$ and moment $\boldsymbol{m}^\times$ distributed over the area, and the external force $\boldsymbol{P}^0$ and moment $\boldsymbol{M}^0$ act on the unit length of the contour. Symmetric tensors $\boldsymbol{\tau}$ and $\boldsymbol{\mu}$ determine the internal force factors in the shell. The rotation is related to the displacement by the orthogonality condition.
The shell displacement vector contains three components, namely $\boldsymbol{u}=u_\theta\boldsymbol{e}_\theta+u_t\boldsymbol{t}+u_n\boldsymbol{n}$. On each shell contour, four scalar conditions should be specified [9]. In the case of rigid fixed edge, $u_\theta=u_t=u_n=0$ and $\gamma_\theta\equiv\partial_s u_n=0$.
On a free contour with the normal $\boldsymbol{t}$, the tensile force $T_t=P^0_t$, the bending moment $\mu_t=M^0_\theta$, and two combinations linking the torque moment with the force components are defined:

$$F_\theta\equiv P^0_\theta+\rho^{-1}\cos\psi M^0_t,\quad F_n\equiv P^0_n+\rho^{-1}\partial_\theta M^0_t.$$

The equations of elastic shell of revolution in statics can be reduced to a system of the following form [10]:

$$\partial_s Y(\theta,s)=f(Y),\quad Y=(u_\theta,u_t,u_n,\gamma_\theta,F_\theta,T_t,F_n,\mu_t)^T.\tag{2}$$

To determine the coefficients of the system (2), we need to specify the meridian; for a corrugated shell, it can be defined as

$$\rho(x)=R+r\sin\Omega x,\quad \Omega=2\pi/w,\tag{3}$$

where $R$, $r$ are the formative radii, and $w$ is the length of one corrugation. For each point of the meridian, the arc coordinate $s(x)$ is calculated, following which the interpolations $x(s)$, $\rho(s)$ are developed, and the remaining coefficients are calculated by Formula (1).
Let us consider the shell equilibrium in case of a self-balanced periodic load:

$$\begin{pmatrix}q_\theta\\m^\times_\theta\end{pmatrix}=\begin{pmatrix}\bar q_\theta(s)\\\bar m^\times_\theta(s)\end{pmatrix}\sin n\theta,\quad\begin{pmatrix}q_t\\q_n\\m^\times_t\end{pmatrix}=\begin{pmatrix}\bar q_t(s)\\\bar q_n(s)\\\bar m^\times_t(s)\end{pmatrix}\cos n\theta,$$

where $n$ is an integer. The solution of the system (2) is found in an analogous form, $u_\theta$, $F_\theta$ are proportionate to $\sin n\theta$, and the unknowns $u_t$, $u_n$, $\gamma_\theta$, $T_t$, $F_n$, $\mu_t$ to $\cos n\theta$. For the amplitudes, a system was obtained of the form $\bar Y'(s)=\bar f\big(\bar Y\big)$

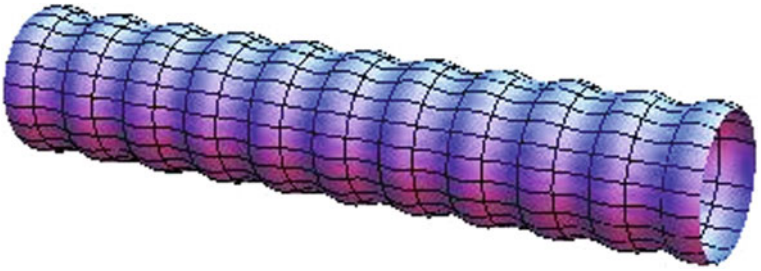

**Fig. 2** Corrugated tube

complemented by the boundary conditions at each edge of the shell. This boundary problem is solved by the finite difference method [11, 12] in the Mathematica package [13].

2. Tensile stiffness
We first determine the tensile stiffness of the equivalent rod. To do this, we consider the problem of static tension of a corrugated shell of rotation.
Let us consider one edge of the shell rigidly fixed and the other at $s = l$, and let us define the displacement $u_x$. The external distributed loads are absent. This is the case of axial symmetry ($n = 0$), and there will be three boundary conditions

$$\begin{aligned} s = 0: &\quad \bar{u}_t = 0,\ \bar{u}_n = 0,\ \bar{\gamma}_\theta = 0; \\ s = l: &\quad \bar{u}_t = u_x \cos\psi(l),\ \bar{u}_n = -u_x \sin\psi(l),\ \bar{\gamma}_\theta = 0. \end{aligned}$$

Having solved the boundary problem, let us find the total force on the shell edge:

$$Q_x = 2\pi\rho(l)\left[\bar{T}_t(l)\cos\psi(l) - \bar{F}_n(l)\sin\psi(l)\right]. \tag{4}$$

The tensile stiffness of the equivalent rod can be found by the formula:

$$b_1 = Q_x L/u_x, \quad L \equiv x(l). \tag{5}$$

Calculations of the 2-mm-thick corrugated shell have been performed with the parameters $R = 50$ mm, $r = 3$ mm, $w = 50$ mm, and $L = 525$ mm (Fig. 2). The material of the shell is steel with the elasticity modulus $E = 200$ GPa and Poisson's ratio $\nu = 0.3$. The equivalent stiffness $b_1 = 37.9$ MN is found.
Alternatively, the calculation of the tensile stiffness of a corrugated tube can be found by the well-known formula for a rod with an annular cross section:

$$\hat{b}_1(x) = ES(x), \quad S(x) = \pi\left(R_2^2 - R_1^2\right), \tag{6}$$

where $S(x)$ is the cross-sectional area, and $R_1$, $R_2$ are the internal and external radii of the corrugation. The difference of stiffness found by formulas (5) and (6) will be shown in Paragraph 4.

3. Bending and shear stiffness
To determine the bending and shear stiffness of the tube, consider the deformation of the shell under the action of a force and a bending moment on the edge $s = l$: $\boldsymbol{P}^0 = P_y \boldsymbol{j}$, $\boldsymbol{M}^0 = M_l \cos\theta \boldsymbol{e}_\theta$ ($P_y$, $M_l$ − const). This load corresponds to the following boundary conditions for amplitudes at $n = 1$:

$$s = 0: \quad \bar{u}_t = 0,\ \bar{u}_n = 0,\ \bar{\gamma}_\theta = 0;$$
$$s = l: \quad \bar{F}_\theta = -P_y,\ \bar{T}_t = P_y \sin\psi(l),\ \bar{F}_n = -P_y \cos\psi(l),\ \bar{\mu}_t = M_l.$$

The total force and the bending moment around the $z$-axis applied will be found by integrating along the contour:

$$P_* = 2\pi\rho(l)P_y, \quad M_* = \int_\Gamma \boldsymbol{k} \cdot \boldsymbol{M}^0 \mathrm{d}\Gamma = \pi\rho(l)M_l. \tag{7}$$

Let us compare the obtained displacements for a shell with a known solution for a Timoshenko beam, which bends in the $xy$-plane under the force $P_*$ and moment $M_*$ specified on the edge $x(l) \equiv L$. It is easy to show that the rotation $\Theta$ and deflection $U$ of an arbitrary section $x = x_*$ of the beam are found by the formulas:

$$\Theta = a^{-1}x_*\left(-P_*\frac{x_*}{2} + P_*L + M_*\right),$$
$$U = a^{-1}\frac{x_*^2}{2}\left(-P_*\frac{x_*}{3} + P_*L + M_*\right) + b_2^{-1}P_*x_*. \tag{8}$$

Knowing the deflection and rotation in any section, it is possible from System (8) to find the stiffness of the rod in bending $a$ and in shear $b_2$. We need to link the displacement in the shell with deflection and rotation of the sections in the beam of Timoshenko. To do this, we use the approximation of the displacement:

$$\boldsymbol{u} = u_y(s)\boldsymbol{j} + \theta_z(s)\boldsymbol{k} \times \rho\boldsymbol{e}_\rho + v(s)\sin\theta\boldsymbol{e}_\theta, \tag{9}$$

here the functions $u_y(s)$ and $\theta_z(s)$ correspond to the displacement and rotation of the shell sections as beam ones with the acceptance of the hypothesis of flat sections; the function $v(s)$ describes the circumferential displacements in the section plane. Using the expression for amplitudes, from (9), we obtain

$$\theta_z = \rho^{-1}(\bar{u}_n \sin\psi - \bar{u}_t \cos\psi), \quad u_y = \bar{u}_t \sin\psi + \bar{u}_n \cos\psi, \quad v = \bar{u}_\theta + u_y. \tag{10}$$

By Formula (10) for an arbitrary coordinate $x_* = x(s_*)$, the rotation $\Theta = \theta_z(s_*)$ and deflection $U = u_y(s_*)$ of the cross section of the equivalent rod can be found, and from the system of Eq. (8) we can find its bending and shear stiffness. They should be calculated in a section remote from the edges, where the approximation (9) is valid.

For the parameters of the tube introduced above, the bending stiffness of the equivalent rod $a = 46.7$ GN mm$^2$ and the shear stiffness $b_2 = 50$ MN were found.

Formulas for calculating the bending and shear stiffness of annular cross section beam are known:

$$\hat{a}(x) = \frac{E\pi}{4}\left(R_2^4 - R_1^4\right), \quad \hat{b}_2(x) = \mu_n N\pi\left(R_2^2 - R_1^2\right), \quad \mu = \frac{E}{2(1+\nu)}, \tag{11}$$

where $\mu$ is the shear modulus of the material, $N = 0.5$ is the shear coefficient for a thin ring [4]. However, their use for thin-walled corrugated tube leads to large errors, which will be shown below.

4. Calculations of corrugated tube as a rod

The found stiffness of the equivalent rod for a given geometry of corrugations can be used for tubes of various lengths, and this is an advantage of the approach under consideration.

We will carry out calculations of a corrugated tube with parameters from Paragraph 2, but with a different length of $L = 750$ mm. We first consider the problem of stretching a tube with an axial force $Q_x = 1$ MN at the end. The other end is fixed. The calculation was carried out using three models—shell, rod with equivalent stiffness $b_1$, and rod with variable stiffness $\hat{b}_1(x)$. For the latter model, the displacement of the rod sections can be found by the formula:

$$u_x(x) = Q_x \int_0^x \frac{\mathrm{d}x}{\hat{b}_1(x)}. \tag{12}$$

The results of calculation of axial displacements are shown in Fig. 3. It has been found that the displacements obtained using the rod model with the equivalent stiffness are practically identical to the ones found using the shell model; the maximum discrepancy is 3% at the edge, to be explained by boundary effects. The discrepancy with the rod model with variable section reaches 70%, and it increases as the amplitude $r$ and frequency $\Omega$ of the corrugation increase.

Next, we calculate the displacement of the tube under a bending force $P_* = 31.4$ kN and a moment $M_* = 15.7$ kN mm at the end of the tube. Calculations are also carried out on three models. Rotation and deflection of sections of a Timoshenko beam with variable stiffness are found by the formulas [14]:

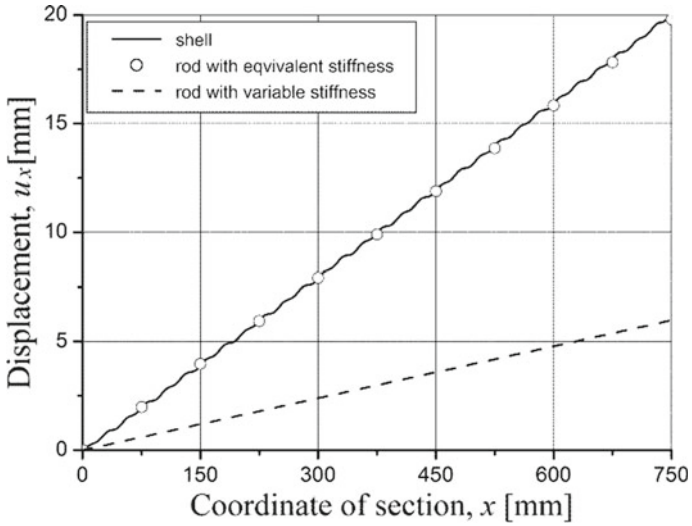


**Fig. 3** Axial displacement of sections of a corrugated tube

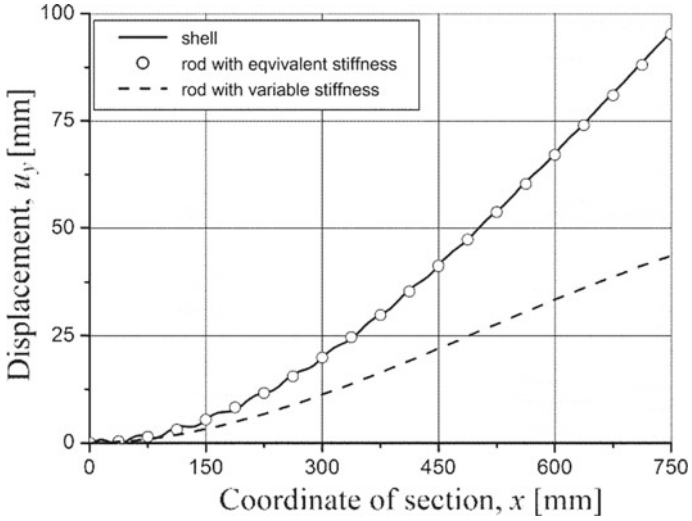


**Fig. 4** Deflection of the corrugated tube under bending

$$\theta_z(x) = \int_0^x \frac{1}{\hat{a}(x)}[P_*(L-x) + M_*]\mathrm{d}x, \quad u_y(x) = P_* \int_0^x \frac{\mathrm{d}x}{\hat{b}_2(x)} + \int_0^x \theta_z(x)\mathrm{d}x. \tag{13}$$

The found displacements are shown in Fig. 4.


**Fig. 5** Buckling mode

It can be seen from the graphs that, as for stretching, a model with equivalent stiffness gives results close to those found by the shell model, and the difference between them is less than 1%. The magnitude of displacement found by the rod model with variable stiffness is much smaller, and the discrepancy with the shell model is more than 50%.

5. The stability of the corrugated tube
We illustrate the possibilities of the tube model with equivalent stiffness on the stability problem. Let the corrugated tube with length of $L = 2.1$ m be rigid-fixed on the one edge and compressed by the axial force $P$ on the other edge with hinge. Let us find the critical value of the force at which the tube loses stability. Neglecting the shear, for the tube deflection function $u(x)$, we have the simplest eigenvalue problem [15]:

$$u^{\mathrm{IV}} + \mu^2 u'' = 0, \quad \mu^2 = P/a,$$

$$u(0) = 0, \quad u'(0) = 0, \quad u(L) = 0, \quad u''(L) = 0. \tag{14}$$

where $a$ is the equivalent bending stiffness. Problem (14) has nontrivial solutions when equality $\mathrm{tg}(\mu L) = \mu L$ is fulfilled, its smallest root is 4.493, where we find the critical value of the compressive force:

$$P_{\mathrm{cr}} = \frac{20.19a}{L^2}. \tag{15}$$

The formula for the critical force considering the transverse shear was first obtained by Engesser [16]:

$$P_{\mathrm{cr}}^{\mathrm{En}} = \frac{P_{\mathrm{cr}}}{1 + b_2^{-1} P_{\mathrm{cr}}}. \tag{16}$$

For the selected tube parameters, we find

$$P_{\mathrm{cr}} = 213,8\,\mathrm{kN}, \quad P_{\mathrm{cr}}^{\mathrm{En}} = 212,9\,\mathrm{kN}.$$

This stability problem was also solved by the finite element method in the Ansys Program [17]. The tube was modeled with shell elements Shell 281. The found critical force is 219.5 kN. The buckling mode of the tube is shown in Fig. 5. The relative difference with the calculation results for the equivalent rod model is no

more than 3%, which makes it possible to recommend the proposed approach for solving stability problems.

## 2 Conclusion

A method for calculating the equivalent tensile stiffness, bending stiffness, and shear stiffness of a corrugated tube is proposed with use of the equations of thin shells of rotation theory. This method allows changing a complex for engineering calculations model of corrugated shell to a rod model with the equivalent stiffness found. This approach can be effectively used in the calculation of corrugated tubes; this is especially important for calculations on stability.

## References

1. Goetsch DL (2014) Structural, civil and tube drafting. Delmar, New York, p 464
2. Yu WW, LaBoube RA (2010) Cold-formed steel design. Wiley, New Jersey, p 528
3. Panovko YaG (2017) Mechanics of solid deformable body (Mekhanika deformiruemogo tverdogo tela). Lenand, Moscow, p 288 (In Russian)
4. Eliseev VV (2003) Mechanics of elastic bodies (Mekhanika uprugih tel) St. Petersburg State Polytechn. University Publishing House, St. Petersburg, p 336 (in Russian)
5. Eliseev VV (2006) To nonlinear theory of elastic shells (K nelineynoy teorii uprugih obolochek) St. Petersburg State Polytechn. University Journal (Nauchno-tekhnicheskie vedomosti SPbGTU) 3:35–39 (in Russian)
6. Eliseev VV, Vetyukov YM (2010) Finite deformation of thin shells in the context of analytical mechanics of material surfaces. Acta Mech 209:43–57. https://doi.org/10.1007/s00707-009-0154-7
7. Zinovieva TV (2012) Computational mechanics of elastic shells of revolution in mechanical engineering calculations. In: Modern engineering: science and education. Proceedings of second international scientific and practical conference. Published by State Polytechnic University, SPb, pp 335–343
8. Zinovieva TV (2016) Calculation of shells of revolution with arbitrary meridian oscillations. In: Modern engineering: science and education. Proceedings international scientific and practical conference. Published by State Polytechnic University, SPb, pp 442–452
9. Eliseev VV, Zinovieva TV (2018) Lagrangian mechanics of classical shells: theory and calculation of shells of revolution. In: Shell structures: theory and applications. Proceedings of the 11th International conference, vol 4. Published by Taylor & Francis Group, London, pp 73–76
10. Zinovieva TV (2017) Calculation of shells of revolution with arbitrary meridian oscillation. Advances in mechanical engineering, Lecture notes in mechanical engineering, Springer, Berlin, pp 165–176. https://doi.org/10.1007/978-3-319-53363-6_17
11. Bakhvalov NS, Zhidkov NP, Kobelkov GG (2011) Numerical methods (Chislennye metody) Binom. Laboratory of knoledges, Moscow, p 640 (In Russian)
12. Chapra SC, Canale RP (2014) Numerical methods for engineers. McGraw-Hill Education, New York, p 992
13. Borwein JM, Skerritt MB (2012) An introduction to modern mathematical computing: with mathematica. Springer, vol. XVI, p 224

14. Yeliseyev VV, Zinovieva TV (2008) Mechanics of thin-wall structures: theory of rods (Mekhanika tonkostennyh konstrukcij: teoriya sterzhnej). St. Petersburg State Polytechn. University Publishing House, St. Petersburg, p 96 (in Russian)
15. Feodosiev VI (2006) Advanced stress and stability analysis: worked examples. Foundations of Engineering Mechanics. Springer Science & Business Media, p 422
16. Svetlitsky VA (2000) Static stability of rods. In: Statics of rods. Foundations of Engineering Mechanics. Springer, Berlin, Heidelberg, pp 89–127. https://doi.org/10.1007/978-3-540-45593-6_4
17. ANSYS Inc. PDF Documentation for Release 15.0

# Vibrations of a Chain in the Braking Regime of the Motion Mechanism in Load-Lifting Machines


**Vassil D. Zlatanov and Svetoslav G. Nikolov**

**Abstract** The article is devoted to the vibrations of a heavy chain in load-lifting machines in the braking regime, assuming that the braking moment is a linear function of the velocity of the motion mechanism and the chain without a mass on the end. A method of approximate analytical solutions of the system of differential equations of motion is presented. The results obtained are illustrated with an example on the basis of the technical characteristics of the crane trolley that the Visual Fortran program is created for.

**Keywords** Vibrations of heavy chain · Eigenfunctions · Bessel functions

## 1 Introduction

The theory of absolutely flexible rope is widely used in various scientific studies, in the calculation and design of engineering devices, machines, musical instruments, etc. Elements of the theory of absolutely flexible rope, which are closest to the engineering problems, from different points of view and with different degrees of completeness are presented in [1–7]. In recent years, there has been an increased interest in the mechanics of heavy ropes, chains, and strings. Various aspects of their mechanics are presented in [8–12].

The mechanical systems with suspended loads are widely used in industry, construction, etc. These systems are basic for hoisting machines, mining machines, etc. The design of such machines requires the creation of rational dynamical models of

V. D. Zlatanov (✉)
University of Food Technologies, Plovdiv, Bulgaria
e-mail: vassilzlatanov@mail.ru

S. G. Nikolov
Todor Kableshkov Higher Transport School, Institute of Mechanics, Bulgarian Academy of Sciences, Sofia, Bulgaria
e-mail: S.Nikolov@imbm.bas.bg



A. N. Evgrafov (ed.), *Advances in Mechanical Engineering*,
Lecture Notes in Mechanical Engineering,
https://doi.org/10.1007/978-3-030-11981-2_20

mechanical systems and the solution of the obtained systems of differential equations of motion.

The aim of this paper was to investigate the vibrations of a heavy chain in the braking regime of load-lifting machines by means of analytical methods, assuming that the braking moment is a linear function of the speed of the motion mechanism.

## 2 Dynamic Model and Differential Equation of the Motion

When operating load-lifting machines, swinging of the chain is observed. This swinging causes both uneven motion of the mechanisms of cranes and other devices, and additional loads on their elements, thus creating inconvenience in their operation. The pendulum vibrations of the chain are practically independent of the elastic vibrations of the crane and can be calculated according to the model, when the metal structure and the transmission of the motion mechanism are absolutely rigid [13, 14]—Fig. 1a.

It is shown in [15] that at small deviations of a chain, it is possible to accept with rather high accuracy that the chain is fixed in the center of the hoisting drum. The dynamic model of the system, with small deviations of the chain, in accordance with [16], is shown in Fig. 1b.

Assuming that the braking moment $T_\mathrm{b}$ is a linear function of the angular velocity $\omega = \dot{\varphi}$, i.e. $T_\mathrm{b} = c' + c_1\dot{\varphi}$ ($c'$ and $c_1$ are constants) and in the absence of a mass on the end ($m_2 = 0$), the differential equations of motion, obtained in [16], take the form

$$M R^2\ddot{\varphi} + \gamma R \int_0^l \ddot{v}\,\mathrm{d}x = -\left(c' + F_W R\right) - c_1\dot{\varphi}, \quad c^* = c' + F_\mathrm{W} R, \tag{1}$$

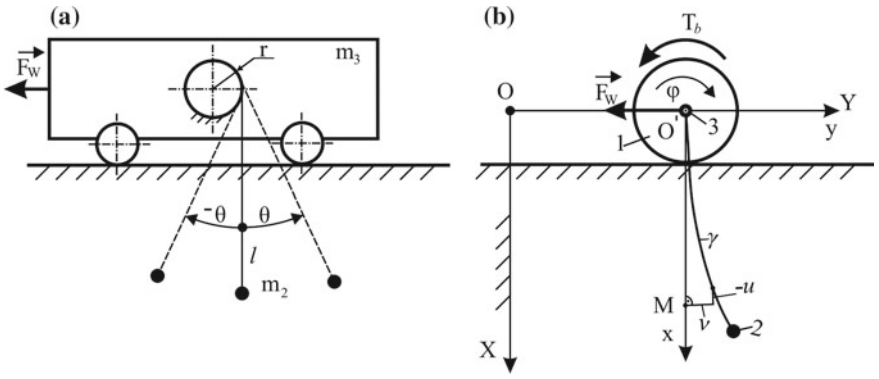


**Fig. 1** **a** Motion mechanism. **b** Dynamic model

$$\gamma g \frac{\partial}{\partial x}\left((l-x)v'\right) = \gamma(\ddot{v} + R\ddot{\varphi}), \tag{2}$$

the boundary conditions are

$$v(0,t) = 0, \quad v(l,t) \neq \infty, \tag{3}$$

and the initial conditions have the form

$$t = 0 \quad \varphi(0) = \varphi_0, \ \dot{\varphi}(0) = \dot{\varphi}_0, \ v(x,0) = f_1(x), \ \dot{v}(x,0) = f_2(x), \tag{4}$$

where $f_1(x)$, $f_2(x)$ are continuous functions, such that $f_1(0) = 0$, $f_2(0) = 0$.

Here, $M = 1.5m_1 + m_3 + \gamma l$, where $m_1$, $R$ denotes the mass and radius of the disk, determined by reduction in the parts of the trolley, crane, or motion mechanism with non-translational motion to the drive wheel shafts; a point mass $m_3$—the mass of the parts of the crane and the motion mechanism with translational motion; $F_W$—resistance force of the motion of the crane or trolley. We consider a flexible, inextensible, homogeneous, heavy chain of length $l$ and $\gamma$ denotes the mass of a unit length of the chain. The position of a generic point $M$ is given by the abscissa $x = OM$ in the equilibrium position, and $v(x,t)$ denotes the horizontal displacement of point $M$ at a moment $t$.

## 3 Solution of the System of Differential Equations

The approximate analytical solution of the system of differential equations "Eqs. 1–2" is determined by two iterations.

### *3.1 First Iteration*

Assuming that $\ddot{v} = 0 \Rightarrow \gamma R \int_0^l \ddot{v} dx = 0$, "Eq. 1" takes the form

$$\ddot{\varphi} + a_0\dot{\varphi} = -c_0, \tag{5}$$

where $a_0 = c_1 / MR^2$, $c_0 = c^* / MR^2$.

With the initial conditions

$$t = 0; \quad \varphi(0) = \varphi_0 = 0, \quad \dot{\varphi}(0) = \dot{\varphi}_0, \tag{6}$$

we easily find

$$\varphi(t) = \frac{\dot{\varphi}_0}{a_0}\left(1 - \mathrm{e}^{-a_0 t}\right) + \frac{c_0}{a_0^2}\left(1 - \mathrm{e}^{-a_0 t}\right) - \frac{c_0}{a_0} t, \tag{7}$$

from where we can find the angular acceleration

$$\ddot{\varphi}(t) = -\underbrace{(c_0 + a_0\dot{\varphi}_0)}_{A_0}\,\mathrm{e}^{-a_0 t} = -A_0 \mathrm{e}^{-a_0 t} \tag{8}$$

Substituting "Eq. 8" into "Eq. 2," we obtain the partial differential equation of motion for the chain

$$g\frac{\partial}{\partial x}\left[(l-x)\frac{\partial v}{\partial x}\right] - \frac{\partial^2 v}{\partial t^2} = -A_0 R \mathrm{e}^{-a_0 t}. \tag{9}$$

We transform "Eq. 9" and the boundary conditions, i.e. "Equation 3," introducing the new independent variable $z$ by means of the equality

$$z^2 = l - x. \tag{10}$$

Equation "Eq. 9" with the variables $v,\ t,\ z$ takes the form

$$\begin{aligned} &-\frac{1}{2z}\frac{\partial}{\partial z}\left[z^2\frac{1}{-2z}\frac{\partial v}{\partial z}\right] - \frac{1}{g}\frac{\partial^2 v}{\partial t^2} = -A_0 R\,\mathrm{e}^{-a_0 t} \Rightarrow \\ &\frac{1}{4z}\frac{\partial}{\partial z}\left(z\frac{\partial v}{\partial z}\right) - \frac{1}{a^2}\frac{\partial^2 v}{\partial t^2} = -A_0 R\,\mathrm{e}^{-a_0 t} \quad \left(a = \sqrt{g}\right), \end{aligned} \tag{11}$$

and the boundary conditions are transformed into the form

$$v\left(\sqrt{l}, t\right) = 0 (x = 0), \quad v(0, t) \neq 0 \quad (x = l). \tag{12}$$

Next, the displacement $v(z, t)$ and the right side of "Eq. 11": $q = -A_0 R\,\mathrm{e}^{-a_0 t}$, which can be considered as a load, are presented by Eigenfunction series $X_n(x)$, $(n = 1, \ldots, \infty)$ of the task for free vibrations [17], i.e., in the form

$$\begin{aligned} v &= X_1(z)T_1(t) + X_2(z)T_2(t) + \cdots, \\ q &= X_1(z)S_1(t) + X_2(z)S_2(t) + \cdots. \end{aligned} \tag{13}$$

The solution of the equation of free vibrations, i.e., the left side of "Eq. 11," is known [5] and for Eigenfunctions $X_k$ is obtained

$$X_k(z) = J_0(\lambda_k z) = J_0\left(\frac{\mu_k}{\sqrt{l}} z\right) \quad (k = 1, 2, 3, \ldots) \tag{14}$$

where $J_0$—Bessel function of the first kind; $\mu_k$—the roots of the Bessel function, $\mu_1 = 2.4048,\ \mu_2 = 5.520,\ \mu_3 = 8.654, \ldots$

To determine the function $S_k(t)$, we multiply both sides of the second "Eq. 13" with $X_n(x)$ and integrate the resulting expression along the entire length of the chain

$$\int_0^l q(t) J_0\left(\mu_k \sqrt{\frac{l-x}{l}}\right) \mathrm{d}x = \sum_{i=1}^{\infty} \int_0^l J_0\left(\mu_k \sqrt{\frac{l-x}{l}}\right) J_0\left(\mu_i \sqrt{\frac{l-x}{l}}\right) S_i(t) \mathrm{d}x. \tag{15}$$

We introduce the new integration variable by means of the equality

$$\frac{l-x}{l} = \frac{w^2}{l^2}$$

On the basis of the property of the orthogonality of the Bessel function on any interval $(0, l)$ [18]

$$\int_0^l w J_0\left(\mu_k \frac{w}{l}\right) J_0\left(\mu_i \frac{w}{l}\right) \mathrm{d}w = \begin{cases} 0, & k \neq i, \\ \dfrac{l^2}{2} J_1^2(\mu_k), & k = i, \end{cases}$$

all the integrals in "Eq. 15" for $k \neq i$ are equal to zero, and if $k = i$ then $l^2 J_1^2(\mu_k)$, where $J_1$ is a Bessel function of the second kind. Therefore, for function $S_k(t)$ from "Eq. 15," we obtain

$$S_k(t) = \frac{q(t) \int_0^l J_0\left(\mu_k \sqrt{\frac{l-x}{l}}\right) \mathrm{d}x}{l^2 J_1^2(\mu_k)}. \tag{16}$$

After substitution of $\frac{l-x}{l} = \frac{w^2}{l^2}$, for the integral in "Eq. 16," we obtain

$$\int_0^l J_0\left(\mu_k \sqrt{\frac{l-x}{l}}\right) \mathrm{d}x = -2 \int_l^0 w\, J_0\left(\mu_k \frac{w}{l}\right) \mathrm{d}w$$

$$= 2 \frac{l^2}{\mu_k^2} \int_0^l \left(\mu_k \frac{w}{l}\right) J_0\left(\mu_k \frac{w}{l}\right) d\left(\mu_k \frac{w}{l}\right) = 2 \frac{l^2}{\mu_k} J_1(\mu_k) \tag{17}$$

and consequently

$$S_k(t) = -2 A_0 R \frac{1}{\mu_k J_1(\mu_k)} \mathrm{e}^{-a_0 t}. \tag{18}$$

The definition of functions $T_k(t)$ is based on the fact that each summand in the right side of the first series in "Eq. 13" causes a motion determined by the corresponding summand of the second series of "Eq. 13." In "Eq. 11," we substitute

$$q = X_k(z)S_k(t), \quad v = X_k(z)T_k(t)$$

and obtain

$$\frac{1}{zX_k}\frac{\partial}{\partial z}\left(z\frac{\partial X_k}{\partial z}\right) = \frac{4}{a^2}\frac{\ddot{T}_k}{T_k} + \frac{S_k}{T_k}. \tag{19}$$

Since the left side of "Eq. 19" is constant and equal to $-\lambda_k^2$ [5], the right side is equal to the same, hence

$$\ddot{T}_k + \frac{\lambda_k^2 a^2}{4}T_k = -a^2 S_k,$$

or

$$\ddot{T}_k + p_k^2 T_k = A_k \mathrm{e}^{-a_0 t}, \quad k = 1, 2, \ldots, \tag{20}$$

where $p_k^2 = \frac{\lambda_k^2 a^2}{4} = \frac{\lambda_k^2 g}{4}$, $\lambda_k = \frac{\mu_k}{\sqrt{l}}$, $A_k = \frac{2g(c^* + c_1\dot{\varphi}_0)}{MR\mu_k J_1(\mu_k)}$.

The solution of "Eq. 20" can be written as a sum of the solution of the corresponding homogeneous equation, obtained with initial conditions, and the particular solution, obtained with zero initial conditions from Duhamel's integral

$$T_k = a_k \cos(p_k t) + b_k \sin(p_k t) + \int_0^t \frac{1}{p_k} \sin p_k(t-\tau) A_k \mathrm{e}^{-a_0\tau}\mathrm{d}\tau,$$

or

$$T_k = a_k \cos(p_k t) + b_k \sin(p_k t) + \frac{A_k}{a_0^2 + p_k^2}\left[\frac{a_0}{p_k}\sin(p_k t) - \cos(p_k t)\right] + \frac{A_k}{a_0^2 + p_k^2} e^{-a_0 t}, \tag{21}$$

where in "Eq. 4," we have [5]: $a_k = \frac{1}{lJ_1^2(\mu_k)}\int_0^l f(x)J_0\left(\mu_k\sqrt{\frac{l-x}{l}}\right)\mathrm{d}x$, $b_k = \frac{2}{a\mu_k\sqrt{l}J_1^2(\mu_k)}\int_0^l F(x)J_0\left(\mu_k\sqrt{\frac{l-x}{l}}\right)\mathrm{d}x$.

The first two terms of the right side of "Eq. 21" correspond to free vibrations, the third term corresponds to free accompanying vibrations, and the fourth term represents forced vibrations.

The particular solution of "Eq. 11" is equal to the product $X_k(z)T_k(t) = J_0(\lambda_k z)T_k(t)$, and a general solution is equal to their sum. Going to the variable $x$ in "Eq. 10," for the general solution of "Eq. 2" in the first iteration, we obtain

$$v(x,t) = \sum_{k=1}^{\infty} X_k(x)T_k(t) = \sum_{k=1}^{\infty} J_0\left(\mu_k\sqrt{\frac{l-x}{l}}\right)\{a_k\cos(p_k t) + b_k\sin(p_k t) + \frac{A_k}{a_0^2+p_k^2}\left[\frac{a_0}{p_k}\sin(p_k t) - \cos(p_k t)\right] + \frac{A_k}{a_0^2+p_k^2}e^{-a_0 t}\Big\} \tag{22}$$

## 3.2 Second Iteration

Taking into account "Eq. 22" and "Eq. 17," we transform "Eq. 1" as follows:

$$MR^2\ddot{\varphi} + c_1\dot{\varphi} = -c^* - \gamma R\int_0^l \sum_{k=1}^{\infty} X_k(x)\ddot{T}_k(t)\mathrm{d}x,$$

$$MR^2\ddot{\varphi} + c_1\dot{\varphi} = -c^* - \gamma R\sum_{k=1}^{\infty}\ddot{T}_k(t)\int_0^l J_0\left(\mu_k\sqrt{\frac{l-x}{l}}\right)\mathrm{d}x,$$

$$MR^2\ddot{\varphi} + c_1\dot{\varphi} = -c^* - \gamma R\sum_{k=1}^{\infty} 2l^2\frac{1}{\mu_k}J_1(\mu_k)\ddot{T}_k(t)$$

and we present the last equation into canonical form

$$\ddot{\varphi} + a_0\dot{\varphi} = -c_0 - \sum_{k=1}^{\infty} d_k\left[c\ddot{s}_k\cos(p_k t) + s\ddot{n}_k\cos(p_k t) + \ddot{B}_k\mathrm{e}^{-a_0 t}\right]. \tag{23}$$

Here, $d_k = \frac{2\gamma l^2}{MR}\frac{J_1(\mu_k)}{\mu_k}$ is set and after double differentiation of $T_k(t)$, we obtain $c\ddot{s}_k = p_k^2\left(\frac{A_k}{a_0^2+p_k^2} - a_k\right)$, $s\ddot{n}_k = -p_k^2\left(\frac{A_k}{a_0^2+p_k^2}\frac{a_0}{p_k} + b_k\right)$, where $p_k^2 = \frac{\lambda_k^2 a^2}{4} = \frac{\lambda_k^2 g}{4}$, $A_k = \frac{2g(c^*+c_1\dot{\varphi}_0)}{MR\mu_k J_1(\mu_k)}$.

The general solution of the inhomogeneous equation "Eq. 23" is presented as the sum of the solution $\Phi(t)$ of the homogeneous equation, obtained in the first iteration, taking into account "Eq. 6"

$$\Phi(t) = \frac{\dot{\varphi}_0}{a_0}\left(1 - \mathrm{e}^{-a_0 t}\right) \tag{24}$$

and the particular solution $\eta(t)$, defined by the Duhamel integral, which can be represented as the sum of three summands $\eta_1, \eta_2, \eta_3$.

The first term $\eta_1(t)$, when acceleration $\ddot{v}$ is not taken into account, is defined in the first iteration as

$$\eta_1(t) = \int_0^t \frac{1}{a_0}\left(1 - \mathrm{e}^{-a_0(t-\tau)}\right)(-c_0)\mathrm{d}\tau = \frac{c_0}{a_o^2}\left(1 - \mathrm{e}^{-a_0 t}\right) - \frac{c_0}{a_0}t. \tag{25}$$

The sum $\Phi(t) + \eta_1(t)$ is the same as in "Eq. 7," and it is the law of motion of the disk in the first iteration, when the influence of the vibrations of the chain is not taken into account.

The second term $\eta_2(t)$ caused by free vibrations and free accompanying vibrations of the chain, is obtained in the following form

$$\begin{aligned}\eta_2(t) &= \int_0^t \frac{1}{a_0}\left(1 - \mathrm{e}^{-a_0(t-\tau)}\right)\left\{-\sum_{k=1}^{\infty} d_k[c\ddot{s}_k\cos(p_k\tau) + s\ddot{n}_k\sin(p_k\tau)]\right\}\mathrm{d}\tau \\ &= -\sum_{k=1}^{\infty} d_k\left\{f_{k1} + f_{k2}\cos(p_k t) + f_{k3}\sin(p_k t) + f_{k4}\mathrm{e}^{-a_0 t}\right\},\end{aligned} \tag{26}$$

where $f_{k1} = \frac{1}{a_0 p_k}s\ddot{n}_k$, $f_{k2} = -\frac{1}{a_0}\left[\frac{a_0}{a_0^2+p_k^2}c\ddot{s}_k - \left(\frac{1}{p_k} - \frac{p_k}{a_0^2+p_k^2}\right)s\ddot{n}_k\right]$, $f_{k3} = \frac{1}{a_0}\left[-\frac{a_0}{a_0^2+p_k^2}s\ddot{n}_k + \left(\frac{1}{p_k} - \frac{p_k}{a_0^2+p_k^2}\right)c\ddot{s}_k\right]$, $f_{k4} = \frac{(a_0 c\ddot{s}_k - p_k s\ddot{n}_k)}{a_0\left(a_0^2+p_k^2\right)}$

The third term $\eta_3(t)$, caused by forced vibrations, is obtained in the following form

$$\begin{aligned}\eta_3(t) &= \int_0^t \frac{1}{a_0}\left(1 - \mathrm{e}^{-a_0(t-\tau)}\right)\left(-\sum_{k=1}^{\infty} d_k\ddot{B}_k\mathrm{e}^{-a_0\tau}\right)\mathrm{d}\tau \\ &= -\sum_{k=1}^{\infty}\underbrace{d_k\frac{A_k a_0^2}{a_0^2+p_k^2}}_{f_k}\left[\frac{1}{a_0^2} - \frac{1}{a_0}\left(\frac{1}{a_0} + t\right)\mathrm{e}^{-a_0 t}\right] \\ &= -\sum_{k=1}^{\infty} f_k\left[\frac{1}{a_0^2} - \frac{1}{a_0}\left(\frac{1}{a_0} + t\right)\mathrm{e}^{-a_0 t}\right],\end{aligned} \tag{27}$$

where $f_k = \gamma\, g\left(\frac{2l}{\mu_k M R}\right)\underbrace{(c^* + c_1\dot{\varphi}_0)}_{\text{moment at } t=0}\frac{a_0^2}{a_0^2+p_k^2}$.

As a result of various inelastic damping, free oscillations gradually die out [19]; therefore, only the influence of steady forced vibrations is of practical importance.

The law of motion of the disk $\varphi(t)$ is obtained in this way, and after differentiation, so is the law of change of angular velocity $\omega = \dot{\varphi}$, which allows for determination of the stopping time of the disk, according to the mechanism of motion.

Like in the first iteration, we transform the partial differential equation of motion for the chain

$$g\frac{\partial}{\partial x}\left[(l-x)\frac{\partial \nu}{\partial x}\right]-\frac{\partial^2 \nu}{\partial t^2}=R\ddot{\varphi} \tag{28}$$

by introducing a new variable $z$ using the Formula (10). The displacement $\nu(z,t)$ and the right side of "Eq. 28" are represented as series of Eigenfunctions of the corresponding problem of free vibrations—"Eq. 13." Performing the steps from the first iteration, we obtain $S_m(t)$ $(m=1,2,\ldots)$ in the form

$$S_m(t)=\frac{2}{\mu_m J_1(\mu_m)}R\ddot{\varphi} \tag{29}$$

and the equation for determining $T_m(t)(m=1,2,\ldots)$ takes the form

$$\ddot{T}_m+p_m^2 T_m=-a^2\frac{2}{\mu_m J_1(\mu_m)}R\ddot{\varphi}, \tag{30}$$

where $p_m^2=\frac{\lambda_m^2 a^2}{4}=\frac{\lambda_m^2 g}{4}$, $\lambda_m=\frac{\mu_m}{\sqrt{l}}$.

The angular acceleration $\ddot{\varphi}$ in the right part of "Eq. 30" is determined by taking into account only the influence of the moment of braking and the forced vibrations of the chain, i.e., $\Phi(t)$ from "Eq. 24," $\eta_1(t)$ from "Eq. 25," and $\eta_3(t)$ from "Eq. 27." In this case, "Eq. 30" is written as

$$\ddot{T}_m+p_m^2 T_m=\frac{2gR}{\mu_m J_1(\mu_m)}\left(A_0+\sum_{k=1}^{\infty}f_k\right)\mathrm{e}^{-a_0 t}-\frac{2gR}{\mu_m J_1(\mu_m)}a_0\left(\sum_{k=1}^{\infty}f_k\right)t\,\mathrm{e}^{-a_0 t} \tag{31}$$

The general solution of the inhomogeneous equation "Eq. 31" as a sum of the solution of the corresponding homogeneous equation, obtained with initial conditions, and the particular solution, obtained with zero initial conditions from Duhamel's integral, is presented in the form

$$\begin{aligned}T_m=&\,a_m\cos(p_m t)+b_m\sin(p_m t)+\\&+\frac{2gR}{\mu_m J_1(\mu_m)}\frac{A_0+\sum\limits_{k=1}^{\infty}f_k}{a_o^2+p_m^2}\left[\frac{a_0}{p_m}\sin(p_m t)-\cos(p_m t)\right]+\\&+\frac{2gR}{\mu_m J_1(\mu_m)}\frac{1}{a_o^2+p_m^2}\left\{A_0+\left[1-a_0\left(t+\frac{2a_0}{a_o^2+p_m^2}\right)\sum_{k=1}^{\infty}f_k\right]\right\}\mathrm{e}^{-a_0 t}.\end{aligned} \tag{32}$$

The first two terms of the right side of "Eq. 32" correspond to free vibrations; the third term corresponds to free accompanying vibrations, and the fourth term

represents forced vibrations, which are of great practical importance to engineering practice.

By introducing the variable $x$, according to "Eq. 10," for the general solution of "Eq. 2" in the second iteration, we obtain

$$v(x,t) = \sum_{m=1}^{\infty} X_m(x)T_m(t) = \sum_{m=1}^{\infty} J_0\left(\mu_m\sqrt{\frac{l-x}{l}}\right)\{a_m\cos(p_m t) + b_m\sin(p_m t)$$
$$+\frac{2gR}{\mu_m J_1(\mu_m)}\frac{A_0 + \sum\limits_{k=1}^{\infty} f_k}{a_o^2 + p_m^2}\left[\frac{a_0}{p_m}\sin(p_m t) - \cos(p_m t)\right] +$$
$$+\frac{2gR}{\mu_m J_1(\mu_m)}\frac{1}{a_o^2 + p_m^2}\left\{A_0 + \left[1 - a_0\left(t + \frac{2a_0}{a_o^2 + p_m^2}\right)\sum_{k=1}^{\infty} f_k\right]\right\}\mathrm{e}^{-a_0 t}\Bigg\}. \tag{33}$$

Thus, the approximate solution of the system of differential equations of motion "Eq. 1" and "Eq. 2" is obtained by applying two iterations in the case when there is not a mass on the end of the chain.

## 4 Numerical Example

The formulas of the approximate analytical solution of the system of differential equations of motion "Eq. 1" and "Eq. 2" are used to study the motion of the crane trolley in the braking regime. The crane trolley's mass is equal to 6200 kg, and its speed is 25 m/min. After reduction of the crane trolley to the dynamic model in Fig. 1b, the following is received

$m_1 = 250.8\,\mathrm{kg}$, $m_3 = 5949.2\,\mathrm{kg}$, $\gamma = 2.274$ kg/m, $R = 0.16\,\mathrm{m}$, $l = 16\,\mathrm{m}$.

Braking of the trolley by the engine occurs during its operation in the reverse-current braking mode [14]. When determining the braking moment $T_{\mathrm{b}}^* = \left(c' + F_{\mathrm{W}}R\right) + c_1\dot{\varphi}\left(c^* = c' + F_{\mathrm{W}}R = 194.456\,\mathrm{Nm}, c_1 = 4,83\,\mathrm{Nms}\right)$, the characteristics of the engine and the resistance force of motion were taken into account.

The nonlinear change in the angular velocity $\omega$ of the disk in the process of stopping is shown in Fig. 2a.

The position of the chain in the process of stopping the motion mechanism is shown in Fig. 2b. At the initial moment of braking, we accept zero initial conditions from "Eq. 4" for the chain, since this state corresponds to a large extent to the stationary motion of the trolley. From left to right, the position of the chain corresponding to 0.25; 0.5; 0.75 of braking time is shown, and to the right—the position of the chain at the time of stopping the trolley. Note that the graphs based on the results take into account the first three Eigenfrequencies. The position of the chain corresponding to the first three Eigenfrequencies at moment $t = 0.5\,T_{\mathrm{stop}}$, represented by numbers 1, 2, 3 in Fig. 2c, and number 4, is the total deflection of the chain. The data for plotting

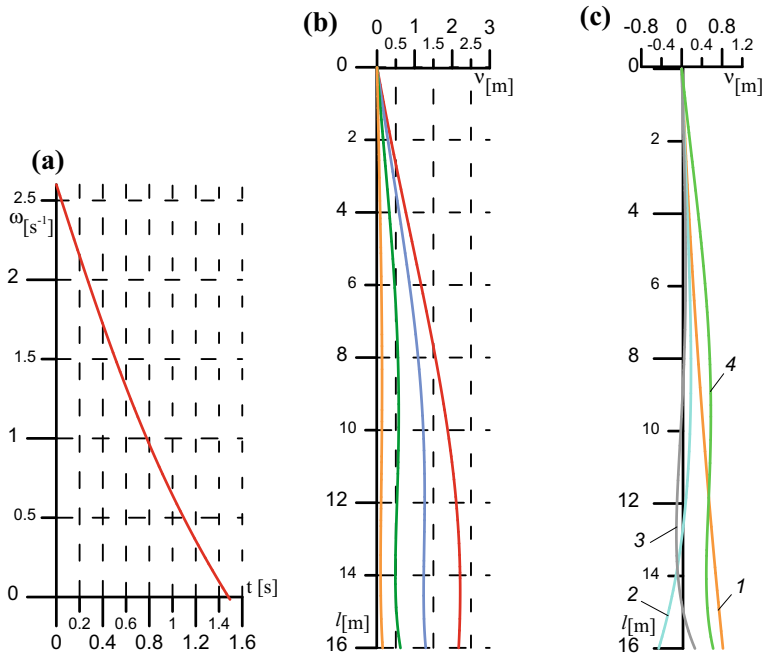


**Fig. 2** **a** Changing of angular velocity $\omega$. **b** Position of the chain during braking time. **c** Position of the chain at the moment $t = 0.5\ T_{\text{stop}}$

Fig. 2 obtained by a program developed in the Visual Fortran environment are based on the method presented in this paper.

## 5 Conclusion

In this paper, the dynamic model of the motion mechanism of load-lifting machines, such as a crane trolley, is presented. The vibrations of the chain in braking regime of the motion mechanism are investigated. First, it is assumed that the chain is flexible, inextensible, homogeneous, and heavy; second, that the braking regime of the motion mechanism is a linear function of its velocity. A method of approximate analytical solutions of the obtained system of differential equations of motion is presented. The solution is obtained by two iterations. The results are illustrated with an example based on the technical characteristics of the crane trolley that the Visual Fortran program was created for.

**Acknowledgements** S. G. Nikolov's research was carried out with the financial support of project № 148/12.04.2018, Todor Kableshkov Higher Transport School, Sofia, Bulgaria.

## References


1. Lurie AI (2002) Analytical mechanics. Springer–Verlag, Berlin
2. De Silva CW (2000) Vibration: fundamentals and practice. CRC Press, Boca Raton
3. Leissa AW, Qatu MS. Vibrations of continuous systems. McGraw Hill, New York
4. Rao SS (2007) Vibrations of continuous systems. Wiley, Hoboken, New Jersey
5. Merkin DR (1980) Introduction to mechanics of elastic chain. Nauka, Moscow (in Russian)
6. Svetlitsky VA (1978) Mechanics of elastic rods and chains. Machinostronie, Moscow (in Russian)
7. Stepanov AG (1999) Dynamics of machines. UrO RAN, Yekaterinburg (in Russian)
8. Malyshev AP (2008) Numerical modeling of the forces nonlinear vibrations of a chain. Mech Solid Body 5:32–38 (in Russian)
9. Islamova OA (2007) Mathematical modeling of vibrations of the suspended heavy chain. News SFU 1(73):204–209 (in Russian)
10. Gadyl'shin TR (2005) On the vibrations of a string with a concentrated mass and rapidly oscillating density. Comptes Rendus Mécanique 343(9):476–481
11. Stulov A, Kartofelev D (2014) Vibration of strings with nonlinear supports. Appl Acoust 76:223–229
12. Sandilo SH, van Horsen Wilm T (2014) On variable length induced vibrations of a vertical string. J Sound Vib 333(11):2432–2449
13. Aleksandrov MP et al (1986) Load-lifting machines. Machinostronie, Moscow (in Russian)
14. Lobov NA (2003) Dynamics of motion of cranes on a railway line. Publishing house of MSTU Bauman, Moscow (in Russian)
15. Bachvarov St, Zlatanov V, Nikolov S (2005) Dynamics of a traveling crane with load during braking regime. In: 10th jubilee national congress on theoretical and applied mechanics, Varna, Bulgaria, September 2005. Proceedings of 10th jubilee national congress on theoretical and applied mechanics, vol 1, Prof. M. Drinov Academic Publishing House, pp 27–33
16. Zlatanov V (2015) Modeling of mechanical system with the suspended loads in lifting device. Eur J Sci Res 1(11) vol III:731–740
17. Panavko IG (1976) Basses of the applied theory of the vibrations and blow. Machinostronie, Leningrad (in Russian)
18. Janke E, Emd F, Losch F (1964) Special functions. Nauka, Moscow (in Russian)
19. Ilyin MM, Kolesnikov KS, Saratov YS (2003) Theory of vibrations. Publishing house of MSTU Bauman, Moscow (in Russian)

# Author Index





A. N. Evgrafov (ed.), *Advances in Mechanical Engineering*,
Lecture Notes in Mechanical Engineering,
https://doi.org/10.1007/978-3-030-11981-2